sciendo

Remediation potential of bacterial mixed cultures for polychlorinated biphenyls (PCBs) biodegradation

Hana Horváthová, Katarína Lászlová, Katarína Dercová

Institute of Biotechnology, Faculty of Chemical and Food Technology, Slovak University of Technology, Radlinského 9, 812 37, Bratislava, Slovak Republic
hana.horvathova@stuba.sk
ORCIDs: Hana Horváthová 0000-0003-3497-2361, Katarína Lászlová 0000-0002-5763-8625, Katarína Dercová 0000-0002-1242-9985

Abstract: Remediation of polychlorinated biphenyls (PCBs) in minimal mineral water media in the presence of bacterial mixed cultures consisting of several individual strains is proposed. Starting from the fact that the properties and features of bacterial strains in mixed cultures can be supplemented and compensated, two-, three- and seven-membered mixed cultures (MC) were performed. The strains used for the construction of the MC were isolated from the waste canal of a former PCB producer. The highest biodegradation of 70 % of the sum of seven defined PCB congeners was achieved by two-membered MC containing the strains *Rhodococcus* sp. and *Stenotrophomonas maltophilia* added in the biomass ratio of 1 : 3 and 3 : 1. PCB biodegradation by a seven-membered MC was lower (58 %) but provided several benefits over the less-membered mixed cultures or the individual strains: similarity to naturally occurring microflora, easier preparation of the inocula, certain and repeatable results. Periodical reinoculation of the water media resulted to PCB biodegradation increase to 65 %. Seven-membered MC was applied to the historically PCB contaminated sediment as well, where a 59 % degradation of the sum of seven PCB congeners was determined.

Keywords: bacteria, biodegradation, bioremediation, mixed cultures, PCBs

Introduction

Polychlorinated biphenyls (PCBs) are dangerous hydrophobic substances containing the biphenyl molecule with varying degree of chlorination. Long-term use and improper storage led to their release into the environment (Wu et al., 2018). The water cycle had spread them across all ecosystems; they were detected even in the cryoconite of alpine glacier (Weiland-Bräuer et al., 2017). PCBs are able to penetrate into the food chain and deposit in adipose tissues (Louis et al., 2016). In higher organisms, they are responsible for a wide range of diseases resulting from their endocrine-disrupting property (Bergman et al., 2001; Fénichel and Chevalier, 2017; Pinson et al., 2017). Usually, some organisms that came in long term contact with PCB contamination — plants, lower soil animals, microbes — have adapted to their presence. For example, Leigh et al. (2006) demonstrated the biodegradation ability of bacterial strain isolated from the root system of plants growing on a PCB contaminated site. Especially microorganisms are able not only to exist in the presence of PCBs but also to decompose them (Chen et al., 2015; Stella et al., 2017; Horváthová et al., 2018). This fact serves as the basis for many bioremediation techniques. Bioremediation can be described as the conversion of organic pollutants (e.g. chlorinated hydrocarbons) by microorganisms into energy, cell mass and biological waste products (Nikolopoulou and Kalogerakis, 2010; Santisi et al., 2015) and can be implemented as bioaugmention of the contaminated sites with propagated biomass (Horváthová et al., 2018) as biostimulation of naturally occurring microflora provided by (bio) surfactants (Lászlová et al., 2018), plant terpenes (Murínová and Dercová, 2014) and additional nutrients, or as phytoremediation by specialized plants and rhizoremediation by plant roots (Liu et Schnoor, 2008; Slater et al., 2011). There is wide evidence of successful bacterial bioremediation provided by individual bacterial strains as well as by mixed cultures either alone or in combination with other microorganisms or an additional process. It is possible to use: 1) individual bacterial strains, 2) mixed cultures obtained by enrichment from a contaminated environmental sample, 3) artificially prepared mixed cultures made from several individual strains, 4) integrated approach combining biodegradation of PCB by individual strains/ mixed cultures with a physico-chemical method for their elimination, e. g. use of nanoscale zerovalent iron (Cecchin et al., 2017), ozonation (Dudášová et al., 2017), or sorption on activated carbon (Ghosh et al., 1999). Soil/sediment microorganisms form a wide synergic or antagonistic community, where the product of metabolism of one group provides a substrate for another group of microbes (Kwon et al., 2008; Murínová et al., 2014). This is the reason why the application of microbial, especially

bacterial, mixed cultures emerges as a promising bioremediation technique. An example of the integration of different (bio)remediation techniques is the removal of 36.46 μmol kg^{-1} of tetrachlorinated congener PCB 61 in 140 days from the original quantity of 50 μmol kg^{-1} of dry sediment using a bio-electrochemical reactor with poised potential of –0.50 V, acetate as carbon source and an addition of Tween 80. During the experiment, several bacterial strains were isolated and identified, which contributed to the degradation of PCB 61 as an aerobic bacterial mixed culture (Yu et al., 2017). Bacterial mixed culture was successful also in the biodegradation of polycyclic aromatic hydrocarbons (PAHs). Strains enriched from manufactured gas plant site applied as bacterial mixed cultures were able to degrade >95 % of LMW and 90 % of HMW PAHs (Kuppusamy et al., 2016). Eio et al. (2014) completely degraded bisphenol-A up to 50 mg L^{-1} using sufficiently adapted non-specific bacterial mixed culture enriched by activated sludge obtained from the wastewater treatment plant. Our previous research focused on bioremediation of PCB contaminated sediment showed that suitably selected combinations of two or three bacterial strains are able to degrade a significant amount of PCBs naturally occurring in the sediment. Biodegradation of 80 % of the sum of seven PCB congeners was achieved using a two-membered mixed culture and biodegradation of 70 % was achieved when a three-membered mixed culture was applied (Horváthová et al., 2018). This research is focused on the bioremediation of defined minimal mineral media artificially contaminated by technical PCB mixture Delor 103 (equivalent to Aroclor 1242 containing 59 PCB congeners) by bacterial mixed cultures consisting of two, three and seven individual bacterial strains isolated from the sediment originating from the waste canal of the Chemko Strážske plant — a former PCB producer.

Materials and Methods

Preparation of cell suspensions

Strains used for the preparation of mixed cultures (MC) were isolated from the waste canal of the Chemko Strážske plant in Eastern Slovakia and characterized using molecular techniques (Dudášová et al., 2014) as *Achromobacter xylosoxidans*, *Stenotrophomonas maltophilia*, *Rhodococcus* sp., *Ochrobactrum anthropi*, *Pseudomonas mandelii*, *Brevibacterium* sp. and *Starkeya novella*. Mixed cultures composed of two (MC2), three (MC3) and seven (MC7) of these strains were investigated to degrade PCBs. MC2 and MC3 were prepared by inoculating liquid Culture broth no. 2 (Biolife, IT) by individual bacterial strains from stored agarised Culture broth no. 2. After 48 h of cultivation on a rotary shaker (180 rpm) at 28 °C, cells were harvested by centrifugation and cell suspensions were prepared by stirring the biomass pellet in distilled water. Concentration of the cell suspension required for the biodegradation experiment was calculated from the optical density at 620 nm (OD_{620}) by calibration curves (not shown). MC7 was prepared by inoculating Culture broth no. 2 with each individual strain from the slant agars. After 48 h of cultivation on a rotary shaker, 10 % (v/v) cell inoculum was used.

Determination of cell concentration

Measuring of OD_{620}. Concentration of bacterial biomass was determined by withdrawing and suitably diluting a sample from the flask and calculated from the calibration curve.

Sowing on the plate agar. The sample was serially diluted (10^7) and sowed on Plate count agar (Sigma-Aldrich, USA) in Petri dishes with a microbiological L-shape spreader. After 48 h of inverse cultivation in the cultivation box at 28 °C, the number of CFU mL^{-1} was determined using a handy colony counter (BIO KOBE, JP).

Biodegradation of Delor 103 mixture in artificially contaminated minimal mineral medium (MM medium)

Biodegradation experiments took place in 500 mL Erlenmeyer flasks closed with cotton stoppers with 100 mL of the MM medium of the following composition: 1 g L^{-1} of $(NH_4)_2SO_4$, 2.7 g L^{-1} of KH_2PO_4, 5.2 g L^{-1} of $NaHPO_4 \cdot 2\ H_2O$, 0.2 g L^{-1} of $MgSO_4 \cdot 7\ H_2O$, 0.01 g L^{-1} of $FeSO_4 \cdot 7\ H_2O$ and 0.03 g L^{-1} of $Ca(NO_3)_2 \cdot 4\ H_2O$ (Lachema Brno, CZ), and the technical mixture Delor 103 (Chemko Strážske, SR) in the final concentration of 100 mg L^{-1}. To examine the biodegradation ability of the individual bacterial isolates, MC2 and MC3 cell suspensions prepared from 48 h inocula of the individual strains were added in the final concentration of 1 g L^{-1}. When MC2 was used, the cell suspensions were added in the biomass ratio of 1 : 3, 1 : 1 and 3 : 1, and in the biomass ratio of 1 : 1 : 1 for MC3. In the biodegradation of PCBs by MC7, 10 % (v/v) 48 h inoculum of seven bacterial isolates was added. The flasks were closed with cotton stoppers and placed on the rotary shaker for 14 days (biodegradation provided by MC2, MC3) and for 21 days (MC7) at 28 °C and rotation speed of 180 rpm. Flasks with PCBs bioremediation by MC7 were reinoculated with fresh 48 h inoculum after seven and 14 days of cultivation. All experiments ran in three parallel measurements. For the determination of PCB biodegradation in each set-

ting, abiotic control (only MM medium with 100 mg L^{-1} of Delor 103 mixture) was used. Seven PCB congeners monitored during the biodegradation represented 30.4 % of the total weight of Delor 103 mixture. At the beginning and at the end of the bioremediation with the individual strains, biomass concentration using calibration curves was calculated after withdrawing and diluting a sample from each flask and measuring the OD_{620}.

Biodegradation of PCBs in historically contaminated river sediment

The following experiments took place in 250 mL Erlenmeyer flasks with 10 g of dried and sieved sediment drenched with 100 mL of MM medium and 10 % (v/v) 48 h inoculum of mixed culture consisting of seven individual strains (MC7). The flasks were stationary cultivated at 28 °C for 21 days with occasional shaking. After the cultivation time, the sediment was harvested by centrifugation, dried and PCBs were extracted with n-hexane (Mikrochem, SR). Sediment used in the experiments was collected from the waste canal of the Chemko Strážske plant using an Uwitec sampler (Austria) according to the Slovak Technical Norm. The total amount of seven monitored PCB congeners was 22.7 mg kg^{-1} (Horváthová et al., 2018).

Analysis of PCBs

After the cultivation, non-degraded PCBs were extracted from the MM media in a two-stage extraction with n-hexane. First, 10 mL of n-hexane were added to each flask and these were placed in an ultrasonic bath for 5 min to release the residual PCBs from the glass and from the bacterial cell structures. The whole flask content was then moved to a separating funnel for intensive shaking (2 min). After the liquid phases settled, water phase was released to the second separating funnel for the second extraction (2 min). n-Hexane phases were combined and dehydrated by filtration via an anhydrous Na_2SO_4 (Centralchem, SR) column. Residual PCBs in the sediment were extracted to n-hexane with a Soxhlet extraction apparatus. The extracts were purified by ultrasonic bath with copper (45 min), filtered through cotton wool and poured into a Florisil column. PCB extracts were subsequently analyzed by gas chromatography with an electron capture detector (GC ECD) under the same conditions as in Murínová et al. (2014). The total biodegradation of seven selected PCB congeners: (PCB 8 (2,4´-), PCB 28 (2,4,4´-), PCB 52 (2,2´,5,5´-), PCB 101 (2,2´,4,5,5´-), PCB 118 (2,3´,4,4´,5-), PCB 153 (2,2´,4,4´-5,5´-)), were evaluated based on the peak area according to Mills et al. (2007).

Statistical analysis

All experiments were done in three parallel measurements. The obtained data were processed using the software package MS Excel One way ANOVA (analysis of variance) for statistical evaluation. Differences in the biodegradation of the sum of seven PCB congeners observed in the applied degradation approaches (single strains, two-, three- and seven-membered mixed cultures) are greater than expected. There is a statistically significant difference if the P-value is below 0.05. P-values obtained from statistical analysis of an appropriate group of results meet these conditions.

Results and Discussion

Biodegradation of Delor 103 mixture by individual bacterial strains, two- and three-membered mixed cultures

When examining the biodegradability of Delor 103 by the individual bacterial strains in artificially contaminated MM medium, the following biodegradations were obtained: *O. anthropi* 60 %; *A. xylosoxidans* 41 %; *S. maltophilia* 40 %; *Brevibacterium* sp. 33 %; *S. novella* 19 %, *Rhodococcus* sp. 18 % and *P. mandelii* 17 % from the initial amount of the sum of seven selected PCB congeners (Tab. 1). Comparable results were obtained with an endophytic bacterial strain isolated from the leaves of *Salix matsudana* f. *pendula*. This strain, identified as *Enterobacter* sp., was able to degrade Aroclor 1242 mixture (equivalent to Delor 103) with the removal ratio of 43.2 % after seven days in liquid minimal medium (Cai et al., 2018). PCB-degrading strains isolated from the surface sediment sampled from Svalbard Islands by Papale et al. (2017) were able to remove Aroclor 1242 at 15 °C within a month in microcosm with the efficiency varying between 7 % and 70 %. From our isolates, *O. anthropi* (O), *A. xylosoxidans* (A), *S. maltophilia* (S) and *Rhodococcus* sp. (R) were selected for the assembly of two- and three-membered mixed cultures (MC2 and MC3). Although our strains were isolated from the same environment, there are some differences in the biodegradation of the sum of seven PCB congeners as well as in that of each congener. Biodegradation of individual PCB congeners by all above mentioned strains, except for *S. maltophilia,* decreased with the increasing amount of chlorine on the PCB molecule. Only *S. maltophilia* was able to degrade various PCB congeners with the same efficiency (data not shown). This variability was the basis for the preparation of the mixed cultures. It was assumed that the application of multiple bacterial strains simulates the

site microbiological composition better than the individual bacterial strains and that it is ultimately beneficial. To determine whether the biodegradation took place in growth or non-growth conditions, OD_{620} was measured immediately after the experiment setting and after 14 days, before the extraction of non-degraded PCBs. No increase in OD_{620} was measured for any individual strain so it was assumed that biodegradation provided by all strains runs at non-growth conditions (Tab. 1). The largest changes in biomass concentration were observed during the biodegradation with *S. maltophilia* and *S. novella* (81 % and 57 % decrease of biomass concentration). On the contrary, the smallest decrease of the biomass concentration was observed in the biodegradation with *A. xylosoxidans* (29 %).

Two-membered mixed cultures — MC2 consisted of two individual bacterial strains added in the biomass ratios of 1 : 3, 1 : 1 and 3 : 1. First MC2 (Fig. 1a) consisting of the strains *Rhodococcus* sp. and *A. xylosoxidans* added in the biomass ratio of 1 : 3 with an excess of *A. xylosoxidans* degraded 61 % of the sum of seven PCB congeners studied. This result is favorable considering that individual strains *Rhodococcus* sp. and *A. xylosoxidans* degraded only 18 % and 41 % of the sum of seven PCB congeners. Independently of the added biomass ratio, biodegradation of individual PCB congeners by this MC decreased with the increasing degree of PCB chlorination. Biodegradation of hexachlorinated PCB 138 was by approximately 40 % less effective than that of dichlorinated congener PCB 8. These differences in the biodegradation of variously substituted PCB congeners were diminished by the second MC2 (Fig. 1b) consisting of the strains *S. maltophilia* and *Rhodococcus* sp, which degraded 70 % of the sum of seven PCB congeners at the added biomass ratio of 1 : 3 and 3 : 1. At the biomass ratio of 1 : 1, the biodegradation was by more than 10 % less efficient. The difference in the congener analysis was not as significant as with the first MC2. All, lower and higher, chlorinated PCB congeners were removed in a comparable extent. Moreover, biodegradation of PCBs by this MC2 was more efficient than application of the relevant individual strains. The lowest efficiency of PCB biodegradation was observed with the third MC2 (Fig. 1c) containing *O. anthropi* and *A. xylosoxidans*. Biomass inoculated in the ratio of 1 : 1 degraded the sum of seven PCB congeners to 59 %, which is comparable with the biodegradation achieved with the individual strain *O. anthropi* (60 %). In this MC2, the highest differences were observed in the biodegradation of PCBs considering the three different biomass ratios.

Three-membered MC3 (Fig. 1d) were not as efficient as expected. Combinations OAS (*O. anthropi*, *A. xylosoxidans*, *S. maltophilia*), ORA (*O. anthropi*, *Rhodococcus* sp., *A. xylosoxidans*) and ORS (*O. anthropi*, *Rhodococcus* sp., *S. maltophilia*) with the biomass ratio of 1 : 1 : 1 removed only 29 %, 39 % and 19 % of the seven PCB congeners despite the presence of the best PCB-degrading strain *O. anthropi*. This result is probably due to a strong antagonism between the strains, and a change in the added biomass ratio should be applied in further experiments. Recently, biodegradation of bacterial mixed cultures also in the historically PCB contaminated sediment has been studied under laboratory conditions. MC2 containing the strains *Rhodococcus* sp. + *A. xylosoxidans*, and *Rhodococcus* sp. + *S. maltophilia*, both in the biomass ratio of 1 : 1 degraded approximately 80 % of the sum of seven PCB congeners, which is much more than the results achieved with the relevant individual strains in the sediment. Biodegradation was higher due to the presence of naturally occurring synergic sediment microflora which contributed to the biodegradation (Horváthová et al., 2018).

Tab. 1. Biodegradation of the sum of seven defined PCB congeners by individual bacterial strains (14 days), biomass concentration at the beginning of biodegradation and after 14 days, before the extraction of residual PCBs, expressed as percentage decrease.

Bacterial strain	Biodegradation of the sum of 7 PCB congeners (%)	Initial biomass concentration ($g\ L^{-1}$)	Final biomass concentration ($g\ L^{-1}$)	Decrease of biomass concentration (%)
O. anthropi	60	0.92	0.58	37
A. xylosoxidans	41	0.88	0.62	29
S. maltophilia	40	0.85	0.16	81
Brevibacterium sp.	33	0.81	0.43	47
S. novella	19	0.85	0.37	57
Rhodococcus sp.	18	0.83	0.39	53
P. mandelii	17	0.80	0.49	39

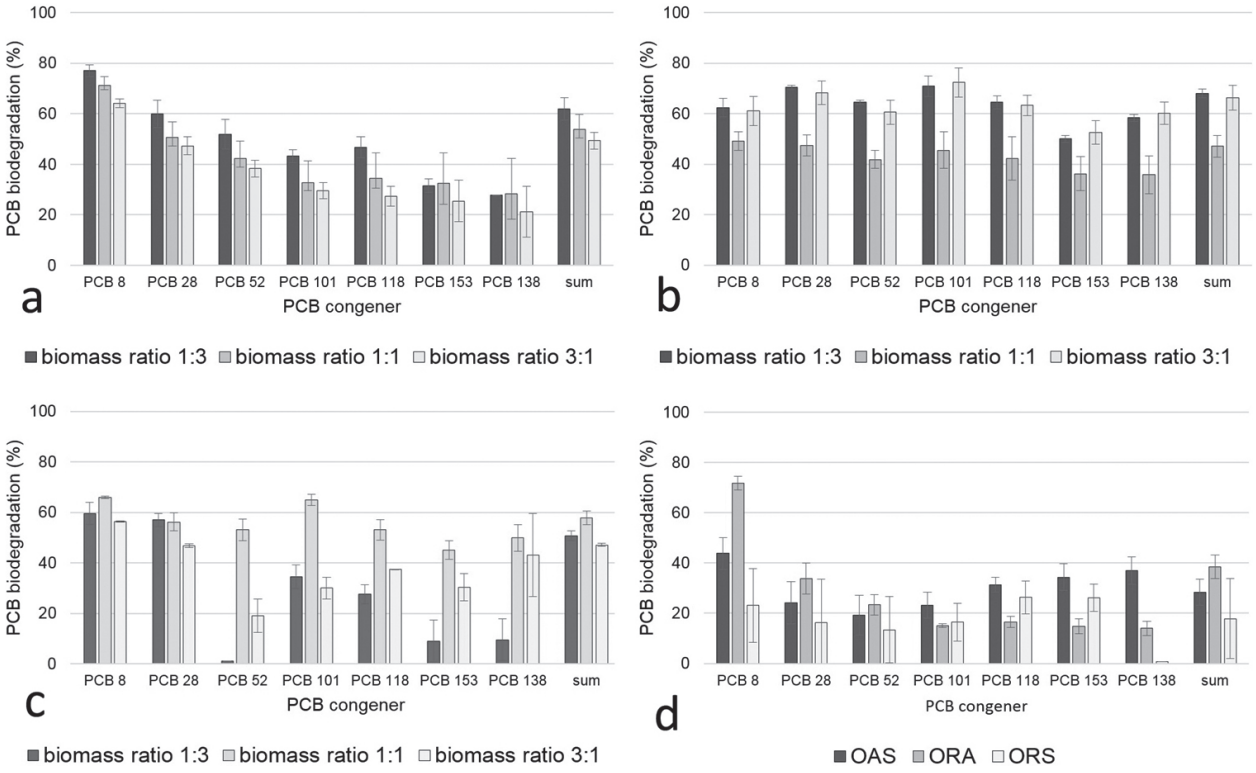

Fig. 1. Biodegradation of seven PCB congeners in minimal mineral medium (MM medium) artificially contaminated with Delor 103 by two-membered mixed cultures (MC2): *Rhodococcus* sp. + *A. xylosoxidans* (a), *Rhodococcus* sp. + *S. maltophilia* (b), *O. anthropi* + *A. xylosoxidans* (c) at the biomass ratio of 1 : 3, 1 : 1 and 3 : 1, and three-membered mixed cultures (MC3) (d) with biomass ratio of 1 : 1 : 1, where O means *O. anthropi*, A means *A. xylosoxidans*, S means *S. maltophilia* and R means *Rhodococcus* sp. Cultivation conditions: 100 mL of MM medium, 100 mg L^{-1} of Delor 103 mixture, rotary shaker — 180 rpm, 28 °C, 14 days. Abiotic control: MM medium + Delor 103 (100 mg L^{-1}).

Biodegradation of PCBs by mixed culture consisting of seven bacterial isolates (MC7)

PCB biodegradation experiments with MC7 were performed using two different sources of contamination: a) Delor 103 mixture added to the MM medium — artificial contamination with PCBs and b) historically PCB contaminated dried sediment flooded with the MM medium (Fig. 2). In the artificially contaminated MM medium, 58 % biodegradation of the sum of seven PCB congeners was observed after 21 days. Three flasks with Delor 103 biodegradation by MC7 were reinoculated after seven and 14 days of cultivation. Addition of 10 % (v/v) of fresh bacterial inocula resulted in an increased PCB biodegradation (65 % of the sum of seven PCB congeners). Generally, this is not the best result achieved by MC but the use of MC7 provides several advantages over the other ones.

Despite MC7 containing only bacterial strains, it is still more similar to the natural consortium occurring on a contaminated site. Also, MC7 is easier to prepare. It is not necessary to make cell suspensions of each individual strain and set the equivalent volume of the suspension by measuring OD_{620}, as mentioned in section 2.1., inoculating the culture broth by one inoculation loop of each strain is sufficient. During the cultivation in the liquid broth, bacterial growth is probably not uniform, the strains stabilize on basis of synergy and antagonism. The use MC7 provides stable and repeatable results in comparison with the use of single strains and two- and three-membered MCs which is fundamentally important for the scale up. In mixed cultures, some species of bacteria possibly beneficial in the degradation of PCBs by removing potentially inhibitory intermediates can be present (Clark et al. 1979). Moreover, MC7 is able to survive longer in the MM medium with Delor 103 (100 mg L^{-1}) than in that with individual strains. Biomass concentration expressed as $CFU \cdot ml^{-1}$ in a sample taken from the flask where Delor 103 biodegradation by MC7 took place increased from 9×10^9 to 19×10^9, OD_{620} of the sample after 21 days had the same value as at the beginning of the bioremediation process. As seen in Tab. 1, biomass concentration (g L^{-1}) of all individual strains decreased. However, heterogenous bacterial cultures are more resistant to PCBs, therefore they are better applicable. Our MC7 was tested

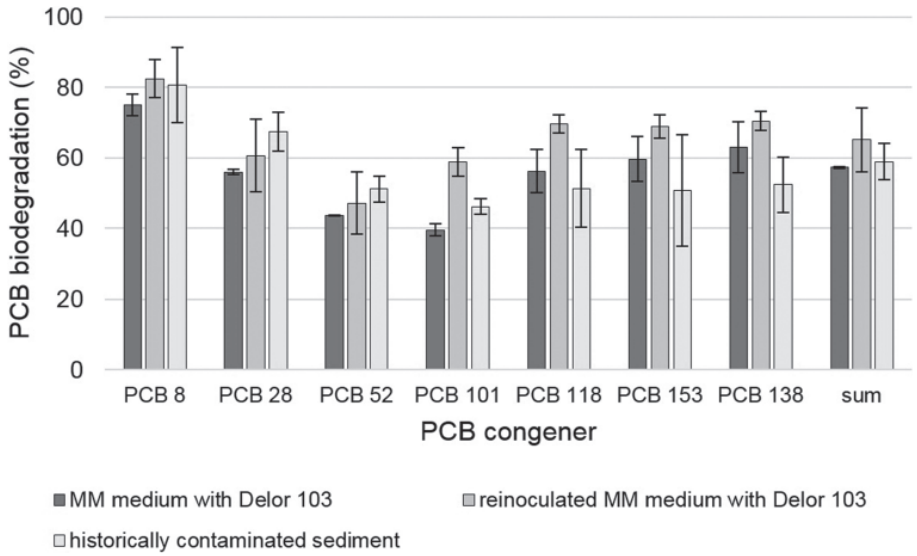

Fig. 2. Biodegradation of seven PCB congeners in the mimimal mineral medium (MM medium) artificially contaminated with Delor 103 and in historically PCB contaminated sediment by mixed culture consisting of seven bacterial strains (MC7): *Achromobacter xylosoxidans*, *Stenotrophomonas maltophilia*, *Rhodococcus* sp., *Ochrobactrum anthropi*, *Pseudomonas mandelii*, *Brevibacterium* sp. and *Starkeya novella*. Cultivation conditions in MM medium: 100 ml of MM medium, 100 mg L^{-1} of Delor 103 mixture, 10 % (v/v) 48 h inoculum of seven strains, rotary shaker — 180 rpm, 28 °C, 21 days, reinoculation after 7 and 14 days of cultivation. Abiotic control: MM medium + Delor 103 (100 mg L^{-1}). Cultivation conditions in the sediment: 100 ml of MM medium, 10 g of dried and sieved historically contaminated sediment, 10 % 48 h bacterial inoculum, stationary cultivation with occasional shaking, 28 °C, 21 days. Abiotic control: non-treated sediment.

for biodegradation of historic PCB contamination in the sediment from the former PCB producer surroundings. Microcosm bioremediation with real contaminated sediment as the PCB source was provided by flooding of the sediment with the MM medium, inoculation with MC7 and stationary cultivation under occasional shaking as mentioned in section 2.2.2. The biodegradation was similar to that achieved in the artificially contaminated MM medium, 59 % biodegradation of the sum of seven PCB congeners, and the decrease of the concentration of each congener was proportional to the total degradation of PCBs. Petrić et al. (2007) isolated two mixed cultures from polluted areas. Both cultures showed degrading activity comparable with that presented in this paper, e.g. 56 to 60 % of the mixture of 50 PCB congeners (containing di- to heptachlorinated congeners) were reduced after 14 days in PAS medium (phosphate-buffered mineral salts medium) supplemented with biphenyl. Both MCs contained the strain *Rhodococcus erythropolis* with its well-known PCB-degradation ability (Chung et al. 1994, Pham et al. 2015). The mixed cultures isolated by enrichment from the marine sediment also exhibited PCB-degrading activity. Strains forming the mixed culture mainly belong to the *Rhodococcus* and *Sphingomonas* species and despite their different PCB-degrading capability, all of them are able to degrade PCB congeners with two to four chlorine substitutions. Mixed cultures degraded the industrial mixture Aroclor 1242 in a seawater mineral salts medium within the range of 40—61 % (Kolar et al., 2007).

Conclusion

This work was focused on biodegradation of PCBs (technical mixture Delor 103) by mixed cultures consisting of two (MC2), three (MC3) and seven (MC7) bacterial strains recently isolated from the waste canal of the former producer of PCB based technical mixtures. Foremost, to consider the use of mixed cultures, biodegradation of Delor 103 mixture by the individual strains in water minimal mineral medium (MM medium) was performed. Then, the most efficient strains — gram negative *O. anthropi*, *S. maltophilia*, *A. xylosoxidans* (60, 41 a 40 % biodegradation of the sum of seven PCB congeners) and gram positive *Rhodococcus* sp. (18 % biodegradation) were used to construct the two- and three-membered mixed cultures. Biodegradation of the PCBs in MM medium contaminated with Delor 103 by three-membered mixed culture (MC3) with the biomass ratio of 1:1:1 was not significant and among two-membered (MC2), combinations, *Rhodococcus* sp.+ *A. xylosoxidans* and *Rhodococcus* sp. + *S. maltophilia* were

more efficient than the relevant single strains. The biodegradation of 61 % and 70 % with biomass added in the ratio of 1:3 was achieved. Finally, the mixed culture consisting of seven bacterial strains was constructed. MC7 degraded 58 % of the sum of seven PCB congeners in the artificially contaminated MM medium and 59 % in the historically contaminated sediment. When the MM medium was periodically reinoculated with MC7, a 65 % biodegradation of PCBs was observed. The application of the seven bacterial isolates mixed culture provides a promising remediation alternative to that of the relevant individual bacterial strains. Simple preparation of inocula tailored to the microbial conditions in the real contaminated site and repeatability are the most significant benefits for future remediation research.

Acknowledgements

This research was supported by the grants VEGA (1/0295/15) and APVV (0656-12) of the Ministry of Education, Science, Research and Sport of the Slovak Republic.

References

Bergman Å, Brouwer A, Hagmar L, Meerts I, Sjödin A (2001) APMIS Journal of Pathology, Microbiology and Immunology 109: S505.

Cai M, Song G, Li Y, Du K (2018) Phytochemistry Letters 23: 66–72.

Cecchin I, Reddy KR, Thomé A, Tessaro EF, Schnaid F (2017) International Biodeteriororation and Biodegradation 119: 419–428.

Chen F, Hao S, Qu J, Ma J, Zhang S (2015) Annals of Microbiology 65: 1847–1854.

Chung SY, Maedam M, Song E, Horikoshi K, Kudo T (1994) Bioscience, Biotechnology and Biochemistry 58: 2111–2113.

Clark RR, Chian ESK, Griffin RA (1979) Applied and Environmental Microbiology 37: 680–685.

Dudášová H, Derco J, Sumegova L, Dercová K, Lászlová K (2017) Journal of Hazardous Materials 321: 54–61.

Dudášová H, Lukáčová L, Murínová S, Puškárová A, Pangallo D, Dercová K (2014) Journal of Basic Microbiology 54: 253–260.

Eio EJ, Kawai M, Tsuchiya K, Yamamoto S, Toda T (2014) International Biodeterioration & Biodegradation 96: 166–173.

Fénichel P, Chevalier N (2017) Comptes Rendus Biologies 340: 446–452.

Ghosh U, Weber AS, Jensen JN, Smith, JR (1999) Water Environment Research 71: 232–240.

Horváthová H, Lászlová K, Dercová K (2018) Chemosphere 193: 270–277.

Kolar AB, Hršak D, Fingler S, Ćetković, Petrić I, Udiković Kolić N (2007) International Biodeterioration & Biodegradation 60: 16–24.

Kuppusamy S, Thavamani P, Megharaj M, Naidu R (2016) International Biodeterioration & Biodegradation 108: 149–157.

Kwong SH, Hong MH, Choi JH, Whang KS, Lee HS, So JS, Koh SC (2018) Biotechnology Bioprocess Engineering 13: 730–737.

Lászlová K, Dercová K, Horváthová K, Murínová S, Škarba J, Dudášová H (2016) International Journal of Environmental Research 10: 367–378.

Lászlová K, Dudášová H, Olejníková P, Horváthová G, Velická Z, Horváthová H, Dercová K (2018) Water Air Soil Pollution 229: 219.

Leigh MB, Prouzová P, Macková M, Macek, M, Nagle DP, Fletcher JS (2006) Applied and Environmental Microbiology 72: 2331–2342.

Liu J, Schnoor JL (2008) Chemosphere 73: 1608–1616.

Louis C, Covaci A, Crocker DE, Debier C (2016) Science of the Total Environment 541: 599–602.

Mills SA, Thal DI, Barney J (2007) Chemosphere 68: 1603–1612.

Murínová S, Dercová K (2014) Water Air Soil Pollution 225: 1980.

Murínová S, Dercová K, Tarábek P, Tölgyessy P (2014) Acta Chimica Slovaca 7: 44–51.

Nikolopoulou M, Kalogerakis N (2010) In: Timmins KN (ed.) Handbook of hydrocarbon and lipid microbiology (pp 2521–2529). Springer-Verlag, Berlin.

Papale M, Giannarelli S, Francesconi S, Di Marco G, Mikkonrn A, Conte A, Rizzo C, De Domenico E, Michaud L, Lo Giudice A (2017) Marine Pollution Bulletin 114: 849–859.

Petrić I, Hršak D, Fingler S, Vončina E, Ćetković H, Kolar AB, Udiković Kolić N (2007) Food Technology and Biotechnology 45: 11–20.

Pham TTM, Pino Rodriquez NJ, Hijri M, Sylvestre M (2015) PLoS ONE 10: E0126033.

Pinson A, Fransses D, Gérard A, Parent AS, Bourguignon JP (2017) Comptes Rendus Biologies 340: 432–438.

Santisi S, Capello S, Catalfamo M, Mancini G, Hassanshahian M, Genovese L, Giuliano L, Yakimov MM (2015) Brazilian Journal of Microbiology 46: 377–387.

Slater H, Gouin T, Leigh MB (2011) Chemosphere 84: 199–206.

Stella T, Covino S, Čvančarová M, Filipová A, Petruccioli M, D'Annibale A, Cajthaml T (2017) Journal of Hazardous Materials 324: 701–710.

Taniyasu S, Kannan K, Holoubek I, Ansorgova A, Horii Y, Hanari N, Yamashita N, Aldous KM (2003) Environmental Pollution 126: 169–178.

Weiland-Bräuer N, Fischer MA, Schramm KW, Schmitz RA (2017) Frontiers in Microbiology 8: 1105.

Wu X, Chen A, Wang S, Zou J, Liu H, Xiao S (2018) Atmospheric Pollution Research 9: 569–576.

Yu H, Wan H, Feng Ch, Yi X, Liu X, Ren Y, Wei Ch (2017) Science of the Total Environment 580: 1371–1380.

sciendo

Electrolytic colouring of anodized aluminium on tin basis

Barbora Šopová, Matilda Zemanová

Institute of Inorganic Chemistry, Technology and Materials,
Faculty of Chemical and Food Technology STU in Bratislava,
Radlinského 9, 812 37 Bratislava, Slovak Republic
xsopova@is.stuba.sk

Abstract: The aim of the study was to find parameters of electrolytic colouring on tin basis to form uniform black coatings on anodized aluminium. A two steps electrolytic process consisting of aluminium anodization in a sulphuric acid electrolyte and colouring in tin acidic electrolyte was used. Among parameters influencing the colouring process, AC colouring voltage, composition of the counter electrode and agitation of the colouring electrolyte were studied. Spectrocolorimetry was applied to analyse the quality of the colouring. Thickness of the coloured and sealed anodized specimens was also evaluated. Optimal parameters for uniform colouring of anodized specimens were found. Unfortunately, colouring electrolyte on tin basis is susceptible to oxidation which negatively influences the colouring.

Keywords: aluminium; anodic oxidation; tin based electrolytic colouring; hydrothermal sealing; *L*a*b** system

Introduction

Architecture, aircraft and nowadays automotive industry require surface treatment of metals applying conversion coatings which are characterised by corrosion resistance and adhesion improvement.
Aluminium and its alloys are used due to their excellent mechanical, chemical and electrical properties. Aluminium reacts with oxygen in the atmosphere and forms a natural aluminium oxide film on the surface with the thickness of about tenths of nm. The oxide layer can be enhanced several times by anodic oxidation (anodization). Sulphuric acid electrolyte is commonly used for the anodization (Wernick et al., 1987; Brace et al., 1979). The anodic oxide film consists of a thin barrier layer formed directly on the metal and a thick oxide layer with hexagonally shaped cells and a central pore as it can be seen in Fig. 1. Advantage of the sulphuric acid electrolyte consists in low power consumption and high reliability (Švorc, 2005; Michna, 2016). Electrolytic colouring uses mostly alternating current (AC) to deposit metal into the pores. Metals like tin, nickel, cobalt, etc., are used. Tin acidic colouring electrolytes are employed mostly in the automotive industry. The main reason for tin colouring is to meet toxicity requirements and to achieve good throwing power, minimal sensitivity to pH and bath contamination; it is also relatively easy to operate. The main disadvantage of the bath is the electrolyte oxidation in the atmosphere (Tsangaraki-Kaplanoglou et al., 2006)
An important part of the surface treatment of the coloured anodized aluminium is the sealing process. During the sealing, pores of the anodic oxide are closed. This process contributes to anticorrosion protection and enhances the decorativeness of the specimens.
Although the process of electrolytic colouring is routinely used, there is still place for improvement. The scope of this project is the study of parameters controlling the electrolytic colouring of anodized aluminium to form uniform black coatings.

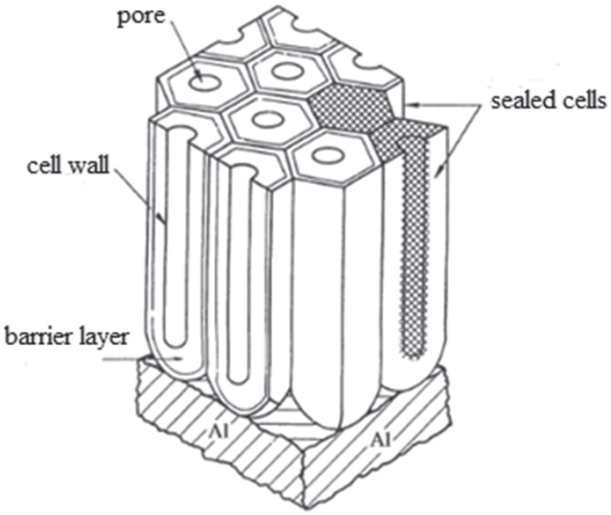

Fig. 1. Structure of aluminium oxide (Brace, Sheasby, 1979).

Materials and Methods

Sample preparation

An aluminium sheet (Al 99.5) was cut to dimensions of 40 × 70 × 1 mm and subsequently the hinge arm was cut, which served as a conductive connection

Acta Chimica Slovaca, Vol. 12, No. 1, 2019, pp. 8—13, DOI: 10.2478/acs-2019-0002

during the pre-treatment operations, anodic oxidation and electrolytic colouring.

Pre-treatment operations

Surface of these samples was pre-treated in four steps:

1. degreasing was realised in commercial solution Aktigal (Slovakia): in this stage, rough dirt and dust were removed from the surface.
2. alkaline etching, in this step, surface of the samples was subjected to an NaOH solution of 90 g/l and the natural oxide layer was removed.
3. satin etching was done in a solution containing 90 g/l of NaOH, 109 g/l of $NaNO_3$ and 1 g/l of sucrose which smoothed the surface.
4. brightening is the last step of the pre-treatment process and it was done in an HNO_3 solution of 400 g/l. Nitric acid removed alloy components from the surface, which produced black spots.

Each step of the pre-treatment process took three minutes at the temperature of 75 °C. After each step, the samples were rinsed with tap water for the time equal to that of the pre-treatment operation and they were left in distilled water before the following treatment. All chemicals used were of the p.a. purity.

Anodic oxidation

In the process of anodic oxidation, sulphuric acid electrolyte was used. Concentration of sulphuric acid was 200 g/l and process current density of 1.5 A/dm^2 was maintained at the temperature of (18—22) °C for the anodization time of 20 minutes. After the anodic oxidation, the samples were rinsed with tap water for the time equal to that of the process and then put into distilled water.

Electrolytic colouring and sealing

Electrolytic colouring was carried out using alternating current in the commercial solution ALFICOLOR 699. The studied parameters of the process included:

— time of colouring — 9, 12 and 15 minutes;
— AC voltage — in the range of (12—19 V);
— composition of electrodes — stainless steel AISI 304 marked electrode 1 and AISI 316 marked electrode 2;
— area of electrodes — ratios of the sample area to the counter electrode 2 : 1 and 1 : 2;
— distance between electrodes — 2 or 3.5 cm;
— agitation of the electrolyte using a magnetic stirrer.

After the colouring, the samples were rinsed with tap water for 10 minutes, dried by a hot-air dryer (2 min both sides of the samples) and subsequently the quality of the coatings was determined by spectrocolorimetry employing parameters *L*a*b**. This system characterizes any colour by the luminance parameter, *L**, and two colour coordinates, *a**, *b**, which specify the point on the chromaticity diagram (Fairchild, 2004). Parameter *L** represents the colour shade of the finishes and parameters *a**, *b**characterize the brightness of the finishes; for an ideal black body, these parameters are 0*0*0. Only the *L** parameter is decisive for the coating quality determination and the results are presented in Figs 3—8. A spectrocolorimeter Spectroguide 45/0 (Germany) was used.

Sealing was carried out in distilled water for 10 minutes after the electrolytic colouring.

Thickness of the specimens was measured by a gauge MINITEST 500 N (Germany) which works on the eddy current principle measuring the insulting coatings on non-ferrous metals. Before the measurement, the gauge was calibrated against an uncoated sample. Presented values of the coating thickness is the mean value of ten readings. The values of layer thickness were measured after anodic oxidation, electrolytic colouring and sealing of the specimens.

Results and discussion

A study on the parameters for uniform black coatings in the process of tin acidic electrolytic colouring was carried out. Fig. 2 shows the layer thicknesses after anodic oxidation (AO), electrolytic colouring (AO + c) and sealing (AO + c + s). Thickness of the layer after anodic oxidation was found to be about 10.5 μm. After colouring, the thickness increased, which can be explained by Al_2O_3 growth occurring in the anodic half-cycle of the colouring process (Tsangaraki-Kaplanoglou et al., 2006). After the sealing process, thickness of the oxide layer decreased due to pores closing. All the presented results are in good correlation with literature (Wernick et al., 1987).

Quality of the coating was evaluated based on the *L** parameter of the spectrocolorimetry coordinates, which was measured after the colouring and sealing processes. The studied parameters of electrolytic colouring are provided in the text below.

First, the influence of the *colouring time* on the coating quality was analysed in the range of (8—15) min under constant voltage of 12 V. The colouring time of 9 min (as it is shown in Fig. 3) displays the lowest value of the *L** parameter. The value of the *L** parameter was 12.0 after the colouring and after the sealing it decreased to 3.9.

The other parameters of the electrolytic colouring were studied at the colouring time of 9 min.

Different composition of the counter electrode was studied as the next parameter. According to the

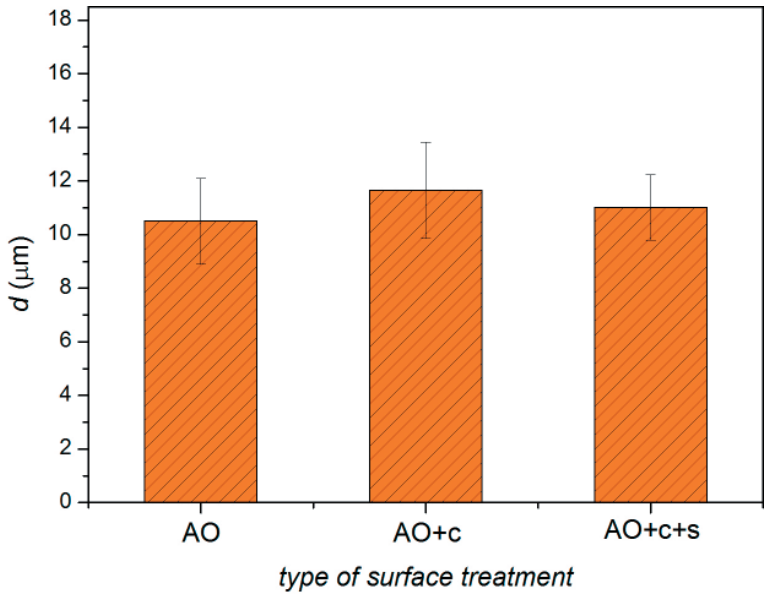

Fig. 2. Average values of thickness measured after anodic oxidation and colouring under the following conditions: *electrode* 1, *ratio of sample area to electrode area* — 1 : 2, *distance between sample and electrode* — 2 cm, t = 9 min, *agitation* = 700 rpm, U = 14 V and sealing time t = 10 min.

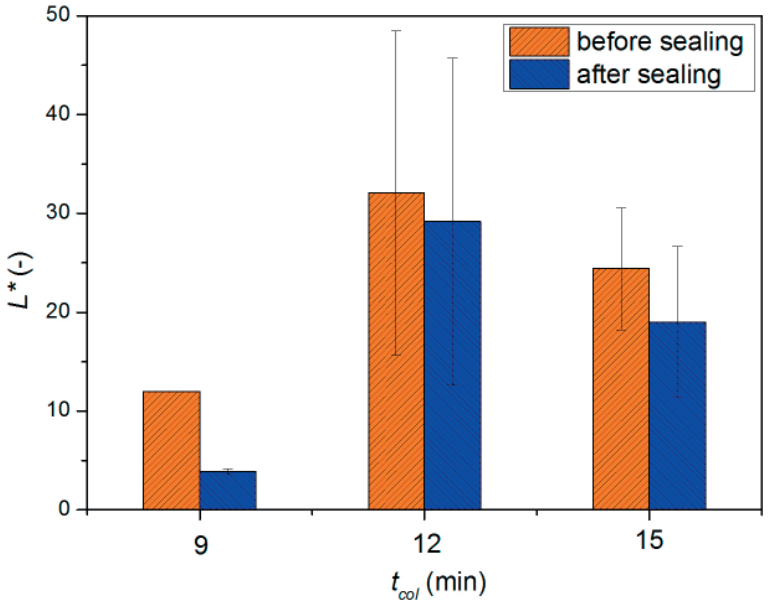

Fig. 3. Dependence of the L^* parameter on the colouring time under the following conditions: *electrode* 1, *ratio of sample area to electrode area* — 2 : 1, *distance between electrodes* — 3.5 cm, U = 12 V, *agitation* = 700 rpm.

results depicted in Figure 4, it can be assumed that the composition of the electrode does not have any effect on the quality of formed coatings. Values of the L^* parameter are comparable with those obtained with electrode 1. It can be also concluded that optimal value of voltage used in this process is 12 V when the lowest values of the L^* parameter were observed.

The following measurements were focused on the *different ratio* of the sample area to the counter electrode area. The ratio of 1 : 2 was used instead of 2 : 1. Based on the results depicted in Fig. 5 it can be stated that the counter electrode with larger area than that of the sample provides more homogeneous coatings.

Fig. 6. shows the results of L^* comparison for the *ratio* the sample area to the counter electrode area of 2 : 1 and 1 : 2.

It can be clearly seen that the ratio of 1 : 2 of the electrode area results in lower L^* values for the coloured finishes. Based on the achieved results, an optimised parameter was applied in the next study — smaller sample area to the counter electrode area.

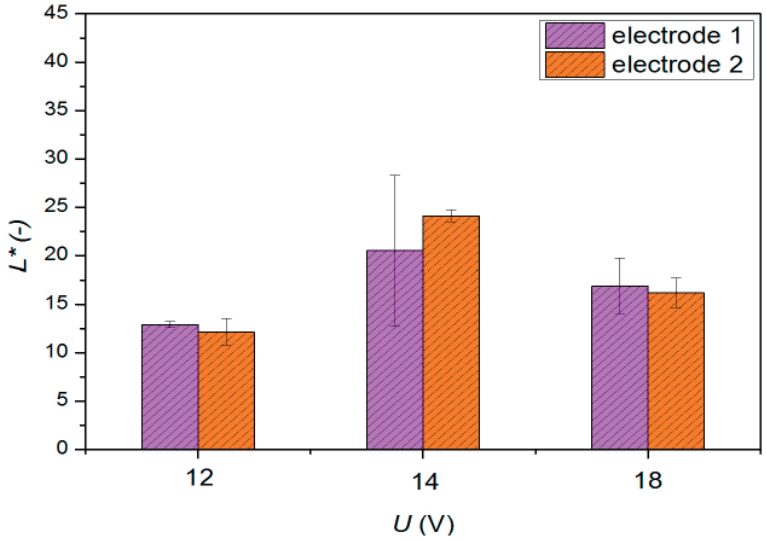

Fig. 4. Comparison of the *L** parameter using the counter electrodes with *different composition.*

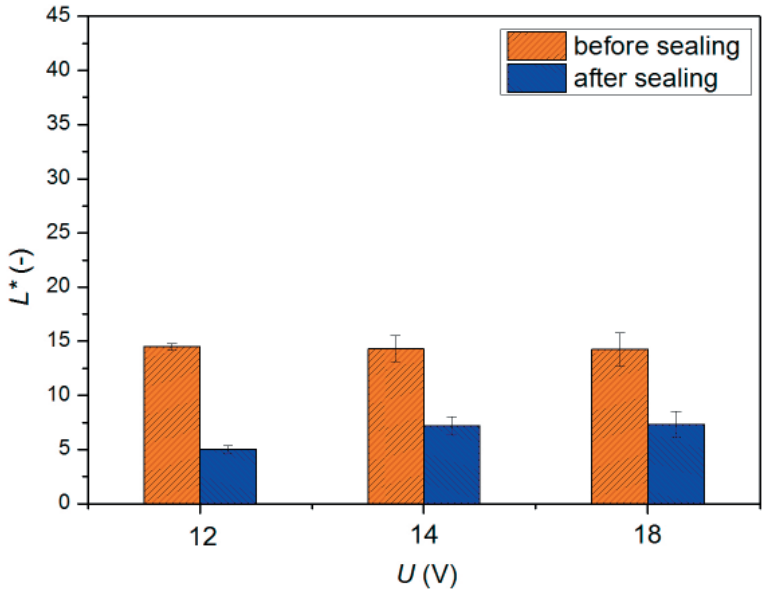

Fig. 5. Dependence of the *L** parameter on applied AC voltage under the following conditions: *electrode* 1, *ratio of sample area to electrode area* — 1 : 2, *distance between electrodes* — 3.5 cm, *colouring time t* = 9 min, *agitation* = 700 rpm.

Distance between the sample and electrode was another studied parameter. It was reduced from 3.5 cm to 2 cm, which positively affected the colouring of the anodized aluminium. The values of parameter *L** were lower for the electrode distance of 2 cm in comparison to those at 3.5 cm as it can be seen in Fig. 7.

The *effect of agitation* of the electrolyte on the quality of coatings was studied as well. The realised measurements were carried out at constant rate of agitation of 700 rpm and without agitation. Results for finishes without agitation depicted in Fig. 8 show higher values of the *L** parameter compared with the finishes obtained under the same conditions with agitation (Fig. 2—7).

The positive effects of agitation, area of the electrodes and distances between the electrodes are in good accordance with the theory of electrodeposition. All of the studied parameters (agitation, distance between electrodes, and area of the electrodes) contribute to the homogeneity of current distribution during the electrodeposition process (Paunovic and Schlesinger 2006).

On basis of the studied parameters it can be concluded that the electrolytic colouring of anodized aluminium species can be successfully done under the following conditions: AC voltage of 12 V, colouring time of 9 minutes, ratio of sample area to counter electrode area of 1 : 2, distance between electrodes of 2 cm, ensures black coatings of satisfying quality.

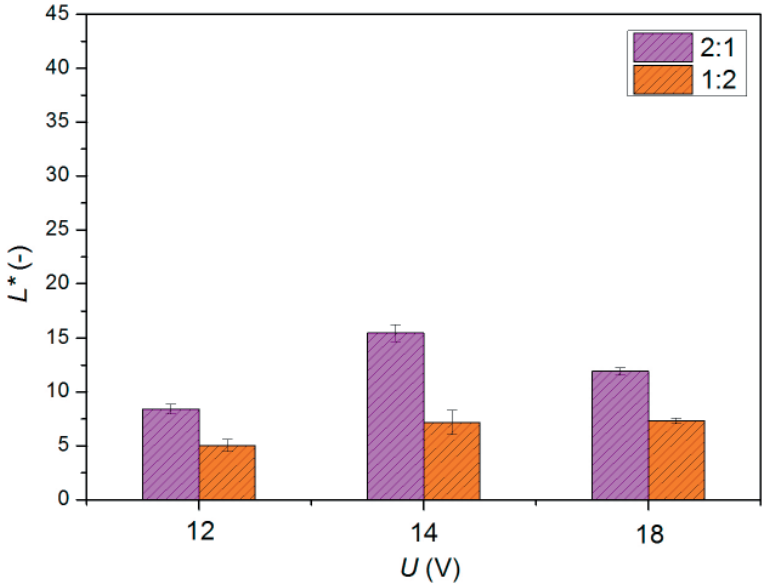

Fig. 6. Comparison of *L** parameter at *different ratios* of sample area to the counter electrode.

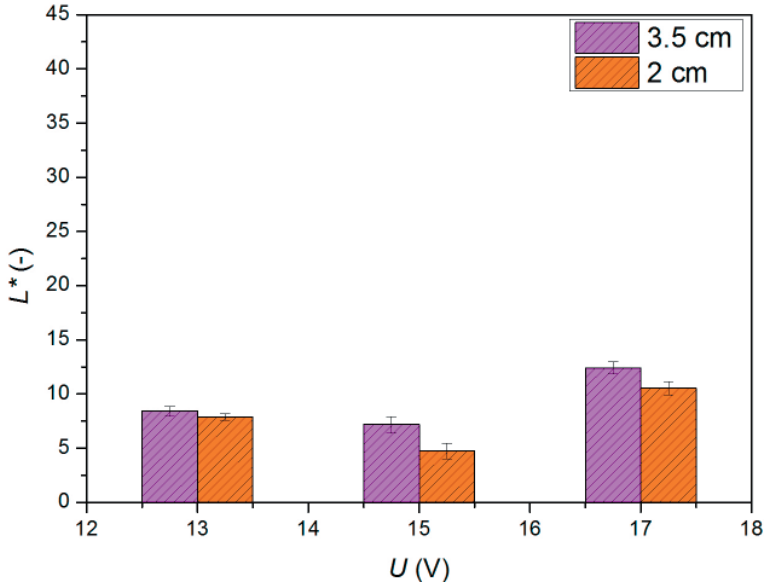

Fig. 7. Comparison of the *L** parameter at 3.5 and 2 cm distance between the sample and the counter electrode.

When applying the optimised parameters of electrolytic colouring for anodized aluminium, the quality of coloured finishes was influenced by the electrolyte due to the instability of tin ions in the acidic electrolyte.

Figure 9 depicts the samples coloured under optimum conditions. It can be seen that the coatings are homogeneous on the whole surface of the samples.

Conclusions

The objective of the study was to find optimum conditions for the electrolytic colouring of anodized aluminium utilising electrolytes containing tin ions. Parameters influencing the quality of the electrolytic colouring process were studied to reach uniform black coatings.

It was found that AC voltage of 12 V, colouring time of 9 minutes, ratio of sample area to counter electrode area of 1 : 2, and distance between electrodes of 2 cm ensure black coatings with satisfying quality. The most important parameter under the studied conditions is the electrolyte freshness due to the instability of tin ions in the acidic electrolyte in time.

Quality of the coloured finishes was improved by the sealing process which contributes to the increase in the corrosion protection as well as the decorativeness of the material.

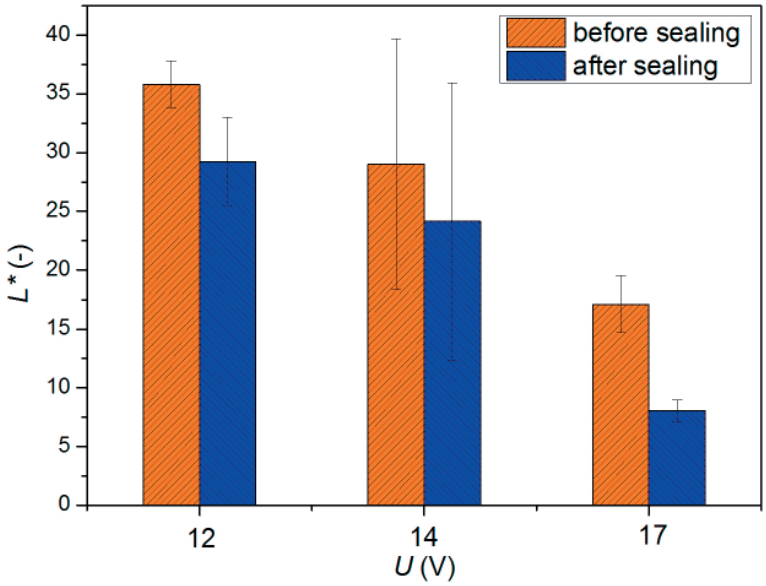

Fig. 8. Dependence of the L^* parameter on applied AC voltage under the following conditions: *electrode* 1, *ratio of sample area to electrode area* — 1 : 2, *distance between electrodes* — 2 cm, *colouring time t* = 9 min, without agitation.

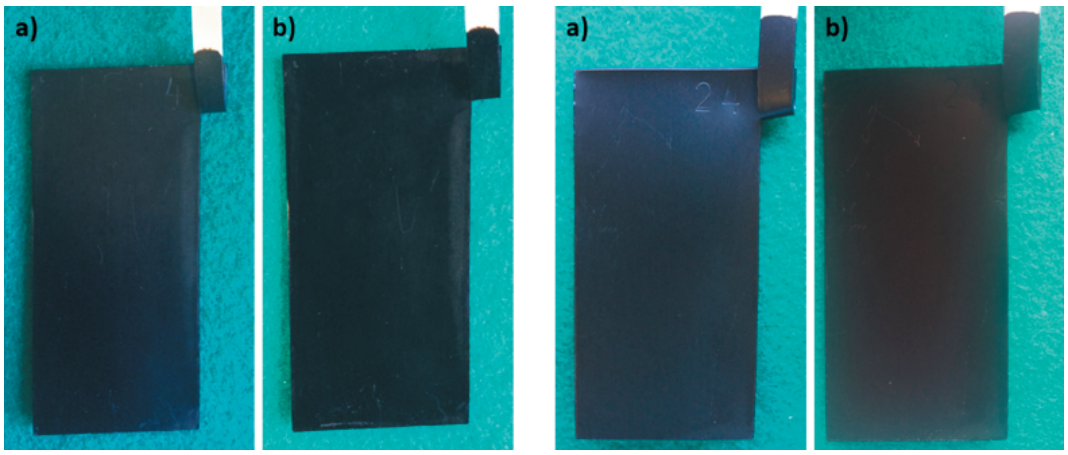

Fig. 9. Samples coloured under optimal conditions: a) before sealing, b) after sealing.

Acknowledgement

Financial support by the Ministry of Education, Science, Research and Sport of the Slovak Republic within the project VEGA 1/0792/17 is greatly acknowledged.

References

Brace AW, Sheasby PG (1979) The Technology of Anodizing Aluminium. Technicopy Ltd, England.

Fairchild MD (2005) Color and Image Appearance Models, Chichester UK, John Wiley and Sons.

Cheng CH (2015) Electro- Chemo- Mechanics of Anodic Porous Alumina Nano- Honeycombs: Self- ordered Growth and Actuation. The University of Hong Kong, Hong Kong.

Michna Š, Lukáč I et al. (2005) Encyclopedia of Aluminium. Adin, s.r.o, Prešov.

Paunovic M, Schlesinger M (2006) Fundamentals of Electrochemical Deposition. John Wiley & Sons, Inc. (USA) Hoboken, New Jersey.

Srinivasan B (2005) Troubleshooting of Electrolytic Color Anodizing of Aluminium. USA.

Švorc J (2016) Sealing of Anodized Aluminium and its Alloys. České vysoké učení technické v Praze, Prague.

Tsangaraki-Kaplanoglou I. et al. (2006) An Investigation of Electrolytic Coloring Process of Anodized Aluminium Coatings. Surface & Coatings Technology: 2749–2759.

Wernick S, Pinner R, Sheasby PG (1987) The Surface treatment and Finishing Aluminium and its Alloys. Vol. 1 and 2. ASM International Finishing Publications Ltd, England.

sciendo

Reactivity of calcium carbonate prepared from flue gas desulfurization gypsum

Jana Jurišová[a], Vladimír Danielik[a], Pavel Fellner[a], Milan Králik[a], Tomáš Foltinovič[b]

[a]Faculty of Chemical and Food Technology, Slovak University of Technology in Bratislava, Radlinského 9, 812 37 Bratislava, Slovakia
[b]Research Institute of Chemical Technology, VUCHT a.s., Nobelova 34, 836 03 Bratislava, Slovakia
jana.jurisova@stuba.sk

Abstract: Reactivity of various calcium carbonate samples for flue gas desulfurization was tested. Two groups of $CaCO_3$ samples were considered; natural limestone containing calcite phase dominantly and samples prepared by the conversion of gypsum with ammonium and carbon dioxide (precipitated $CaCO_3$) containing different amounts of calcite, aragonite and vaterite.

Reactivity of precipitated calcium carbonate depends primarily on the particle size, similarly as in case of industrial samples. The initial reaction rate was comparable with the industrial limestones for samples with the average particle size lower than 15 μm. However, the conversion of laboratory samples was significantly higher after 5 min of the reaction.

Phase composition of the precipitated calcium carbonate has a minor but noticeable impact on the reactivity. The presence of vaterite slightly increased the reactivity, which is in accordance with its lower compact structure in comparison with calcite and aragonite. Unexpected effect of the increased content of aragonite, which is the most compact phase in comparison with calcite and vaterite, was observed. If calcium carbonate contains up to approximately 30 % of aragonite the reactivity increases, which can be explained by the SEM pictures showing agglomerate composition with relatively high specific surface. At higher contents of aragonite, the reactivity decreases. All the obtained results proved the suitability of precipitated $CaCO_3$ prepared from flue gas desulfurization gypsum to be recycled in the flue gas desulfurization process.

Keywords: flue gas desulfurization, $CaCO_3$ reactivity, aragonite, calcite, vaterite

Introduction

Fossils fuels are still the main energetic source. Endeavour for minimizing the exploitation of fossil fuels is evident but coal will remain important at least until 2050 (BP Energy outlook 2018 Edition; Exxon Mobil, 2018; EU Reference Scenario 2016). Besides other impurities, various sources of coal contain from 0.1 up to 4 % of sulfur which generates SO_2 during coal combustion. Harmful effects of SO_2 on living organisms are generally known and therefore treatment of flue gass is necessary (IEA 2016). Recently, desulfurization techniques have been summarized showing the wet limestone procedure to be one of the most frequently used (Králik et al., 2017). Wet flue gas desulfurization (FGD) provides one of the highest efficiencies of SO_2 removal. This method is highly reliable (Zhong et al., 2008) and belongs to the least expensive ones to operate (Olausson et al., 1993). The efficiency and reliability of this technology has improved considerably in the past 20 years (Dou et al., 2009) and combined with other purifying processes significantly decreased the harmful effects of flue gases from coal power plants.

The product of desulfurization technology is gypsum. Properties and utilization of gypsum were well described by Wirsching (2000); prefabricated gypsum building components, gypsum plaster and gypsum constructing materials generally, are its main application areas (about 70 %). Another possibility is to use gypsum as a fertilizer; directly as a water suspension or a raw material for the production of other sulfur containing fertilizers, mainly in form of ammonium sulfate and blends containing it (Králik et al., 2017; Jang et al., 2014). Ammonium sulfate can be prepared by the conversion reaction of gypsum with CO_2 and ammonia (Danielik et al., 2018). Except for ammonium sulfate, calcium carbonate is produced as a by-product which can be recycled back to the FGD process (Jang et al., 2001; CN101337684A). In this case it is important to know the reactivity of produced calcium carbonate in the FGD process.

Understanding of the limestone dissolution/reaction kinetics of the FGD processes has attracted quite serious attention (Siagi and Mbarawa, 2009; Toprac and Rochelle, 1982; De Blasio et al., 2012; Ye and Bjerle, 1994; Ahlbeck et al., 1993; Ahlbeck et al., 1995; Pepe, 2001; Ukawa et al., 1993; Chan and Rochelle, 1982; Shih et al., 2000). It is assumed that limestone dissolution is the rate controlling step of SO_2 absorption processes (Siagi and Mbarawa,

2009; Pepe, 2001). When SO_2 diffuses into the liquid phase its hydrolysis takes place and hydrogen ions are produced. These ions are neutralized by the dissolved limestone. When limestone is added into water, it dissolves to a low extent (Ahlbeck et al., 1993; Ahlbeck et al., 1995). Considering the carbonate and bicarbonate equilibrium, the dissolution of limestone is enhanced under acidic conditions. According to Wallin and Bjerle (1989), the limestone dissolution rate in low pH environments is mass transfer controlled; the diffusion of hydroxonium ions is crucial. At higher pH, kinetics of the reaction on the limestone surface prevails. Ukawa et al. (1993) reported a method for measuring the rate of limestone dissolution in both batch and continuous reaction systems. They used continuous measuring of the particle size distribution during the reaction and obtained a good agreement with a model based on the mass transfer. It is commonly accepted that particle size distribution, limestone composition and its origin are the limestone characteristics determining its reactivity in the FGD process.

Reactivity of limestone can be determined by different methods. Measurements showed reactivity dependence on pH, particle size and reactor volume. Reactivity of several types of limestones used in FGD measured as neutralization rate with strong and weak acids at constant and/or varying pH was presented by Stumpf et al. (1984a, b). A detailed analysis of the methods characterizing limestone samples and their reactivity was summarized by Brown et al. (2009). The most accurate measurement of limestone reactivity in the flue gas desulfurization process can be achieved with a suspension of the ground limestone and SO_2 containing gas. However, tests with mineral acids (Ahlbeck et al., 1995; Fellner and Khandl, 1999; De Blasio et al., 2012; Stumpf et al. 1984a, b) proved the validity of "the pH constant method" for the estimation of limestone reactivity. In this method, a suspension of limestone is titrated with a mineral acid solution (H_2SO_4 or HCl) at virtually constant pH chosen from the range of 4 to 5. Time dependence of added acid as well as reaction rates at certain time points are evaluated. This titration is much more reproducible than bubbling of an SO_2 containing gas through the slurry of limestone. It is possible to compare reactivity of various limestone samples easily. For this reason, we have also used this method in our tests.

All the above mentioned papers deal with natural (mineral) limestones, typically with calcite phase as the dominant one. Calcium carbonate precipitated during the reaction of gypsum with CO_2 and ammonia may show different reactivity, mainly due to the different crystallographic modification of calcium carbonate. A comparison of the reactivity and properties of limestone and calcium carbonate precipitate consisting of calcite was presented by Dragan and Ozunu (2012). Reactivity strongly depends on the particle size, the difference between the limestone and calcium carbonate precipitate was negligible. However, the influence of different crystallographic modifications of calcium carbonate (calcite, aragonite, vaterite) has not been thoroughly studied for the purposes of FGD.

In this paper, reactivity of calcium carbonate prepared by the conversion reaction of gypsum and with varying content of calcite, aragonite and vaterite was studied. The reactivity was compared considering the phase composition, particle size distribution and specific surface area.

Materials and Methods

Nine laboratory samples of limestone prepared by the conversion of FGD gypsum with NH_3 and CO_2 in water solution were tested. Their reactivity was compared with: (i) ground natural mineral sample LietLuc, (ii) precipitated limestone from paper industry Monkal. Content of $CaCO_3$ was above 90 % in all samples. Samples LietLuc and Monkal consisted mainly of calcite. Laboratory samples contained different amounts of aragonite, calcite and/or vaterite. Average particle size in all samples was in the range of (10—25) μm.

The BET specific surface area was calculated from nitrogen adsorption isotherms at –196 °C using ASAP–2400 (Micromeritics, Norcross, USA). Degasification was carried out for 24 hours at 80 °C and 2 kPa. Reproducibility of measurements derived from three repetitions was ±7 % related to specific surface area calculated from the BET isotherm.

Particle size distribution was measured using a CILAS 930 Liquid laser diffraction granulometer. Water was used as the liquid phase; ultrasound was applied to disorder solid agglomerates. Morphology of the specimens was observed using a scanning electron microscope (SEM) ZEISS ZVO 40 coupled to an energy dispersive X-ray spectrometer analyzer (EDX) Bruker AXS.

Reactivity tests were performed as follows: about 1.500 g of dried powder calcium carbonate sample were added to 200 ml of deionized water and stirred by a magnetic stirrer (500 rpm) for 5 min at laboratory temperature (25 ± 0.5) °C in order to disintegrate the formed agglomerates. Then, the suspension was titrated with 1 M HCl at constant pH equal to 4. The control of pH was provided by a control loop consisting of a pH electrode, computer and a switcher controlling the peristaltic pump dosing the solution of HCl. Dependence of the

amount of added HCl on time was monitored every second. The maximum length of an experiment was 60 min. Conversion of limestone was calculated with respect to the total weight of the sample. Three parallel measurements were carried out.

Results and Discussion

Characteristics of all samples are summarized in Tables 1 and 2. Laboratory samples have Gauss-like distribution of the particle size, i.e. the size distribution of unimodal type. Industrial samples LietLuc and Monkal showed several Gauss-like peaks in the particle size distribution, i.e. they represent multimodal type of size distribution (three-modal in this case).

In Fig. 1, SEM figures of the laboratory samples are presented. It can be seen that the particle size of samples CC1—CC5 is lower than that of the other samples, which is in accordance with the particle size distribution. However, the particles are of different shape due to the different phase composition of the samples. Needles of aragonite may significantly increase the particle surface. On the other hand, calcite particles may form conjunct crystals, which results in the formation of large particles.

A comparison of the time dependencies of calcium carbonate conversion is shown in Figs. 2 and 3. It can be seen that the initial reaction rate of the laboratory samples with small particles (CC1—CC4) is comparable with the reaction rate of the industrial samples. However, the reaction rate of industrial samples decreased after a short initial time (ca 5 min), probably due to the multimodal particle size distribution and complete conversion of the smallest particles. Moreover, the effect of dolomite present in Lietluc and Monkal samples can also decrease the reaction rate. After 10 minutes of the reaction, conversion of samples CC1—CC4 was above 70 %. This is the point when the reaction rate of the industrial samples is at one level with laboratory samples containing large particles (CC5—CC9).

Tab. 1. Particle size distribution and specific surface area of samples.

	Particle size [μm]				Specific surface
	Diameter at 10 %	Diameter at 50 %	Diameter at 90 %	Mean diameter	area [m²/g]
CC1	1.9	9.51	18.03	9.9	2.52
CC2	2.66	10.12	17.66	10.3	4.84
CC3	3.56	13.87	23.55	14.02	2.89
CC4	2.41	11.93	21.65	12.46	2.66
CC5	2.21	13.38	28.09	14.63	1.64
CC6	12.15	23.63	41.78	25.55	1.54
CC7	10.7	23.55	41.79	25.14	2.55
CC8	7.54	18.93	34.82	20.18	1.29
CC9	11.88	22.00	34.37	22.67	0.43
LietLuc	1.68	8.58	45.56	16.31	–
Monkal	2.19	16.46	42.68	20.10	–

Tab. 2. Phase composition of samples.

	Composition [%]			
	Calcite	Aragonite	Vaterite	Dolomite
CC1	68.0	27.1	0.0	3.8
CC2	38.0	54.2	0.0	3.3
CC3	1.6	2.6	91.0	3.7
CC4	1.0	0.0	93.3	3.9
CC5	50.0	10.2	35.0	3.7
CC6	1.0	90.0	0.0	3.7
CC7	0.2	95.7	0.0	3.7
CC8	11.0	7.8	75.3	3.9
CC9	92.3	2.2	0.0	3.8
LietLuc	91.4	0.0	0.0	6.5
Monkal	94.6	0.0	0.0	2.4

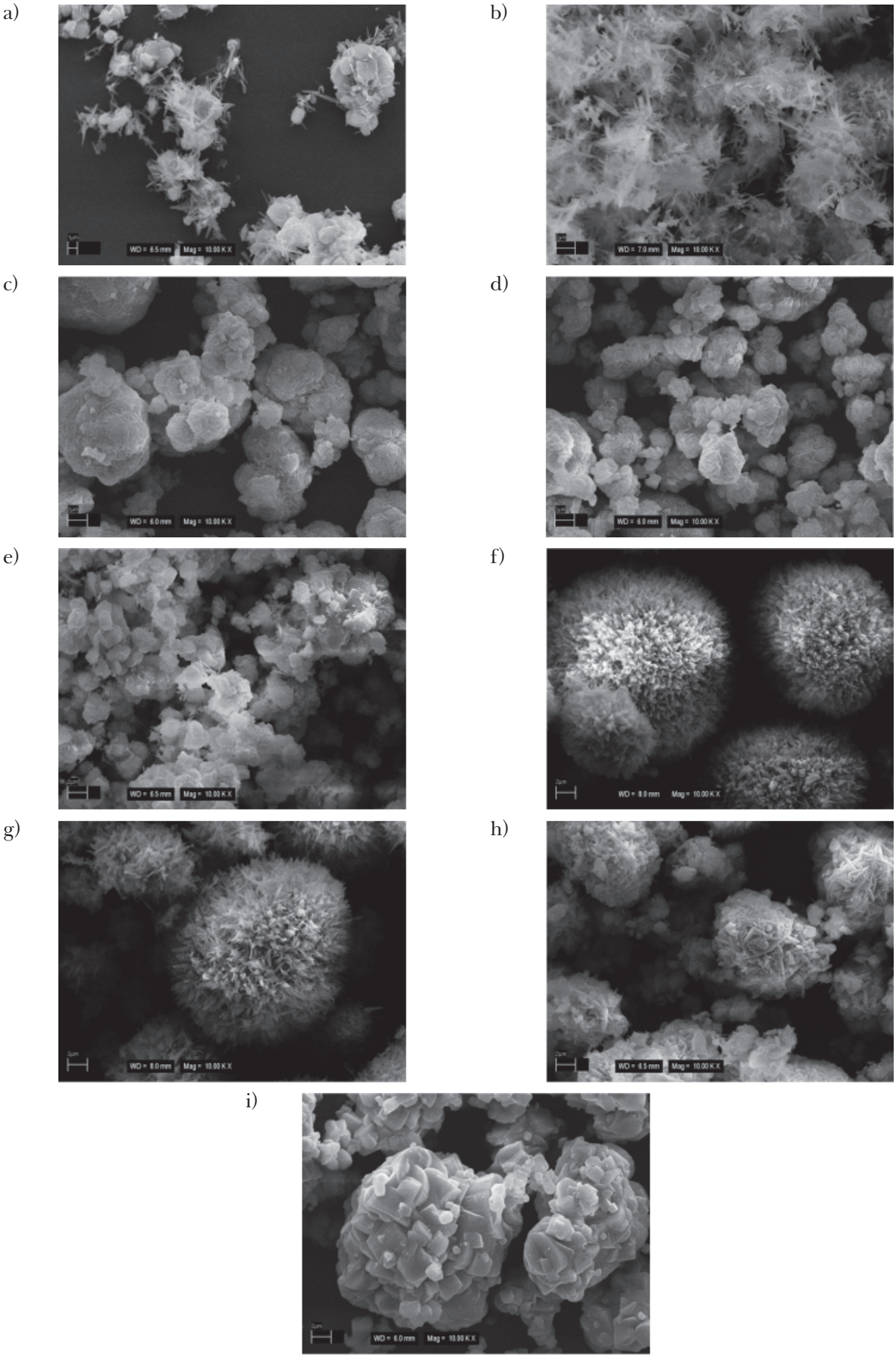

Fig. 1. SEM records of precipitated laboratory calcium carbonate samples.
a) CC1; b) CC2; c) CC3; d) CC4; e) CC5; f) CC6; g) CC7; h) CC8; i) CC9.

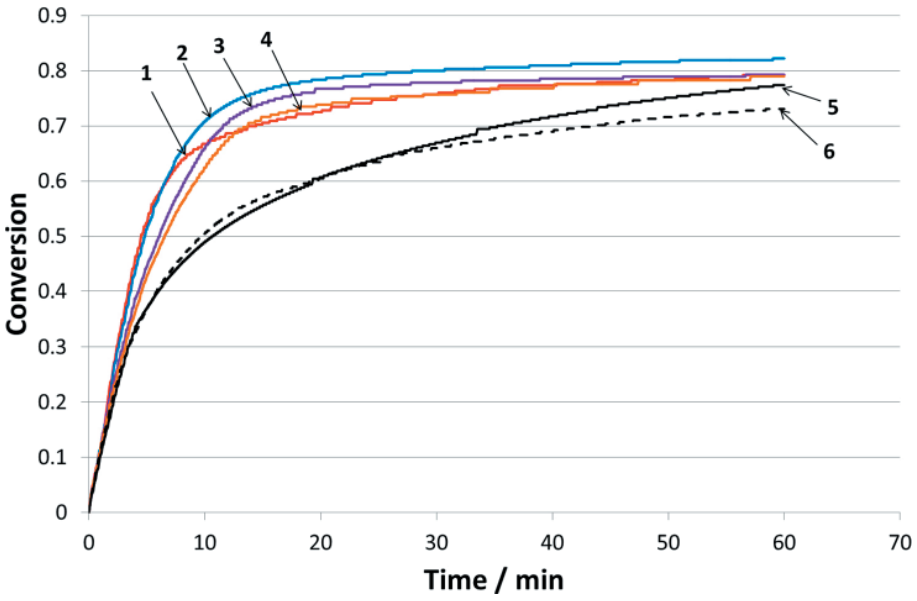

Fig. 2. Time dependence of the conversion of samples CC1 (1); CC2 (2); CC3 (3); CC4 (4); LietLuc (5); Monkal (6).

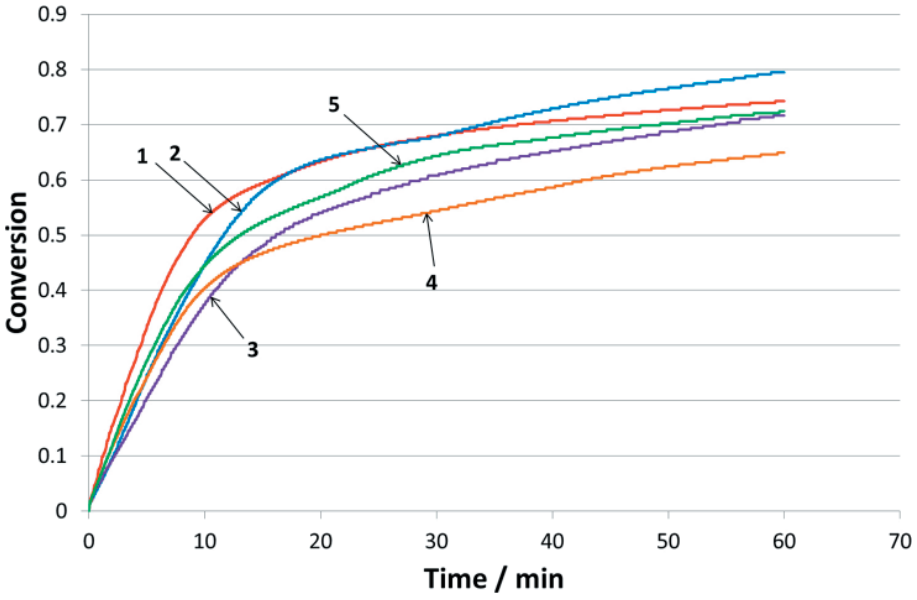

Fig. 3. Time dependence of the conversion of samples CC5 (1); CC6 (2); CC7 (3); CC8 (4); CC9 (5).

Detailed comparison of the reactivity of laboratory samples was carried out 3 min and 15 min after the beginning of the reaction. The initial reaction rate can be studied at the time of 3 min while 15 min after the reaction beginning, the conversion is above 50 % and the reaction rate significantly decreases compared to the initial one. The comparison is shown in Fig. 4. As it can be seen, the conversion correlates very well with the average size of the particles and with the parameter diameter at 90 % (Fig. 4a) 3 minutes after the reaction beginning. Later (15 min), the correlation is satisfactory for the diameter at 90 % (Fig. 4b). It can be assumed that small particles completely reacted at this time and the size of the large particles is decisive. On the other hand, there is only a slight correlation between the reaction rate and the specific surface area of the samples, which is in accordance with the published data (Ahlbeck et al., 1993; Ahlbeck et al., 1995; Ukawa et al., 1993; Wallin and Bjerle, 1989; Dragan and Ozunu, 2012; Claudio A. Carleti G., 2015).

Good correlation of the reaction rate and the particle size indicates that the influence of aragonite and vaterite is not crucial for the initial reaction rate. However, the impact of different solid phases can prove to be of increasing importance at higher conversion of $CaCO_3$.

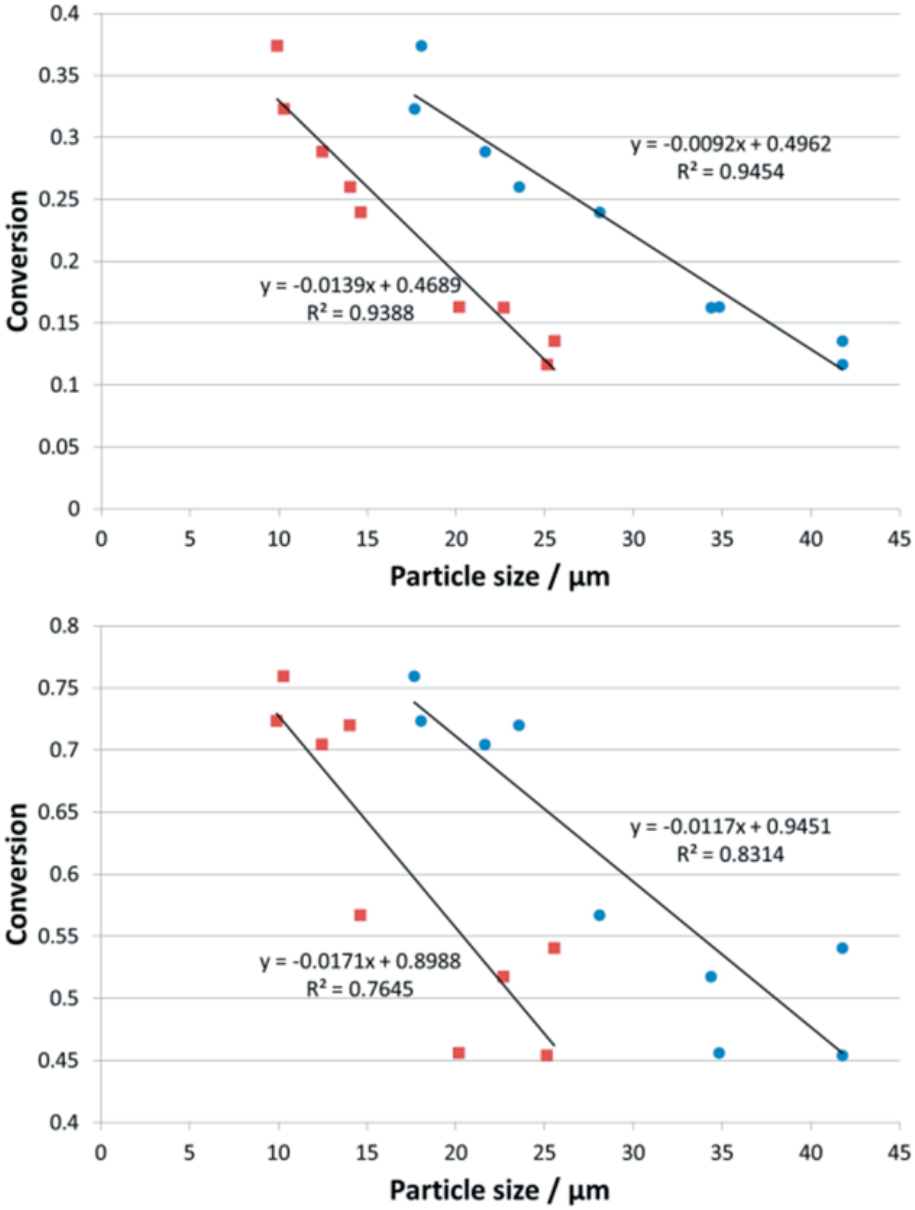

Fig. 4. Conversion of samples CC1—CC9 vs. particle size in 3 min (upper) and 15 min (bottom). (squares): mean diameter; (circles): diameter at 90 %.

It is assumed that limestone dissolution is the rate controlling step (Siagi and Mbarawa, 2009; Pepe, 2001). Based on the solubility products shown in Table 3, vaterite is more soluble and the reaction rate should increase, which is in accordance with our experimental data when higher content of vaterite resulted in increased reaction rate (Fig. 5a). The influence of aragonite content is not so obvious as its solubility is slightly higher than that of calcite. If calcium carbonate consists of calcite with a portion of aragonite, the reactivity increases. Besides the higher solubility of aragonite, morphology of the particle surface may be reflected in the reactivity. As it can be seen in Figs. 1a and 1b, needles of aragonite grow from the calcite particles and the particle surface is significantly larger while their size is still small. On the other hand, when calcium carbonate consists mainly of aragonite, the particles are huge and solid (Figs. 1f and 1g). Therefore, the reactivity of calcium carbonate with high content of aragonite is lower compared

Table 3. Solubility products of aragonite, calcite and vaterite

Aragonite	Calcite	Vaterite
$K_s = 6.0 \times 10^{-9}$	$K_s = 3.3 \times 10^{-9}$	$K_s = 1.3 \times 10^{-8}$
(Plummer and Busenberg, 1982)	(Benjamin, 2002)	(Plummer and Busenberg, 1982)

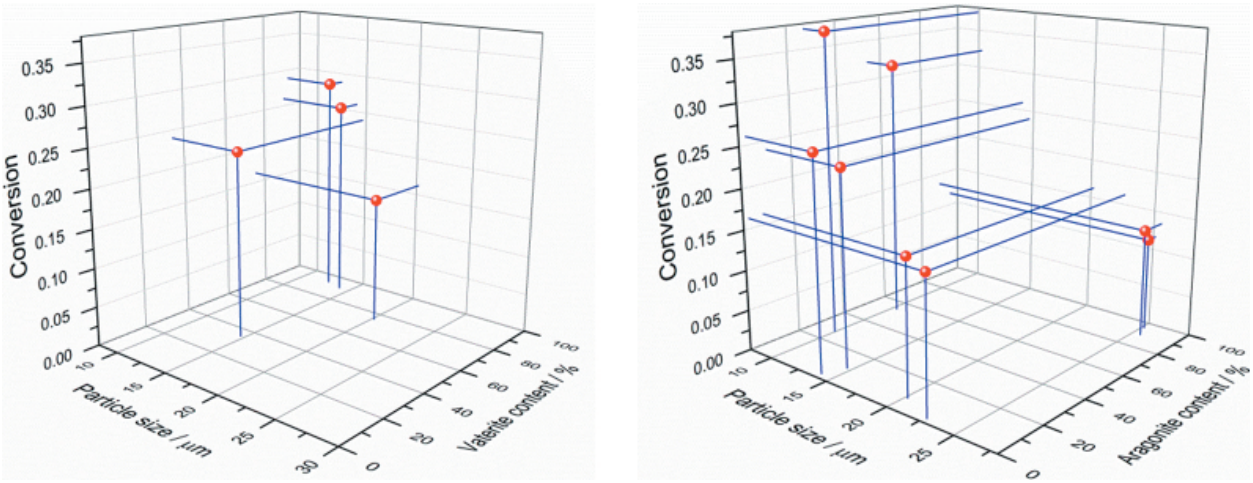

a) b)

Fig. 5. Conversion of samples CC1—CC9 in 3 min vs. particle size and content of vaterite (a) and aragonite (b).

to that containing calcite. This has also been proven experimentally. The reactivity of calcium carbonate containing aragonite and calcite increases up to 30 % of aragonite then it decreases (Fig. 5b).

Conclusions

Calcium carbonate samples prepared by the conversion reaction of FGD gypsum with CO_2 and ammonia were tested. Their reactivity was determined for the purpose of flue gas desulfurization and compared with the ground natural mineral (industrial) samples. The comparison showed that such prepared calcium carbonate is suitable for the FGD process and it can be recycled. The side product from the conversion of FGD gypsum is ammonium sulfate, which is a very valuable fertilizer compound.

In case of industrial samples, the reactivity of precipitated calcium carbonate depends primarily on the particle size. If the particle size is below 15 µm, the initial reaction rate is comparable with industrial limestones. After a short initial time, the reaction rate of industrial limestones significantly decreases while the reaction rate of precipitated samples remains high.

Phase composition of the precipitated calcium carbonate has a minor impact on the reactivity. The presence of vaterite slightly increases the reactivity. If calcium carbonate contains up to approximately 30 % of aragonite, the reactivity increases while it decreases at higher contents of aragonite.

Acknowledgement

This work was supported by the Slovak Research and Development Agency under the contract NO. APVV-14-0217 (Exploitation of gypsum into valuable chemical products and intermediates — EGYVACHEP) and co-funding by VUCHT a.s.

References

Ahlbeck J, Engman T, Fältén S, Vihma M (1993) Chemical Engineering Science 48: 3479—3484.

Ahlbeck J, Engman T, Fältén S, Vihma M (1995) Chemical Engineering Science 50: 1081—1089.

Benjamin MM (2002) Water Chemistry, McGraw-Hill. ISBN-10: 1577666674.

BP Energy outlook 2018 Edition. https://www.bp.com/content/dam/bp/en/corporate/pdf/energy-economics/energy-outlook/bp-energy-outlook-2018.pdf

Brown SR, De Vault RF, Williams PJ, Babcock & Wilcox Power Generation Group Inc. http://www.powermag.com/techniques-for-determining-limestone-composition-and-reactivity/? Printmode=1 (2009, accessed 5. 5. 2018)

Chan PK, Rochelle GT (1982) American Chemical Society Symposium Series 188: 75—97.

Claudio A, Carletti G (2015) New Aspects in Limestone Dissolution for Wet Flue Gas Desulfurization, PhD Thesis, Åbo, Finland.

CN101337684A, Method for recovering sulfur and co-producing calcium carbonate from desulfurization gypsum.

Danielik V, Fellner P, Jurišová J, Králik M (2018) Chemical Papers 72: 2631—2639.

De Blasio C, Mäkilä E, Westerlund T (2012) Applied Energy 90: 175—181.

Dou B, Pan W, Jin Q, Wang W, Li Y (2009) Energy Conversion and Management, 50(10): 2547—2553.

Dragan S and Ozunu A (2012) Cent. Eur. J. Chem. 10(5): 1556—1564.

EU Reference Scenario 2016, Energy, transport and GHG emissions, Trends to 2050 (https://ec.europa.eu/energy/sites/ener/files/documents/ref2016_report_final-web.pdf).

Exxon Mobil, 2018 Outlook for Energy: A View to 2040 (http://cdn.exxonmobil.com/~/media/global/files/outlook-for-energy/2018/2018-outlook-for-energy.pdf).

Fellner P, Khandl V (1999) Characterization of Limestone Reactivity for Absorption of SO_2 from Fume Gases. CHEMICAL PAPERS-SLOVAK ACADEMY OF SCIENCES, 53: 238—241.

IEA. Energy and Air pollution World Energy Outlook 2016. Special report (2016) © OECD/IEA, 2016, International Energy Agency, 9 rue de la Fédération, 75739 Paris Cedex 15, France. (https://www.iea.org/publication/freepublications/publication/WorldEnergyOutlookSpecialReport2016EnergyandAirPollution.pdf)

Jang HG, Lee GJ, Mo SY (2001) KR100303388.

Jang YN, Ryu KW, Lee MK (2014) US2014161692 (A1) — 2014-06-12.

Králik M, Balko J, Foltinovič T, Štefancová R, Kučera M, Fellner P, Danielik V, Jurišová J (2017) 44th International Conference of SSCHE, May 22—26, 2017, Demänovská dolina, Slovakia: 662.

Pepe F (2001) Industrial Engineering Chemistry Research 40: 5378—5385.

Plummer LN, Busenberg E (1982) Geochimica et Cosmochimica Acta 46(6):1011—1040.

Olausson S, Wallin M, Bjerle I (1993) The Chemical Engineering Journal 51(2): 99—108.

Shih SM, Lin JP, Shiau GY (2000) Journal of Hazardous Materials B 79: 159—171.

Siagi ZO, Mbarawa M (2009) Journal of Hazardous Materials 163: 678—682.

Stumpf Th, Roeder A, Hennicke HW (1984a) Das Reaktionsverfahren von Carbonatgesteinsmehlen in sauren, insbesondere schwefligsauren Lösungen. Teil I. (in German). Zement-Kalk-Gips 37: 262.

Stumpf Th, Roeder A, Hennicke HW (1984b) Das Reaktionsverfahren von Carbonatgesteinsmehlen in sauren, insbesondere schwefligsauren Lösungen. Teil II. (in German). Zement-Kalk-Gips 37: 454.

Toprac A, Rochelle GT (1982) Environmental Progress 1: 52—58.

Ukawa N, Takashina T, Shinoda N, Shimizu T (1993) Environmental Progress 12: 238—242.

Wallin M, Bjerle I (1989) Chemical Engineering Science 44: 61—67.

Wirsching F (2000) Calcium Sulfate. In: Ullmann's Encyclopedia of Industrial Chemistry. Wiley-VCH Verlag GmbH & Co. KGaA. doi: 10.1002/14356007.a04_555

Ye Z and Bjerle I (1994) Powder Technology 79: 273—277.

Zhong Y, Gao X, Wang H, Luo ZY, Ni MJ, Cen KF (2008) Fuel Processing Technology 89(11): 1025—1032.

sciendo

Electrical conductivity of low-temperature sodium-potassium cryolite melts

Emília Kubiňáková, Ján Híveš, Vladimír Danielik, Andrea Červenková, Michaela Benköová

Institute of Inorganic Chemistry, Technology and Materials, Faculty of Chemical and Food Technology STU in Bratislava, Radlinského 9, 812 37 Bratislava, Slovak Republic
emilia.kubinakova@stuba.sk

Abstract: Electrical conductivity of NaF-KF-AlF_3 melts with different ratios of sodium fluoride and potassium fluoride was measured using a pyrolytic boron nitride tube-type cell with constant distance of electrodes. Molar cryolite ratios MR = (n(NaF) + n(KF))/n(AlF_3) varied from 1.5 to 1.2 (with a step 0.1) in the temperature range of (675—900) °C. *AC*-techniques with a sine wave signal with small amplitude in the high frequency range were applied. Electrolyte resistance was obtained from nonlinear regression analysis according to equivalent circuit. Concentration and temperature dependency of electrical conductivity was described and defined. Experimental data were compared with literary sources and regression equations.

Keywords: electrical conductivity; aluminium electrowinning; low-temperature electrolytes

Introduction

Electrochemical preparation of primary aluminium has been invented over 132 years ago. In this process, alumina (Al_2O_3) is dissolved in an electrolyte consisting mainly of liquid sodium cryolite (Na_3AlF_6) at the temperatures of around (950—960) °C. The electrolyte is usually modified by additions of aluminium fluoride (AlF_3), calcium fluoride (CaF_2), magnesium fluoride (MgF_2) or other additives (Thonstad et al., 2001). This process has been optimized and innovated for more than a century (Kvande and Drabløs, 2014). Innovations of the aluminium electrolysis process are focused on using inert electrodes (Galasiu et al., 2007) and new types of electrolytes with lower temperature of primary crystallization (Cassayre et al., 2010). The most fundamental benefits are environmental, economic, and energetic aspects. The NaF-KF-AlF_3 system seems to be one of the best possible low-temperature electrolytes for aluminium reduction.
The main physico-chemical properties of these new low-temperature electrolytes have been studied in lesser extent. Electrical conductivity is a very important physico-chemical parameter of electrolytes (Híveš and Thonstad, 2004). Huang et al. (2008) measured the electrical conductivity of (Na_3AlF_6-40 %K_3AlF_6)-AlF_3-Al_2O_3 melts by the continuously varying cell constant (CVCC) technique. Different additions of AlF_3 and Al_2O_3 to the basic melt (Na_3AlF_6-40 %K_3AlF_6) were studied. However, the composition of measured electrolytes before the melting, types of fractions (mol % or wt %) and molar ration (MR), are not listed. Dedyukhin et al. (2009) studied KF-NaF-AlF_3 melts with an addition of LiF and/or Al_2O_3 with MR = 1.3 (and 1.5 for three-component melts). The systems were measured from their temperature of primary crystallization (TPC) up to 800 °C. Basic three-component melts were measured in capillary cell and multicomponent melts were measured in a cell with two parallel molybdenum electrodes. Apisarov et al. (2010) described the electrical conductivity of the KF-NaF-AlF_3 system at the same MRs, temperature ranges, measuring technique as in the previously mentioned paper (Dedyukhin et al., 2009). The last publication by this research group (Dedyukhin et al., 2011) studied the influence of CaF_2 on the electrical conductivity of a mixture of cryolite-based electrolytes with MR = 1.3 and 1.5. A four-component system was measured in a cell with two parallel Mo electrodes. The melts were studied in a broad temperature range >50 °C, as it was stated. Another paper focused on the electrical conductivity of KF-NaF-AlF_3 mixtures was published by Yang et al. (2013), where the CVCC technique was applied to measure electrical conductivity of the basic melt with MR = 1.2 to 1.5 and with an addition of Al_2O_3 in the temperature range from 750 °C to 820 °C. The latest paper focused on electrical conductivity of the sodium-potassium cryolite system in wide concentration and temperature ranges were studied by Kubiňáková et al. (2018_1). The operating temperature varied from 660 °C to at least 870 °C and MR changed from 1.5 to 1.2. The influence of different mutual ratios of KF and NaF on electrical conductivity was determined. The addition of NaF was constant for all studied MR; the studied concentrations were (10, 20, 40, and 50) mol %.

This paper follows our previous work (Kubiňáková et al., 2018_1). Electrical conductivity was measured for four different MRs (1.5—1.2) and for three various ratios of KF and NaF. Investigated NaF : KF ratios (in mol %) were 25 : 75, 50 : 50, and 75 : 25 for all selected MRs. Experimental data were compared with data for low-temperature sodium, potassium and (sodium-potassium) mixture cryolite systems available in literature.

Experimental

Chemicals

Sodium fluoride (NaF, p.a., Merck) and sodium chloride (NaCl, p.a., CentralChem) were dried for (3—5) hours at (400—500) °C before use. Aluminium fluoride (AlF_3, Sigma Aldrich) was purified by sublimation (20 hours) in a platinum crucible at the temperature of 1250 °C. Potassium fluoride (KF, p.a., Merck) was dried in a vacuum dryer with P_2O_5 for four days and then at 200 °C under vacuum for another three days.

Apparatus and measuring techniques

The basic apparatus and electrical conductivity measuring process were described in detail in our previous paper (Kubiňáková et al., 2016). The tube-type conductivity cell consisted of a pyrolytic boron nitride tube with electrodes in constant distance. A Solartron Impedance/Gain Phase Analyzer 1260 and a Solartron ECHI 1287 were used to measure cell impedance. *AC*-techniques were used with a sine wave signal and a small amplitude in the high frequency range. The value of the amplitude was about 10 mV, frequency was varied from 100 Hz to 100 kHz, and 61 readings were taken within this range. The measured impedance diagrams were evaluated by the nonlinear regression analysis using the method of equivalent circuit. The obtained values of electrolyte resistance were used to evaluate electrical conductivities of the melts using Eq. 1;

$$\kappa = \frac{l}{S \cdot R_{el}} = \frac{C}{R_{el}} \qquad (1)$$

where κ is electrical conductivity (Ω^{-1} cm^{-1}), l and S represents parameters of the cell (cm, respectively cm^2), C is the cell constant (cm^{-1}), and R_{el} is the electrolyte resistance (Ω). The cell constant was determined by calibration using the sodium chloride melt (Janz, 1988).

Liquidus temperature

Phase diagrams of the binary NaF-AlF_3 (Solheim et al., 1996) and KF-AlF_3 (Phillips et al., 1966; Danielik, 2005) systems are known. Temperature of primary crystallization in the system Na_3AlF_6-K_3AlF_6 was first studied by Fellner et al. (1990). A recent study of liquidus temperatures of KF-NaF-AlF_3 with CaF_2 melts with low MR completes the information about TPC of mixture cryolite melts (Apisarov et al., 2011). Multicomponent systems were measured at three MR values and at different mutual ratios of KF and NaF. The relevance of the temperature of primary crystallization estimation was verified by experimental measurements. It is not possible to measure electrical conductivity even in slightly heterogeneous systems with the method applied.

Results and discussion

Electrical conductivity of pure sodium cryolite and potassium cryolite systems (NaF-AlF_3 and KF-AlF_3, respectively) was measured in the low temperature area (Kubiňáková et al., 2018_2; Kubiňáková et al., 2018_3). Electrical conductivity higher than that of KF-AlF_3 melts is an advantage of the NaF-AlF_3 system. On the other hand, operating temperatures are lower and alumina solubility is higher in KF-AlF_3 melts than in the sodium ones. However, KF-AlF_3 electrolytes in the industrial process will never be pure potassium mixtures. Sodium oxide is always present in alumina as an impurity and regular additions of alumina into the electrolyte cause accumulation of sodium in the system (Dedyukhin et al., 2009). From an industrial point of view, NaF-KF-AlF_3 systems are more suitable as low temperature electrolytes for aluminium electrolysis. The studied area of ternary NaF-KF-AlF_3 mixtures in this paper is shown in Fig. 1.

Electrical conductivity of the three-component system NaF-KF-AlF_3 was studied for four different MR values (1.5—1.2) at various temperatures. Three different ratios between NaF and KF were studied for all MRs. The investigated mutual ratios (in mol %) between NaF and KF were 25 : 75, 50 : 50, and 75 : 25. Mole fractions of NaF, KF and AlF_3 in the ternary systems and the corresponding temperature ranges are given in Tables 1—3.

Electrical conductivity was sequentially measured for all NaF:KF ratios at the given MRs and tem-

Tab. 1. Concentrations of NaF, KF, and AlF_3 and working temperature range of ternary systems for each MR. Mutual ratio of NaF : KF was 25 : 75.

MR	x_{NaF} (mol %)	x_{KF} (mol %)	x_{AlF_3} (mol %)	t (°C)
1.2	0.136	0.409	0.455	678—776
1.3	0.141	0.424	0.435	718—824
1.4	0.146	0.437	0.417	766—825
1.5	0.150	0.450	0.400	825—902

Tab. 2. Concentrations of NaF, KF, and AlF_3 and working temperature range of ternary systems for each MR. Mutual ratio of NaF : KF was 50 : 50.

MR	x_{NaF} (mol %)	x_{KF} (mol %)	x_{AlF_3} (mol %)	t (°C)
1.2	0.273	0.273	0.454	684–786
1.3	0.283	0.283	0.434	723–826
1.4	0.292	0.292	0.416	733–824
1.5	0.300	0.300	0.400	815–879

Tab. 3. Concentrations of NaF, KF, and AlF_3 and working temperature range of ternary systems for each MR. Mutual ratio of NaF : KF was 75 : 25.

MR	x_{NaF} (mol %)	x_{KF} (mol %)	x_{AlF_3} (mol %)	t (°C)
1.2	0.409	0.136	0.455	690–792
1.3	0.424	0.141	0.435	715–827
1.4	0.437	0.146	0.417	731–833
1.5	0.450	0.150	0.400	819–901

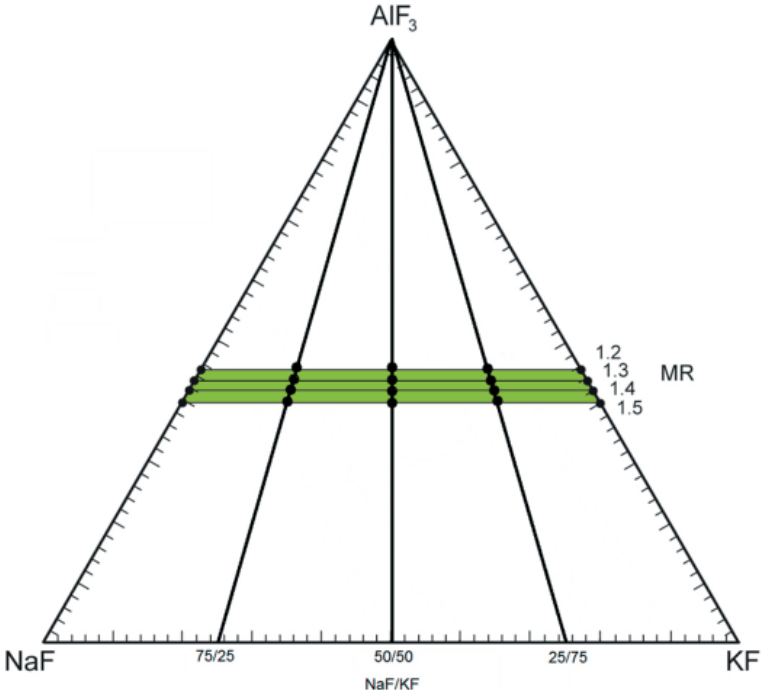

Fig. 1. Measured points of three-component NaF-KF-AlF_3 mixtures.

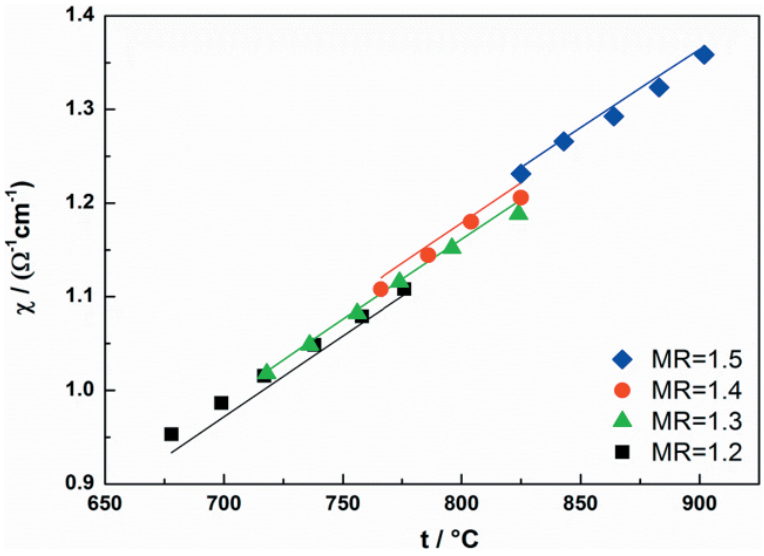

Fig. 2. Electrical conductivity of NaF-KF-AlF_3 system as a function of temperature for various MRs. NaF : KF ratio was 25 : 75. Points are experimental data, lines are data calculated from Eq. 2.

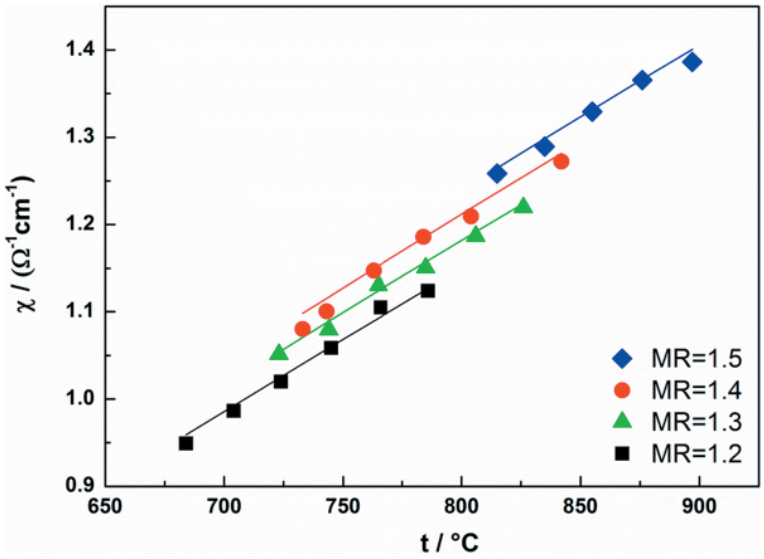

Fig. 3. Electrical conductivity of NaF-KF-AlF_3 system as a function of temperature for various MRs. NaF : KF ratio was 50 : 50. Points are experimental data, lines are data calculated from Eq. 2.

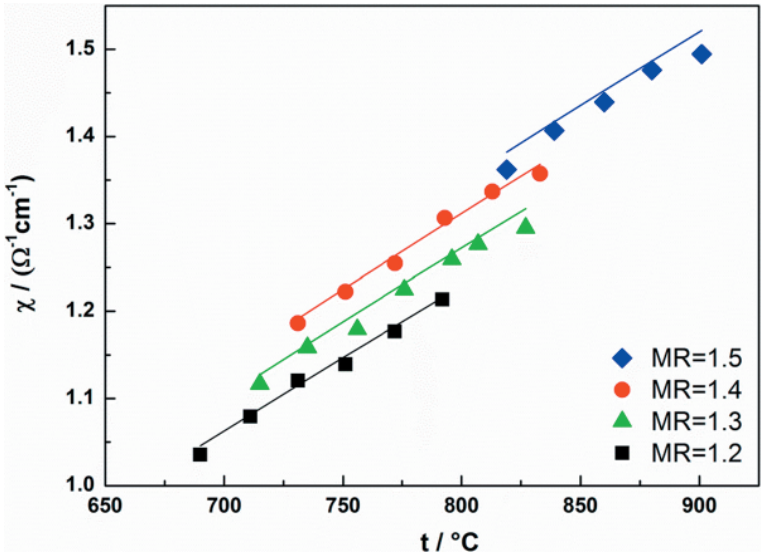

Fig. 4. Electrical conductivity of NaF-KF-AlF_3 system as a function of temperature for various MRs. NaF : KF ratio was 75 : 25. Points are experimental data, lines are data calculated from Eq. 2.

perature ranges. The values of electrical conductivity decreased with lower MR and decreasing temperature in all measured systems. This trend is the same as in previous investigated binary systems NaF-AlF_3 (Kubiňáková et al., 2018_2) or KF-AlF_3 (Kubiňáková et al., 2018_3). The higher addition of NaF leads to higher electrical conductivity (Fig. 2—4.). For the NaF : KF ratios of (25 : 75) mol % and (50 : 50) mol %, the values of electrical conductivity for all measured MRs were quite similar probably due to the very similar ionic structure of the melt at these additions in the NaF-KF-AlF_3 system. The decrease of electrical conductivity for the NaF : KF ratio of (25 : 75) mol % was about 3.67 % in average, compared to the NaF : KF ratio of (50 : 50) mol %. Differences between individual MRs were not very significant (Fig. 2. and Fig. 3.). Lower additions of KF to the mixture system (75 mol % of NaF to 25 mol % of KF) led to a significant increase of electrical conductivity, which was between the first two NaF : KF ratios of (25 : 75) and (50 : 50). Differences of the electrical conductivities between the NaF : KF ratios of (50 : 50) and (75 : 25) were about 8.13 % in average (Figs. 3. and 4.). Higher additions of NaF to the mixture system showed a more significant positive impact on the values of electrical conductivities.

The NaF-KF-AlF_3 system was measured (Kubiňáková et al., 2018_1) for various constant additions of NaF at different MRs. Mutual ratio of NaF and KF

changed with the MRs. The measured experimental data were compared to literary available regression equation for electrical conductivity calculation (Kubiňáková et al., 2018_1):

$$\kappa / \left(\Omega^{-1}\ \mathrm{cm}^{-1}\right) = \left[3.219x_{NaF} + 1.630x_{KF} + \right.$$
$$\left. + x_{AlF_3}\left(1.805 - 4.861x_{NaK} + 5.156x_{NaK}^2 - 2.341x_{NaK}^3\right)\right] \times$$
$$\times \exp\left[\left(1361x_{NaF} + 1517x_{KF} + x_{AlF_3}(2094 - 587.7x_{NaK}\right) \cdot \right.$$
$$\left. \cdot \left(\frac{1}{1300} - \frac{1}{T}\right)\right] \qquad (2)$$

where T is temperature in (K), x_i are mole fractions of the components, and term $x_{Na\text{-}K}$ represents the mole fraction of NaF in the binary NaF-KF system ($x_{Na\text{-}K} = x_{NaF}/(x_{KF} + x_{NaF})$). This equation is valid in the concentration range of x(AlF_3) = (40—45.5) mol %, x(NaF) = (0—60) mol %, x(KF) = (0—60) mol % and in the temperature interval from TPC up to 100 °C overheat. The regression equation (Eq. 2) is an Arrhenius type equation (exponential temperature dependence of electrical conductivity). More detailed description of Eq. 2 derivation was published in a previous paper (Kubiňáková et al., 2018_1).
Equation (Eq. 2) describes all our experimental data very well. The maximum deviation is up to 2.4 % which confirms the validity of the given equation in the defined concentration and temperature ranges.

Conclusion

Electrical conductivity of NaF-KF-AlF_3 low-temperature cryolite molten systems was investigated. Four different MRs (1.5—1.2) and three various NaF to KF ratios (25 : 75, 50 : 50, and 75 : 25) were applied. The AlF_3 concentration increasing up to 45.5 mol % was found to decrease the working temperature to (680—690) °C for sodium-potassium cryolite melts (if the NaF concentration varied from 25 mol % to 75 mol %). Electrical conductivity decreased with the decreasing MR and temperature. An increase in the NaF content led to higher electrical conductivity. The obtained experimental data were compared with the regression equation data available in literature (Kubiňáková et al., 2018_1). Small deviations between experimental and calculated values of electrical conductivity confirm the validity of the regression equation in the defined concentration and temperature ranges.

Acknowledgement
This publication is the result of the project implementation: Centre for materials, layers and systems for applications and chemical processes under extreme conditions – Stage II, ITMS No.: 26240120021 supported by the Research and Development Operational Program funded by the ERDF. This work was supported also by the Ministry of Education, Science, Research and Sport of the Slovak Republic within the project VEGA 1/0792/17 and by the Slovak Research and Development Agency under the contract no. APVV-17-0183.

References

Apisarov A, Dedyukhin A, Redkin A, Tkacheva O, Zaikov Y (2010) Russ. J. Electrochem. 46: 633—639.
Apisarov A, Dedyukhin A, Nikolaeva E, Tinghaev P, Tkacheva O, Redkin A, Zaikov Y (2011) Metall. Mater. Trans. B 42: 236—242.
Cassayre L, Palau P, Chamelot P, Massot L (2010) J. Chem. Eng. Data 55: 4549—4560.
Danielik V (2005) Chem. Papers 59: 81—84.
Dedyukhin A, Apisarov A, Tkacheva O, Redkin A, Zaikov Y, Frolov A, Gusev A (2009) ECS Trans 16: 317—324.
Dedyukhin A, Apisarov A, Tinghaev P, Redkin A, Zaikov Y (2011) Light Metals 563—565.
Fellner P, Chrenková M, Gabčová J, Matiašovský K (1990) Chem. Papers 44: 677—684.
Galasiu I, Galasiu R, Thonstad J (2007) Inert Anodes for Aluminium Electrolysis, Düsseldorf.
Híveš J, Thonstad J (2004) Electrochim. Acta 49: 5111—5114.
Huang Y, Lai Y, Tian Z, Li J, Liu Y, Li Q (2008) J. Cent. South. Univ. T. 15: 819—823.
Kubiňáková E, Danielik V, Híveš J (2018_1) J. Electrochem Soc. 165: E793—E797.
Kubiňáková E, Danielik V, Híveš J (2018_2) Electrochim. Acta 265: 474—479.
Kubiňáková E, Danielik V, Híveš J (2018_3) J. Electrochem Soc. 165: E274—E278.
Kubiňáková E, Híveš J, Danielik V (2016) Acta Chimica Slovaca 9: 141—145.
Kvande H, Drabløs PA (2014) J. Occup. Environ. Med 56: 23—32.
Phillips B, Warshaw C, Mockrin I (1966) J. Am. Ceram. Soc. 49: 631—634.
Solheim A, Sterten Å (1996) In: Thonstad J (Ed) Ninth International Symposium on Light Metals Production (pp 225—234). Thondheim.
Thonstad J, Fellner P, Haarberg GM, Híveš J, Kvande H, Sterten Å (2001) Aluminium Electrolysis, Fundamentals of the Hall-Héroul Process. Düsseldorf.
Yang J, Li W, Yan H, Liu D (2013) Light Metals 689—693.

sciendo

Plasma treatment of gelatin photography

Blanka Zachariášová, Katarína Haberová, Michal Oravec, Viera Jančovičová

Department of Graphic Arts Technology and Applied Photochemistry, Faculty of Chemical and Food Technology, Slovak University of Technology in Bratislava, Radlinského 9, 812 37 Bratislava, Slovakia
blanka.zachariasova@gmail.com

Abstract: Plasma pre-treatment represents the key enabler technology for microfine cleaning, surface activation and plasma coating of almost all types of materials – from plastics, metals and glasses to textiles, composites and photographs. More and more conventional industrial treatment methods are being replaced by plasma technology in order to make processes more effective and environmentally friendly. This study is oriented on the characterization of a photographic image on two types of photographic paper (glossy and matt photographic paper with a barite layer), and monitoring the effects induced by the Atmospheric Discharge with Runaway Electrons (ADRE) plasma in air atmosphere on the photographic image layers. To evaluate their long-term stability before/after plasma treatment, degradation of black and white gelatin photographic components upon accelerated light aging using Q-SUN was investigated and the photoinduced changes were recorded by FTIR spectroscopy, densitometry and colorimetry. The results obtained demonstrated that the plasma discharge had no significant destructive effect on the photographic image as only negligible changes in the structure of the gelatin were detected due to plasma processing. Consequently, it can be concluded that low-temperature ADRE plasma in air atmosphere has the potential for successful applications in microbial decontamination and purification of damaged gelatin photographs.

Keywords: ADRE plasma, colorimetry, densitometry, FTIR spectroscopy, gelatin photography

Introduction

Photographs are typical of their uniqueness and artistic value. For this reason, there are many efforts to preserve them and prevent their mechanical or microbial damage. Also avoiding various changes caused by the aging process such as color fading or loss of color density has been attempted. (Badea et al., 2008; Haberová, 2018) Because photographs are composed mainly of organic materials such as gelatin or cellulose, they represent suitable culture medium for different fiber fungi as well as for many other microorganisms. (Ioanid et al., 2010; Korachi and Aslan, 2013; Scholtz et al., 2015) Consequently, a great deal of historical photographs is damaged and devaluated as these detrimental processes may lead to their decomposition.

In recent years, more and more information on the applications of low-temperature atmospheric plasma, particularly in the domain of cultural heritage objects including photography, appeared in literature. (Tiňo et al., 2018; Pietrzak et al., 2017) It has been known for a long time that electrical discharges and plasma generated by them have disinfection effect. Plasma is a highly ionized gas composed of a set of neutral particles, free electrons and ions (positive and negative). Ionized gas becomes plasma only at the moment when it begins to exhibit collective behavior and quasi-neutrality. Under this term, we understand approximately identical concentration of positively and negatively charged particles. Plasma can be categorized as low- and high-temperature plasma. (Haberová, 2018; Martišovitš, 2004) In our experiments, low-temperature air plasma was used.

The advantage of ADRE plasma is its ability to process larger areas at the same time, which makes it suitable for material sterilization. Its discharge has the potential to destroy viruses, bacteria and also fungi (Ioanid et al., 2010; Korachi and Aslan, 2013; Scholtz et al., 2015) and it is applicable also for coarse materials treatment. Another benefit of this type of low-temperature plasma (LTP) is the activation and modification of materials surfaces, curing of deposited layers and formation of required layers on the material surface (hydrophobic, hydrophilic, antibacterial etc.).

The first use of plasma treatment in cultural heritage was in the preservation of historic metallic materials. Plasma is also used in the treatment of daguerreotypes, i.e. photographs on a metal mat (Haberová, 2018; Daniels, 1984; Grieten et al., 2017) and success has also been noted in case of testing its disinfection effect on paper. Also, experiments with plasma treatment of smoke-stained paintings were done to attempt their cleaning or to remove various organic impurities from their surface (Scheider et al., 2013; Vohrer et al., 2001; Banks and Rutledge, 1996). However, all these plasma applications were carried out in vacuum while the use of air plasma

has been overlooked and its utilization appears in literature only rarely. Direct application of plasma to historical photographs on a paper mat has so far been described only in two publications. (Ioanid et al., 2010; Ioanid et al., 2011) In 2010, positive effect of high-frequency plasma on the decontamination of photographs from fungi as *Aspergillus*, *Cladosporium*, *Alternaria*, *Penicillium* or *Rhizopus* was monitored. (Ioanid et al., 2010) In the second case, the effect of low-temperature high-frequency plasma using an H_2/Ar gas mixture on the surface of two types of historical photographs was determined. In case of gelatin photography, roughness increase and gloss decrease were observed; while in albumin-based photographs, the changes found after plasma treatment were exactly opposite. In both cases, plasma resulted in photobleaching. (Ioanid et al., 2011)

The goal of our work was to determine the effect of plasma discharge on the properties and long-term stability of a photographic image, especially that of low-temperature air plasma on optical properties of photographs and on the structure of gelatin as the main component of the light-sensitive layer. It is necessary to ensure that plasma is not destructive to the photographic image and therefore it is crucial to evaluate all changes of densitometric and colorimetric characteristics as well as FTIR spectra of the prepared samples and their stability depending on the time of plasma treatment.

Materials and Methods

Materials

Two types of barytic photographic paper FOMABROM from Foma Bohemia (Hradec Králové, Czech Republic): N 112 (normal, matt), N 111 (normal, glossy) were used.

Preparation of samples

The above mentioned two types of photographic paper (N 112, N 111) were used for sample preparation (Fig. 1). Exposure by Magnifax 4 (Meopta Přerov, Czech Republic) was done to samples of a photographic image with different optical densities of the P1—P8 fields (P1 is the lightest area and P8 is the darkest area). The exposure time was 0—32 s (with the step change of 4 s) thus, the white area was not exposed. Then, the samples were activated, fixed and washed to obtain a permanent photographic image.

Fig. 1. Sample of photographic image with different optical densities P1—P8.

Plasma treatment

ADRE plasma — Atmospheric Discharge with Runaway Electrons is a low-temperature plasma generated at atmospheric pressure. Fast electrons with the energy of 20—350 keV are formed in the mid-electrode space and behind the anode. Volume stream of the fast electrons is detected behind the anode and is shown as bright light across the area. When the voltage pulse increases two to three times, a change in the radiation between the electrodes can be observed.

The prepared samples were exposed to the ADRE plasma treatment (KAMEA ELECTRONICS, s.r.o., Piešťany, Slovakia) in air atmosphere at 0.6 J, frequency of 2000 Hz and gas flow rate of 6 L min^{-1}. The plasma treatment time was 0.5, 1, 3, 5 and 10 minutes.

Accelerated light aging in Q-SUN Xenon test chamber (Model Xe-1-S, Q-Lab Corporation, Cleveland, USA) according to ISO 4892-2: 2013 for daylight simulation

Aging occurred under window glass filters with black body temperature of 65 °C; the radiance at 420 nm was 1.1 W m^{-2}; E = 89 klx; incidence of radiation in the range of 300—800 nm was 494 W m^{-2}. Aging was performed for one and for five days.

Densitometry

Densitometry is a photometric method used to evaluate the proportion of light reflected from a colored surface (reflective densitometry) or passing through this layer (transmission densitometry). (Panák et al., 2000) The result is given in form of optical (photographic) density *D*. In our case, the reflective densitometry measurement was applied. Spectrophotometer SpectroDens (TECHKON, Königstein, Germany), which uses spectral re-measurement according to ISO 5-3/4 and Spectro Connect 2.4, was used to measure the optical density values. The settings were as follows: illumination — D50, standard observer — 2 °, polarization filter turned on, white standard absolute. The resulting values were calculated as the average of five measurements.

Colorimetry

Colorimetry is a photometric method used to measure and characterize color. (Panák et al., 2000) The color space CIELAB serves to evaluate color characteristics of the actual and desired color. Coordinates *L**, *a**, *b** in the CIELAB color space were measured by Spectrophotometer SpectroDens (TECHKON), which uses spectral re-measurement according to ISO 5-3/4 and Spectro Connect 2.4. The settings were as follows: illumination — D50,

standard observer – 2 °, polarization filter off, white standard absolute. The resulting values were calculated as the average of five measurements.
The total color difference ΔE^*_{ab} was calculated using Eq. (1),

$$\Delta E^*_{ab} = \sqrt{\left(\Delta L^*\right)^2 + \left(\Delta a^*\right)^2 + \left(\Delta b^*\right)^2} \quad (1)$$

where ΔL^*, Δa^* and Δb^* are the differences between relevant values attributed to treated/aged and non-treated/non-aged samples.

Fourier Transform Infrared (FTIR) spectroscopy
Infrared spectra were measured with an FTIR spectrophotometer (Excalibur Digilab FTS 3000MX, USA) using an ATR adapter with a single reflection diamond crystal at defined positions of fields P1–P8. The measurement range was from 4000 to 700 cm^{-1}; sensitivity – 8; 30 scans. Reference environment was air. The FTIR spectra were evaluated using the Origin software. In case of samples after plasma treatment, the average of three measurements was used in MS Excel.

Results and Discussion

Characterization of a photographic image
Coordinates *L**, *a**, *b** and optical density values obtained during characterization of all the fields for both types of photographic paper are presented in Table 1. With the increasing optical density of the photographic field, the value of *L** (lightness) decreases. Since these are achromatic colors, coordinates *a** and *b** are close to zero. Slightly negative values of *b**, especially in low optical density fields, are probably due to the addition of optical brighteners to photographic paper and slight differences in the layer thickness.
Figure 2 shows the normalized FTIR spectra (Amide I) obtained for N 112 paper with a photographic image (field P1–P8). As it can be seen, the shape of the spectra depends only slightly on the optical density of the photographic image, i.e. on the silver content of the light-sensitive layer (1000–700 cm^{-1}). Typical features in the spectra are protein bands, i.e. Amide I (*AI*) at 1635 cm^{-1}, Amide II (*AII*) at 1557 cm^{-1}, and Amide III (*AIII*) between 1200–1350 cm^{-1}. (Singh et al., 2014) The band of Amide A (*A*) is detectable at 3300 cm^{-1} and it is usually in form of a doublet with Amide B (*B*) at 3073 cm^{-1}. (Badea et al., 2008) The shape and intensity of these bands are also affected by vibrations of —OH groups, which can cause problems in their evaluation. The intensive band at 1060 cm^{-1} belongs to barium sulfate (barite), which is a component of the barrier layer. (Zhang et al., 2011) In the spectrum of paper N 111 (Fig. 3), this band is not so evident, which may be caused by a thicker light sensitive layer of the glossy paper.

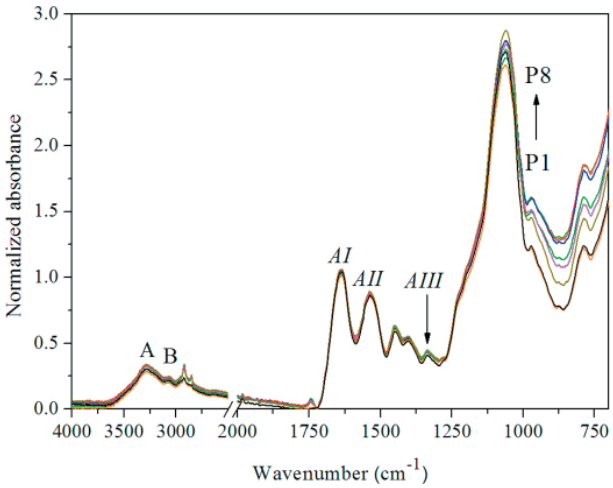

Fig. 2. Normalized FTIR spectrum (Amide I) of photographic image with different optical density *D* on photo paper N 112, *D* of individual areas is shown in Table 1 *(P1 – black, P2 – orange, P3 – dark yellow, P4 – purple, P5 – green, P6 – blue, P7 – red, P8 – light green).*

Tab. 1. Coordinates L^*, a^*, b^* and values of optical density D for two types of photographic paper: N 112 and N 111 (all values were calculated as the average of five measurements).

Field	N 112				N 111			
	*L**	*a**	*b**	*D*	*L**	*a**	*b**	*D*
P1	95.5	0.8	–2.8	0.06	96.8	0.8	–2.4	0.05
P2	91.5	0.7	–2.2	0.13	95.2	0.7	–2.4	0.06
P3	74.5	0.4	–0.7	0.39	85.0	0.5	–1.2	0.14
P4	55.6	–0.1	0.2	0.77	65.9	0.3	0.5	0.33
P5	44.3	–0.2	0.0	1.08	49.1	0.0	1.2	0.63
P6	38.2	0.0	–0.3	1.32	38.1	0.1	1.3	0.93
P7	34.9	–0.1	–0.5	1.49	31.3	0.3	1.2	1.15
P8	33	–0.1	–0.6	1.57	26.6	0.6	0.9	1.31

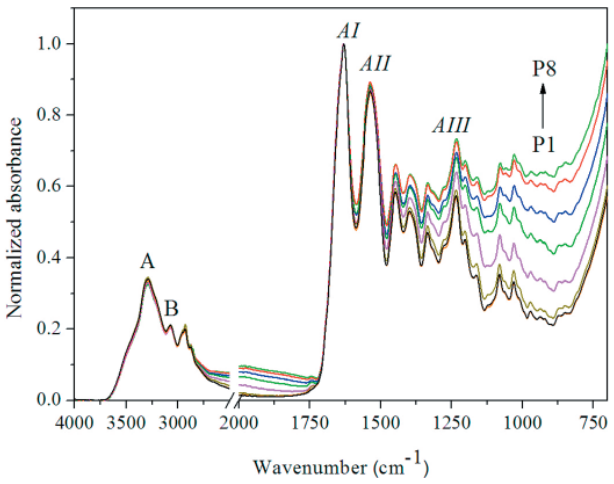

Fig. 3. Normalized FTIR spectrum (Amide I) of photographic image with different optical density *D* on photo paper N 111, *D* of individual areas is shown in Table 1 *(P1 – black, P2 – orange, P3 – dark yellow, P4 – purple, P5 – green, P6 – blue, P7 – red, P8 – light green).*

Influence of plasma treatment on photographic image

As a result of plasma treatment, a slight decrease in the optical density across the photographic image on N 112 matt paper can be observed, except for the P1 field (white), while the most significant decrease was determined for the dark fields P5—P8, where it reached the value of 0.12 after ten minutes of plasma treatment. On the other hand, optical density increase was observed on gloss paper N 111 especially in the gray fields of the photographic image (in P5, optical density increased by 0.15) due to plasma treatment. Based on measured *L**, *a**, *b** coordinates, the values of ΔE^*_{ab} were calculated over the whole range of the photographic image (fields P1—P8). The evaluated ΔE^*_{ab} were minimal (~1.3), not exceeding the declared limit of 2.0, which corresponds to the minimum difference that is not perceptible even in direct comparison of the samples. (Panák et al., 2000)

FTIR spectra at individual sites of the photographic image were measured and compared in order to identify changes caused by plasma treatment. In FTIR spectra of photographic image on N 112 paper after plasma exposure, minor changes in the range of 1650—1250 cm^{-1} were detected. The absorbance of band *AII* decreased and the absorbance of band *AIII* increased. These changes are similar in all fields (independent of optical density of the photographic image) and indicate possible hydrolytic damage of gelatin. Simultaneously, certain changes in the area typical of CH_x groups (2800—2900 cm^{-1}) was observed. As an illustrative example, FTIR spectra of the photographic image of field P1 and P8 for N 112 photographic paper are shown in Fig. 4.

Absorbance of individual amide bands was evaluated from the FTIR spectra using the baseline method and the calculated ratios of Amide I and Amide II (*AI/AII*); their increase indicates the degree of hydrolytic damage of gelatin and is summarized in Fig. 5. From the given results it appears that on all the fields of the photographic image of both paper types, this ratio is slightly increased due to plasma treatment, revealing a little higher increment for N 112 paper.

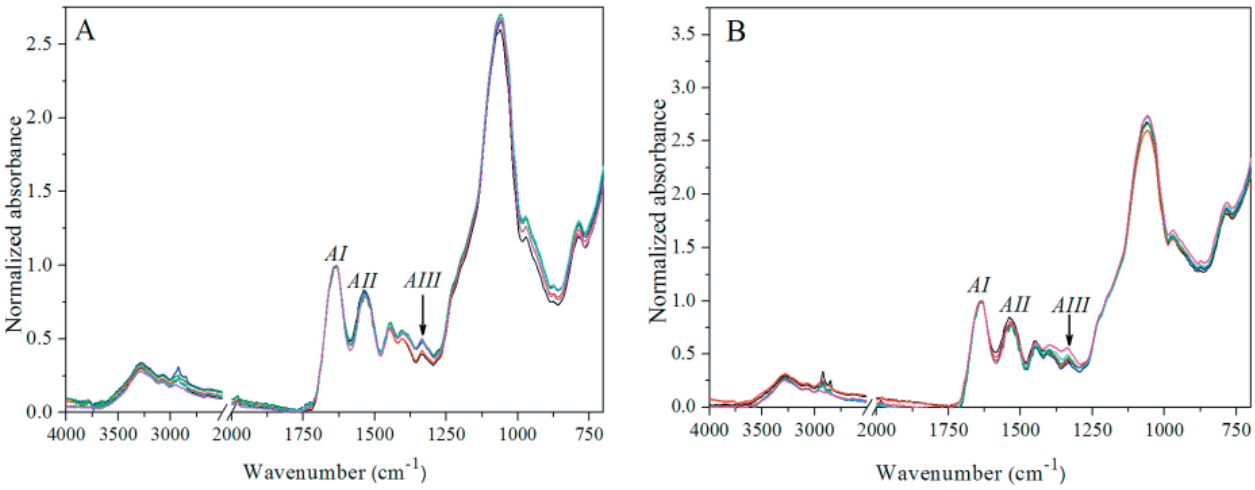

Fig. 4. Normalized FTIR spectra (Amide I) of photographic images of fields P1(A) and P8 (B) on photographic paper N 112 and their changes after plasma treatment *(untreated samples – black line and samples after 30 seconds of plasma treatment – red line, 1 min – blue line, 3 min – green line, 5 min – azure line and 10 min – pink line).*

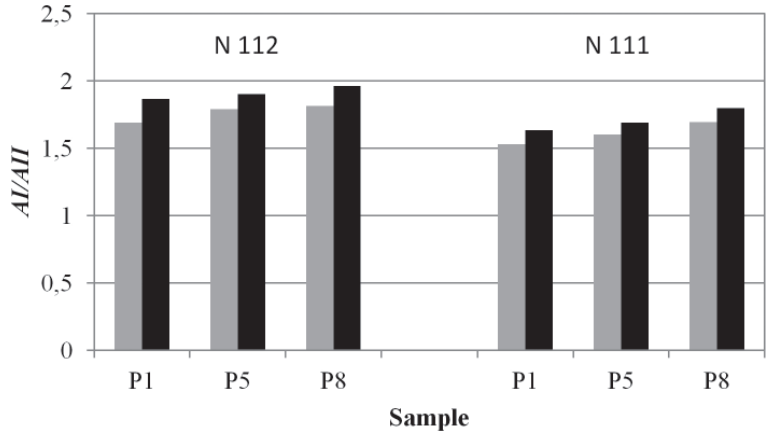

Fig. 5. Graphical representation of calculated ratios of Amide I (*AI*)/Amide II (*AII*) (untreated samples — gray, samples after 10 min of plasma treatment — black) for the selected fields P1, P5 and P8.

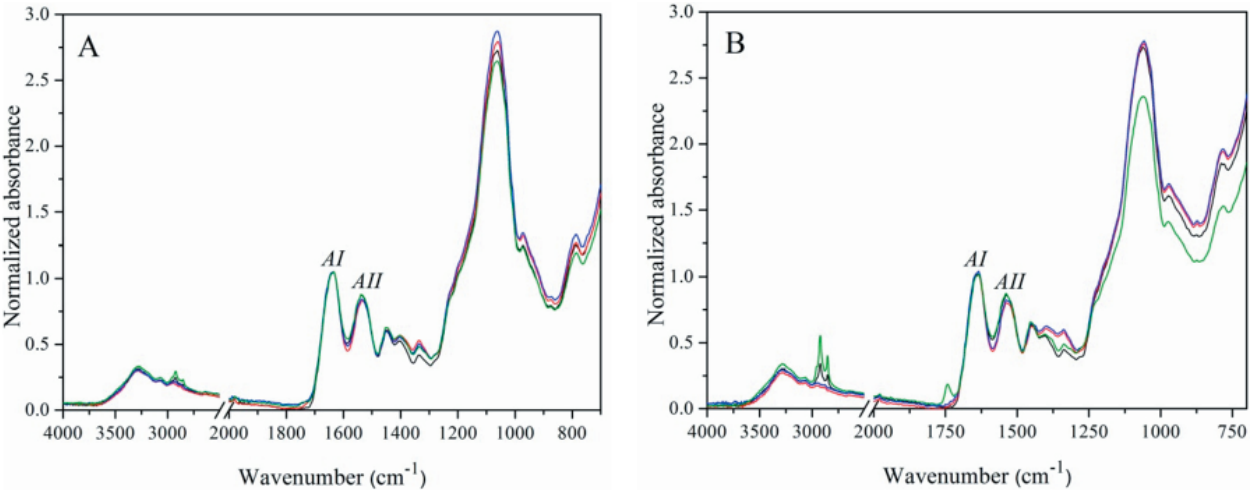

Fig. 6. Normalized FTIR spectra (Amide I) of photographic images of fields P1(A) and P8 (B) on N 112 photographic paper (untreated sample — black line, samples after plasma treatment, spectra of which were measured immediately after plasma treatment — red line, two days after plasma treatment — blue line and seven days after plasma treatment — green line).

Also changes occurring in the samples immediately after plasma treatment and after steady-state (2—7 days) storage of the plasma-treated samples under laboratory conditions in dark were monitored (Fig. 6). While the samples with low optical density of the photographic image (field P1) returned to their original values as they were before plasma treatment, for samples with high optical density (P8), a band appeared at 1730 cm^{-1} (oxidation products), accompanied with changes in the region of the CH_x bands (2800—2900 cm^{-1}).

Accelerated aging in Q-sun chamber

To assess the effect of plasma treatment on long-term photostability, the prepared samples were aged in a Q-sun chamber. Untreated and also samples after a 10-min plasma treatment were aged using the total exposure of 120 hours representing the total energy of 475 kJ/m^2.

A change was noticed after the accelerated light aging of untreated samples. On photographic paper N 112, a decrease in optical densities, especially in the darker fields (P6—P8) was observed, while on glossy paper N 111, the optical density increased mainly in the gray fields (P4—P6). It is interesting that in case of plasma-treated samples, light aging did not change the optical density.

*L**, *a**and *b**coordinates of untreated samples and of samples after plasma treatment were compared. Untreated paper N 112, due to accelerated aging of the photographic image, showed changes in the *L**, *a** and *b**values depending on the initial optical density of the photographic fields. While the *L** coordinate (lightness) for the low optical density fields (P1—P3)

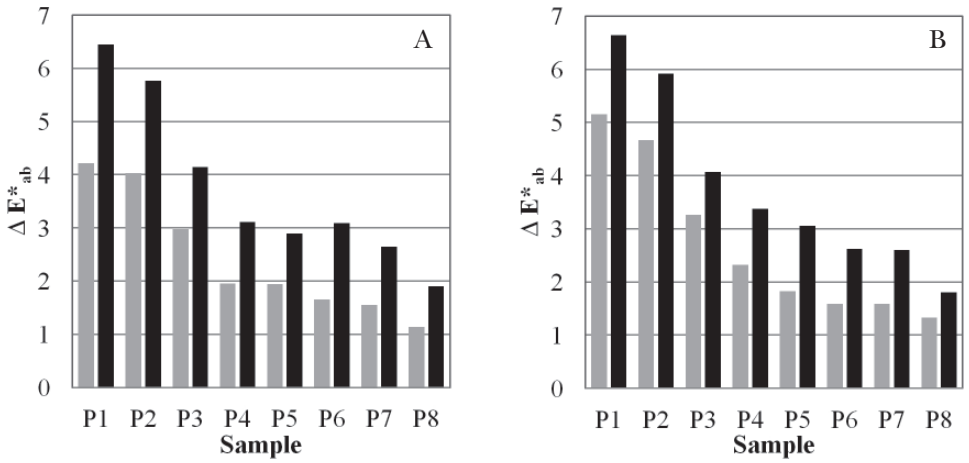

Fig. 7. Total color difference ΔE^*_{ab} after aging for one day (gray columns) and for five days (black columns) for untreated (A) and plasma treated photographic paper (B) N 112.

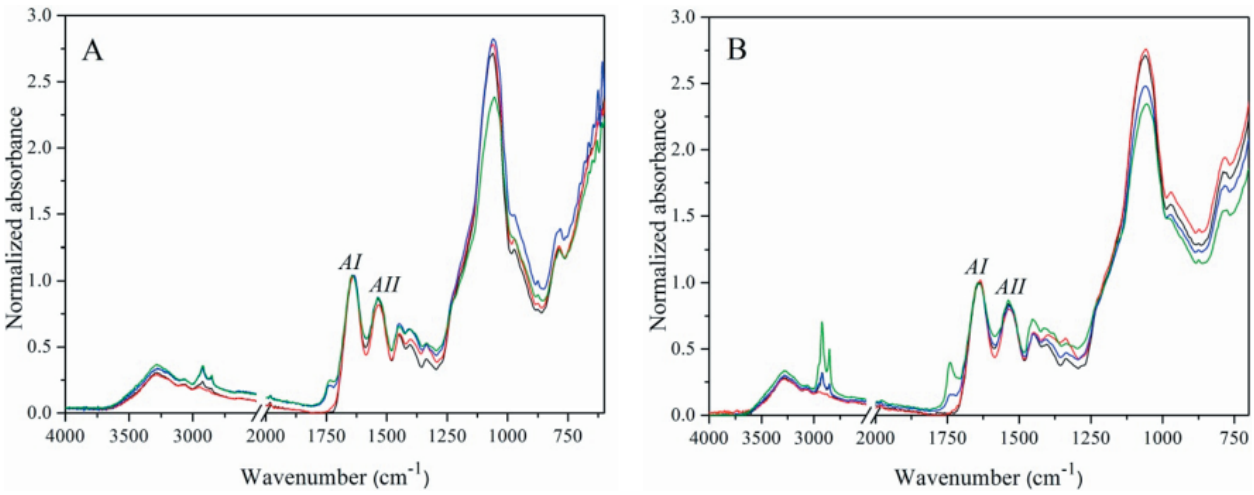

Fig. 8. Normalized FTIR spectra (Amide I) of photographic images of fields P1 (A) and P8 (B) for photographic paper N 112 (untreated sample — black line, sample after plasma treatment for 10 min — red line, untreated sample aged in Q-SUN for five days — blue line, sample after plasma treatment for 10 min and then aged in Q-SUN for five days — green line.

was almost identical to control values, slight increase associated with image bleaching was detected in the dark samples. Differences in coordinate a^* were small, and the most significant changes were observed for coordinate b^* for low optical density fields (e.g. for field P1, $\Delta b^* = 6.3$). With the optical density increase of the photographic field, the increase in Δb^* was less significant. The total color difference (ΔE^*_{ab}) correlates well with the major changes of the b^* coordinate. As it can be seen in Fig. 7, for the low optical density fields (P1—P3) ΔE^*_{ab} after five days of accelerated aging is in the range of 4—6.5, which represents changes observable only in direct comparison. (Panák et al., 2000) Almost identical differences also occurred in plasma-treated samples subjected to accelerated aging. It can be assumed that the use of ADRE plasma does not promote light aging of photographic image.

FTIR spectra shown in Fig. 8 show that during accelerated light aging in the Q-SUN chamber, an increase in absorbance coupled with the formation of a band at 1730 cm^{-1} occurs in all samples (non-treated/plasma-treated samples). This band can be attributed to oxidative products generated in materials upon accelerated light aging, and its more pronounced appearance in paper N 112 may reflect the different properties of the studied papers. Whereas matt paper (N 112) absorbs a significant amount of radiation, glossy paper (N 111) reflects this radiation. In case of matt paper, photoinduced formation of oxidation products is more significant. The extent of oxidative degradation is closely related to the optical density of the photographic image, therefore it is most pronounced in the darkest fields (P8) of both papers. In case of oxidation products generated upon accelerated light aging,

the promoting effect of plasma processing can be seen in comparison to the non-treated samples (green line in Fig. 8B).

Conclusions

Colorimetry, densitometry and FTIR spectroscopy were applied for the characterization of optical and spectral properties of a photographic image with different optical densities prepared on two types of photographic paper FOMABROM (matt and glossy) with a barite layer. Also, the changes observed after the air plasma treatment and accelerated aging in a Q-SUN chamber were monitored.

Using densitometry and colorimetry, minimal changes in optical density and colorimetric coordinates due to air ADRE plasma treatment were observed and the plasma processing did not damage the photographic image. Using FTIR spectroscopy, the changes in the gelatin structure in the image layer were evaluated. It was found that, due to plasma activity, the Amid I/Amid II ratio slightly increased, indicating possible hydrolytic damage of gelatin and, in some cases, simultaneously forming a smaller amount of oxidation products. Under dark storage, this phenomenon is permanent for the darker photographic fields; however, plasma-induced changes disappeared for the low density fields.

Upon accelerated light aging of non-treated/plasma-treated samples in the Q-SUN chamber, no significant difference in optical density and in the stability of the photographic image were found. The only negative phenomenon detected was a slightly increased production of oxidation products in case of accelerated light aging of plasma-treated samples in the fields with the highest optical density of the photographic image.

The fact that low-temperature ADRE plasma does not have a negative effect on the photographic image and its long-term stability in air atmosphere and that plasma-treatment induces no significant changes in the gelatin layer support, this technique seems to be a perspective tool for microbial decontamination and cleaning of photographs.

Acknowledgements

The authors thank the Slovak Grant Agencies APVV (Project No. 15-0460 SK) and VEGA (Project No. 1/0602/19) for financial support.

References

Badea E, Miu L, Budrugeac P, Giurginca M, Masic A, Badea N, Della Gatta G (2008) Journal of Thermal Analysis and Calorimetry 91: 17–27.

Banks BA, Rutledge SK (1996) US Patent 5 560781.

Daniels V (1984) Studies in Conservation 26: 45–49.

Grieten E, Schalm O, Tack P, Bauters S, Storme P, Gauquelin N, Caen J, Patelli A, Vincze L, Schryvers D (2017) Journal of Cultural Heritage 28: 56–64.

Haberová K (2018) Written work on the dissertation test, STU Bratislava.

Ioanid EG, Rusu D, Dunca S, Tanase C (2010) Ann Microbiol 60: 355–361.

Ioanid EG, Ioanid A, Rusu DE, Doroftei F (2011) Journal of Cultural Heritage 12: 296–317.

Korachi M, Aslan N (2013) In: Méndez-Vilas (Ed.), Microbial pathogens and strategies for combating them: science, technology and education, Vol. 1: 453–459.

Martišovitš V (2004) Základy fyziky plazmy, Univerzita Komenského, Bratislava.

Panák J, Čeppan M, Dvonka V, Karpinský Ľ, Kordoš P, Mikula M, Jakucewicz S (2008) Polygrafické minimum, TypoSet, Bratislava.

Pietrzak K, Puchalski M, Otlewska A, Wrzosek H, Guiamet P, Piotrowska M, Gutarowska B (2017) Journal of Cultural Heritage 24: 69–77.

Scheider JP, Vepřek S (2013) Studies in Conservation, 31: 29–37.

Scholtz V, Pazlarova J, Souskova H, Khun J, Julak J (2015) Biotechnology Advances 33: 1108–1119.

Singh BR, DeOliveira DB, Fu F, Fuller MP (1993) Proc. SPIE 1890, Biomolecular Spectroscopy III, Los Angeles.

Tiňo R, Vizárová K, Krčma F (2018) In: Lazzara G, Fakrullin R (Ed) Nanotechnologies and nanomaterials for diagnostic, conservation and restoration of cultural heritage, (pp 239–275). Elsevier Publishing.

Vohrer U, Trick I, Bernhardt J, Oehr C, Brunner H (2001) Surface and Coatings Technology 142–144: 1069–1073.

Zhang M, Zhang B, Li X, Yin Z, Guo X (2011) Applied Surface Science 258: 24–29.

sciendo

Sewage sludge as a source of triclosan-resistant bacteria

Kristína Lépesová[a], Monika Krahulcová[a], Tomáš Mackuľak[b], Lucia Bírošová[a]

[a]Institute of Food Science and Nutrition, Faculty of Chemical and Food Technology, STU in Bratislava, Radlinského 9, 812 37 Bratislava, Slovak Republic
[b]Institute of Chemical and Environmental Engineering, Faculty of Chemical and Food Technology, STU in Bratislava, Radlinského 9, 812 37 Bratislava, Slovak Republic
kristina.lepesova@stuba.sk

Abstract: Subinhibitory concentrations of antibiotics and biocides in wastewaters and sewage sludge have a great impact on the development of antibiotic resistance and its spread among bacteria. The aim of this work was to determine the occurrence of coliform bacteria and enterococci resistant to biocide triclosan in samples of sewage sludge. Subsequently, isolated strains of coliform bacteria were identified and characterized in terms of their antibiotic susceptibility and ability to form a biofilm. Occurrence of the studied bacteria was monitored in three samples of stabilized sludge from three different wastewater treatment plants (Vrakuňa, Petržalka, and Senec). The number of triclosan-resistant coliforms was the highest in the sludge sample from the wastewater treatment plant in Senec and the lowest in the sludge sample from the wastewater treatment plant in Petržalka. Triclosan-resistant *Enterococcus* spp. were not found in any sample of stabilized sludge. Most isolates were identified as *Citrobacter freundii* and *Serratia* spp. Triclosan-resistant isolates showed also resistance to antibiotics and the majority of them were strong biofilm producers.

Keywords: antibiotic resistance, biofilm, coliform bacteria, stabilized sludge, triclosan, wastewater treatment plant

Abbreviations: AMP — ampicillin, ATB — antibiotics, CFU — colony forming units, CIP — ciprofloxacin, CLSI — Clinical Laboratory Standards Institute, CMP — chloramphenicol, EQ — equivalent inhabitants, EU — European Union, EUCAST — European Committee on Antimicrobial Susceptibility Testing, GEN — gentamicin, MALDI-TOF — Matrix–Assisted Laser Desorption/Ionization–Time of Flight, MDR — multidrug-resistance, MIC — minimal inhibitory concentration, QAC — quaternary ammonium compounds, TET — tetracycline, WWTP — wastewater treatment plant

Introduction

Nowadays, the use of synthetic antimicrobial agents for disinfection and hygiene purposes is widespread not only in hospitals but also in industry and households (Carey and McNamara, 2015). Antiseptics, disinfectants and preservatives are biocidal products intended to destroy or control harmful or unwanted microorganisms (Kalkanci et al., 2015).

In hospital settings, they found their application externally to disinfect the skin surface for infection prevention of microbial origin or in pre-operative procedures, as well as to disinfect other surfaces and tools (Nuñez and Moretton, 2007). In addition, biocides are widely used in the food industry particularly for disinfecting containers and equipments (Kalkanci et al., 2015). In households, they are sold for the decontamination of food preparation surfaces (e.g. Dettol), those perceived as microbiologically contaminated (e.g. toilets) and for general improvement of household cleanliness (Fraise, 2002). Recently, the use of antibacterial soaps is also widespread. These products of daily hygiene often contain triclosan or quaternary ammonium compounds (QACs). However, it has been found that soaps containing triclosan at commonly used concentrations (0.1—0.45 % w/v) are no more effective in preventing infection symptoms and reducing the amount of bacteria on hands than regular soaps (Aiello, 2007).

Inappropriate and excessive use of biocides in various areas may lead to increased tolerance to biocides including triclosan, QACs, chlorhexidine and sodium phosphate. Since biocides enter the environment at low concentrations, the risk of resistant microorganism selection increases and cross-resistance to antibiotics (ATBs) can also occur (Kalkanci et al., 2015; Lavilla Lerma et al., 2015). Another problem compared to ATBs is that biocides are non-prescriptive and can occur at higher concentrations in wastewaters as ATBs. Therefore, resistance to biocides is currently attracting great interest (Kalkanci et al., 2015).

The most important biocide triclosan (5-Chloro-2-(2,4-dichlorophenoxy)phenol) (Fig. 1) is a synthetic chlorinated phenyl ether bisphenol with broad-spectrum antimicrobial properties (Middleton and Salierno, 2013).

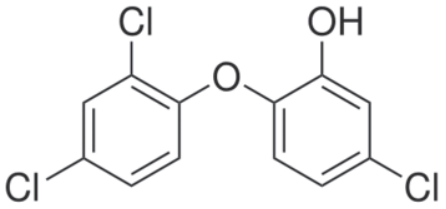

Fig. 1. Chemical structure of triclosan.

It is used as a component of many products such as soaps, toothpastes, shower gels, body lotions and deodorants (Kim et al., 2011; Carey and McNamara, 2015). According to the European Union Directive for cosmetics 76/768/EEC in products of daily use (including cosmetic products), the maximum permitted concentration of triclosan is 0.3 % (Pintado-Herrera et al., 2014). Recently, the use of triclosan has been associated with many health and environmental impacts such as skin irritation, allergies or ecotoxicity of aquatic and terrestrial environment (for Japanese medaka fishes) (Chen et al., 2011). Triclosan can react with free chlorine in water and form chloroform which is classified as a carcinogen. Other compounds formed after their interaction are 2,4-dichlorophenols. Most of these molecules are subsequently after UV exposure converted to dioxins, which are thought to be endocrine disruptors (Rule et al., 2005). According to European Food Safety Authority in up to 450 tons of triclosan for commercial use were produced in the European Union (EU) in 2006, while in the USA its production ranged from 500 to 5000 tons in 1998 (EC, 2010; Carey and McNamara, 2015).

In general, biocide compounds act on multiple target sites in the microbial cell resulting in cell damage and bactericidal effect. However, triclosan in subinhibitory concentrations specifically targets the biosynthesis of fatty acids by the inhibition of NADH-dependent enoyl-ACP reductase *fabI* in *Escherichia coli* (EC, 2010; Sheridan et al., 2012). Recent studies also suggest that triclosan has a weak androgenic and anti-estrogenic effect making it a potential endocrine disruptor (Gatidou et al., 2007). Due to the wide and long-term use of triclosan, it can be found almost everywhere in the environment including wastewaters, soil, surface and drinking water, wastewater treatment plants (WWTPs), sediments as well as breast milk, blood and urine (Lee and Chu, 2013; Carey and McNamara, 2015). It has been shown that up to 79 % of the original amount of triclosan flowing into a WWTP is removed by biodegradation and 15 % is absorbed by activated sludge (Singer et al., 2002). Despite the high rate of degradation in WWTPs, its concentration in purified water is still relatively high (11—98 ng/L) due to high inlet concentrations (42—213 ng/L) (Baková, 2016). It is alarming that the minimal inhibitory concentration (MIC) values of triclosan for different microorganisms are significantly exceeded in the environment, especially in case of sediments, biomass or activated sludge (EC, 2010). The occurrence of triclosan was detected in agricultural soils as a result of fertilization with biomass originating from WWTPs (Kim et al., 2011). On the other hand, triclosan may also break down into methyl-triclosan, which is more stable and has higher potential for bioaccumulation (Rule et al., 2005).

The aim of the present work was to determine the occurrence of triclosan-resistant coliform bacteria and enterococci in samples of stabilized sludge. Subsequently isolated triclosan-resistant coliforms were identified and characterized in terms of their ATB susceptibility and the ability to form a biofilm.

Materials and Methods

Characterization of collection points

Samples of stabilized sludge were taken from the WWTPs in Petržalka, Vrakuňa and Senec. Those in Vrakuňa and Petržalka belong to the largest WWTPs in Slovakia. The Central WWTP in Vrakuňa as well as the WWTP in Petržalka include a mechanical and a biological treatment system and their own sludge and gas economy. While the capacity of the WWTP in Vrakuňa is 300 000 equivalent inhabitants (EQs), WWTP in Petržalka serves for 120 000 EQs. Technical characteristics of these WWTPs were described previously (Mackuľak et al., 2015a, 2015b). The sewage treatment system is the same for both WWTPs. Sludge is stabilized anaerobically. During digestion, a part of organic matter is converted to biogas which is either used for the production of hot tap water or electricity. The second part of sludge is drained and anaerobically stabilized sludge is formed which is used as bio-compost. The WWTP in Senec was built in 1964, but it has been in permanent operation only since 2000. This WWTP serves for 68 000 EQ. Samples of stabilized sludge were taken in December in 2015.

Monitoring of triclosan-resistant coliform bacteria and enterococci occurrence in stabilized sludge

Coliform bacteria were detected on Chromocult Coliform agar plates (VWR Chemicals, USA), while Slanetz-Bartley agar (Biolife, Italy) was used in case

of enterococci. Based on previous results obtained in the laboratory, concentrations of triclosan applied in the media were determined to be 100 μg/mL, 200 μg/mL and 300 μg/mL, thus significantly exceeding the MIC values of this biocide defined for the studied groups of bacteria. Coliforms were cultivated for 24 h at 37 °C, while cultivation conditions for *Enterococcus* spp. were 48 h and 40 °C. Colony forming units (CFU) of the observed bacteria were counted on parallel inoculated Petri dishes and the results were expressed as the number of CFU per gram (CFU/g) of stabilized sludge. Each experiment was repeated three times.

Isolation and identification of triclosan-resistant coliform bacteria

Coliform bacteria showing resistance to triclosan were isolated by the streak plate method on Mueller Hinton agar (Biolife, Italy) plates (24 h, 37 °C) and identified by a Matrix-Assisted Laser Desorption/Ionization—Time of Flight (MALDI-TOF) mass spectrometer according to Lépesová et al. (2018).

Determination of ATB susceptibility

Susceptibility of triclosan-resistant coliform bacteria to ATBs including ampicillin (AMP), gentamicin (GEN), ciprofloxacin (CIP), chloramphenicol (CMP) and tetracycline (TET) was detected by the plate dilution drop method previously described in the study by Lépesová et al. (2018).

Detection of biofilm formation

Quantitative assessment of biofilm formation was detected by measuring the absorbance of biofilm eluate at 570 nm using a plate reader (BioTek, US) according to Beenken et al. (2003). Experiment was run in six parallels and it was repeated three times. The exact method for biofilm detection has been in details described by Lépesová et al. (2018).

Results and Discussion

Occurrence of triclosan-resistant coliform bacteria and enterococci in stabilized sludge

As a result of low acute toxicity and general safety for humans, triclosan has been used as an additive in various consumer products including toothpastes, soaps, deodorants or disinfectants for households and hospitals. However, frequent use of such products has resulted in an increased release of triclosan into wastewaters, stabilized sludge as well as recipients (Middleton and Salierno, 2013; Wang et al., 2018). Thus, occurrence of coliform bacteria and *Enterococcus* spp. resistant to triclosan in different samples of stabilized sludge was determined in the first part of the study. Since, in case of biocide agents such as triclosan, resistance limits are not given, concentrations nearly 1000 times higher than the MIC of triclosan defined for studied bacteria (c1 = 100 μg/mL, c2 = 200 μg/mL and c3 = 300 μg/mL) were chosen for the selection of resistant bacteria. The MIC value for triclosan ranges from 0.3 μg/mL to 0.64 μg/mL (Chuanchuen, 2003).

Figure 1 describes the ratio of coliform bacteria resistant to triclosan in the studied samples of stabilized sludge taken in December in 2015. The highest number of coliforms was recorded in the sludge sample from the WWTP in Petržalka (6.6 log CFU/g), while in the sample from the largest WWTP in Vrakuňa, their number was slightly lower (6.0 log CFU/g). In the stabilized sludge from the WWTP in Senec, the total number of coliform

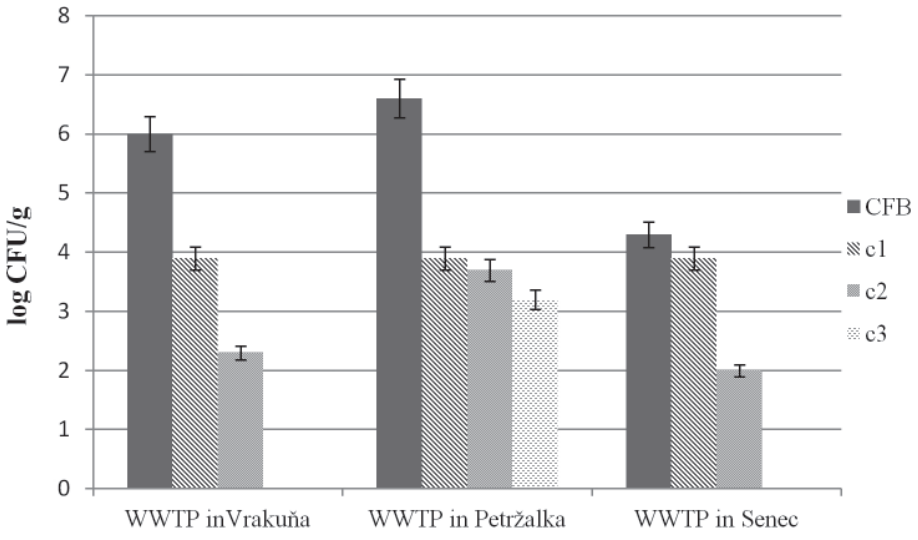

Fig. 2: Number of total and triclosan-resistant coliform bacteria in stabilized sludge. CFB — total coliform bacteria, c1 — triclosan 100 μg/mL, c2 — triclosan 200 μg/mL, c3 — triclosan 300 μg/mL.

bacteria was by 2.0 logarithmic orders lower (4.3 log CFU/g). While in case of the WWTP in Petržalka, about a half of the coliform strains showed resistance to all three applied concentrations of triclosan, in stabilized sludge from the WWTPs in Vrakuňa and Senec, coliforms resistant to the highest concentration of triclosan (c3 = 300 μg/mL) were not detected. Although, the sample of stabilized sludge taken from the WWTP in Senec contained the lowest number of coliform bacteria, most of them (about 90 %) tolerated the lowest applied triclosan concentration (Fig. 2).

The presence of total enterococci was detected in all of three samples of stabilized sludge. The highest values were recorded again in the WWTP in Petržalka (5.2 log CFU/g) and the lowest ones in the WWTP in Senec (4.2 log CFU/g). However, no stabilized sludge sample contained triclosan-resistant enterococci. Other studies also confirmed the presence of triclosan resistant bacteria in waste and surface water, but none has studied triclosan resistance in sewage sludge nor in such high concentration of triclosan (Middleton and Salierno, 2013; Coetzee et al., 2017). As this biocide is lipophilic, its adsorption to sludge is much better compared to hydrophilic compounds. This also confirms our results that bacteria found in sewage sludge are more tolerant to very high triclosan concentrations.

Identification of triclosan-resistant coliform isolates

For qualitative analysis of coliform isolates, MALDI-TOF mass spectrometry, recently introduced in many microbiological laboratories for routine identification of microorganisms (Hrabák et al., 2013), was employed. When identifying microorganisms by MALDI-TOF, an approach based on the generation of a unique spectrum ("fingerprint") of intact cells is used this is then compared to the reference spectrum (Santos et al., 2015).

Triclosan-resistant isolates were identified as *Citrobacter freundii*, *Morganella morganii*, *Serratia fonticola* and *Serratia liquefaciens* (Tab. 1). These types of bacteria can be found typically in soil, wastewaters, sewage, but also in food or in the intestinal tract of humans or animals (Wang, 2000; Liu et al., 2016). *C. freundii* can become an opportunistic pathogen that is mostly associated with urinary and respiratory infections (Santos et al., 2017). *M. morganii* were previously considered as pathogens of minor importance, however, they have been declared a significant cause of nosocomial infections in recent years (Liu et al., 2016). *S. fonticola* and *S. liquefaciens* are conditional human pathogens responsible for nosocomial, lower respiratory tract and urinary tract infections as well as for infections of skin or soft tissues (Aljorayid et al., 2016; Liu et al., 2017).

ATB susceptibility profile of triclosan-resistant coliform isolates

The increasing phenomenon of ATB and biocide resistance is a global problem that has been threatening public health for several decades. Increasing trend of bacterial resistance is due to the misuse of ATBs as well as the widespread use and misuse of biocidal agents not only in the hospital environment but also in the food industry and households. Most pharmaceuticals used in human infection treatment and prevention are only partially metabolized. Their metabolites are subsequently directed into the municipal wastewaters that flow through the sewage system to WWTPs. ATB residues resist the process of degradation in spite of the well-developed process of wastewater treatment (including biological degradation of drugs under anaerobic conditions in sludge towers) and consequently can accumulate in sludge (Birošová et al., 2014; Birošová and Mikulášová, 2014). Studies pointed out the problem of cross-resistance in triclosan-resistant isolates which are also ATB resistant (Birošová et al., 2009; Middleton and Salierno, 2013). Therefore, susceptibility of coliforms showing resistance to triclosan isolated from different samples of stabilized sludge to ATBs was tested. ATBs of different classes were applied in concentrations given by resistance limits reported for *Enterobacteriaceae* by the European Committee on Antimicrobial Susceptibility Testing for the EU (EUCAST) and by the Clinical Laboratory Standards Institute (CLSI) for the United States (Tab. 1).

Among β-lactam ATBs, AMP was chosen because of its frequent use in Slovakia (ECDC, 2017). However, according to Magiorakos et al. (2012) isolates identified as *M. morganii* and *C. freundii* are characterized by an intrinsic resistance to this ATB thanks to the chromosomally encoded *ampC* gene responsible for β-lactamase production. While *S. fonticola* is resistant to AMP in the CLSI concentration, isolates of *S. liquefaciens* showed resistance against this ATB according to the EUCAST (tab. 1). Both GEN and CIP can be present in wastewaters in higher levels due to their frequent use in the community as well as hospital sector (Lépesová et al., 2018). GEN resistance was observed only in *M. morganii* and *C. freundii* (CLSI) isolated from the stabilized sludge taken from the WWTP in Petržalka. Resistance to CIP showed only one isolate identified as *C. freundii*. Application of CMP is currently delimited, but bacterial strains exhibiting resistance to this ATB persist due to the possible mechanisms of cross-resistance (Birošová et al., 2014). Decreased susceptibility to CMP was observed in case of two coliform isolates (*M. morganii* and *C. freundii*) from the WWTP in Petržalka, which were able to grow

Tab. 1. Identification and susceptibility testing of triclosan-resistant coliform isolates from stabilized sludge.

Stabilized sludge	Triclosan content (∝g/mL)	Identification	AMP	GEN	CIP	CMP	TET	MDR
WWTP in Petržalka	100	*M. morganii*	INR	R2	–	R1	INR	–
	100	*C. freundii*	INR	–	–	-	–	–
	300	*C. freundii*	INR	–	–	-	–	–
	300	*C. freundii*	INR	–	–	-	–	–
	200	*C. freundii*	INR	–	R2	R1	–	–
	300	*C. freundii*	INR	–	–	-	–	–
	200	*C. freundii*	INR	R2	–	-	–	–
WWTP in Senec	200	*S. fonticola*	R2	–	–	-	–	–
	200	*S. liquefaciens*	R1	–	–	-	–	–
WWTP in Vrakuňa	200	*S. liquefaciens*	R1	–	–	-	–	–

AMP — ampicillin, GEN — gentamicin, CIP — ciprofloxacin, CMP — chloramphenicol, TET — tetracycline.
MDR — multidrug-resistant, INR — intrinsic resistance.
R1 — resistance according to the EUCAST, R2 — resistance according to the CLSI.

only at the concentration defined by the EUCAST (Tab. 1).

Although TET is not used as much as AMP or CIP, its selection pressure persists particularly because of the use of oxytetracycline for veterinary praxis (Birošová et al., 2014). From Table 1 it is evident that *M. morganii* can be characterized by intrinsic resistance to TET (Magiorakos et al., 2012). Except for this isolate, resistance to TET was not recorded in any triclosan-resistant isolates.

Based on the number of ATB classes against which coliform isolates showed resistance, their multidrug-resistance (MDR) character was recorded. According to Magiorakos et al. (2012), only microorganisms resistant to antimicrobial substances included in three or more ATB classes can be considered as MDR. This condition was not met in case of the tested coliform isolates (Tab. 1).

Biofilm forming ability of triclosan-resistant coliform isolates

Biofilm is defined as microbial population adhering to biotic and abiotic surfaces which is enclosed in an extracellular matrix of a polymeric substance (exopolysaccharides) (Donlan, 2002). Biofilms are a source of severe infections and are difficult to remove and problematic to control. Benefit of biofilm community is the protection against ATBs, disinfectants and environmental dynamics (Garrett et al., 2008). Biofilm formation can also be beneficial for the human population; it is used in biological wastewater treatment in WWTPs and in biotechnological processes, in particular for the removal of pollutants such as metals, radionuclides, oil or nitrogen compounds (Sehar and Naz, 2016). On the other hand, high bacterial density and diversity are found in biofilms from wastewater systems; especially from activated sludge of sewage treatment plants which support horizontal gene transfer in the bacteria population (Lépesová et al., 2018).

Since bacteria in biofilms can be much more resistant to ATBs as well as to other environmental stress factors, the ability of triclosan-resistant coliforms isolated from stabilized sludge to form biofilm was determined (Fig. 3).

Based on the absorbance values, the tested isolates were classified as weak, medium, strong and very strong producers of bacterial biofilm according to the scale developed by Taniguchi et al. (2009). All isolates of *C. freundii* as well as those of *M. morganii* and *S. liquefaciens* were strong producers of bacterial biofilm. Second isolate of *S. liquefaciens* from the WWTP in Senec and *S. fonticola* from the WWTP in Vrakuňa were able to form biofilms with medium intensity (Fig. 3).

The annual production of stabilized sludge in Slovakia is about 58 000 tons, most of which is transferred to the composting plant where it is mixed with compost. In 2012, 36 832 tons of stabilized sludge were processed into compost and up to 1 139 tons were applied directly to soil (Birošová et al., 2014). Many studies highlight the risk of sludge application because of the content of ATBs and their metabolites, biocides or heavy metals at subinhibitory concentrations, which play a role in stimulating both the emergence of bacterial resistance by mutations as well as the horizontal

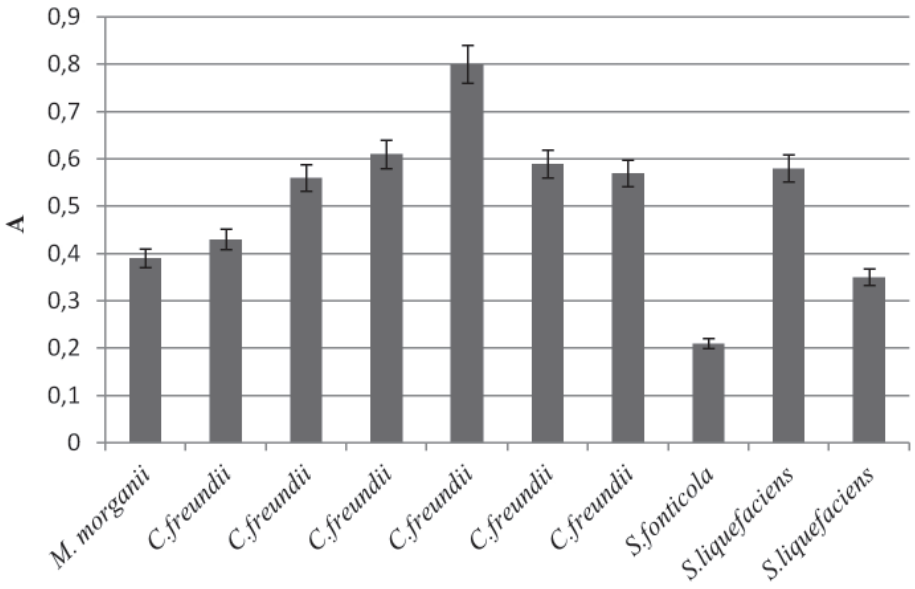

Fig. 3. Biofilm forming ability of triclosan-resistant coliform bacteria. A — Absorbance.

gene transfer rate (Baquero a kol., 2008; Birošová et al., 2014; Makowska a kol., 2016). In addition to the spread of chemical agents from the stabilized sludge into the environment, it was also shown that sludge contains an abundant number of coliform bacteria able to spread the resistance phenomenon (Reinthaler et al, 2010; Birošová et al., 2014).

Conclusions

Currently, there is convincing evidence that common mechanisms responsible for resistance to biocides and ATBs are present in bacteria and can be acquired by mobile genetic elements. Our data show that coliform bacteria present in sewage sludge are able to resist very high concentrations of triclosan. Approximately half of coliform isolates were also ATB resistant and the majority of them are strong biofilm producers.

The high prevalence of triclosan-resistant coliform bacteria in stabilized sludge represents a potential risk of direct application of sludge to soil due to the development and spread of bacterial resistance in the ecosystem.

Acknowledgements

This work was supported by the Slovak Research and Development Agency (grant no. APVV-16-0171), the Scientific Grant Agency VEGA (grant no. VEGA 1/0096/17) and by a project for building of infrastructure for modern research of civilization diseases (ITMS 26230120006).

References

Aiello AE, Larson EL, Levy SB (2007) Clinical Infectious Diseases 1, Oxford Journals 45: S137—S147.

Aljorayid A, Viau R, Castellino L, Jump RLP (2016) Idcases 5: 6—8.

Baková A (2016) Bachelor Thesis, p. 1—56, Bratislava (In Slovak).

Baquero F, Martínez JL, Cantón R (2008) Current Opinion In Biotechnology 19: 260—265.

Beenken KE, Blevins JS, Smeltzer MS (2003) Infection And Immunity 7: 4206—4211.

Birošová L, Mikulášová M (2009) Journal Of Medical Microbiology 58: 436—441.

Birošová L, Mikulášová M (2014) Biomedical Papers 158 (2): 315—320.

Birošová L, Mackuľak T, Bodík I, Ryba J, Škubák J, Grabic R (2014) Science Of The Total Environment 490: 440—444.

Butler E, Whelan MJ, Sakrabani R, Egmond R (2012) Environmental Pollution 167: 107—109.

Carey DE, Mcnamara PJ (2015) Frontiers In Microbiology 5: 1—11.

Chen X, Nielsen JL, Furgal K, Liu Y, Lolas IB, Bester K (2011) Chemosphere 84: 452—456.

Chuanchuen R (2003) American Journal Of Infection Control 31(2): 124—127.

Coetzee I, Bezuidenhout CC, Bezuidenhout JJ (2017) Water Science & Technology 76(6): 1500—1509.

Donlan RM (2002) Emerging Infectious Diseases 8(9): 881—890.

European Centre for Disease Prevention and Control (2017) Stockholm, Sweden: ECDC; 2017, ISBN 978-92-9498-099-1, p. 1—11.

European Comission, Scientific Committee On Consumer Safety, EC (2010) European Union, ISBN 978-92-79-12484-6, p. 1—56.

Fraise AP (2002) Journal Of Antimicrobial Chemotherapy 1, Oxford Journals 49: 11—12.

Garrett TR, Bhakoo M, Zhang Z (2008) Progress In Natural Science 18 (9): 1049—1056.

Gatidou G, Thomaidis NS, Stasinakis AS, Lekkas TD (2007) Journal Of Chromatography A 1138: 32—41.

Hrabák J, Chudáčková E, Walková R (2013) Clinical Microbiology Reviews 26: 103—114.

Kalkanci A, Elli M, Adil Fouad A, Yesilyurt E, Jabban Khalil I (2015) Journal De Mycologie Médicale 25: 280—286.
Kim Y, Murugesan K, Schmidt S, Bokare V, Jeon JR, Kim EJ, Chang YS (2011) Bioresource Technology 102: 2206—2212.
Lavilla Lerma L, Benomar N, Casado Muñoz Mdel C, Gálvez A, Abriouel H (2015) Food Microbiology 51: 33—44.
Lee DG, Chu KH (2013) Chemosphere 93: 1904—1911.
Lépesová K, Kraková L, Pangallo D, Medveďová A, Olejníková P, Mackuľak T, Tichý J, Grabic R, Birošová L (2018) Journal Of Global Antimicrobial Resistance 14: 145—151.
Liu H, Zhu J, Hu Q, Rao X (2016) International Journal Of Infectious Diseases 50: 10—17.
Liu J, Yu S, Han B, Chen J (2017) Food Control 78: 196—202.
Mackuľak T, Birošová L, Grabic R, Škubák J, Bodík I (2015a) Environmental Science And Pollution Research 22: 14000—14006.
Mackuľak T, Nagyová K, Faberová M, Grabic R, Koba O, Gál M, Birošová L (2015b) Environmental Toxicology And Pharmacology 40: 492—497.
Magiorakos AP, Srinivasan A, Carey RB, Carmeli Y, Falagas ME, Giske CG, Harbarth S, Hindler HF, Kahlmeter G, Olsson-Liljequist B, Paterson DL, Rice LB, Stelling J, Struelens MJ, Vatopoulos A, Weber JT, Monnet DL (2012) Clinical Microbiology And Infection 18: 268—281.
Makowska N, Koczura R, Mokracka J (2016) Chemosphere 144: 1665—1673.
Middleton JH, Salierno JD (2013) Ecotoxicology and Environmental Safety 88: 79—88.
Nuñez L, Moretton J (2007) Brazilian Journal Of Microbiology 38: 644—648.
Pintado-Herrera MG, González-Mazo E, Lara-Martín PA (2014) Chemosphere 95: 478—485.
Reinthaler FF, Feierl G, Galler H, Haas D, Leitner E, Mascher F, Melkes A, Posch J, Winter I, Zarfel G, Marth E (2010) Water Research 44: 1981—1985.
Rule KL, Ebett VR, Vikesland PJ (2005). Journal Environmental Science and Technology 39(9): 3176—85.
Santos C, Ramalheira E, Da Silva G, Mendo S (2017) Journal of Global Antimicrobial Resistance 8: 18—22.
Santos T, Capelo JL, Santos HM, Oliveira I, Marinho C, Gonçalves A, Araújo JE, Poeta P, Igrejas G (2015) Journal of Proteomics 127: 321—331.
Sheridan À, Lenahan M, Duffy G, Fanning S, Burgess CM (2012) Food Control 26: 98—106.
Sehar S, Naz I (2016) Intech Open, Chapter 7: 121—144.
Singer H, Müller S, Tixier C, Pillonel L (2002) Environmental Science & Technology 36: 4998—5004.
Taniguchi L, De Fátima Faria B, Rosa RT, De Paula E Carvalho A, Gursky LC, Elifio-Esposito SL, Parahitiyawa N, Samaranayake LP, Rosa EA (2009) Journal of Microbiological Methods 78: 171—174.
Wang JT, Chang SC, Chen YC, Luh KT (2000) Journal Of Microbiology, Immunology And Infection 33(4): 258—62.
Wang S, Poon K, Cai Z (2018) Journal Of Hazardous Materials 342: 643—650.

sciendo

Prevalence of *Staphylococcus aureus* and antibiotic resistant *Staphylococcus aureus* in public transport in Bratislava, Slovakia

Alžbeta Medveďová, Romana Györiová

Department of Nutrition and Food Quality Assessment,
Faculty of Chemical and Food Technology, Slovak University of Technology in Bratislava,
Radlinského 9, Bratislava 812 37, Slovakia
alzbeta.medvedova@stuba.sk

Abstract: There is evidence that the transmission of *Staphylococcus aureus* and methicillin-resistant *S. aureus* between the community and environmental surfaces still exists. Even the means of this transmission remain uncertain, the public transport system may serve as a potential source of different bacteria, and the contact with contaminated public surfaces may increase the risk for bacterial diseases emergence. This study aimed to investigate *S. aureus* contamination on Bratislava's public transport vehicles. Forty samples of hand-touched surfaces were collected during December 2015 and March 2017 by using surface sampling method. *S. aureus* was detected in all analysed swabs. Simultaneously, antibiotic resistance of *S. aureus* from swabs was evaluated. Of 40 samples, only 23 % did not contain *S. aureus* resistant to some of 10 analysed antibiotics. On the other hand, the severe prevalence of highly resistant *S. aureus* to penicillin, methicillin, ampicillin, and cefoxitin was confirmed. 15 % of isolates displayed resistance to at least three antimicrobial classes. The amount of *S. aureus* was not significantly influenced by the lines or by the analysed surface (grabs rails or on-board stop buttons). However, there was a statistically significant effect of year period, both between samples from December and March and between samples from the same month but different year. The study confirmed the widespread occurrence of resistant *S. aureus* in public transport vehicles in Bratislava, Slovakia.

Keywords: antibiotic resistance, Bratislava, environmental contamination, public transport, *Staphylococcus aureus*

Introduction

Public vehicles, among other public areas, are places with easy transfer of bacteria from individual to individual, and connecting people with different social, ethnic, hygienic and health conditions. The bacteria transmission may be unsettling if pathogenic and resistant bacteria occur. While some bacteria are mainly nosocomial, some are also community-acquired. These include coagulase-positive staphylococci and *Staphylococcus aureus*, which frequently colonize the nasal vestibule and the skin (ECDC, 2017) of about 10—50 % asymptomatic human. However, *S. aureus* disposes of a remarkably wide range of virulent factors leading to smooth and skeletal muscle paralysis, blood vessels damage, the formation of extensive skin lesions and finally affecting the central nervous system (Arbuthnott et al., 1990).

Moreover, pathogenic *S. aureus* is regarded as a "superbug", due to its amazing capacity to be resistant to a wide range of antibiotics. Strains resistant to methicillin (MRSA), vancomycin (VISA/VRSA) and many other antibiotics represent an urgent global problem in community as well as in hospital-acquired infections. The mortality of *S. aureus* bacteraemia remains approximately 20—40 % despite the availability of effective antimicrobials (Mylotte et al., 1987; ECDC, 2017). Most hospital-acquired MRSA in Europe belongs to only five clonal lineages, which have distinct geographical patterns of occurrence, whereas the background populations of methicillin-susceptible *S. aureus* (MSSA) are highly diverse, consisting of many lineages that have been widely disseminated due to leisure travel and migration flows (Gaymard et al., 2016).

In the community, *S. aureus* can be quickly transferred from carriers or infected persons via direct contact (Stepanović et al., 2008). It has also been shown that they can survive under dry conditions and can persist on different surfaces for a very long time (Bremer et al., 2004). Moreover, it is well known for its ability to stick to plastic surfaces. Teichoic acids are essential compounds present in the cell wall and are important for adhesion on plastic surfaces thanks to its interaction with other surface polymers (Reffuveille et al., 2017). In this connection, public vehicles may allow its transmission due to the high number of hand-touched surfaces and their permanent contact with transport users (Gaymard et al., 2016).

Bratislava is the capital and the biggest city in the Slovak Republic. Annually, the city public transport provides transfer for approximately 250.000 people in approximately 850 vehicles

(buses, trams, and trolleybuses). These may serve as a critical reservoir of staphylococci, due to their ability to colonize human skin and also environmental surfaces. In this connection, we decided to describe the prevalence of *S. aureus* and its antibiotic resistance profile on hand-touched surfaces in vehicles moving around the capital city of Slovakia.

Materials and methods

Sampling

In December 2015, March 2016, December 2016 and March 2017, 40 samples from 5 different public transport lines were collected by using a surface sampling method. Samples were taken concerning to have a high level of skin-to-touch surfaces, like grab rails and on-board stop buttons. The public transport lines were chosen concerning copy the routes with high passengers' frequency, such as proximity to Central bus or train station, proximity to Central Hospital and cemetery or students Hall of residences (Fig. 1).

The samples were collected from a predetermined area in vehicles (about 300 cm^2) using sterile swab moistened in sterile peptone-saline solution. The samples were kept refrigerated at 4—6 °C until they were brought in the laboratory (not longer than 1 hour).

In Fig. 1, empty crosses represent proximity of the hospital, filled crosses represent proximity of cemetery and triangles represent proximity to the Hall of residence. Solid black circles represent places of sampling.

Determination of S. aureus and S. aureus resistant to antibiotics

Samples (without dilution and after their 10-fold dilution in peptone-saline solution) from each swab were plated onto Baird-Parker agar (Sigma-Aldrich, St. Louis, USA) in order to determine the total counts of *S. aureus* according to EN ISO 6888-1 (2003). Samples from each swab were also spread on Baird-Parker agar containing different antibiotics (ampicillin, ciprofloxacin, cefoxitin, erythromycin, gentamicin, chloramphenicol, tetracycline, vancomycin, penicillin, methicillin), all purchased from Sigma-Aldrich (St. Louis, USA). Antibiotic resistance was detected according to European (EUCAST, 2018) or for methicillin-resistance according to US (CLSI, 2007) resistance breakpoints. Before bacteriological counting, the plates were incubated for 48 h at 37 °C aerobically. Each experiment was run in triplicate. The suspected colonies were confirmed by tube coagulase test, by the presence of catalase by using 3 % (v/v) solution of hydrogen peroxide, by microscopy examination and by MALDI-TOF technique.

Statistical analysis

The data analysis was performed using Microsoft Excel tools 2007 (Microsoft, Redmond, Washington, USA). Data were treated by independent Student t-test and confirmed by ANOVA test with statistical significance of $p < 0.05$.

Results and discussion

In all samples, the presence of *S. aureus* was confirmed. Its counts ranged from 1.40 to

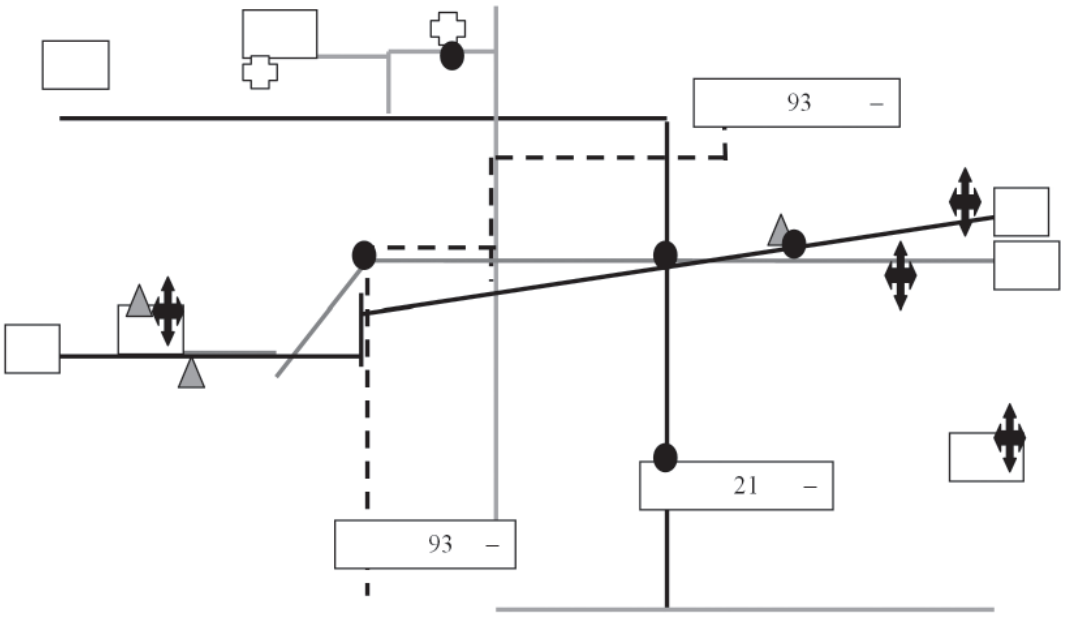

Fig. 1. Scheme of selected public transport lines in Bratislava.

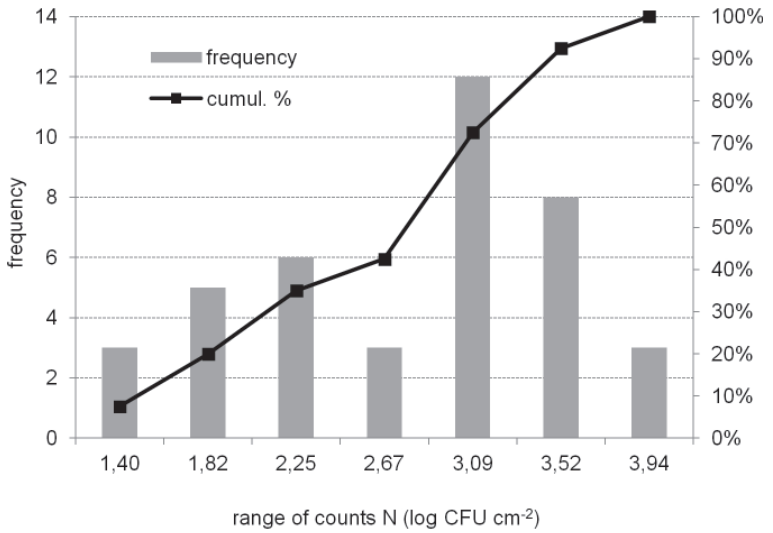

Fig. 2. The concentration of *S. aureus* contamination on hand-touched surfaces in vehicles (n = 40).

3.94 log CFU cm^{-2}, with average value of N = = 2.65 ±0.70 log CFU cm^{-2} (%V = 26.6 %). The distribution of staphylococcal contamination on analysed surfaces is presented in Fig. 2. Also, Sexton et al. (2007) detected MRSA in all 2959 samples from subways, buses, trains, and other public surfaces. MRSA was also isolated from all 55 vehicles analysed by Stepanović et al. (2008). However, the proportion of samples positive for the presence of MRSA per vehicle ranged from 4.5 % to 57.1 %. Similar results were also obtained by Otter and French (2009) who analysed the occurrence of *S. aureus* in buses, trains, stations, and other public places in London. They found out that 95 % of analysed surfaces were colonized by *S. aureus* and its average density was about 1.08 CFU cm^{-2}. On the other hand, in Lyon only 22 % of analysed surfaces in buses were positive for *S. aureus* presence (Gaymard et al., 2016) and in Porto, only 16 % of buses (mean count 6.1 CFU 100 cm^{-2}) and 9 % of trains (mean count 4.0 CFU 100 cm^{-2}) was contaminated by *S. aureus* (Mendes et al., 2015). These differences could be a result of specifically targeted sampling places close to hospitals in some studies. Moreover, as reported Mendes et al. (2015), the prevalence of *S. aureus* in public transport system in Porto decreased from 26 % in 2009–2010 to 9–16 % in 2015, mainly as a result of proper cleaning and disinfection practices of vehicles' surfaces.

In our samples, the amount of *S. aureus* was not significantly influenced ($p < 0.05$) by the lines or by the analysed surface (grabs rails or on-board stop buttons). No significant difference between mean counts of *S. aureus* in buses and trains was also found out by Mendes et al. (2015). However, there was statistically significant ($p < 0.05$) effect of the year period, both between samples from December and March and between samples from the same month but different year.

The occurrence of resistant S. aureus

The occurrence of *S. aureus* resistant to 10 different antibiotics is summarized in Figure 3, where are shown all analysed samples and samples positive for the presence of *S. aureus* resistant to selected antibiotics. Only 22.5 % of samples did not contain resistant *S. aureus* at all. 37.5 % of samples were positive for the presence of *S. aureus* resistant to only one antibiotic, mostly to a penicillin (36.8 % of them) and methicillin (31.6 % of them). These two antibiotics, together with vancomycin were the most ineffective antibiotics in general. Altogether, 50 % of samples contained *S. aureus* resistant to penicillin, and their portion in samples ranged from 67 to 99 %. There was also a high prevalence of resistant *S. aureus* to ampicillin (65–85 %) and cefoxitin (81–95 %). However, these isolates were detected only in 5 or 6 swabs, respectively.

The resistance to methicillin in analysed swabs ranged within 75 to 95 %, and 30 % of swabs were positive to the presence of methicillin-resistant *S. aureus*. These findings are in accordance with the data presented in the Antimicrobial resistance surveillance report (ECDC, 2017). While the prevalence of MRSA strains in EU countries is continuously decreasing from 18.8 % in 2012 to 16.8 % in 2015, in Slovakia a significantly increasing trend is observed. Their prevalence in 2012 was 21.7 %, and in 2015 it was 28.1 %. MRSA strains remain a public health priority not only in Slovakia but also in whole Europe, as MRSA percentages remain high (34.1 to 57.2 %) in several countries, e.g., Italy, Greece, Cyprus,

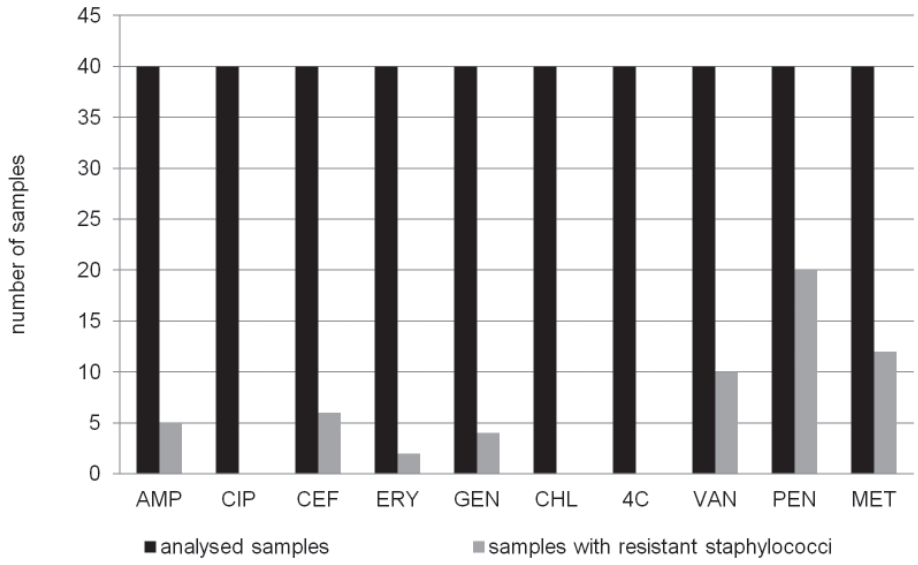

Fig. 3. The ratio of total analysed samples (n = 40) and samples with *S. aureus* resistant against selected antibiotics. AMP — ampicillin, CIP — ciprofloxacin, CEF — cefoxitin, ERY — erythromycin, GEN — gentamicin, CHL — chloramphenicol, 4C — tetracycline, VAN — vancomycin, PEN — penicillin, MET — methicillin.

Portugal, Malta, and Romania. There is also a high prevalence of MRSA strains in the United States (0.2 isolates pre 1,000 patient days) with Panton-Valentine leukocidin-positive strains as a predominant compared with the United Kingdom (0.1 per 1,000) with Panton-Valentine leukocidin-negative strains as a predominant ones (Otter et al., 2009). The increased MRSA infections reported in different countries led to the detection of unique SCCmec element, that appears more genetically mobile, and it is suggested that it has been heterologously transferred from other staphylococcal species (Lowy, 2014). MRSA isolates are often also resistant to fluoroquinolones, further limiting the treatment options available for severe infections. In this context, it was surprising, that there was no ciprofloxacin-resistant *S. aureus* in our samples.

Furthermore, there was also no *S. aureus* resistant to chloramphenicol and tetracycline. Contrary results obtained by Stepanović et al. (2005) indicating a high prevalence of coagulase-negative staphylococci resistant to tetracycline (63.1 %), followed by gentamicin (33.7 %) and erythromycin (33 %) resistant strains. From vehicles moving around Bratislava, *S. aureus* resistant to gentamicin and erythromycin were confirmed in 10 or 5 % of swabs, respectively. Stepanović et al. (2005) also found out that 46.9 % of staphylococci detected in Belgrade's public transport were multidrug-resistant. In our case, only 15 % of isolates can be considered as multidrug-resistant *S. aureus* according to criteria proposed by Magiorakos et al. (2011).

Conclusion

In conclusion, we found out that *S. aureus* was detected in all samples from public transport surfaces. Only 23 % of samples did not contain *S. aureus* resistant to some of 10 analysed antibiotics. On the other hand, the severe prevalence of highly resistant *S. aureus* to penicillin, methicillin, ampicillin, and cefoxitin was confirmed. So, public surfaces can be a significant reservoir not only for *S. aureus* but also for its resistant variants.

Further work is required to assess the prevalence of *S. aureus* also in other Slovak and European cities and also to assess the transfer of resistant bacteria from the community to environment, and vice versa. Also, the appropriate cleaning and disinfection practices are needed in order to reduce the prevalence of pathogenic bacteria in the environment together with appropriate personal hygiene practices. Last (but) not least, the well-considered and reasonable usage of antibiotics is a global necessity.

Acknowledgment

This work was supported by the Slovak Research and Development Agency (Contract No. APVV-16-0171) and by the Scientific Grant Agency of the Ministry of Education of the Slovak Republic and Slovak Academy of Science – VEGA 1/0096/17.

References

Arbuthnott J, Coleman D, DeAzavedo J (1990) Journal of Applied Bacteriology Symposium Supplement 69: 1S–8S.

Bremer P, Fletcher G, Osborne C (2004) Staphylococcus aureus, New Zealand Institute for Crop and Food Research Limited, Christchurch. pp. 1—6.

CLSI Performance Standards for Antimicrobial Susceptibility Testing (2007) 17th Informational Supplement 27: 1—182.

ECDC (2017) Antimicrobial resistance surveillance in Europe 2015, Surveillance report, Avialable in May 2017: http://ecdc.europa.eu/en/publications/Publications/antimicrobial-resistance-europe-2015.

EN ISO 6888-1 (2003) Microbiology of food and animal feeding stuffs — Horizontal method for the enumeration of coagulase-positive staphylococci (*Staphylococcus aureus* and other species) — Part 1: Technique using Baird-Parker agar medium, 1—11.

European Committee on Antimicrobial Susceptibility Testing (EUCAST, 2018) Breakpoint tables for interpretation of MICs and zone diameters. Version 7.1., Available in July 2018: http//www.eucast.org.

Gaymard A, Pichon M, Degaud M, Tasse J, Dupieux C, Laurent F (2016) International Journal of Antimicrobial Agents 48: 459—462.

Lowy FD (2014) Journal of Clinical Investigation 111: 1265—1273.

Magiorakos A-P, Srinivasan A, Carey RB, Carmeli Y, Falagas ME, Giske CG et al. (2011) Clinical Microbiology and Infection 18: 268—281.

Mendes Â, Martins da Costa P, Rego D, Beça N, Alves C, Moreira T, Conceiçao T, Aires-de-Sousa M (2015) Public Health 129: 1125—1131.

Mylotte JM, McDemott C, Spooner JA (1987) Reviews of Infectious Diseases 9: 891—907.

Otter JA, French GL (2009) Letters in Applied Microbiology 49: 803—805.

Otter JA, Havill NL, Boyce JM, French GL (2009) Journal of Clinical Microbiology and Infectious Diseases 28: 835—839.

Reffuveille F, Josse J, Vallé Q, Mongaret C, Gangloff SC (2017) In Enany S, Crotty Alexander LE (Eds.) The rise of virulence and antibiotic resistance in *Staphylococcus aureus*, (pp. 189—214). InTech, Zagreb.

Sexton J, Maxwell S, Gerba S (2007) 107th Annual Meeting of the American Society for Microbiology.

Stepanović S, Ćirković I, Djukić S, Vuković D, Švabić-Vlahović M (2008) Letters in Applied Microbiology 47: 339—341.

sciendo

Trichoderma atroviride: an isolate from forest environment with secondary metabolites with high antimicrobial potential

Ján Víglaš, Petra Olejníková

Institute of Biochemistry and Microbiology, Slovak University of Technology in Bratislava, Radlinského 9, 81237 Bratislava, Slovakia
jan.viglas@stuba.sk

Abstract: This work was focused on the characterization of novel isolate of *Trichoderma atroviride* O1, found in the forest around the village of Zázrivá (the Northern Slovakia, region Orava). The isolate was identified by sequencing its *internal transcribed spacer* (ITS) region of rDNA. *T. atroviride* O1 stimulated the development of lateral roots of model plant *Lepidium sativum*. Simultaneously, the isolate has proved its high mycoparasitic potential as it displayed the ability to attack colonies of phytopathogenic fungi (*Alternaria alternata, Fusarium culmorum, Botrytis cinerea*). This isolate produced secondary metabolites, which were isolated and tested for the antimicrobial activity against gram-positive bacteria *Staphylococcus epidermidis* and *Staphylococcus aureus*. The growth of these bacteria was suppressed to 10 % and 40 %, respectively. The suppression of the growth of two *Candida* species was also strong (10 % growth). However, growth parameters of three phytopathogenic fungi (*Alternaria alternata, Botrytis cinerea* and *Fusarium culmorum*) were less affected (75 % growth in comparison with the control). Attempts were made to characterize secondary metabolites isolated from *T. atroviride* O1. Known peptaibols, 20–21 amino acid long, but also shorter peptides, were detected by MALDI-TOF mass spectrometry. Thus, this study demonstrates the plant growth promotion, strong mycoparasitic potential and antimicrobial activity of the isolate *T. atroviride* O1, which could be in part ascribed to the production of secondary metabolites. This isolate does have a potential in the biocontrol in eco-farming. Further study, particularly, the identification of produced secondary metabolites, is needed.

Keywords: antimicrobial activity, mycoparasitism, plant-growth promotion, secondary metabolites, *Trichoderma*

Abbreviations: CCM – Czech Collection of Microorganisms, CWDE – cell wall degrading enzymes, DMSO – dimethylsulfoxide, GKCH – Sabouraud Chloramphenicol agar, ITS – internal transcribed spacer, MALDI-TOF – Matrix Associated Laser Desorption Ionisation with Time of Flight detector, MHA – Mueller Hinton Agar, NRPs – non-ribosomal peptides, PDA – Potato Dextrose Agar, SMs – secondary metabolites, TLC – Thin Layer Chromatography, 6-PP – 6-pentyl-α-pyrone

Introduction

Trichoderma (teleomorph *Hypocrea*) is a genus of typical soil filamentous fungi. It obtains nutrients through the three different lifestyles: saprophytic, symbiotic and parasitic one. *Trichoderma reesei* is a typical saprophyte. It colonizes dead woody and herbaceous material and produces cellulolytic and hemicellulolytic enzymes to digest substrate. Interaction with plants is an example of a symbiotic lifestyle. Plant root exudates are a valuable source of nutrients, while *Trichoderma* sp. promotes plant growth and provides defense against biotic and abiotic stress. Other enzymatic apparatus is involved in parasitic interactions with plant pathogenic fungi, so-called cell wall degrading enzymes that are chitinases, glucanases, and proteases (Druzhinina et al., 2011; Harman et al., 2004). These findings suggest *Trichoderma* sp. can combat phytopathogenic fungi. It is just plant-growth promotion and mycoparasitism that mark the potential of *Trichoderma* sp. in the area of biocontrol agents. In fact, European Commission has approved five species as biopesticides: *Trichoderma atroviride* (strain IMI 206040, T11, AGR2, I-1237, SC1); *Trichoderma asperellum* (strain ICC012, T25, TV1 and T34); *Trichoderma gamsii* (strain ICC080); *Trichoderma harzianum* (strain T-22 and ITEM 908); *Trichoderma polysporum* (IMI 206039) [http://ec.europa.eu/food/plant/pesticides/eu-pesticides-database].

However, *Trichoderma*-plant and *Trichoderma*-phytopathogenic fungus interactions are much more complex, mainly because they involve not only the direct effect of hydrolytic enzymes, but also the role of secondary metabolites (SMs) (Vinale et al., 2008b; Liu et al., 2016; Alwhibi et al., 2017; Antasova et al., 2013). SMs are numerous heterogeneous groups of compounds, which are not essential for survival but

are supposed to have functions in signalling and defense (Mukherjee et al., 2013). SMs of filamentous fungi are divided into four groups, according to the origin of synthesis and structure: non-ribosomal peptides (NRPs), polyketides, terpenes and pyrones (Zeilinger et al., 2016).

By interactions with other organisms, compounds of each group are involved, to various extent. Peptaibiotics, specific NRPs consisting of both proteinogenic, as well as non-proteinogenic amino acids (typical is α-aminoisobutyric acid = AIB) are intensively studied (Nawrocka and Małolepsza, 2013; Druzhinina et al., 2011; Neuhof et al., 2007). The subfamily of peptaibols, 18—21 amino acids long with C-terminal alcohol, was described to have its function in signalling by activation of induced systemic resistance of plants (Mukherjee et al., 2013; Nawrocka and Małolepsza, 2013; Druzhinina et al., 2011). Peptaibiotics were also described as inhibitors of ß-glucan synthase (an enzyme involved in cell wall synthesis) of plant pathogenic fungi (Vinale et al., 2008a). Alamethicins and paracelsins are particular peptaibols, known to be produced by *Trichoderma* sp. (Reino et al., 2008), which are involved in previously mentioned processes. One of the best known SMs produced by *Trichoderma* sp. is 6-pentyl-α-pyrone (6-PP) (Collins a Halim, 1972), described as the auxin-like compound in terms of its effect on plant growth, especially enhancement of root and shoot development (Vinale et al., 2008a). Its production was also observed by a mycoparasitic attack on the colony of phytopathogen (Antasova et al., 2013). This volatile organic compound with the aroma of coconut is produced by *T. atroviride* (Druzhinina et al., 2011). Another group of SMs, polyketides, are also known as molecules that have the role in signalling, such as chrysophanol, member of a subgroup of anthraquinonons (Liu et al., 2016). They are synthesized by polyketide synthases; one of them, encoded by the gene *pks4* is responsible for green pigmentation of conidia (Antasova et al., 2013). Out of the last group, terpenes (based on the structural unit of isoprenyl pyrophosphate), the production of trichothecenes is significant. *Trichoderma brevicompactum* and *Trichoderma arundinaceum*, which produce trichothecenes can inhibit the growth of *Fusarium* sp. (dangerous plant pathogen), while *Trichoderma gamsii*, which has genes for trichothecene production but their own trichothecenes were not detected, appears to tolerate trichothecenes of *Fusarium* sp. (Tijerino et al., 2011). To sum up, SMs of *Trichoderma* sp. are studied because of their potential to provide new antimicrobial compounds.

This paper provides a characterization of the isolate of *T. atroviride* O1, obtained from the forest environment. The paper shows the potential of the obtained isolate in interaction with the plant by promoting its growth; in mycoparasitic activity on phytopathogenic fungi and production of secondary metabolites with antimicrobial activity. Using MALDI-TOF mass spectroscopy, detection of peptaibiotics was performed.

Materials and methods

Microbial strains and culture conditions

Isolate *Trichoderma atroviride* O1 as well as *Trichoderma viride* CCM (Czech Collection of Microorganisms): F534, phytopathogenic filamentous fungi: *Alternaria alternata* CCM: F128, *Fusarium culmorum* CCM: F21, *Botrytis cinerea* CCM: F16 were maintained on Potato Dextrose Agar (PDA) (Biolife, Milan, Italy) slants at 4 °C and sub-cultured on fresh growth medium every two weeks. Fungi were cultivated at the room temperature. Yeast: *Candida albicans* SC 5341, *Candida parapsilosis* ATCC 22019 were stored in glycerol (30 %) at –80 °C and three days before experiments were inoculated on GKCH = Sabouraud Chloramphenicol agar (Biorad, Marnes-La-Coquette, France) and cultivated at 37 °C. Model bacteria: *Staphylococcus aureus* CCM 3953, *Staphylococcus epidermidis* CCM 4505 and *Escherichia coli* CCM 3988 were stored in glycerol at –80 °C and two days before experiment inoculated on MHA = Mueller Hinton Agar (Biolife, Milan, Italy), and cultivated at 37 °C.

Isolation of Trichoderma sp. from the wood material obtained from the forest in Northern Slovakia – Orava

The piece of wood with assumed *Trichoderma* sp. was transferred to the laboratory, conidia (Fig. 1) were stamped at PDA growth medium (Biolife, Milan, Italy). After one week of cultivation at room temperature, part of mycelium was transferred on fresh PDA. Next, we repeated the process until we obtained pure culture (Fig. 1).

DNA isolation and PCR amplification

The isolate was grown on PDA medium, covered with cellophane, at 25 °C, in the dark for two days. Mycelium was harvested and homogenized in liquid nitrogen. For isolation of genomic DNA, the DNA Fast Isolation Kit (Spin-column) was used (Ecoli s.r.o., Bratislava, Slovakia).

The internal transcribed spacer (ITS) region was amplified using a set of primers ITS1 (forward primer): 5´— CTT GGT CAT TTA GAG GAA GTA A — 3´ and ITS4 (reverse primer): 5´— TCC TCC GCT TAT TGA TAT GC — 3´ (E.coli s.r.o., Bratislava, Slovakia) and Hot-start DNA poly-

merase (Biotechrabbit GmbH, Germany). The initial denaturation was held at 94 °C for 3 min, followed by 30 cycles of amplification (94 °C 30 second, 55 °C 30 s and 72 °C for 1 min). At the end, the reaction mixture was heated at 72 °C for 10 min and cooled down to 4 °C. After verification of correct amplification by electrophoresis on 1 % agarose gel, the obtained PCR product was purified (GenUp^{TM} PCR/Cleanup Kit, Biotechrabbit GmbH, Germany) and sequenced with the Sanger method. The final sequence was inserted into Nucleotide-Blast (PubMed), and the similarity with present ITS sequences was evaluated. Finally, the sequence was submitted into GenBank and is available under the Accession number: MK522147.

Evaluation of T.atroviride O1 – plant interaction

The plant *Lepidium sativum* (Nohel Garden a.s., Dobříš, Czech Republic) was used as a model plant. Sowing was preceded by seed disinfection. Seeds were submerged in Sanosil Super 25 Ag (S010) disinfection solution (Sanosil CZ s.r.o., Praha) and incubated for 10 min. Then, Sanosil Super 25 Ag was removed by pipetting, and this step was repeated 2-times. Then, seeds were swirled three times in sterile H_2O. As for the next stage, 10 seeds were placed on Murashige and Skoog nutrition medium in a glass Petri dish (diameter 20 cm). The distance between seeds was approximately 1 cm. For the first 24 h, cultivation was performed in a horizontal position at laboratory temperature until seeds began to germinate. Then Petri dishes were placed at 60 ° angle. 48 h after sowing, 5 mm disc of isolate mycelium was put in the position opposing forming roots. One week after inoculation, the morphology of plants was evaluated by measuring the length of the main root and counting the number of lateral roots.

Determination of mycoparasitic activity by dual-culture assay

Determination of mycoparasitic activity took place on PDA medium in Petri dish (diameter 10 cm). First, 5 mm disc of the mycelium of phytopathogen was inoculated on the growth medium, close to the edge of Petri dish and after 4-day cultivation, at the laboratory temperature, *T. atroviride* O1 was inoculated at the place opposing pathogenic fungus and cultivation continued for next 13 days.

After this period, conidiation on the colony of *T. atroviride* O1, as well as on phytopathogen colony was determined. The number of conidia was evaluated by direct counting in the hemocytometer and by cultivation method. Briefly, the spore suspension was prepared by vortexing of two 5 mm disc of mycelia (cut out from the colony) in the 0.1 % Tween 80 water solution (Biolife, Milan, Italy). The spore suspension obtained from the dual-culture zone (the zone of overgrowth) was prepared using the same procedure as mentioned previously, then it was diluted by factor 10 to 10^{-4}, and 200 µL of each dilution was spread on fresh PDA medium (Biolife, Milan, Italy). After short cultivation (48 h) colony forming units (CFU) were counted. Simultaneously, according to the morphology of obtained colony, we were able to evaluate if colonies of phytopathogenic fungi were present or not, meaning the fungistatic or fungicidal effect of *T. atroviride* O1 on plant pathogenic fungi.

Production and isolation of SMs

T. atroviride O1 was inoculated on PDA medium and cultivated in static circadian mode, at laboratory temperature for two weeks, so the colony entered stationary phase of growth when production of SMs is expected to culminate.

The isolation of metabolites was performed by using extraction into ethyl acetate (Centralchem, s.r.o., Bratislava, Slovakia). SMs were isolated from both mycelium and cultivation medium. Water present in the extract was removed using anhydrous Na_2SO_4 (Lachema Brno, Czech Republic) and the extract was concentrated by vacuum evaporation of ethyl acetate. Obtained metabolites were dissolved in a small amount of ethyl acetate. The tiny fraction was separated by Thin Layer Chromatography (TLC) in a mixture of benzene : acetone 3 : 1 (Centralchem, s.r.o., Bratislava, Slovakia) and then the solvent was removed entirely again. Concentrated SMs were dissolved in dimethyl sulfoxide (DMSO) (Centralchem, s.r.o., Bratislava, Slovakia).

Antimicrobial activity of SMs

For evaluation of antimicrobial activity, microdilution method was applied. Bacteria were cultivated in Mueller Hinton Broth (MHB), and yeasts were cultivated in Sabourad Glucose Broth (SGB) (Biolife, Milan, Italy). The overnight inoculum was prepared and used for inoculation of the growth media. Microorganisms were cultivated at 37 °C under shaking (350 rpm) in microtitration plates. To 198 µL of 1 % inoculum, 2 µL of SMs dissolved in DMSO were added. Absorbance at 630 nm (A_{630}) was measured as the growth parameter. The measurement was performed until microorganisms reached the stationary phase of growth. The growth of microorganisms treated with an extract of isolated secondary metabolites was compared with control (inoculum with 1 % DMSO) according to the formula (1) for the percentage of growth.

$$\%_{growth} = \frac{A_{630,sample}}{A_{630,control}} \times 100\ \% \quad (1)$$

The plate dilution method was used for the evaluation of the antifungal potential of secondary metabolites on plant pathogenic filamentous fungi. Three mL of PDA medium was supplemented with 30 µL of the extract of SMs (in control, SMs were replaced by 30 µL of DMSO, the solvent) and was poured in 3 cm diameter Petri dish. Once it solidified, it was inoculated with spore suspension in 0.1 % Tween 80 water solution (*A. alternata*, *F. culmorum*) or with the mycelium disc of *B. cinerea*. The spore suspension (5 µL = 10^3 conidia/disc) was applied on filter paper disc placed in the center of the growth media, or the growth medium was inoculated with a disc of the mycelium of *B. cinerea* (5 mm diameter). The filamentous fungi were cultivated at the laboratory temperature until the control reached its stationary phase of growth. The growth of fungi was evaluated by measuring the diameter of the fungal colony. The growth was compared to the growth of control (3 mL of PDA medium with 30 µL of DMSO). The evaluation was performed according to the following equation:

$$\%_{growth} = \frac{diameter\ of\ colony_{sample}}{diameter\ of\ colony_{control}} \times 100\ \% \quad (2)$$

MALDI-TOF analysis of produced peptaibiotics

For isolation of peptaibiotics, the method of Neuhof et al. (2007) was used with some modifications. Isolate of *Trichoderma* spp. was cultivated on PDA medium covered with cellophane at laboratory temperature, in the circadian rhythm (sun-light), for 13 days to make sure that the production of SMs had already started. Peptaibiotics were extracted into acetonitrile/methanol/water (1 : 1 : 1, by vol.) (Sigma Aldrich, St. Louis, USA), centrifuged (12000 rpm, 3 min, microcentrifuge) and 1 µL of the extract was mixed with 1 µL matrix solution [10 mg of 2.5-dihydroxybenzoic acid mL^{-1} (Bruker Daltonics, Billerica, Massachusetts, USA) in acetonitrile/methanol/water (1 : 1 : 1, by vol.) and 0.3 % trifluoroacetic acid (Sigma Aldrich, St. Louis, USA)]. One µL of the sample – matrix mixture was directly spotted onto the target plate (MTP 384 plate ground steel BC, Bruker Daltonik GmbH, Germany) and allowed to air dry before analysis. Alternatively, mycelium was disintegrated in liquid nitrogen, and then peptaibiotics were extracted in 60 % ethanol. After centrifugation (12000 rpm, 3 min, microcentrifuge), 1 µL of the extract was mixed with 1 µL matrix solution, and 1 µL of the resulting solution was spotted onto a MALDI target plate.

Measurements were performed in a reflector positive mode. Protein standard (Bruker Daltonics, Billerica, Massachusetts, USA) solution served for calibration with m/z between 700–3500 (Tab. 1). From obtained mass spectra, the peaks with highest m/z were identified, which represented the peptaibotics. Spectra of m/z were compared with spectra described by Neuhof et al. (2007), as well as Comprehensive peptaibiotics database (Neuman et al., 2015), which helped to identify present peptaibiotics.

Tab. 1. Peptides and their *m/z* (given by producer), which were in solution for calibration of mass spectrometer.

Protein	*m/z*
Bradykinin (1-7) [M+H]+ mono	757.399
Angiotensin II [M+H]+ mono	1046.542
Angiotensin I [M+H]+ mono	1296.685
Substance P [M+H]+ mono	1347.735
Bombesin [M+H]+ mono	1619.822
Renin Substrate [M+H]+ mono	1758.933
ACTH-clip (1-17) [M+H]+ mono	2093.086
ACTH-clip (18-39) [M+H]+ mono	2465.198
Somatostatin (28) [M+H]+ mono	3147.471

Results and discussion

Identification of obtained fungal isolate

Biological material was isolated from the forest around the village Zázrivá, located in the northern part of Slovakia; region Orava. The underlying assumption in our work was the fact that *Trichoderma* sp. is a saprophytic filamentous fungus, which uses its cellulolytic enzymes for degradation of plant material. After isolation of pure culture (Fig. 1), we observed green concentric rings on fungal colonies with soft mycelium and coconut aroma – feature typical for *Trichoderma* sp. Secre-

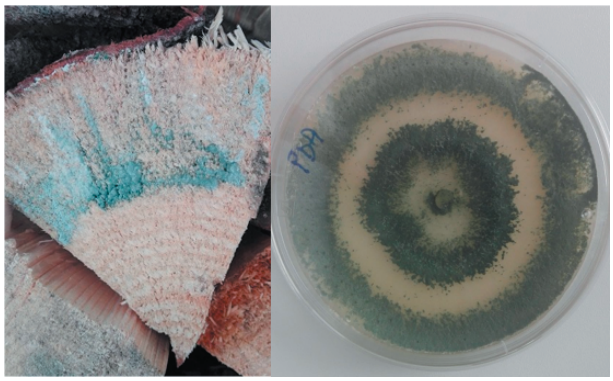

Fig. 1. Colony of isolate of *Trichoderma* sp. on natural substrate and Potato-Dextrose Agar.

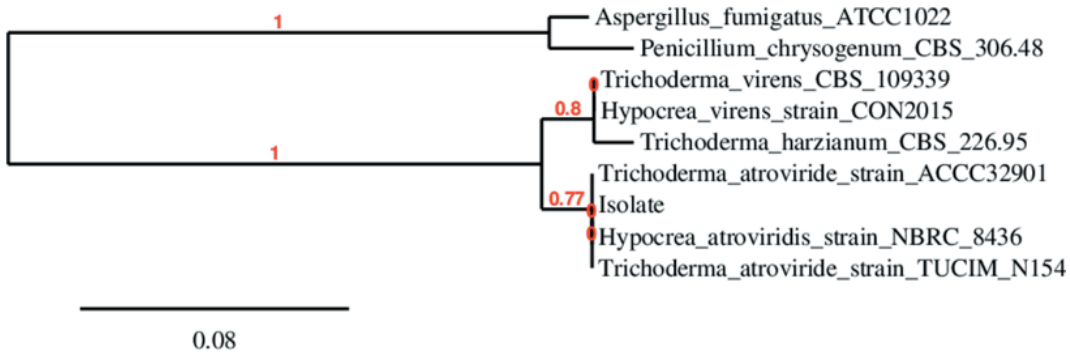

Fig. 2. Phylogenetic analysis of *T. atroviride* O1 isolate.

tion of yellow-green guttation droplet was also observed on the colony.

The phenotypic analysis was followed by genetic identification of ITS region, localized between ITS1 and ITS4 primers. After obtaining the genomic DNA, amplification of the desired region and its sequencing by Sanger method, the resulting sequence compared with GeneBank was similar to the ITS region of *Trichoderma atroviride* at 99 %. The sequence was submitted into GenBank database and is available under the Accession number MK522147. Identity was also confirmed by insertion into a phylogenetic tree (Dereeper et al., 2008 [http://www.phylogeny.fr]), and the classification of the isolate was noticeable (Fig. 2).

Growth promotion of the model plant L. sativum

Due to well-known abilities of *Trichoderma* sp. to promote plant growth, the characterization of isolate started in this field. After one week of co-cultivation with *L. sativum*, the positive effect on the model plant was visible (Fig. 3). For both, control plants (not exposed to *T. atroviride* O1) and plants exposed to *T. atroviride* O1, the length of the primary root was similar (11 ± 0.8 cm and 11 ± 0.9 cm, respectively), while the number of lateral roots showed a significant increase. For control plants, we detected only 5 ± 1 lateral roots per plant. The number of lateral roots of inoculated plants increased to 19 ± 2 per plant. Obviously (Fig. 3), so did the length of these roots (instead of a couple of millimeters, the longest lateral root was around 1 cm long). To conclude, it is highly probable that the isolate *T. atroviride* O1 promotes plant growth in the way that stimulates the development of lateral roots. The observed phenotype is very similar to the observed effect of auxins and auxin-like compounds – the elicitors of plant growth. Auxins and auxin-like compounds act as signal molecules for stimulation of genes involved in plant growth. The effect of lateral roots promotion was observed for indole-3-acetic acid (IAA), one of the most studied compounds in the area of biocontrol of the plant growth (Druzhinina et al., 2011). Recently, the focus on the role of SMs in this process is increased because of the discoveries of several metabolites with the same growth-promotion effect. Among SMs described as elicitors of plant growth, 6-PP, peptaibols, harzianolides, and polyketide chrysophanol are known (Liu et al., 2016, Zeilinger et al., 2016; Mukherjee et al., 2013; Vinale et al., 2008a).

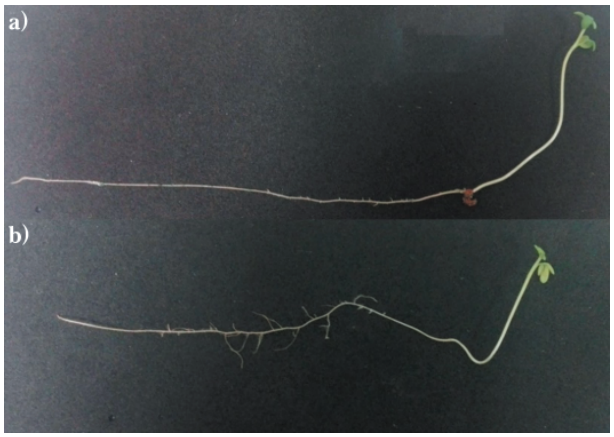

Fig. 3. The growth of *L. sativum*: a) control; b) inoculated plant with *T. atroviride* O1.

The mycoparasitic activity of T. atroviride O1

The mycoparasitism is a trophic relationship, where a parasitic fungus lives in association with host fungus while derives the nutrients from it (Mukherjee et al., 2013). It is one of the main features of *Trichoderma* sp., which uses its enzymatic apparatus (cell wall degrading enzymes) to attack the colony of phytopathogen (host organism) (Druzhinina et al., 2011). Our experiment revealed that the isolate *T. atroviride* O1 is not only able to attack the colonies of three different phytopathogens, including *F. culmorum* but also wholly overgrows host fungi (Fig. 4). *Fusarium* sp. is one of the most problematic plant pathogens due to its production of trichothecenes (Tijerino et al., 2011). The mycoparasitic activity was evaluated by conidiation criteria and by the ability of the fungus

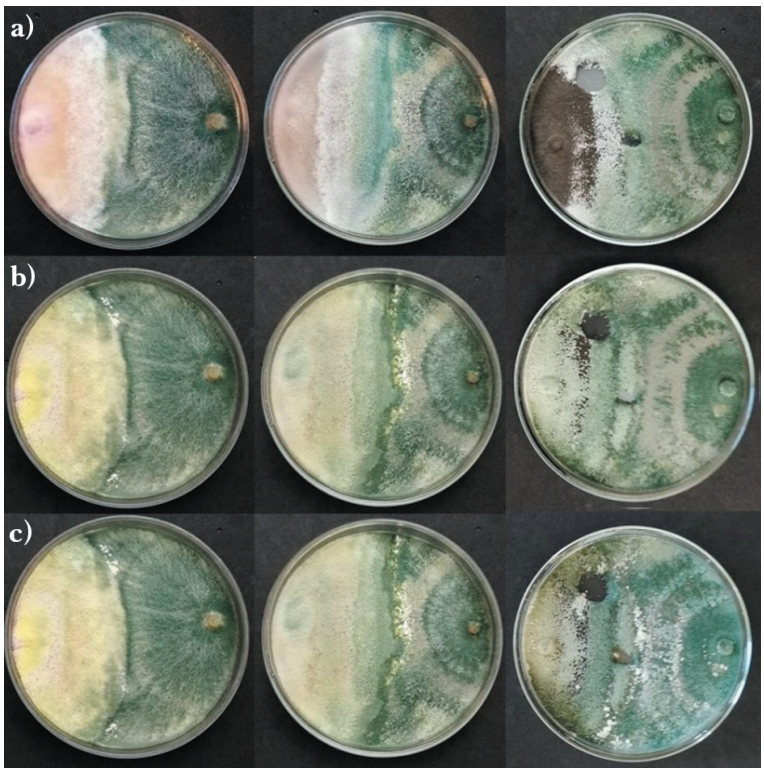

Fig. 4. Dual-culture of *T. atroviride* O1 and *F. culmorum* (on the left), *B. cinerea* (in the middle), and *A. alternata* (on the right) after a) 6-day; b) 10-day; c) 13-day cultivation.

to overgrow the colony of phytopathogen. We observed that the intensity of conidiation of *T. atroviride* O1 was decreased. At the zone of overgrowth, the conidiation reached 10^5—10^6 conidia per cm^2. The effect of isolate on all phytopathogens was fungicidal. Phytopathogens were not able to grow in fresh culture medium after the attack of *T. atroviride* O1. To sum up, it is clear that the isolate *T. atroviride* O1 showed high potential for biocontrol processes.

Secondary metabolites with antimicrobial potential

Production of secondary metabolites (SMs) of *Trichoderma* sp. peaks in the late stationary phase, when specific metabolites can be detected, for instance, 6-pentyl-α-pyrone (6-PP), which is a volatile organic compound responsible for coconut aroma, typical of *Trichoderma* sp. (Collins and Halim, 1972), with observed antifungal and plant-promoting activity (Vinale et al., 2008a). Such coconut aroma (production of 6-PP) was noticeable fairly soon, specifically after one week of cultivation, when the production of yellow-green guttation droplets was also observed, and the growth PDA medium was changing its colour in the way of getting a yellow tint. At this time, secondary metabolites were extracted in the ethyl acetate. Obtained concentrated extract of metabolites had a brownish color. The TLC analysis of the metabolic profile of *T. atroviride* O1 is shown in Fig. 5. Together, eight spots were detected (over the limit of detection) what, presumably, represent eight different types of metabolites, according to their polarity. Metabolites (at the start line of chromatogram) are considered to be most polar compounds, unable to separate in benzene : acetone 3 : 1. Furthermore, these spots

Fig. 5. TLC chromatogram of SMs of *T. atroviride* O1 detected under UV light (254 nm).

were the only observable metabolites in visible light, in which they were brown.

The involvement of SMs in the interaction of *Trichoderma* sp. with organisms such as plants (growth promoting), phytopathogens (mycoparasitism), and other microorganisms have been extensively studied and reviewed (Zeilinger et al., 2016, Antasova et al., 2013, Malmierca et al., 2012, Druzhinina et al., 2011, Vinale et al., 2008a). In our work, we have focused on the inhibition effect of SMs of *T. atroviride* O1 on model bacteria, yeasts, and phytopathogenic filamentous fungi. Except extracted mixture, 2-times (2×) and 4-times (4×) diluted mixtures of obtained metabolites were used, in order to detect antimicrobial effect dependent on their concentrations.

Antibacterial activity of SMs is presented in Fig. 6. It is clear that the growth of gram-negative bacteria *E. coli* was not influenced, while inhibition activity was intense in the case of gram-positive bacteria *S. aureus* and *S. epidermidis*. In the presence of SMs, the growth of *S. aureus* reached only 40 %, in comparison with control. Moreover, the extract of SM showed the 90 % inhibition effect on the growth of *S. epidermidis*. In both cases, the inhibitory effect was concentration dependent. Therefore, it may be suggested that SM of the isolate of *T. atroviride* O1 can play a role as antibacterial compounds.

SMs have shown antifungal activity on model yeasts (Fig. 7). In comparison with the control, only 7 % growth of *C. albicans* was observed when the non-diluted extract was used, while the percentage of growth has increased to 30 % and 32 %, when 2× and 4× diluted mixtures, respectively, were added. *C. parapsilosis* was also significantly affected. The addition of undiluted extract resulted in very similar growth inhibition to *C. albicans*; only 8 % growth has been observed (Fig. 7). Further study is needed in order to identify the inhibition effect of either one metabolite or, more probable, to the mixture of metabolites to evaluate the possible synergistic activity of SMs.

When it comes to plant pathogenic fungi, the inhibition effect of SMs was not as strong as by yeast. *B. cinerea* was not inhibited at all, while the growth of other two fungi was at just under 75 % in comparison with the control, namely at 74 % for *A. alternata* and 73 % for *F. culmorum* (Tab. 2). Based

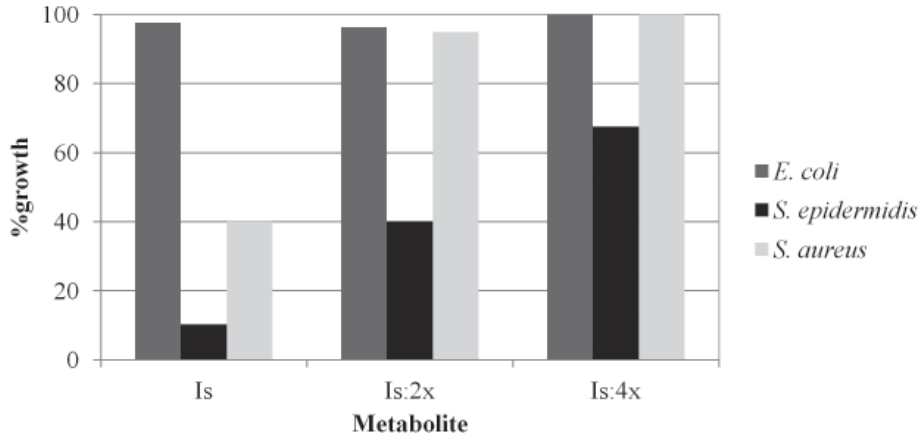

Fig. 6. Growth of model bacteria in the presence of SMs of *T. atroviride* O1.
Is stands for non-diluted extract, Is: 2× — 2-times diluted, Is: 4× — 4-times diluted.

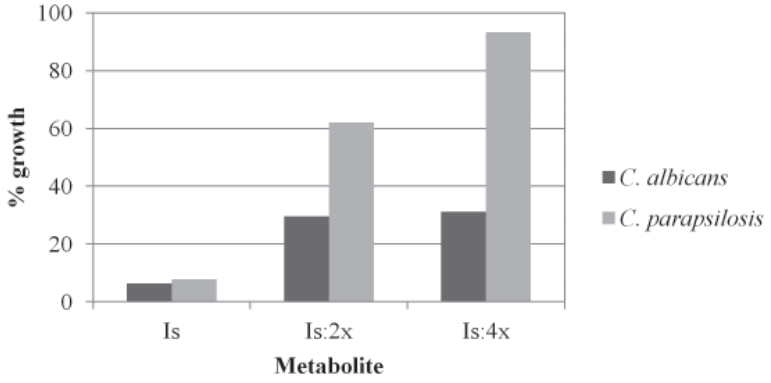

Fig. 7. Growth of *C. albicans* and *C. parapsilosis* in the presence of SM of *T. atroviride* O1.
Is stands for non-diluted extract, Is: 2× — 2-times diluted, Is: 4× — 4-times diluted.

on this result, it can be assumed that SMs plays a secondary role in the mycoparasitic attack of *T. atroviride* (the foremost importance still belongs to hydrolytic enzymes).

Tab. 2. Growth of phytopathogenic fungi in the presence of SMs of *T. atroviride* O1. Is stands for non-diluted extract, Is: 2x–2-times diluted, Is: 4x–4-times diluted.

Metabolites	% growth	
	A. alternata	*F. culmorum*
Is	74	73
Is: 2×	87	82
Is: 4×	97	85

MALDI-TOF analysis of peptaibiotics produced by T. atroviride O1

Peptaibiotics are non-ribosomal peptides with a length of 4—21 residues and a molecular weight of 500—2100 Da. Linear chain and presence of non-canonical amino acids (α-aminoisobutyric acid, isovaline) are typical for this group of SMs (Neumann et al., 2015). MALDI-TOF analysis of mass spectra allows us to determine the production of peptaibiotics (Neuhof et al., 2007). In this experiment, we also analyzed strain of *Trichoderma viride* F534 from Czech Collection of Microorganisms. According to the publication of Neuhof et al. (2007), samples for analysis were prepared by extraction into two different solvents. One of them was the mixture of acetonitrile : methanol : water (AMW) (1 : 1 : 1, by volume) and the alternative was 60 % ethanol. We compared the mass spectra of these two extracts (Tab. 3) and found out that they are comparable.

The similarities between strains depended on a range of molecular weight we were analyzing. Peaks m/z values ranging from 1900 to 2000 were almost the same (Fig. 8), according to the Comprehensive peptaibiotics database, they most probably correspond to the 20—21 amino acid long peptaibols (group of peptaibiotics), named alamethicins, paracelsins, suzukacillins and atroviridines (Tab. 4) — SMs, which production was described for *Trichoderma* sp. (Reino et al., 2008). Besides, alamethicins are known for their antifungal activity as well as signal functions in plant growth stimulation (Vinale et al., 2008b). On the other hand, the spectrum of lower m/z was completely different (Fig. 9). Their identity was not revealed due to significant differences with values in the publication of Neuhof et al. (2007) and in the Comprehensive peptaibiotics database. However, we were able to estimate the length of peptides according to data in previously mentioned works. m/z 1008 and 1024 are, presumably, 8—10 amino acids long, while m/z 700—750 should have 6—8 residues, and m/z 600—700 4—6 amino acids. Peptides in these values can be either new peptaibiotics or fragments of longer peptaibiotics, as was suggested by Brito et al. (2014). This experiment was only a first step towards a potential study of peptaibiotics in isolate *T. atroviride* O1.

Tab. 4. Identities of some detected peptaibiotics.

m/z	Name	Number of amino acids
1949; 1963; 1964; 1977; 1991	Alamethicin F-30	20
1934; 1948; 1962; 1976; 1990	Alamethicin F-50	20
1908; 1922; 1936	Paracelsin A-I	20
1908, 1922, 1936, 1950	Suzukacillin A 1-11	20
1948, 1962	Atroviridin A-D	20
2016	Alamethicin type	21
2001	Alamethicin type	21
2002	Paracelsine type	21

Tab. 3. Petaibiotics obtained from *Trichoderma* sp. after two different types of extraction procedure. Underlined are with intensity over 0.8×10^4 *arbitrary units* (a.u.).

Trichoderma sp.	Method	Peaks of mass spectrum [m/z]
T. viride F534	EtOH	681; 756;769; 782; 804; 813; 820; 994; 1008; 1024; 1935; 1949; <u>1963</u>; 1972; 1976; 1988; 2002; 2016
	AMW	621; 637; 665; 681; 709; 725; 756; 769; 782; 797; 813; 820; 857; 885; 901; 945; 989; 1008; <u>1024</u>; 1033; 1905; 1919; <u>1935</u>; <u>1949</u>; <u>1963</u>; <u>1977</u>; <u>1988</u>; <u>2002</u>; 2016
T. atroviride O1	EtOH	<u>621</u>; 637; <u>665</u>; 681; 699; <u>709</u>; 725; 740; <u>753</u>; 769; 797; 804; 813; 841; 857; 885; 901; 929; 945; 973; 989; 1008; 1017; 1024; 1033;1061; 1077; 1121; 1149; 1193; 1919; 1933; 1947; 1956; 1963; 1972; 1986; 2002; (2010; 2016; 2024)
	AMW	621; 637; 665; 681; 709; 725; 758; <u>782</u>; <u>804</u>; <u>820</u>; 857; 901; 945; 992; <u>1008</u>; <u>1024</u>; 1033; 1077; 1340; 1905; <u>1933</u>; <u>1919</u>; <u>1949</u>; <u>1963</u>; <u>1972</u>; <u>1988</u>; <u>2002</u>; <u>2016</u>

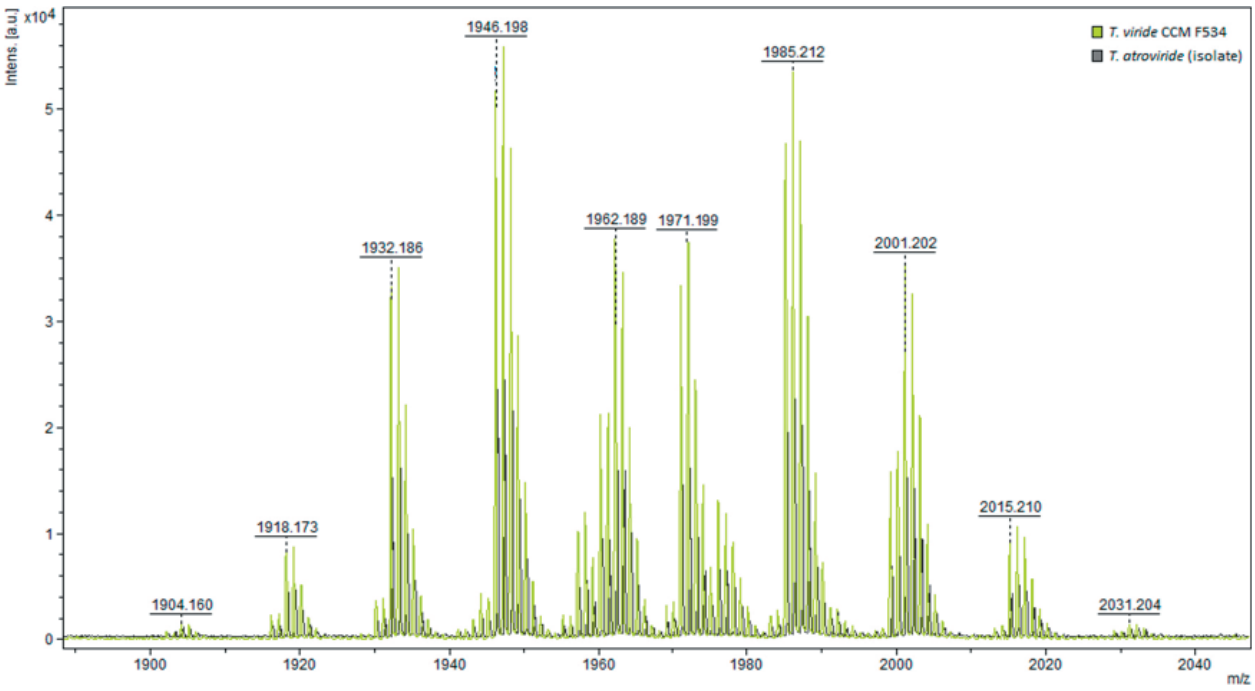

Fig. 8. Mass spectra of *Trichoderma* sp. between m/z values 1900–2000.

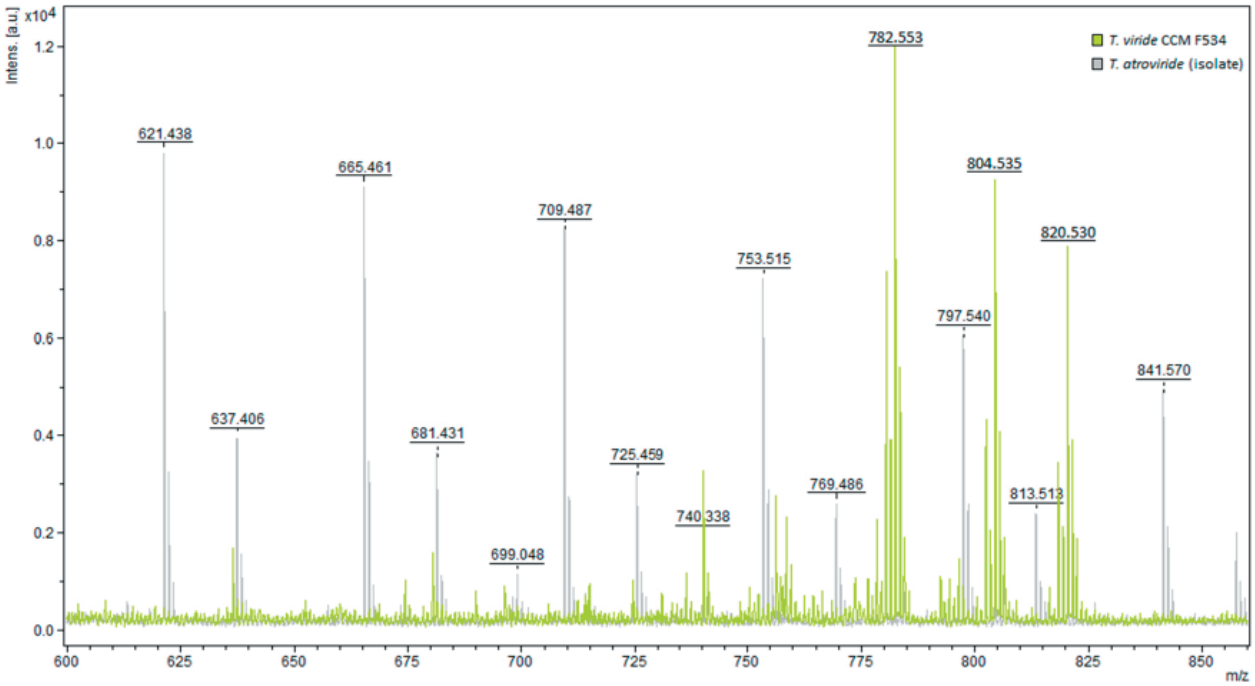

Fig. 9. Mass spectra of *Trichoderma* sp. between m/z values 600–825.

Conclusion

The characterization of some essential features typical of *Trichoderma* sp. was conducted on isolate of *T. atroviride* O1 obtained from the environment. Isolate has shown strong mycoparasitic activity, as well as the ability to promote plant growth. *T. atroviride* O1 has produced typical peptaibiotics described for *Trichoderma* sp. However, unknown peptides were also detected. The role of secondary metabolites seems to be auxiliary in the mycoparasitic attack, while the inhibition activity against gram-positive bacteria and yeast indicates the potential of this isolate for further study as a biocontrol agent, and as a source of antimicrobial compounds.

Acknowledgment

This work has been supported by the Slovak Scientific Grant Agency (VEGA 1/0697/18) and ITMS: 26230120006.

References

Alwhibi MS, Hashem A, Abs Allah EF et al. (2017) Journal of Integrative Agriculture 16: 1751—1757.

Antasova L, Crom SL, Gruber S et al. (2013) BMC Genomics 14: 121.

Antasova L, Knox BP, Kubicek CHP et al. (2013) Eukaryotic Cell 12: 1499—1508.

Brito JPC, Ramada MHS, de Magalhães MTQ, Silva LP, Ulhoa CJ (2014) Springerplus 3: 600.

Collins RP, Halim AF (1972) Journal of Agricultural and Food Chemistry 20: 437—438.

Dereeper A, Guignon V, Blanc G et al. (2008) Nucleic acid research 36: 465—469.

Druzhinina I, Seidl-Seiboth V, Herrera-Estrella A, Horwitz BA et al. (2011) Nature reviews. Microbiology 9: 749—759.

Harman GE, Howel CR, Viterbo A, Chet I, Matteo L (2004) Nature reviews. Microbiology 2: 43—56.

Liu SH, Liao CHK, Lo CHT et al. (2016) Physiological and Molecular Plant Pathology 96: 1—7.

Mukherjee PK, Horwitz BA, Herrera-Estrella A, Schmoll M, Kenerley CHM (2013) Annual Review of Phytopathology 51: 105—129.

Nawrocka J, Małolepsza U (2013) Biological Control 67: 149—156.

Neuhof T, Dieckmann R, Druzhinina I, Kubicek CP, von Döhren H (2007) Microbiology 153: 3417—3437.

Neumann NKN, Stoppacher N, Zeilinger S et al. (2015) Chemistry & Biodiversity 12: 743—751.

Reino JL, Guerrero RF, Hernández-Galán R, Collado IG (2008) Phytochemical reviews 7: 89—123.

Tijerino A, Cardoza RE, Moraga J et al. (2011) Toxins 3: 1220—1232.

Vinale F, Sivasithamparam K, Ghisalberti EL et al. (2008a) Soil Biology & Biochemistry 40: 1—10.

Vinale F, Sivasithamparam K, Ghisalberti EL et al., (2008b) Physiological and Molecular Plant Pathology 72: 80—86.

Zeilinger S, Gruber S, Bansal R, Mukherjee PK (2016) Fungal Biology Reviews 30: 74—90.

sciendo

Synthesis, crystal structure, infrared spectrum, and thermal properties of [Ni(1,10-phenanthroline)$_3$](fumarate)·9H$_2$O complex with hydrogen bonded supramolecular layers involving fumarate anions

Anna Uhrinová[a, b], Juraj Černák[a]

[a]*Department of Inorganic Chemistry, Institute of Chemistry, P. J. Šafárik University in Košice, Moyzesova 11, 041 54 Košice, Slovakia*
[b]*Department of Chemistry, Biochemistry and Biophysics, University of Veterinary Medicine and Pharmacy in Košice, Komenského 73, 041 81 Košice, Slovakia*
juraj.cernak@upjs.sk

Abstract: From the aqueous-ethanolic system Ni(OH)$_2$—H$_2$*fum*—*phen* (H$_2$*fum* = fumaric acid, *phen* = 1,10-phenanthroline), novel complex [Ni(*phen*)$_3$](*fum*)·9H$_2$O (**1**) was isolated and characterized by chemical analyses and FT-IR spectroscopy. Results of single crystal X-ray structure analysis have shown that the ionic crystal structure of **1** is built of [Ni(*phen*)$_3$]$^{2+}$ complex cations, fumarate dianions and nine crystallographically independent water molecules of crystallization. The Ni(II) atom exhibits hexa-coordination by three *phen* ligands with mean Ni-N bond length of 2.090 Å. Water molecules form hydrophilic supramolecular layers with fumarate dianions via extended network of O—H···O type hydrogen bonds with O···O distances from the range of 2.676(2)—2. 916(2) Å; hydrophobic complex cations are embedded between these layers. Thermal study of **1** has shown that endothermic dehydration in the temperature range of 95—195 °C takes at least two steps of the process.

Graphical Abstract: Crystal structure of [Ni(*phen*)$_3$]*fum*·9H$_2$O (*phen* = 1,10-phenanthroline; H$_2$*fum* = fumaric acid) which is built of supramolecular layers formed by hydrogen bonded water solvate molecules and *fum* dianions and between the supramolecular layers embedded [Ni(*phen*)$_3$]$^{2+}$ complex cations is described here.

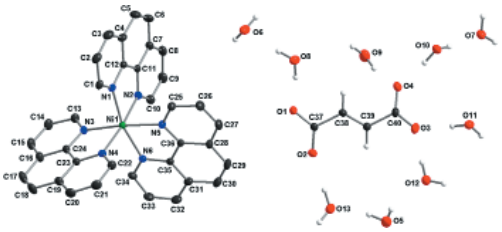

Keywords: Nickel(II), fumarato ligand, crystal structure, hydrogen bond, thermal analysis

Introduction

Fumarate dianion is a versatile ligand exhibiting, due to four potentially donor oxygen atoms, a large number of bonding possibilities ranging from terminal to various bridging modes of coordination. However, it can also act simply as a counter ion (Oldham, 1987; Zheng et al., 2003; Devereux et al., 2000, Bora and Das, 2012; Téllez-López et al., 2015; Zhang et al., 2009). The ability of fumarate dianion to link magnetically active central atoms was used in synthetic design of magnetically interesting low-dimensional complexes (Téllez-López et al., 2015; Neuman et al., 2014; Téllez-López et al., 2014); in order to obtain low-dimensional systems, it is necessary to block some coordination sites of the central atom with suitable blocking ligands, e.g. with aromatic N,N-chelates like *phen* or *bpy* (*phen* = 1,10-phenanthroline; *bpy* = 2,2'-bipyridine). Previously, using this approach, [Ni(*phen*)(*fum*)] (Černák et al., 2009) and [Ni(H$_2$O)(*phen*)(*fum*)]$_n$ complexes were isolated from systems Ni(II)—*phen*—*fum* (H$_2$*fum* = fumaric acid) and characterized (Uhrinová et al., 2012). Surprisingly, to our knowledge, only two complexes from these systems have been structurally characterized up to now, namely [Ni$_2$(*phen*)$_4$(*fum*)(H$_2$O)$_2$](*fum*)·16H$_2$O containing a dinuclear complex cation (Ma et al., 2003) and ionic [Ni(*phen*)$_3$](*fum*)·2H$_2$*fum*·4H$_2$O with solvate molecules of fumaric acid (Lin and Zheng, 2004). Within a deeper study of low-dimensional Ni(II) complexes (Černák et al., 2009; Čerák et al., 2015; Vráblová et al., 2016), system Ni(II)—*phen*—*fum* was added to our research. As the result of our experiments, the title complex **1** was isolated in single crystal form in case of full occupancy of the coordination sites around the Ni(II) central atom by blocking ligand (3x *phen*)

and its synthesis, IR spectroscopic characterization and crystal structure as well as its thermal properties are reported here.

Experimental

Materials

Nickel(II) hydroxide, $Ni(OH)_2$, fumaric acid, $C_4H_4O_4$ (H_2*fum*), 1,10-phenantroline, aqueous ammonia (25 %) and ethanol (96 %) were purchased from commercial sources and used as received.

Synthesis of [Ni(phen)$_3$](fum)·9H$_2$O (1)

Fumaric acid, 232 mg (2 mmol), was dissolved in 15 cm^3 of ethanol (96 % vv). To the formed solution, 2 mmol of freshly prepared precipitate of $Ni(OH)_2$ and 1180 mg (6 mmol) of solid 1,10-phenantroline (*phen)* were added under stirring. The resulting red solution was filtered and left aside for crystallization at room temperature. Within a few days, red platelets formed on the surface of the mother liquor, these were collected and dried in air. Yield: 6 %

Anal. Calc. for $C_{40}H_{44}Ni_1N_6O_{13}$ (Mr = 875.51) (%): C, 54.88; H, 5.07; N, 9.60; Ni, 6.70. Found: C, 54.64; H, 4.98; N, 9.55; Ni, 6.69.

IR (cm^{-1}; s = strong, m = medium, w = weak, vs = very strong, sh = shoulder): 3405vs, 3037w, 2990w, 1639w, 1625w, 1578vs, 1516s, 1495wsh, 1425vs, 1397s, 1340wsh, 1306w, 1257vw, 1225m, 1143m, 1104m, 1010m, 955w, 868sh, 846s, 812m, 774w, 725s, 667w, 643w, 576w.

Physical measurements

Elemental analyses (C, H, N) were performed on a CHNS Elemental Analyzer Flash EA 1112 Thermo Finnigan. Nickel content was estimated using the AAS method (Varian Spectr AA-30).

Infrared spectra were recorded on a FT-IR Avatar 330 Thermo-Nicolet instrument using the KBr pellets technique (2 : 200) in the range of 4000—400 cm^{-1}.

Thermal analysis was performed on a NETZSCH STA 409 PC instrument using ceramic crucibles. Measurements were carried out under dynamic conditions (heating rate was 9 deg/min) in air atmosphere in the temperature range of 25—900 °C.

X-ray Crystallography

Single crystal X-ray experiments on **1** were carried out on an IPDS Stoe diffractometer equipped with an imaging plate area detector system with graphite-monochromatized MoKα radiation (λ = 0.71073 Å) at 100 K. Rotation method data acquisition using ω scans was used. Structure was solved by direct methods and further refined using the SHELXS–97 (Sheldrick, 2008) and SHELXL-2014/7 programs (Sheldrick, 2015) incorporated in the WinGX program package (Farrugia, 2012). Hydrogen atoms in the *phen* ligands and *fum* dianion were placed in the calculated positions and allowed to ride on the parent atoms with isotropic thermal parameters tied with the thermal motion of the parent atoms (U(H) = 1.2 U(CH)). Isotropic thermal parameters of water hydrogen atoms were tied with thermal parameters of the parent oxygen atom (U(H) = 1.5 U(O)), other positional parameters of these hydrogen atoms were allowed to refine freely. Structural figures were drawn using the Diamond software (Brandenburg and Putz, 2008). Crystal data and final parameters of the structure refinement are summarized in Table 1, selected geometric parameters are presented in Table 2 while possible hydrogen bonds are given in Table 3.

Tab. 1. Crystal data and structure refinement for **1.**

Empirical formula	C40 H44 N6 Ni O13
Formula weight	875.52
Crystal system	monoclinic
Space group	$P2_1/c$
Unit cell dimensions:	
a (Å)	10.9212(12)
b (Å)	20.6837(17)
c (Å)	18.348(2)
β (°)	96.505(13)
Z	4
V (Å^3)	4118.0(7)
$D_{calc.}$ (g·cm^{-3})	1.412
T (K)	100(2)
μ (mm^{-1})	0.544
Index ranges for data collection	$-13 \le h \le 13$
	$-23 \le k \le 26$
	$-23 \le l \le 23$
θ range for data collection	2.12—27.00
Reflections collected	31894
Independent reflections (R_{int})	8975 (0.0341)
Observed reflections [$I > 2\sigma(I)$]	6475
Data/restrains/parameters	8975/0/595
Goodness-of-fit on F^2	0.938
Final R indices [$I > 2\sigma(I)$]	R_1 = 0.0344, wR_2 = 0.0782
R indices (all data)	R_1 = 0.0548, wR_2 = 0.0840
Data completeness	0.999
Largest peak and hole (e.Å^{-3})	0.39(5) and –0.39(5)

Results and Discussion

Synthesis and identification

From the aqueous-ethanolic system Ni^{2+}—*phen*—*fum*, under mild conditions, single crystals of [Ni(*phen*)$_3$] *fum*·9H_2O (**1**) were isolated and chemically characterized. Similar experimental conditions were used

to prepare $[Ni_2(phen)_4(fum)(H_2O)_2]fum \cdot 16H_2O$ (Ma et al., 2003) and $[Ni(phen)_3](fum) \cdot 2H_2fum \cdot 4H_2O$ (Lin and Zheng, 2004). The formed mother liquor exhibited a tendency towards jellification, so the formed crystals were separated immediately after their appearance which led to low yield of the product.

Spectroscopic characterization

Characteristic absorption bands in the IR spectrum of **1** (Fig. 1) were observed at 1578 and 1397 cm^{-1}; these were ascribed to the asymmetric and symmetric carboxylate stretching vibrations ν(COO) according to literature (Nakamoto, 1997). In the IR spectrum of the analogous complex $[Ni(en)_3](fum) \cdot 3H_2O$ with ionic bonding of the fum^{2-} dianion, the corresponding absorption bands were found at very similar values of 1583 and 1395 cm^{-1} (Padmanabhan et al., 2008). The calculated value of Δ = 181 cm^{-1} ($\Delta = \nu_{as}(COO) - \nu_s(COO)$) for **1** is in line with the corresponding value of 188 cm^{-1} found for $[Ni(en)_3](fum) \cdot 3H_2O$ (Padmanabhan et al., 2008), suggesting that the dicarboxylate dianion acts only as a counter ion; this was later corroborated by the results of X-ray structure analyses (see below). The well identifiable shoulder positioned at 3037 cm^{-1} can be assigned to $\nu(C_{ar}—H)$ stretching vibrations due to the presence of aromatic rings. In the analogous complex $[Ni(phen)_2]_2[Ni(mnt)_2]_3 \cdot 2DMF$ (*mnt* = 1,2-dicyanovinylene-1,2-dithiolato, DMF = N,N-dimethylformamide), the corresponding weak band was observed at 3063 cm^{-1} (Wang et al., 2004). The broad strong absorption band observed around 3405 cm^{-1} corresponds well to ν(OH) stretching vibrations for hydrogen bonded solvate water molecules. The IR spectrum of **1** below 1300 cm^{-1} is rich mainly due to the presence of *phen* ligands and unambiguous assignment of the observed bands to various types of vibrations is difficult.

Crystal structure of $[Ni(phen)_3](fum) \cdot 9H_2O$

Ionic crystal structure of $[Ni(phen)_3](fum) \cdot 9H_2O$ (**1**) consists of $[Ni(phen)_3]^{2+}$ complex cation, fumarato dianion and nine crystallographically independent molecules of crystal water (Fig. 2). Within the complex cation,

Tab. 2. Selected geometric parameters [Å, °] for $[Ni(phen)_3](fum) \cdot 9H_2O$.

Ni1—N1	2.0822(14)	O4—C40	1.249(2)
Ni1—N2	2.0888(14)	C38—C37	1.499(2)
Ni1—N3	2.0965(14)	C38—C39	1.317(2)
Ni1—N4	2.0782(14)	C39—C40	1.502(2)
Ni1—N5	2.1167(14)	N1—Ni1—N2	80.09(6)
Ni1—N6	2.0802(14)	N3—Ni1—N4	79.78(5)
O1—C37	1.253(2)	N5—Ni1—N6	79.61(5)
O2—C37	1.250(2)	O1—C37—O2	124.66(16)
O3—C40	1.253(2)	O3—C40—O4	125.52(17)

the Ni(II) central atom is hexacoordinated by six nitrogen atoms from three chelate bonded *phen* molecules. Although the complex cation is chiral, both enantiomers are present in the crystal structure due to its centrosymmetric character. The same complex cation was found in analogous complexes $[Ni(phen)_3](succBr_2) \cdot 7H_2O$ ($H_2(succBr_2)$ = 2,3-dibromosuccinic acid) (Li et al., 2005) or $[Ni(phen)_2(phen\text{-}dione)][Ni(phen)_3]$

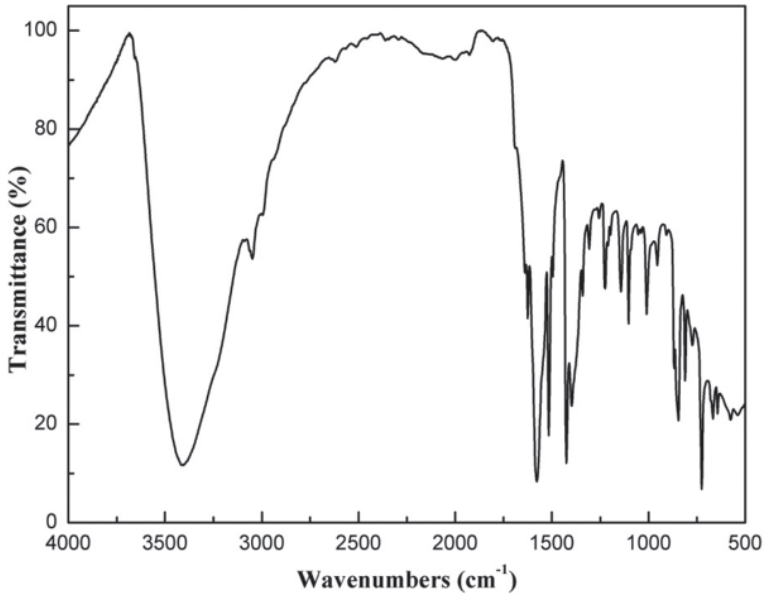

Fig. 1. FT-IR spectrum of $[Ni(phen)_3](fum) \cdot 9H_2O$.

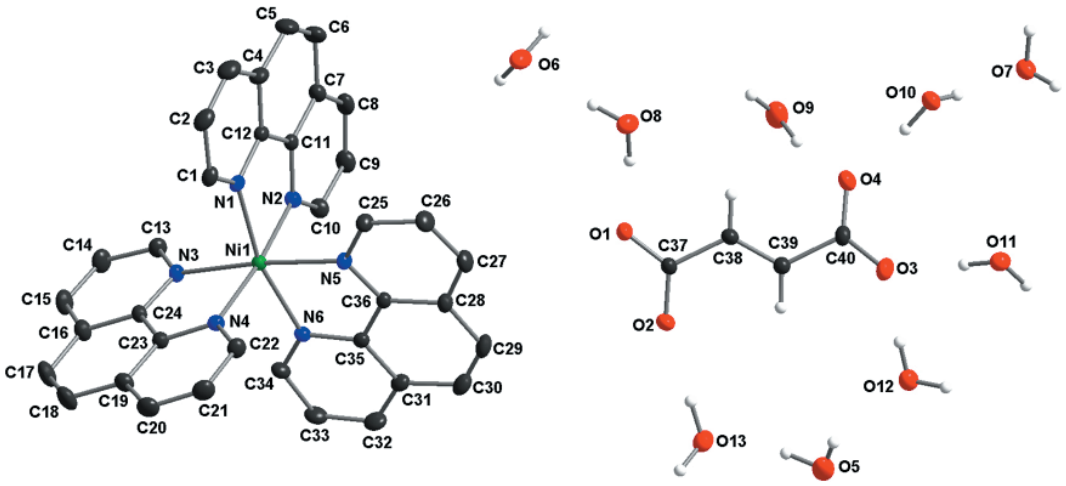

Fig. 2. Structure of [Ni(*phen*)$_3$](*fum*) · 9H$_2$O with atoms numbering scheme. Thermal ellipsoids are drawn at the 30 % probability level. Hydrogen atoms from *phen* ligand are omitted for clarity.

(PF$_6$)$_4$ · CH$_3$CN (*phen-dione* = 1,10-phenanthroline-5,6-dione) (Hadadzadeh et al., 2012). The Ni—N bonds in **1** are within the range of 2.0782(14)—2.1167(14) Å (Table 2). Similar ranges for Ni—N bonds, 2.082(4)—2.194(5) Å and 2.081(6)—2.137(7), were reported for the already mentioned [Ni(*phen*)$_3$](*succ*Br$_2$) · 7H$_2$O (Li et al., 2005) and [Ni(*phen*)$_2$(*phen-dione*)][Ni(*phen*)$_3$](PF$_6$)$_4$ · CH$_3$CN (Hadadzadeh et al., 2012), respectively. Fumarate dianion acts as a counter ion and its carboxylate groups are somewhat twisted out of the plane formed by the four carbon atoms C37—C40 as it can be seen from the values of the torsion angles O1—C37—C38—C39 and O3—C40—C39—C38, –172.93(1) and –159.45(1) °, respectively; this deviation from the planarity may reflect the tendency to maximize the formation of hydrogen bonds (see below). The remaining geometric parameters of **1** correspond well to those observed of [Ni(*phen*)$_3$](*fum*) · 2H$_2$*fum* · 4H$_2$O (Lin and Zheng, 2004).

An outstanding feature of the presented structure **1** is the formation of a 2D supramolecular structure perpendicular to the *a* axis built of O—H · · · O type hydrogen bonds; fumarate dianions together with nine crystallographically independent solvate water molecules are involved in this structure (Figs. 3 and 4, Table 3). Within the hydrogen bonded layers, ten different hydrogen bonded ring systems can be distinguished and these can be described using the graph-set analysis (Bernstein et al., 1995); descriptors for the respective ring systems are (see also Fig. 3) : *R1*: $R_4^4(13)$, *R2*: $R_5^3(10)$, *R3*: $R_4^3(10)$,

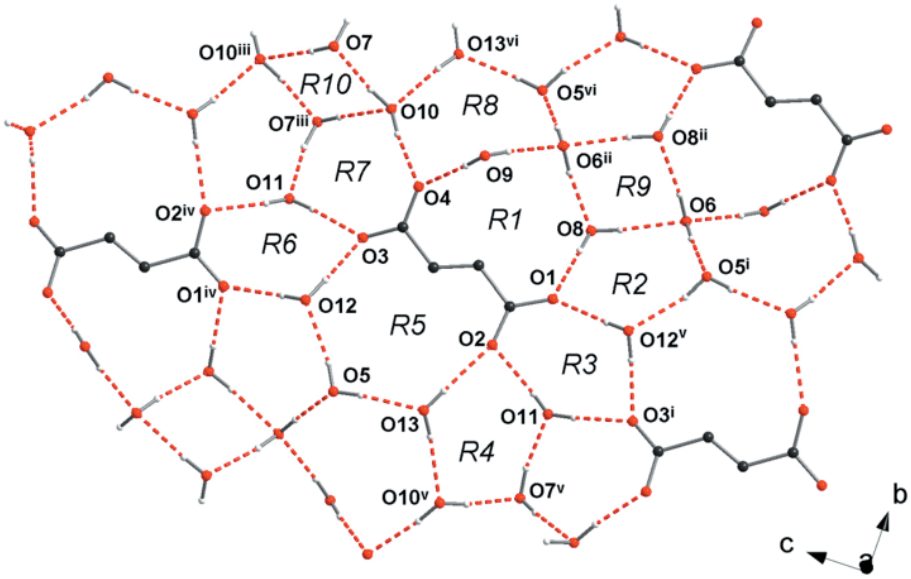

Fig. 3. A part of hydrogen bonded supramolecular layers in **1**. Symmetry codes: i: x, 1/2 – y, z – 1/2; ii: 1 – x, 1 – y, 1 – z; iii: 1 – x, 1 – y, 2 – z; iv: x, 1/2 – y, 1/2 + z; v: 1 – x, y – 1/2, 3/2 – z; vi: 1 – x, y + 1/2, 3/2 – z.

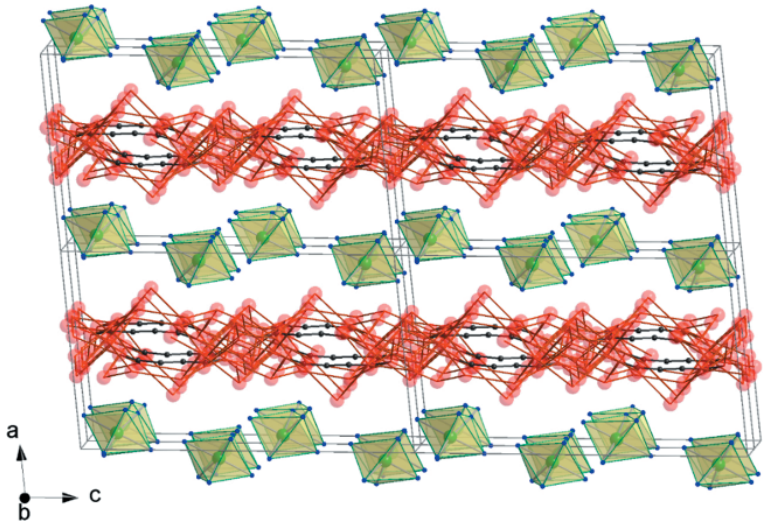

Fig. 4. Approximate crystal structure of 1 along b axis showing the hydrogen bonded hydrophilic host part of the structure (red balls are oxygen atoms, black balls are carbon atoms, brown lines are O—H · · · O hydrogen bonds) and embedded hydrophobic guest part of the structure formed by $[Ni(phen)_3]^{2+}$ complex cations (light green octahedrons).

R4: $R_5^4(10)$, *R5*: $R_4^4(13)$, *R6*: $R_4^4(10)$, *R7*: $R_4^4(10)$, *R8*: $R_6^5(12)$, *R9*: $R_4^4(8)$, *R10*: $R_4^4(8)$. Similarly hydrogen bonded supramolecular layers with auxiliary anionic species were observed in $[Ni(bpy)_3]Cl_2 \cdot 5.5H_2O$ (*bpy*=2,2´-bipyridine; chloride anions are involved as anionic species) (Ruiz-Pérez et al., 2002), $[Ni(bpy)_3][Cu(CN)_3] \cdot 4.5H_2O$ (tricyanidocuprate(2-) anions are the anionic species) (Kočanová et al., 2010) or in $[Ni(phen)_3](HB)_2 \cdot 7H_2O$ (HB^- = diphenylglycolate; with HB^- anions as anionic species) (Covelo et al., 2008). As a consequence of the formed supramolecular layers in **1,** the title compound can be viewed as a host-guest (HG) system in which the hydrophilic host part of the structure is built of hydrogen bonded water solvate molecules and fumarate dianions, while hydrophobic $[Ni(phen)_3]^{2+}$ complex cations as guest species are enclosed between the formed layers (Fig. 4). The presented crystal structure thus displays some similarity with the well-know Hofmann-type clathrates in which

Tab. 3. Possible hydrogen bonds in **1** [Å, °].

D—H · · · A	D—H	H · · · A	D · · · A	D—H · · · A
O5—H51 · · · O12	0.84(4)	1.93(4)	2.747(2)	162(4)
O5—H52 · · · O13	0.84 (4)	1.93(4)	2.771(2)	173(3)
O6—H61 · · · O5^{i}	0.83(3)	1.86(3)	2.685(2)	177(3)
O6—H62 · · · O8^{ii}	0.87(3)	1.91(3)|	2.775(2)	172(3)
O7—H71 · · · O10^{iii}	0.79(3)	2.04(3)	2.824(2)	172(3)
O7—H72 · · · O11^{iii}	0.90(3)	1.79(3)	2.676(2)	168(2)
O8—H81 · · · O1	0.84(3)	1.87(3)	2.710(2)	177(3)
O8—H82 · · · O6	0.79(3)	2.03(3)	2.803(2)	171(3)
O9—H91 · · · O4	0.79(3)	2.04(3)	2.828(2)	175(3)
O9—H92 · · · O6^{ii}	0.90(3)	2.01(4)	2.900(3)	173(3)
O10—H101 · · · O4	0.87(3)	1.87(3)	2.728(2)	170(3)
O10—H102 · · · O7	0.86(3)	1.93(3)	2.776(2)	169(2)
O11—H112 · · · O2^{iv}	0.79(3)	2.00(3)	2.788(2)	174(3)
O11—H111 · · · O3	0.84(3)	1.93(3)	2.766(2)	175(3)
O12—H121 · · · O3	0.88(3)	1.87(3)	2.741(2)	177(3)
O12—H122 · · · O1^{iv}	0.78(3)	2.00(3)	2.781(2)	178(3)
O13—H131 · · · O2	0.80(3)	2.01(3)	2.812(2)	177(3)
O13—H132 · · · O10^{v}	0.84(3)	2.08(3)	2.916(2)	176(3)

Symmetry codes: i: x, 1/2 – y, z – 1/2; ii: 1 – x, 1 – y, 1 – z ; iii: 1 – x, 1 – y, 2 – z; iv: x, 1/2 – y, 1/2 + z; v: 1 – x, y – 1/2, 3/2 – z.

the aromatic guest molecules are enclosed between the cyanidometallate layers (Iwamoto, 1996). Additional much weaker hydrogen bonding interactions of the C—H···O type (C···O distances are from the range of 3.2040(4)—3.4555(4) Å and C—H···O angles are from the range of 138—166 °) link complex cations with the solvate water molecules.

Thermal analysis

Thermal curves of **1** are shown in Fig. 5. From the TG curve it follows that decomposition starts at 95 °C. The observed weight loss of 17.5 % in the temperature range of 95—195 °C corresponds well to the complete dehydration of **1** (calculated 18.5 % for nine water molecules from the formula unit). The DTA curve suggests that the observed dehydration is formed of three weak endothermic processes. Endothermic dehydration of the analogous complex [Ni(*en*)$_3$](*fum*)·3H$_2$O occurred in the similar temperature range of 90—165 °C (Padmanabhan et al., 2008) while [Ni(*fum*)]·4H$_2$O dehydrates at somewhat higher temperature from the range of 130—225 °C (Randhawa and Kaur, 2007). On the TG curve of **1** after its dehydration, a plateau in the temperature range of 195—220 °C can be seen; which is accompanied by a weak exothermic peak on the DTA curve at 210 °C suggesting a possible phase transition. The second mass loss of 21.7 % was observed in the temperature range of 200—290 °C; this weight loss corresponds well to the release of one *phen* ligand from the formula of **1** (calc. 20.6 %).

In the temperature range of 360—650 °C, a strongly exothermic process associated with the mass loss of 52.4 % can be observed; the experimental mass loss corresponds well to the release (or decomposition) of the remaining organic part of the studied compound (calculated value is 54.2 %). The solid residue after thermal decomposition represents 8.4 % of the initial weight, which is in line with the assumed formation of NiO (calculated value is 8.5 %). The formation of NiO as the solid residue was also reported in case of thermal decomposition of [Ni(*phen*)(*fum*)] (Černák et al., 2009), [Ni(*fum*)]·4H$_2$O (Randhawa and Kaur, 2007) and [Ni(*en*)$_3$](*fum*)·3H$_2$O (Padmanabhan et al., 2008).

Conclusions

Complex [Ni(*phen*)$_3$](*fum*)·9H$_2$O was synthesized and chemically and spectroscopically characterized. Crystal structure of **1** is ionic and it is formed of [Ni(*phen*)$_3$]$^{2+}$ complex cations with a hexacoordinated Ni(II) atom, *fum* counter dianion and nine water molecules of crystallization. Water molecules and *fum*$^{2-}$ dianions interact *via* hydrogen bonds forming a 2D supramolecular structure with complex cations embedded between the hydrophilic layers, which enables considering the presented crystal structure as a host-guest system built of hydrophilic hydrogen bonded host part and hydrophobic guest complex cations. A study of the thermal properties has shown that dehydration is the first step of thermal decomposition.

Supplementary materials

Crystallographic data for the compound have been deposited with the Cambridge Crystallo-

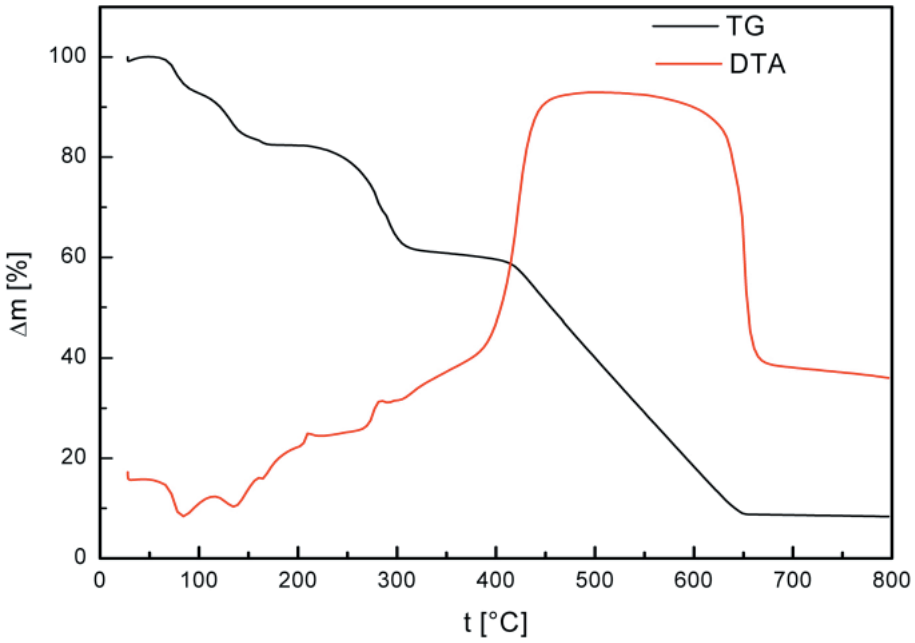

Fig. 5. Thermal curves for [Ni(*phen*)$_3$](*fum*)·9H$_2$O.

graphic Data Centre, CCDC 1542632. Copies of the information may be obtained free of charge from The Director, CCDC, 12 Union Road, Cambridge, CB21EZ, UK (fax: +44-1223-336033; e-mail: deposit@ccdc.cam.ac.uk or www: http://www.ccdc.cam.ac.uk).

Acknowledgements

This work was supported by the Slovak grant agency VEGA (grant No. 1/0063/17). We thank prof. W. Massa from the Philipps-Universität in Marburg (Germany) for his kind permission to use the single crystal diffractometer. Anna Uhrinová thanks DAAD for financial support of her study stay in Marburg.

References

Bernstein J, Davis RE, Shimoni L, Chang N-L (1995) Angew Chem Int Ed Engl 34: 1555—1573.

Bora SJ, Das BK (2012) J Solid State Chem 192: 93—101.

Brandenburg K, Putz H (2008) DIAMOND Crystal Impact (version 3.1f), GbR, Postfach 1251, D-53002 Bonn, Germany.

Covelo B, Carballo R, Vásquez-López EM, Lago AB (2008) Synthesis and Reactivity in Inorganic, Metal-Organic and Nano-Metal Chemistry 38: 49—54.

Černák J, Farkašová N, Tomás M, Kavečanský V, Čižmár E, Orendáč M (2015) J Coord Chem 68: 2788—2797.

Černák J, Pavlová A, Orendáčová A, Kajňaková M, Kuchár J (2009) Polyhedron 28: 2893—2898.

Devereux M, McCann M, Leon V, Geraghty M, McKee V, Wikaira J (2000) Polyhedron 19: 1205—1211.

Farrugia LJ (2012) J Appl Crystallogr 45: 849—854.

Hadadzadeh H, Mansouri G, Rezvani AR, Khavasi HR (2012) Chem Crystallogr 42: 486—493.

Iwamoto T (1996) J Incl Phenom 24: 61—132.

Kočanová I, Kuchár J, Orendáč M, Černák J (2010) Polyhedron 29: 3372—3379.

Li D-X, Xu D-J, Xu Y-Z (2005) Acta Crystallogr E61: m471—m473.

Lin JL, Zheng YQ (2004) Z Kristallogr—New Cryst Struct 219: 230—232.

Ma JF, Yang J, Liu JF (2003) Acta Crystallogr E59: m900—m902.

Nakamoto K (1997) Infrared and Raman Spectra of Inorganic and Coordination Compounds, Part B: Applications in Coordination, Organometallic, and Bioinorganic Chemistry, Wiley, New York.

Neuman NI, Winkler E, Peña O, Passeggi MCG, Rizzi, AC, Brondino CD (2014) Inorg Chem 53: 2535—2544.

Oldham C (1987) Carboxylates, Squarates and Related Species. In Wilkinson G, Gillard RD, McCleverty JA, editors. Comprehensive Coordination Chemistry. 1st ed. Pergamon Press, Oxford, UK: 2 (1987). pp. 435—460.

Padmanabhan M, Joseph JC, Huang X, Li J (2008) J Mol Struct 885: 36—44.

Randhawa BS, Kaur M (2007) J Therm Anal Calorim 89: 251—255.

Ruiz-Pérez C, Lorenzo Luis PA, Lloret F, Julve M (2002) Inorg Chim Acta 336: 131—136.

Sheldrick GM (2008) Acta Crystallogr A64: 112—122.

Sheldrick GM (2015) Acta Crystallogr C71: 3—8.

Téllez-López A, Jaramillo-García J, Martínez-Domínguez R, Morales-Luckie RA, Camacho-Lopez MA, Escudero R, Sánchez-Mendieta V (2015) Polyhedron 100: 373—381.

Téllez-López A, Sánchez-Mendieta V, Jaramillo-García J, Rosales-Vázquez LD, García-Orozco I, Morales-Luckie RA, Escudero R, Morales-Leal F (2016) Trans Met Chem 41: 879—887.

Uhrinová A, Kuchár J, Černák J (2012) Acta Crystallogr E68: m92—m93.

Vráblová A, Falvello LR, Campo J, Miklovič J, Boča R, Černák J, Tomás M (2016) Eur J Inorg Chem 928—934.

Wang CG, Peng ZH, Guo WY, Zhou YH, Cheng GZ (2004) J Mol Struct 702: 1—7.

Zheng YQ, Lin JL, Chen BY (2003) J Mol Struct 646: 151—159.

Zhang KL, Zhou F, Wu RT, Yang B, Ng SW (2009) Inorg Chim Acta 362: 4255—4259.

sciendo

Magnetic composites based on NR and strontium ferrite

Ján Kruželák[a], Andrea Kvasničáková[a], Rastislav Dosoudil[b], Ivan Hudec[a]

[a]Department of Plastics, Rubber and Fibres, Faculty of Chemical and Food Technology, Slovak University of Technology in Bratislava, Radlinského 9, 812 37 Bratislava, Slovakia
[b]Department of Electromagnetic Theory, Faculty of Electrical Engineering and Information Technology, Slovak University of Technology in Bratislava, Ilkovičova 3, 812 19, Bratislava, Slovakia
jan.kruzelak@stuba.sk

Abstract: Two types of composites based on natural rubber (NR) and strontium ferrite were tested in this study. Composites of the first type were prepared by incorporation of strontium ferrite in the concentration range ranging from 0 to 100 phr (parts per hundred rubber) into pure NR based rubber matrix, while with those of the second type, strontium ferrite was dosed in the same concentration level into NR based rubber batch with constant amount of carbon black – 25 phr. For rubber matrices cross-linking, a standard sulfur based curing system was used. This work is focused on the effect of magnetic filler content on physico-mechanical, magnetic and thermo-physical properties of composite materials. Subsequently, the cross-link density and the structure of the formed sulfidic cross-links were examined. The results showed that the cross-link density of both types of composites increased with the increasing content of magnetic filler, while the structure of the sulfidic cross-links was almost not influenced by the amount of strontium ferrite. Tensile strength of rubber composites with pure rubber matrix was slightly improved by the incorporation of ferrite, while in case of composites based on a carbon black batch, the incorporation of magnetic filler resulted in the decrease of this characteristic. The presence of magnetic filler in both types of composites leads to a significant increase of the remanent magnetic induction.

Keywords: rubber composite, magnetic filler, cross-link density, tensile strength, remanent magnetic induction

Introduction

Ferrite permanent magnets of the general formula $SrFe_{12}O_{19}$ or $BaFe_{12}O_{19}$ contain approximately 80 % of iron oxide and 20 % of strontium or barium. They are a class of technologically important magnetic materials with high values of magneto-crystalline anisotropy as well as magnetic characteristics (mainly coercivity and remanent magnetic induction) (Wang at al., 2009; Namai at al.; Li at al., 2015). Moreover, they exhibit good chemical stability with high resistance to solvents, salts, lubricants, alkalis, harmful gases, soft acids and atmospheric effects. Operating temperature of ferrites ranges between –40 °C to +250 °C. These outstanding properties include ferrites in important magnetic materials which cannot be easily replaced. Magnetic properties of ferrites for specific applications can be adapted by selection of components, composition, by supplying suitable metal ions and by other suitable techniques (Lechevallier and LeBreton, 2005; Xie at al., 2013; Pullar, 2012).

Incorporation of magnetic crystalline ferrites into various rubber matrices leads to the preparation of magnets known as ferrite rubber magnets (Pattanayak at al., 2016; Gutiérrez at al., 2015; Jung at al., 2016; Bellucci at al., 2016; Sýkora at al., 2016). Rubber magnetic composites are materials consisting of at least two phases: magnetic powder as filler and continuous rubber matrix. An important advantage of these materials is they can be prepared and processed by technologies typically used for polymer composites processing. They can be bent, coiled and shaped without the loss of their magnetic characteristics. Additionally, they are very resistant to corrosion and therefore no surface treatment is necessary. Due to their elasticity and easy processability, they are suitable for applications in which good elasticity and high flexibility are required. These attributes in combination with unique magnetic characteristics rank them among progressive developing materials which have already found the utilization in microwave and radar technology, vibration absorbers, motor parts, memory devices, variable impedance surfaces, inductor cores, sensors of magnetic and electromagnetic fields and in many other technological applications (Vinayasree at al., 2016; Tong at al., 2013; Das at al., 2015).

In this work, rubber magnetic composites were prepared by the incorporation of strontium ferrite into NR based pure rubber matrix or carbon black batch. The main aim was to observe the influence of magnetic filler content on physico-mechanical, magnetic and thermo-physical properties of the tested composites. Cross-link density and structure of the formed cross-links were also investigated.

Experimental

Materials

Natural rubber (NR), type SMR20 (Mardec, Malaysia), and carbon black batch based on natural rubber, type SMR 20 (content of carbon black N330 — 25 phr, Elastorsa, Martin, SR), were used as rubber matrices. Strontium ferrite, $SrFe_{12}O_{19}$, type FD 8/24, supplied as magnetic filler by Magnety, Světlá Hora, Czech Republic, was dosed to the rubber formulations in the concentration range from 0 to 100 phr. Characteristics of the applied strontium ferrite are provided in Tab. 1. For rubber matrices cross-linking, a standard semi EV-sulfur curing system consisting of zinc oxide — 3 phr (Slovlak, Košeca, Slovakia), stearic acid — 2 phr (Setuza, Ústí nad Labem, Czech Republic), N-Cyclohexyl-2-benzothiazole sulfenamide CBS — 1.5 phr (Duslo, Šaľa, Slovakia), and sulfur — 1.3 phr (Siarkopol, Tarnobrzeg, Poland) was used. Phr stands for parts per hundred rubber.

Tab. 1. Characteristics of strontium ferrite.

Characteristics	Value
Particle size (μm)	0.1—30
Specific surface area (m^2/g)	4.06
Total porosity (%)	55.62
Total volume of pores (cm^3/g)	0.254
Density (g/cm^3)	4.73
Coercivity (kA/m)	117
Remanent magnetic induction (T)	0.17

Methods

Preparation and curing of rubber compounds

Rubber compounds were prepared in a laboratory appliance Brabender in two mixing steps. Temperature of the chamber was set to 90 °C and the mixing process was carried out at the rotor speed of 50 rpm. In the first step, rubber and filler were compounded. Mixing of ingredients in the first step was performed for 9 min in the temperature range of 90—95 °C. Components of the curing systems were introduced in the second step (4 min, 90—95 °C). Then, the mixed rubber compounds were shaped into thin sheets by a two roll calender.

Curing characteristics were investigated from the corresponding curing isotherms measured on Rheometer Monsanto R100 at 150 °C. The rubber compounds were cured at 150 °C with regard to their optimum cure time under the pressure of 15 MPa. Hydraulic press FONTIJNE was employed to carry out the curing process.

Determination of cross-link density and cross-link structure

Two different methods were used to determine the cross-link density of rubber composites.

Chemical cross-link density, ν_{ch}, was determined based on equilibrium swelling of samples in xylene. First, the samples were swelled in xylene until equilibrium swelling was reached. The cross-link density was then calculated based on the equilibrium swelling degree by applying the Krause modified Flory-Rehner equation (1) for filled vulcanizates (Kraus, 1963):

$$\nu_{ch} = -\frac{V_{r0}}{V_S}\frac{\ln(1-V_r)+V_r+\chi V_r^2}{V_r^{1/3}V_{r0}^{2/3}-0,5V_r} \qquad (1)$$

ν_{ch} — cross-link density (mol/cm^3), V_{r0} — volume fraction of rubber in equilibrium swelling sample of vulcanizate in absence of fillers, V_r — volume fraction of rubber in equilibrium swelling sample of filled vulcanizate, V_S — molar volume of solvent (for xylene = 123.45 cm^3/mol), χ — Huggins interaction parameter (for measuring conditions χ = 0.4106).

In the second method, based on deformation measurements, the total cross-link density, ν_t, was calculated by means of the Mooney-Rivlin equation (Hamed, 1992) (2), utilizing relation (3):

$$\frac{\sigma}{2(\alpha-\alpha^{-2})} = C_1 + \frac{C_2}{\alpha} \qquad (2)$$

σ — tension (MPa), α — relatively extension (%), C_1, C_2 — constants,

$$\nu_t = 2C_1/RT \qquad (3)$$

R = 8.314 J/K · mol, T = 293.15 K.

The measurements were carried out using an Inspekt desk 5kN apparatus (Metrotest) up to 100 % deformation with the deformation velocity of 10 mm/min.

Cross-link structure of vulcanizates was determined using the thiol-amine method in argon atmosphere as described in (Saville and Watson, 1967; Morrison and Porter, 1984; Warner, 1994). Propane-2-thiol was used, which has the ability to decompose polysulfidic cross-links. First, the chemical cross-link density, ν_{ch}, of original samples was determined. Then, the samples were treated with a solution of propane-2-thiol for two hours at laboratory temperature in argon atmosphere and the cross-link density was determined again (ν_{PT} — the cross-link density of samples after propane-2-thiol treatment). The content of polysulfidic *Sx* was then calculated by equation (4) and combinations of disulfidic *S2* a monosulfidic *S* cross-links.

$$Sx = \nu_{ch} - \nu_{PT},\ Sx = [(\nu_{ch} - \nu_{PT}) \cdot 100]/\nu_{ch} \qquad (4)$$

Determination of physico-mechanical properties

Tensile properties of rubber magnetic composites were determined using a Zwick Roell/Z 2.5 appliance. The measurements were carried out in accordance with the valid technical standards at the laboratory temperature and cross-head speed of 500 mm/min. The tested composites were cut into double side dumbbell-shaped test specimens (width of 6.4 mm, length of 8 cm, thickness of 2 mm). Hardness was measured using a durometer and the unit was expressed in Shore A.

Determination of magnetic characteristics

Magnetic characteristics of composites were evaluated using a magnetometer TVM–1 at the maximum coercivity of H_m = 750 kA/m. The basic principle of measurement was the induction method of scanning of scattering magnetic flux, Φ, induced by magnetic vibrating sample. Magnetic field is generated by two cores of a Weiss electromagnet at the minimum distance of poles adapters of 7.5 mm. The induced tension proportional to magnetic flux time dependence in the sample is scanned with a system of four small cores. The cores eliminate the influence of electromagnet magnetic fields time instability and the change of magnetic flux is directly proportional to magnetic induction, *B*. Specimens for magnetic characteristics evaluation were of prism shape (8 × 4 × 2 mm).

Evaluation of thermo-physical characteristics of composites

An Isomet appliance was applied to evaluate the thermo-physical characteristics of prepared materials. The measurement is based on the analysis of time dependence of thermal response to the impulses of the thermal flow into the analyzed material. The thermal flow is generated by scattered electric discharge in a probe resistor, which is thermal-conductively connected with the analyzed material. Temperature of the resistor was scanned by a semiconductive detector.

Results and discussion

Influence of ferrite on cross-link density and structure

Cross-link density and structure of the formed cross-links are important structural parameters of all rubber products determining their service properties. Not only the original properties but also their changes in time are dependent on these characteristics. Two different methods were used to determine cross-link density of the prepared composites. Chemical cross-link density, ν_{ch}, was determined based on equilibrium swelling of samples in xylene and the total cross-link density, ν_t, was determined based on deformation measurements of the prepared samples. In the first case, xylene diffuses into the samples and disrupts all physical interactions between the macromolecules of rubber. When equilibrium swelling is reached, the cross-link density is calculated by the Flory-Rehner equation (1). During the deformation measurements to a low deformation degree, the disruption of physical interactions between the macromolecules is not expected. As a result, concentration of all cross-links (chemical and physical) in the analyzed samples can be determined. From the difference between the total and chemical cross-link density, physical cross-link density, ν_{ph}, can be calculated. Polymer-polymer physical interactions, polymer-filler physical interactions, also various intramolecular and intermolecular entanglements are involved in physical cross-link density.

From Fig. 1 it is evident that chemical cross-link density, ν_{ch}, of composites based on pure NR shows

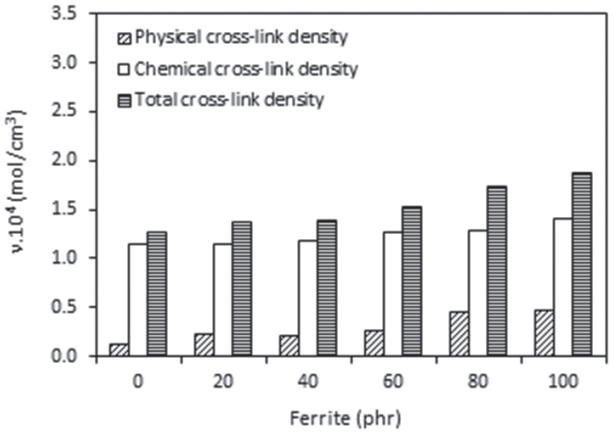

Fig. 1. Influence of ferrite content on physical ν_{ph}, chemical ν_{ch} and total ν_t cross-link density of composites based on NR.

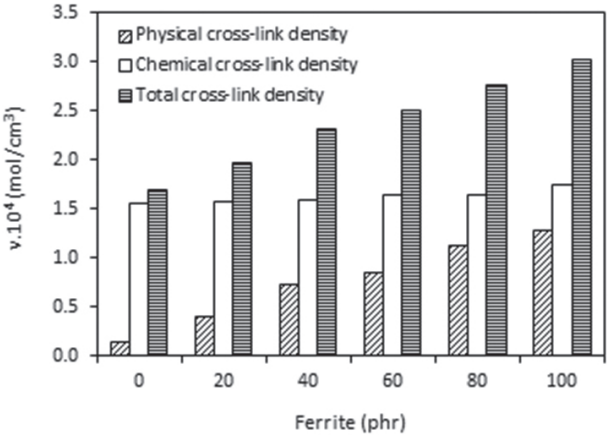

Fig. 2. Influence of ferrite content on physical ν_{ph}, chemical ν_{ch} and total ν_t cross-link density of composites based on carbon black batch.

a slightly increasing trend with the increasing amount of strontium ferrite. Physical cross-link density, which represents the difference between the total and the chemical cross-link density (ν_t – ν_{ch}), is much lower than ν_{ch} and also increases non-linearly with the increasing content of the magnetic filler. The physical and chemical cross-link density of composites based on carbon black batch was higher compared to that of equivalent composites based on pure NR (Fig. 2). This can be attributed to the presence of carbon black which, as a reinforcing filler, contributes to the formation of chemical and mainly physical couplings in the rubber matrix. Thus, also the total cross-link density of composites based on NR batch is higher than the total cross-link density of composites based on pure NR.

An analysis revealed that the cross-link structure of both type composites was formed mainly from polysulfidic cross-links (about 50—60 %), the rest cross-links are formed by mono- and disulfidic bridges (Figs. 3, 4). The achieved results are in line with general knowledge, according to which, in case semi-EV curing systems applied in cross-linking of rubber compounds, all three types of sulfidic cross-links are formed in the rubber matrix with dominance of polysulfidic cross-links. The amount of incorporated magnetic filler has no significant influence on the structure of the formed cross-links.

Influence of ferrite on physico-mechanical properties

The incorporation of strontium ferrite into both composite types resulted in the increase of modulus M300 and hardness (Figs. 5, 6). The increase of modulus and hardness (in addition to the fact that hardness of strontium ferrite is much higher than that of the rubber matrix) can be attributed to the increase in cross-link density of both composite types. It can be also stated that higher cross-link density

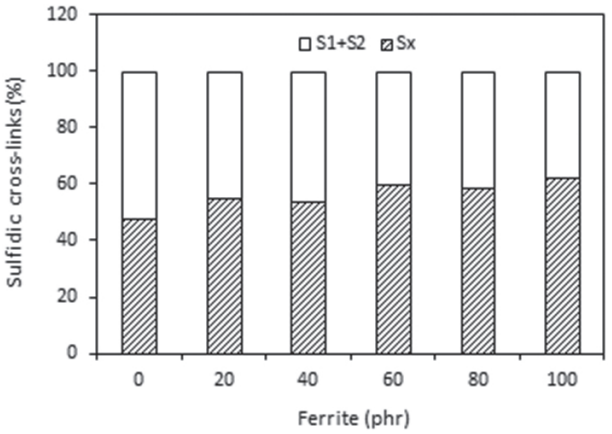

Fig. 3. Influence of ferrite content on the structure of sulfidic cross-links of composites based on NR (S1 — monosulfidic cross-links, S2 — disulfidic cross-links, Sx — polysulfidic cross-links).

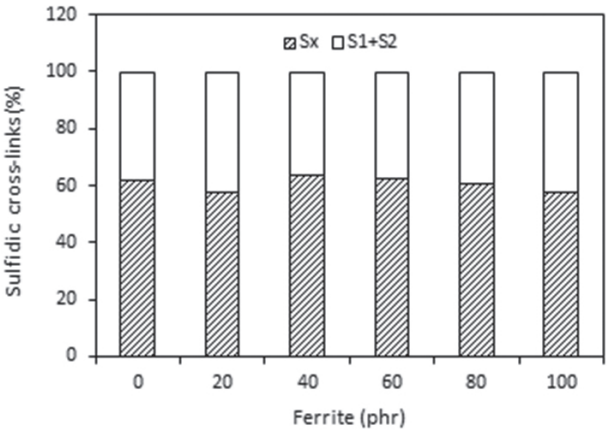

Fig. 4. Influence of ferrite content on the structure of sulfidic cross-links of composites based on carbon black batch (S1 — monosulfidic cross-links, S2 — disulfidic cross-links, Sx — polysulfidic cross-links).

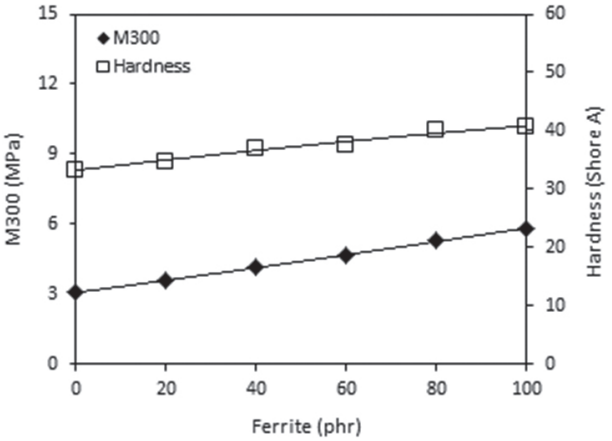

Fig. 5. Influence of ferrite content on modulus M300 and hardness of composites based on NR.

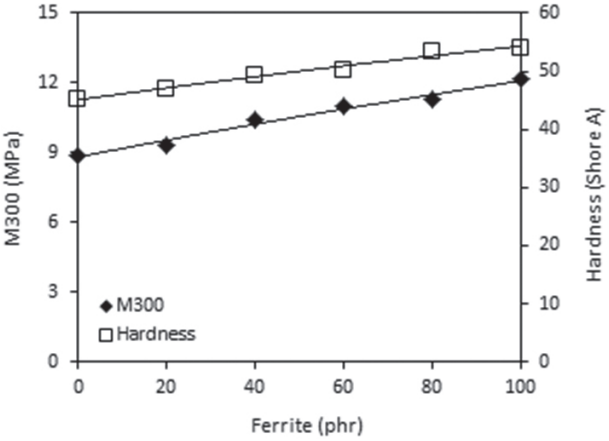

Fig. 6. Influence of ferrite content on modulus M300 and hardness of composites based on carbon black batch.

and the presence of carbon black in the composites based on carbon black batch are responsible for higher values of these characteristics compared to equivalent composites based on pure NR.

On the other hand, the increase in cross-link density of both composite types with the increasing amount of strontium ferrite was responsible for the decrease of elongation at break (Fig. 7, 8). Again, higher cross-link density of composites based on carbon black batch was responsible for their lower elongation at break. The different character of tensile strength of both composite types in dependence on the strontium ferrite content was recorded. Incorporation of 40 phr of strontium ferrite into the rubber matrix based on pure NR resulted in an enhancement of tensile strength by about 2 MPa in comparison with the unfilled sample. Then, a slightly decreasing tendency of the tensile strength was recorded. As it can be seen in Fig. 7, the tensile strength of maximally filled composite reached the level of reference – unfilled sample. From Fig. 8 it is evident that the highest tensile strength of composites based on carbon black batch exhibited a reference sample filled only with carbon black. When ferrite was incorporated, the tensile strength decreased. Composite with maximum ferrite content showed the lowest tensile strength. Comparing both composite types, higher tensile strength was found in composites based on the carbon black batch. However, with the increasing amount of magnetic filler, the differences in tensile strength of both composite types became lower and the composites based on pure NR with 80 and 100 phr of ferrite already exhibited slightly higher tensile strength than equivalent composites based on the carbon black batch. This is interesting as in case of composites based on carbon black, much higher values of tensile strength were expected. Carbon black is a well-known reinforcing filler in rubber compounds. Therefore, higher tensile strength of composites based on pure NR with higher ferrite content is very surprising and it shows a promising aspect in the preparation of rubber composites with magnetic fillers. The results point out a slight reinforcing effect of strontium ferrite in the rubber matrix.

Influence of ferrite on magnetic and thermo-physical characteristics

The most important magnetic characteristics of all permanent magnets are the remanent magnetic induction, B_r, which represents the value of residual magnetism in the material when the external magnetic field is removed, and the coercive intensity of magnetic field (coercivity, H_c), which represents energy needed to abolish the remanent magnetic induction. The higher are the values of both characteristics, the better are the permanent magnets. Ferrites as hard magnetic materials have unique magnetic properties and their incorporation into rubber matrix should impart magnetic properties to the rubber composites as well. Therefore, the influence of strontium ferrite content on the magnetic properties of both composite types was investigated. As shown in Figs. 9, 10, the incorporation of ferrite resulted in a significant increase of remanent magnetic induction of both composite types. The remanent magnetic induction increased by more than 400 % when the amount of strontium ferrite increased from minimum up to its maximum content. Slightly higher values of remanent magnetic induction were found for composites based on the carbon black batch. On the other hand, composites based on the carbon black batch exhibited lower coercivity compared with the equivalent composites based on NR. It is also apparent from Figs. 9, 10 that the coercivity of both composite types fluctuated only in the low range of experimental values

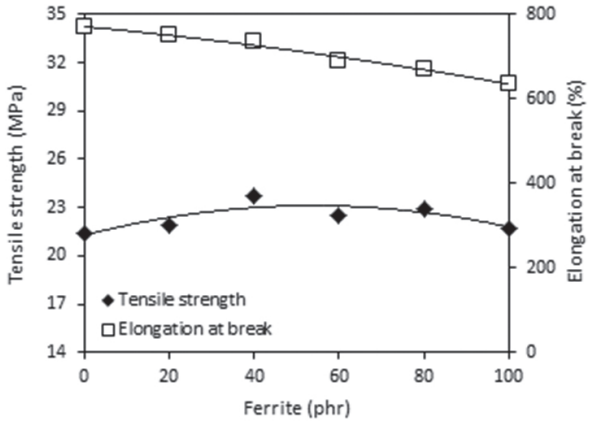

Fig. 7. Influence of ferrite content on tensile strength and elongation at break of composites based on NR.

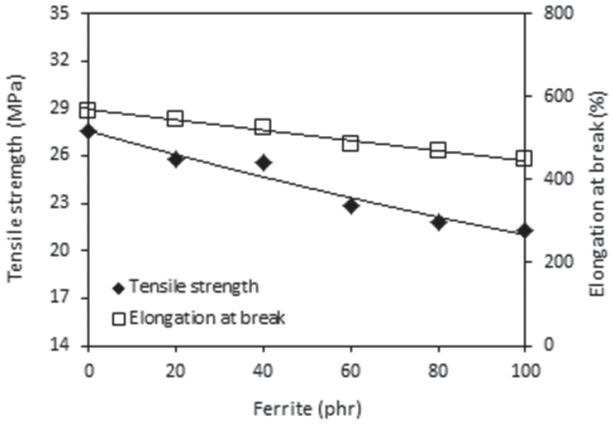

Fig. 8. Influence of ferrite content on tensile strength and elongation at break of composites based on carbon black batch.

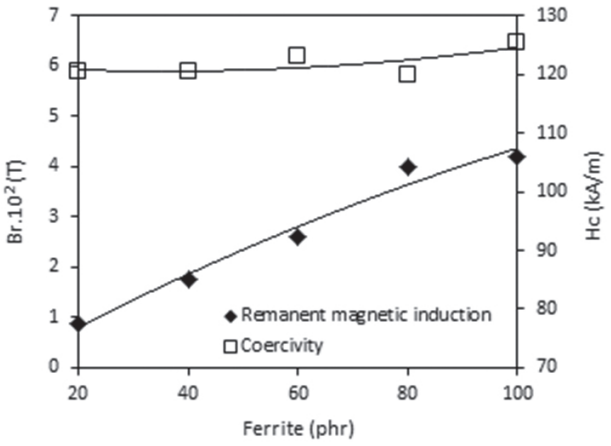

Fig. 9. Influence of ferrite content on remanent magnetic induction B_r and coercivity H_c of composites based on NR.

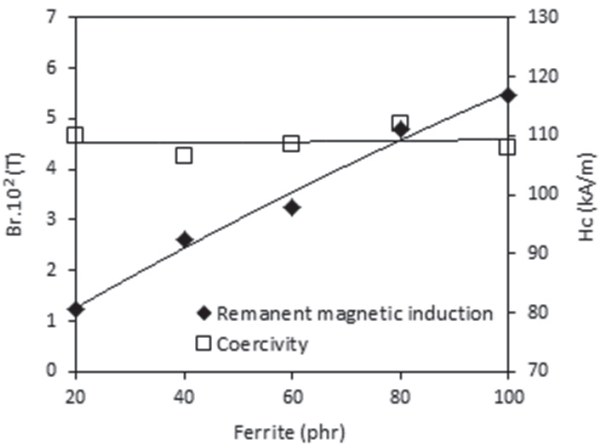

Fig. 10. Influence of ferrite content on remanent magnetic induction B_r and coercivity H_c of composites based on carbon black batch.

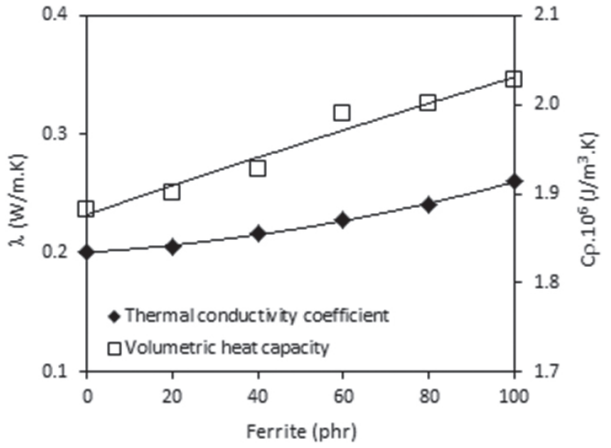

Fig. 11. Influence of ferrite content on thermal conductivity coefficient λ and volumetric heat capacity $C\rho$ of composites based on NR.

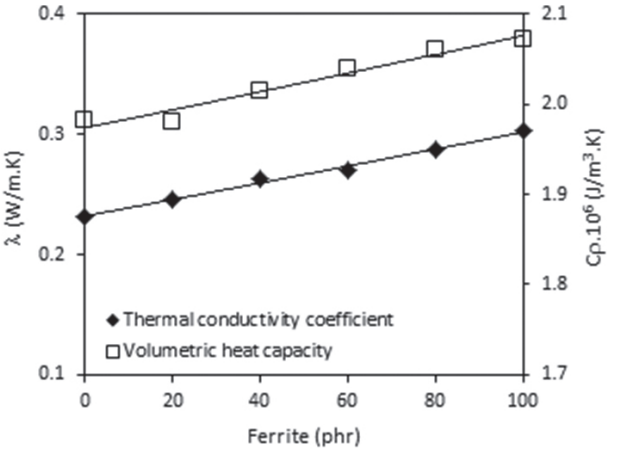

Fig. 12. Influence of ferrite content on thermal conductivity coefficient λ and volumetric heat capacity $C\rho$ of composites based on carbon black batch.

almost independently on the amount of strontium ferrite.

Similarly, ferrites as metal oxide powders have higher thermal conductivity than elastomers and therefore their presence in rubber compounds should lead to increased thermal conductivity and thermal flow through the composites. Thus, the thermal conductivity coefficient, λ, and the volumetric heat capacity, $C\rho$, of rubber magnets were also examined. As expected, thermal conductivity coefficient and volumetric heat capacity of composites increased with the increasing amount of strontium ferrite although the increase of both parameters in dependence on the ferrite content was not very significant (Figs. 11, 12). Based on the achieved results it can be assumed that even at the maximum ferrite content in the rubber matrix, the percolation threshold of the filler is not reached and therefore the increase of thermal conductivity is not substantial. When comparing both composite types, higher values of both parameters were found for composites based on carbon black batch. Thus, it can be concluded that carbon black also contributes to the increase of thermal conductivity of composite materials.

Conclusion

Rubber magnetic composites tested in this work were prepared by incorporation of strontium ferrite into rubber compounds based on pure NR and carbon black batch. The main aim was to investigate the influence of magnetic filler content on the cross-link density and properties of the prepared composites.

The results revealed that the incorporation of strontium ferrite leads to an increase of the cross-link density of composites, while the structure of

the formed sulfidic cross-links remained almost unchanged with the change of the magnetic filler content. Dependences of modulus M300, hardness and elongation at break followed the those of cross-link density showing that the higher is the cross-link density, the higher is modulus and hardness and the lower is elongation at break. Tensile strength of composites based on carbon black batch showed a decreasing trend with the increasing content of magnetic filler, while positive effect of strontium ferrite was recorded in case of composites based on pure NR. This indicates a reinforcing effect of strontium ferrite on the rubber matrix. The remanent magnetic induction of both composite types significantly improved with the increasing amount of strontium ferrite. Incorporation of a magnetic filler into rubber matrices leads also to an increase of the thermo-physical characteristics of rubber magnets.

Ackowledgement
This work was supported by the Slovak Research and Development Agency under the contract No. APVV-16-0136.

References

Bellucci FS, de Almeida, FCL, Nobre MAL, Rodríguez-Pérez MA, Paschoalini AT, Job AE (2016) Magnetic properties of vulcanized natural rubber nanocomposites as a function of the concentration, size and shape of the magnetic fillers. Composites Part B. 85: 196—206.

Das S, Nayak GC, Sahu SK, Routray PC, Roy AK, Baskey H (2015) Microwave absorption properties of double-layer composites using CoZn/NiZn/MnZn-ferrite and titanium dioxide. Journal of Magnetism and Magnetic Materials. 377: 111—116.

Gutiérrez J, Martins P, Gonçalves R, Sencadas V, Lasheras A, Lanceros-Mendez S, Barandiarán JM (2015) Synthesis, physical and magnetic properties of $BaFe_{12}O_{19}$/P(VDF-TrFE) multifunctional composites. European Polymer Journal. 69: 224—231.

Hamed GR, editor (1992) Materials and Compounds: Engineering with Rubber. New York: Oxford University Press.

Jung HS, Kwon SH, Choi HJ, Jung JH, Kim YG (2016) Magnetic carbonyl iron/natural rubber composite elastomer and its magnetorheology. Composite Structures. 136: 106—112.

Kraus G (1963) Swelling of filler-reinforced vulcanizates. Journal of Applied Polymer Science. 7: 861—871.

Lechevallier L, LeBreton JM (2005) Substitution effects in M-type hexaferrite powders investigated by Mössbauer spectrometry. Journal of Magnetism and Magnetic Materials. 290—291: 1237—1239.

Li J, Zhang HF, Shao GQ, Chen D, Zhao GG, Gao ZS, Liu JH, Lu JS, Li XB (2015) Synthesis and properties of new multifunctional hexaferrite powders. Procedia Engineering. 102: 1885—1889.

Morrison NJ, Porter M (1984) Temperature effects on the stability of intermediates and crosslinks in sulfur vulcanization. Rubber Chemistry and Technology. 57: 63—86.

Namai A, Yoshikiyo M, Yamada K, Sakurai S, Goto T, Yoshida T, Miyazaki T, Nakajima M, Suemoto T, Tokoro H, Ohkoshi S. Hard magnetic ferrite with a gigantic coercivity and high frequency millimetre wave rotation. Nature Communications. DOI:10.1038/ncomms2038.

Pattanayak R, Muduli R, Panda RK, Dash T, Sahu P, Raut S, Panigrahi S (2016) Investigating the effect of multiple grain—grain interfaces on electric and magnetic properties of [50 wt % $BaFe_{12}O_{19}$—50 wt % $Na_{0.5}Bi_{0.5}TiO_3$] composite system. Physica B. 485: 67—77.

Pullar RC (2012) Hexagonal ferrites: A review of the synthesis, properties and applications of hexaferrite ceramics. Progress in Materials Science. 57: 1191—1334.

Saville B, Watson AA (1967) Structural characterization of sulfur-vulcanized rubber networks. Rubber Chemistry and Technology. 40: 100—149.

Sýkora R, Babayan V, Ušáková M, Kruželák J, Hudec I (2016) Rubber composite materials with the effects of electromagnetic shielding. Polymer Composites. 37(10): 2933—2939.

Tong, SY, Tung MJ, Ko WS, Huang YT, Wang YP, Wang LCh, Wu JM (2013) Effect of Ni fillers on microwave absorption and effective permeability of NiCuZn ferrite/Ni/polymer functional composites. Journal of Alloys and Compounds. 550: 39—45.

Vinayasree S, Soloman MA, Sunny V, Mohanan P, Kurian P, Anantharaman MR (2016) A microwave absorber based on strontium ferrite-carbon black-nitril rubber for S and X-band applications. Composites Science and Technology. 82: 69—75.

Wang YF, Li QL, Zhang CR, Jing HX (2009) Preparation and magnetic properties of different morphology nano-$SrFe_{12}O_{19}$ particles prepared by sol-gel method. Journal of Alloys and Compounds. 467: 284—287.

Warner WC(1994) Methods of devulcanization. Rubber Chemistry and Technology. 67: 559—566.

Xie T, Xu L, Liu Ch, Ding S, Yang J, Wu W (2013) Synthesis and adsorption properties of high specific area strontium ferrite from Industrial Strontium Residue. Vacuum. 93: 71—78.

sciendo

On local aromaticity of selected model aza-[n]circulenes (n = 6, 7, 8 and 9): Density functional theoretical study

Denisa Cagardová, Vladimír Lukeš, Ján Matúška, Peter Poliak

Faculty of Chemical and Food Technology, Slovak University of Technology in Bratislava, Radlinského 9, SK-812 37 Bratislava, Slovakia
denisa.cagardova@stuba.sk

Abstract: A computational study using density functional theory is reported for selected model aza[n]circulenes (n = 6, 7, 8 and 9) and their derivatives consisting of pyrrole and benzene units. Local aromaticity of central rings was discussed and analyzed using theoretical structural indices. Depending on their molecular structures, energies of the highest occupied and lowest unoccupied molecular orbitals change from –5.23 eV to –4.08 eV and from –1.97 eV to –0.41 eV, respectively. Based on B3LYP calculated optimal geometries, electronic structure of molecules and their charge transport properties resulted in the suggestion of three planar molecules containing three or four pyrrole units as potential candidates for p-type semiconductors. Hole drift mobilities for ideal stacked dimers of these potential semiconductors were calculated and they range from 0.94 $cm^2 \cdot V^{-1} \cdot s^{-1}$ to 7.33 $cm^2 \cdot V^{-1} \cdot s^{-1}$.

Keywords: aromaticity index, HOMED, hole mobility, molecular orbitals, reorganization energy

Introduction

Hydrocarbon [n]circulenes represent a group of fully conjugated polycyclic compounds characterized by a central ring with [n] sides surrounded by ortho-fused benzene rings (Hensel et al., 2015). Nowadays, synthesized [n]circulenes and their π-extended derivatives include bowl-shaped [4]circulene (Bharat et al., 2010) and [5]circulene (Barth and Lawton, 1996), planar [6]circulene (Scholl and Meyer, 1932), saddle-shaped [7]circulene (Yamamoto et al., 1983) and [8]circulene (Feng et al., 2013). Optimal geometries of all hydrocarbon [n]circulenes from [3]circulene to [20]circulene were theoretically predicted by Christoph and co-workers (Christoph et al., 2008), who described the dependence of strain energy on the enlargement of the [n]circulene structure compared to the energy of [6]circulene using the Density Functional Theory (DFT) to predict molecular structure and implied properties. On the other hand, the existence of [3]circulene is considered to be unfeasible.

Replacing outer fused benzene rings by heterocyclic rings results in planar condensed heterocyclic compounds with highly π-conjugated electronic structures which can eventually be used in many important applications (Huong et al., 2015). Octathio[8]circulene ($C_{16}S_8$), called "sulflower", is a promising compound for optoelectronic applications, where all fused benzene rings are replaced by eight fused thiophene rings. It was synthesized in 2006 for the first time (Chernichenko et al., 2006). This compound was found to be a promising p-type organic semiconductor by both experimental and theoretical approaches (Dadvand et al., 2008; Datta and Pati, 2007). Subsequently, electronic structure and charge transport properties of various tetra-hetero[8]circulenes have also been extensively studied (Mohakud and Pati, 2009; Gahungu et al., 2009; Huong et al., 2012). Among them, organic molecules as azatrioxa-, diazadioxa-, diazadithia-, diazadiselena-[8]circulenes and tetrabenzotetraaza[8]circulene (Xiong et al., 2017; Sakamoto and Suzuki, 2013) have also attracted considerable attention because of functional motifs based on the unique optical and electronic properties of pyrroles. All the above mentioned heterocyclic [8]circulenes were suggested as either p-type or n-type organic semiconducting materials.

The concept of aromaticity is fundamental to rationalize and understand the electronic structure of compounds containing fused benzene and heterocyclic rings. It has been studied and characterized by many theoretical and organic chemists. Electronic structure of aromatic molecules can be investigated and described using different experimental techniques and theoretical methods. From the theoretical point of view, DFT represents one of many chemical approaches for the quantification of electron structure of conjugated systems with moderate computational cost (Hohenberg and Kohn, 1964; Runge and Gross, 1984). The DFT method is convenient for the gas-phase optimal geometry investigation of large molecules because

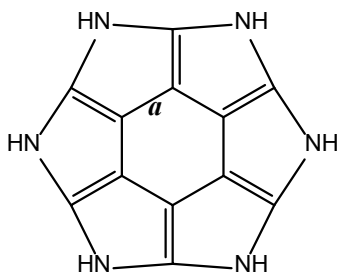

VI-N6

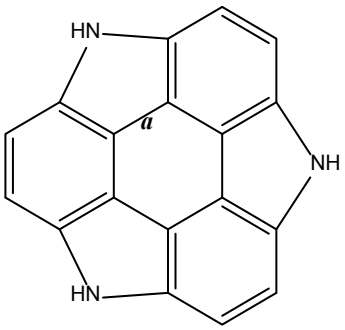

***VI-N3**

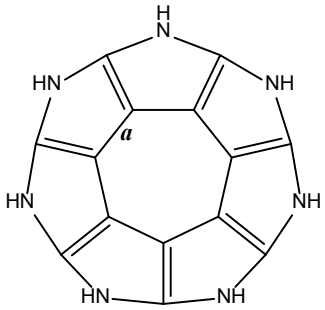

VII-N7

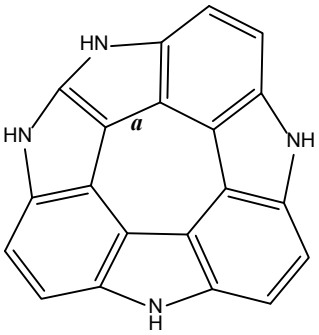

VII-N4

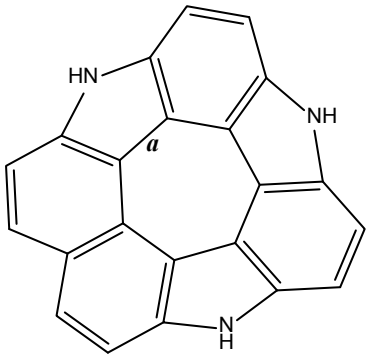

***VII-N3**

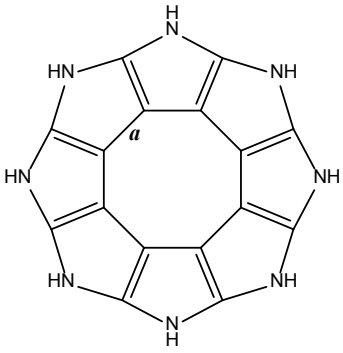

***VIII-N8**

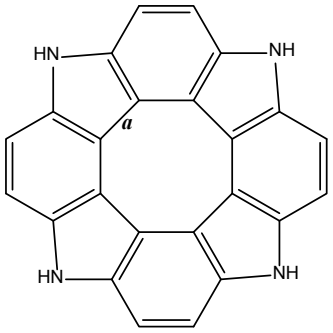

***VIII-N4**

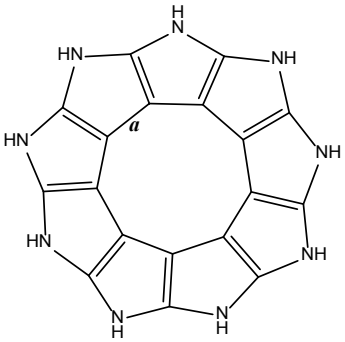

IX-N9

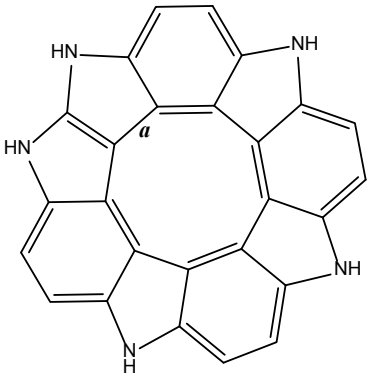

***IX-N5**

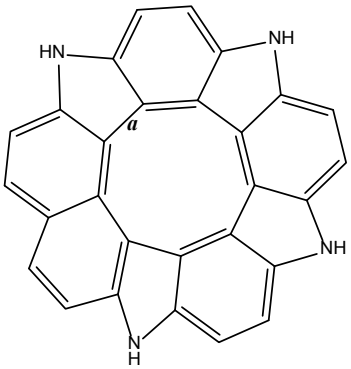

IX-N4

Fig. 1. Schematic structures of studied molecules and bond notation of central ring. Bonds (*a–i*) are ordered in clockwise direction. Asterisk symbol (*) indicates the planar B3LYP geometry.

it includes most effects of electron correlation. Although the electronic structure of various aza-[8] circulenes has been well characterized theoretically, systematic theoretical comparative study on model aza-[n]circulenes (n = 6, 7 and 9) and their derivatives is absent in literature.

With respect to this fact, we decided to present a theoretical analysis of electronic structures of the model series of ten aza-[n]circulenes (n = 6, 7, 8 and 9) and their derivatives (Fig. 1). Partial aims of this study are: (1) to calculate optimal geometries; 2) evaluate energies of frontier molecular orbitals and visualize their shapes and (3) calculate reorganization energies and drift mobilities. Consequently, the local aromaticity of central rings is discussed and hole mobilities are evaluated for selected model π-stacking configurations of dimers.

Quantum chemical calculations method

Quantum chemical calculations were performed using the Gaussian 09 program package (Frisch et al., 2010). Optimal geometries of the studied molecules were calculated by the DFT method with B3LYP (Becke's three parameter Lee—Yang—Parr) (Lee et al., 1988; Becke, 1988) functional without any constraints with the energy cut-off of 10^{-5} kJ · mol^{-1} and final RMS energy gradient below 0.01 kJ · mol^{-1} · A^{-1}. For open-shell systems, such as cations and anions, the unrestricted formalism (UB3LYP) was used. The SVP/SVPFit basis set of atomic orbitals was applied for all atoms (Eichkorn et al., 1995; Eichkorn et al., 1997). Next, the basis set for nitrogen atoms was minimally augmented with diffuse s- and p- functions by the set of diffusion functions in a systematic way (exponents of functions set to 1/3 of the exponent of the lowest function in the non-augmented basis set) (Zheng et al., 2011). Optimized structures were confirmed to be stable by vibrational analysis (no imaginary vibrations). For the model π-dimers, the interaction energy was corrected on Basis Set Superposition Error (BSSE) (Boys and Bernardi, 1970) using the Counterpoise method (Simon et al., 1996; Xantheas et al., 1996) and the B3LYP-D functional including the Grimme's dispersion D3 corrections on the van der Waals interactions was used (Grimme et al., 2010). The corresponding keyword in Gaussian input was GD3BJ. Molecules and molecular orbitals were visualized using the Molekel program package (Flukiger et al.; 2002).

Strain energies of the molecules were calculated to characterize structure modification of molecules in comparison with fixed planar structure, which is defined as the difference between electronic B3LYP energy of optimal geometry and electronic B3LYP energy of planar geometry with fixed atom arrangement.

One possible way of central ring aromaticity quantification is to express the geometrical changes of carbon-carbon bond lengths with respect to the structural changes using the Harmonic Oscillator Model of Electron Delocalization (HOMED) index (Frizzo and Martins, 2012)

$$\mathrm{HOMED} = 1 - \frac{\alpha}{j}\left\{\sum_{i=1}^{j}\left(R_{\mathrm{ref}} - R_{\mathrm{i}}\right)^2\right\} \tag{1}$$

where j represents the number of bonds considered and R_{i} is the actual carbon-carbon bond length (see Tab. 1). The B3YPL/SVP/SVPFit optimized reference carbon-carbon bond length (R_{ref}) obtained from the benzene molecule is of 1.3988 Å. The normalization constant, α, was calculated using the following equation (Ośmiałowski et al., 2006)

$$\alpha = 2\left\{\left(R_{\mathrm{ref}} - R_{\mathrm{sin}}\right)^2 + \left(R_{\mathrm{ref}} - R_{\mathrm{doub}}\right)^2\right\}^{-1} \tag{2}$$

where the reference single bond R_{sin} and the reference double bond R_{doub} were estimated from ethane and ethene molecules respectively. Our calculated single C—C and double C═C bond lengths were 1.5277 Å and 1.3330 Å, respectively. Based on these bond lengths, the normalization constant is of 95.6 Å^{-2}.

Internal reorganization energy ($\lambda^{\pm}$) is another important quantity describing structural changes in molecules upon electron abstraction or addition. These energies refer to the energy required for geometry relaxation from the electroneutral to charged state of molecule and *vice versa* (Brédas et al., 2004; Wang et al., 2014; Da Silva Filho et al., 2005; Marcus, 1993). Based on the optimized electroneutral molecule and cation/anion geometries, reorganization energies are given by the equation

$$\begin{aligned}\lambda^{\pm} &= \lambda_1^{\pm} + \lambda_2^{\pm} = \\ &= \left[E_{\pm}(Q_N) - E_{\pm}(Q_{\pm})\right] + \left[E_N(Q_{\pm}) - E_N(Q_N)\right]\end{aligned} \tag{3}$$

where $E_{\pm}(Q_N)$ is the total energy of charged state in the electroneutral geometry, $E_{\pm}(Q_{\pm})$ is the total energy of the charged state in the charged state geometry, $E_N(Q_{\pm})$ is the total energy of the neutral state in the charged state geometry, and $E_N(Q_N)$ is the total energy of the electroneutral state in the neutral geometry (Malagoli et al., 2004; Brédas et al., 2004).

To describe conductive properties, the hole-transfer rate, k_{hole}, between two interacting subsystems can be evaluated using classical Marcus formula (Marcus, 1993; Sakanoue et al., 1999; Malagoli and Brédas, 2000)

Tab. 1. Selected B3LYP/SVP/SVPFit optimal bond lengths (in Ångstroms) and HOMED parameters of central rings of all studied molecules.

Molecule	*a*	*b*	*c*	*d*	*e*	*f*	*g*	*h*	*i*	HOMED
VI-N3	1.3773	1.3572	1.3773	1.3573	1.3772	1.3572				0.8950
VII-N3	1.4057	1.3839	1.4259	1.4204	1.4205	1.4258	1.3839			0.9606
VII-N4	1.3940	1.4332	1.4055	1.4332	1.3940	1.4130	1.4130			0.9610
VIII-N4	1.4151	1.4409	1.4151	1.4410	1.4151	1.4409	1.4151	1.4410		0.9026
IX-N4	1.4677	1.4877	1.4444	1.4597	1.4311	1.4597	1.4444	1.4877	1.4676	0.5979
IX-N5	1.4680	1.4533	1.4870	1.4533	1.4680	1.4249	1.4453	1.4453	1.4249	0.6926
VI-N6	1.4641	1.4389	1.4389	1.4641	1.4389	1.4389				0.7621
VII-N7	1.4378	1.4378	1.4303	1.4483	1.4283	1.4484	1.4301			0.8529
VIII-N8	1.3624	1.3625	1.3624	1.3625	1.3624	1.3625	1.3624	1.3625		0.8734
IX-N9	1.4300	1.4274	1.4278	1.4296	1.4259	1.4320	1.4249	1.4323	1.4257	0.9159

$$k_{hole} = t^2 \left(\frac{\pi}{\hbar^2 k_B \lambda^+ T} \right)^{1/2} \exp\left(-\frac{\lambda^+}{4 k_B T} \right) \quad (4)$$

where t represents an intermolecular hole-transfer integral between the interacting molecular sites, $\hbar$ is the reduced Planck constant, k_B is the Boltzmann constant, T is the thermodynamic temperature and λ^+ represents the hole reorganization energy. The hole-transfer integrals for optimal dimer geometries were calculated in the one-electron approximation using the direct evaluation method (Nan et al., 2011).

At constant temperature, the hole drift mobility, μ_{hole}, can be calculated by the Einstein—Smoluchowski relation (Maier and Ankerhold, 2010; Cornil et al., 2002)

$$\mu_{hole} = \frac{e}{k_B T} \frac{1}{2m} k_{hole} d^2 \quad (5)$$

where e is the elementary charge. The length of hopping pathway, d, is defined as the centroid-to-centroid distance. Symbol m stands for space dimensionality and k_{hole} is the hole-transfer rate. Considering a two-dimensional transfer, m value equals 2.

Results and Discussion

Chemical structure

Chemical structure of the investigated molecules depends on the size of their central ring as well as on the number of outer heterocyclic units. According to the notation in Fig. 1, symmetric [n]aza-[n]heterocirculenes containing [n] pyrrole units (n = 6, 7 and 9) are distorted and exhibit bowl-shaped structures (**VI-N6, VII-N7** and **IX-N9**, respectively). Within the group of studied [n]aza-[n]heterocirculenes, the **VIII-N8** molecule is planar. Only the **IX-N4** molecule shows a saddle-shaped optimal geometry. Interestingly, theoretical results obtained for fully [n]thiophenyl-[n]circulenes showed planarity and minimal strain energy for molecules containing eight and nine thiophene rings (Chernichenko et al., 2006). In case of the remaining investigated molecules, separation of pyrrole units by benzene ring supports the planarity for almost all [n/2]aza[n]circulenes (n = 6, 8). The theoretically predicted planar structure of the **VIII-N4** molecule is in agreement with the X-ray structure of alkyl substituted tetraaza-[8]circulene (Nagata et al., 2017). The largest **IX-N5** molecule is planar because of two condensed pyrrole rings which results in the strain decrease in the central ring compared with **IX-N4**. Interestingly, planarity of **VII-N3** is caused by two condensed benzene rings in its structure. Generally, planarity of a molecule is supported by lower strain in the structure characterized by strain energies and dihedral angles. Strain energies, ΔE_s, calculated with respect to the fixed planar geometries changed from 57.3 kJ·mol^{-1} to 210 kJ·mol^{-1} for the bowl-type structures (Fig. 2). Only one molecule, **IX-N4,** exhibited the saddle-type structure and the corresponding strain energy was 17.6 kJ·mol^{-1}. Dihedral angles studied are defined by three atoms from the central ring characterizing one plane, the fourth atom is carbon in fused pyrrole rings (see Fig. 2). Bowl-shaped molecule **VI-N6** provides the smallest range of dihedral angles (118—126 °) and so it is obvious that this molecule has the most significant strain (with strain energy of 210 kJ·mol^{-1}) compared with its fixed planar structure. On the other hand, in case of the **IX-N9** molecule, dihedral angles are in the range from 143 ° to 153 ° and its strain energy is of 57.3 kJ·mol^{-1}, which means that this molecule is not significantly deformed related to the planar structure.

Although the pyrrole and benzene building units have aromatic character, central rings of the studied aza-[n]circulenes do not have to be aromatic. The

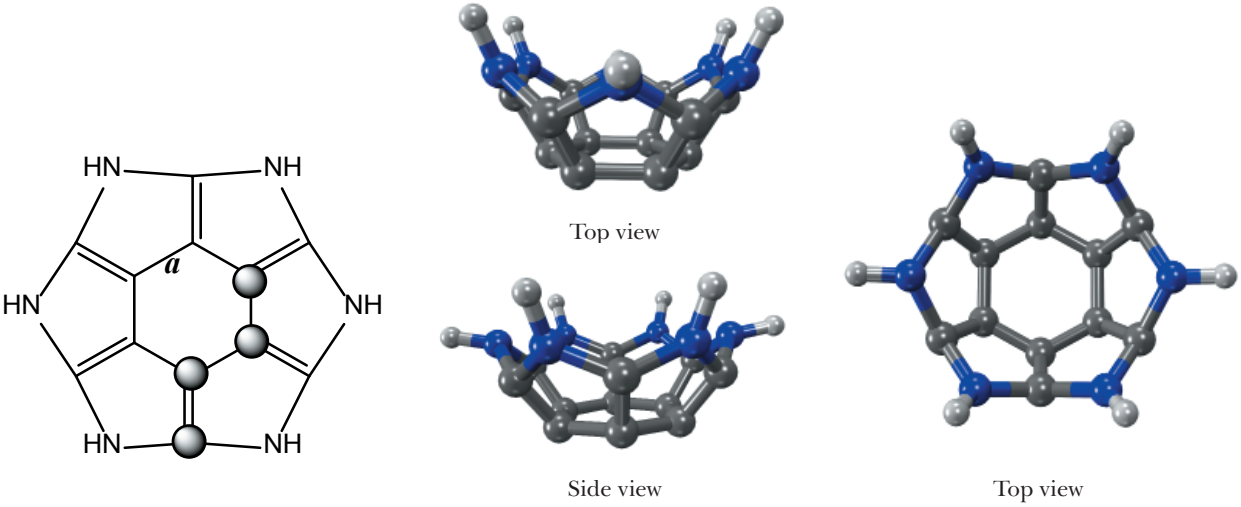

VI-N6 (ΔE_s = 210.0 kJ · mol^{-1}; ϑ = 118–126 °)

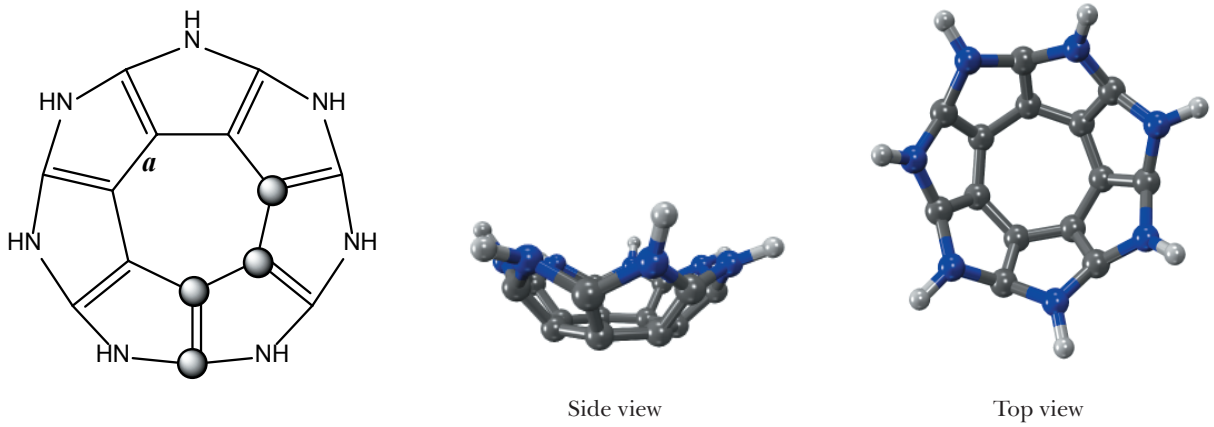

VII-N7 (ΔE_s = 165.4 kJ · mol^{-1}; ϑ = 127–135 °)

VII-N4 (ΔE_s = 196.5 kJ · mol^{-1}; ϑ = 142–161 °)

Fig. 2. Front and side views of the investigated non-planar molecules. B3LYP strain energies ΔE_s and dihedral angles ϑ are written in parentheses. Grey balls (on left) symbolize carbon atoms providing a dihedral angle ϑ. Corresponding colors of atoms: black – carbon, white – hydrogen, blue – nitrogen.

HOMED parameters evaluated for the central molecular rings of the studied molecules exhibit differences in the π-electron delocalization. An increase of the HOMED index is related to significant increase of π-electron delocalization in molecular structures. Comparison of the HOMED parameters collected in Tab. 1 shows that **VII-N3** and **VII-N4** molecules exhibit the highest HOMED values of 0.96. On the other hand, the less aromatic character (HOMED = 0.60) results in the saddle-shaped **IX-N4** molecule. Interestingly, molecular planarity does not depend on the aromaticity of the central ring.

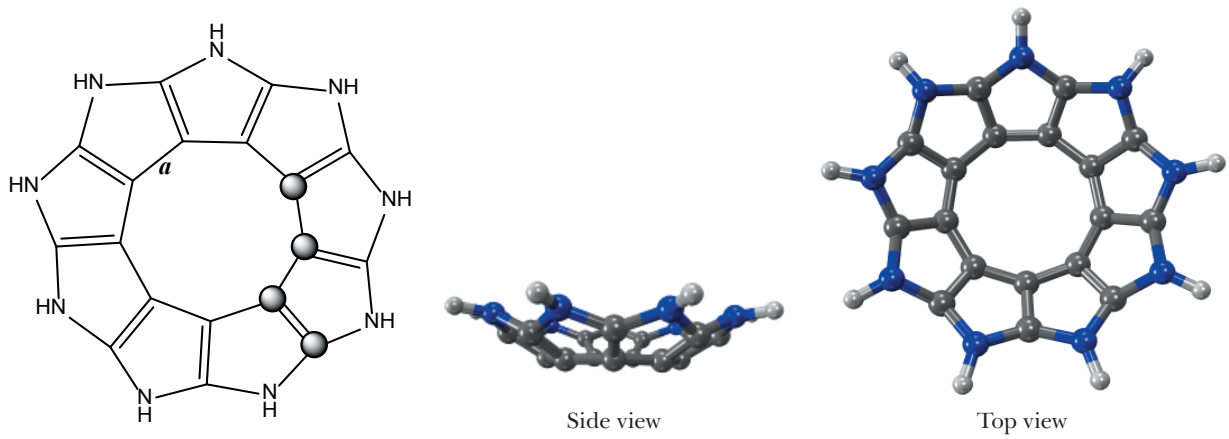

IX-N9 (ΔE_s = 57.3 kJ · mol^{-1}; ϑ = 143—153 °)

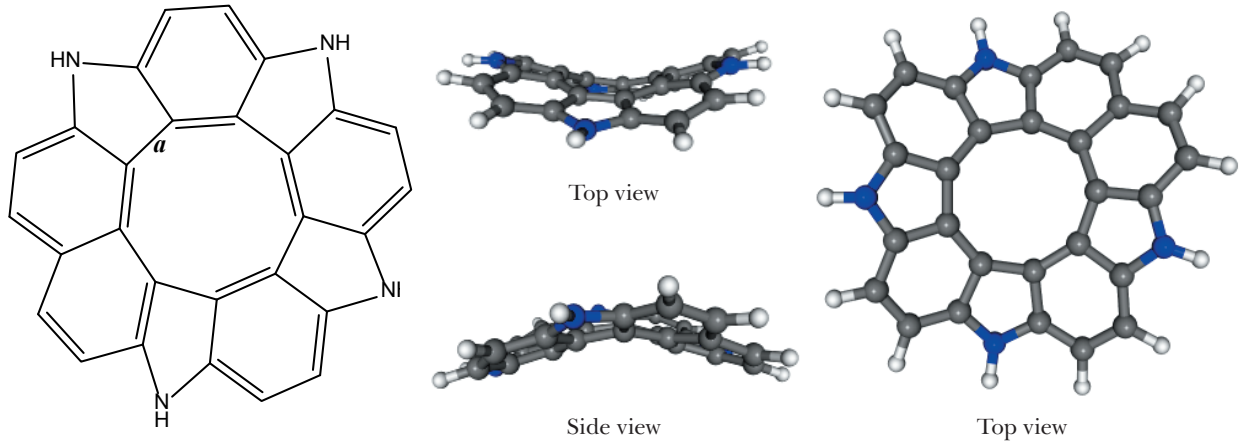

IX-N4 (ΔE_s = 17.6 kJ · mol^{-1})

Fig. 2. (continued) Front and side views of the investigated non-planar molecules. B3LYP strain energies ΔE_s and dihedral angles ϑ are written in parentheses. Grey balls (on left) symbolize carbon atoms providing dihedral angle ϑ. Corresponding colors of atoms: black — carbon, white — hydrogen, blue — nitrogen.

Calculated values of energy parameters for both charged states are listed in Tab. 2. For planar molecules, the B3LYP hole reorganization energy, λ^+, connected with the formation of cationic state varies from 0.144 eV for **IX-N5** to 0.332 eV for **VII-N3**. In case of bowl-shaped molecules, the **VII-N7** molecule has the highest value of λ^+ (0.713 eV). The saddle shaped molecule **IX-N9** provides the hole reorganization energy of 0.638 eV. In case of anionic state formation, the electron reorganization energies, λ^-, change from 0.167 eV for the planar **VIII-N8** molecule to 0.685 eV for the bowl-shaped **VI-N6** molecule. The hole reorganization energy decreases as the size of the π-conjugated system increases. The presented results are in good agreement with the general trends suggested in literature. For example, the calculated intramolecular hole reorganization energy for an isolated tetracene is of 0.114 eV (Da Silva Filho et al., 2005), which is nearly by 30 % lower than that of the rubrene molecule (0.159 eV) containing four perpendicularly oriented phenyl rings. However, these values remain significantly lower than that of bis-(triarylamine) derivative of tetraphenyl-diamino-biphenyl (TPD) (0.290 eV) (Malagoli et al., 2004), a well-established hole-transport material. The low electron reorganization energy of fullerenes can also be attributed to their extended π-conjugation and their rigid molecular structures. For example, the C_{60} molecule has been found to be an excellent n-type acceptor with low electron reorganization energy of 0.060 eV (Larsson et al., 1998). On the other hand, theoretical B3LYP λ^- values reported for donor-acceptor 1,8-naphthalimide derivatives are of 0.216—0.235 eV (Chai and Jin, 2016). For a smaller fluorinated pentacene, the electron reorganization energy is of 0.246 eV (Lukeš et al., 2018) and for tris(8-hydroxyquinolinato)aluminum (Alq_3) it is of 0.296 eV (Friederich et al., 2016).

Table 2: Vertical ionization potentials (*VIP*), adiabatic ionization potentials (*AIP*), vertical electron affinities (*VEA*), adiabatic electron affinities (*AEA*), reorganization energies for hole and electron transfer (λ^+ and λ^-, respectively) of studied molecules. All energies are in eV. Asterisks (*) indicate planar molecules.

Molecule	*VIP*	*AIP*	*VEA*	*AEA*	λ^+	λ^-
***VI-N3**	6.727	6.640	–0.593	–0.471	0.181	0.245
***VII-N3**	6.400	6.150	–0.156	–0.055	0.332	0.205
VII-N4	6.279	6.014	–0.278	–0.114	0.421	0.339
***VIII-N4**	6.309	6.233	0.237	0.329	0.149	0.184
IX-N4	5.923	5.830	0.058	0.185	0.176	0.262
***IX-N5**	5.614	5.542	–0.291	–0.200	0.144	0.183
VI-N6	6.259	5.958	0.368	0.793	0.598	0.685
VII-N7	6.233	5.880	–0.040	0.268	0.713	0.606
***VIII-N8**	5.646	5.537	–0.250	–0.169	0.220	0.167
IX-N9	5.480	5.136	–0.829	–0.620	0.638	0.645

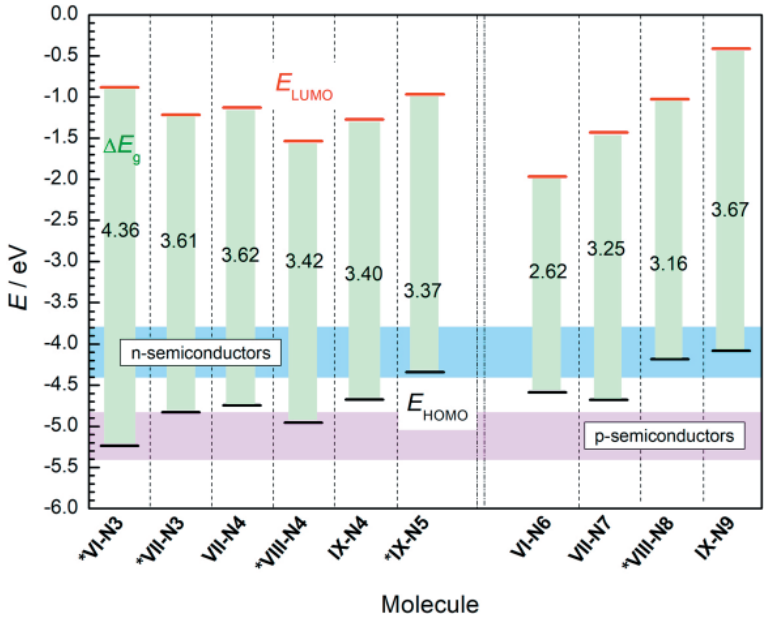

Fig. 3. Energy diagram of B3LYP/SVP frontier molecular orbitals for electroneutral states of studied molecules. HOMO—LUMO energy gaps ΔE_g (green band) are in eV. Asterisks (*) indicate planar molecules.

Frontier molecular orbitals

Energy levels of frontier molecular orbitals have direct influence on the carrier injection ability and oxidation stability of the material. Based on the B3LYP/SVP optimized structures of the electroneutral state, energy levels of the Highest Occupied (HOMO) and Lowest Unoccupied (LUMO) Molecular Orbitals were calculated. The obtained results and corresponding energy gaps (ΔE_g) for all molecules are depicted in Fig. 3. Enlargement of molecular structures with respect to the number of building aromatic units significantly affects the energy of frontier molecular orbitals. However, there is no significant trend. In Fig. 3, the depicted blue bars represent LUMO energies within the energy interval from –4.4 eV to –3.8 eV, which are suitable to stabilize electrons during charge transfer in electron transport materials (Liu et al., 2010; Chang et al., 2010; Murphy and Fréchet, 2007). Our theoretical calculations showed that LUMO energies vary between –2.0 eV and –0.4 eV. These values do not meet the above-mentioned criteria; thus it is not an optimal setting for n-type semiconductivity.

On the other hand, the depicted pink bars indicate the range of HOMO energy values typical for commercial p-type organic semiconductors. For example, the reported HOMO energies of

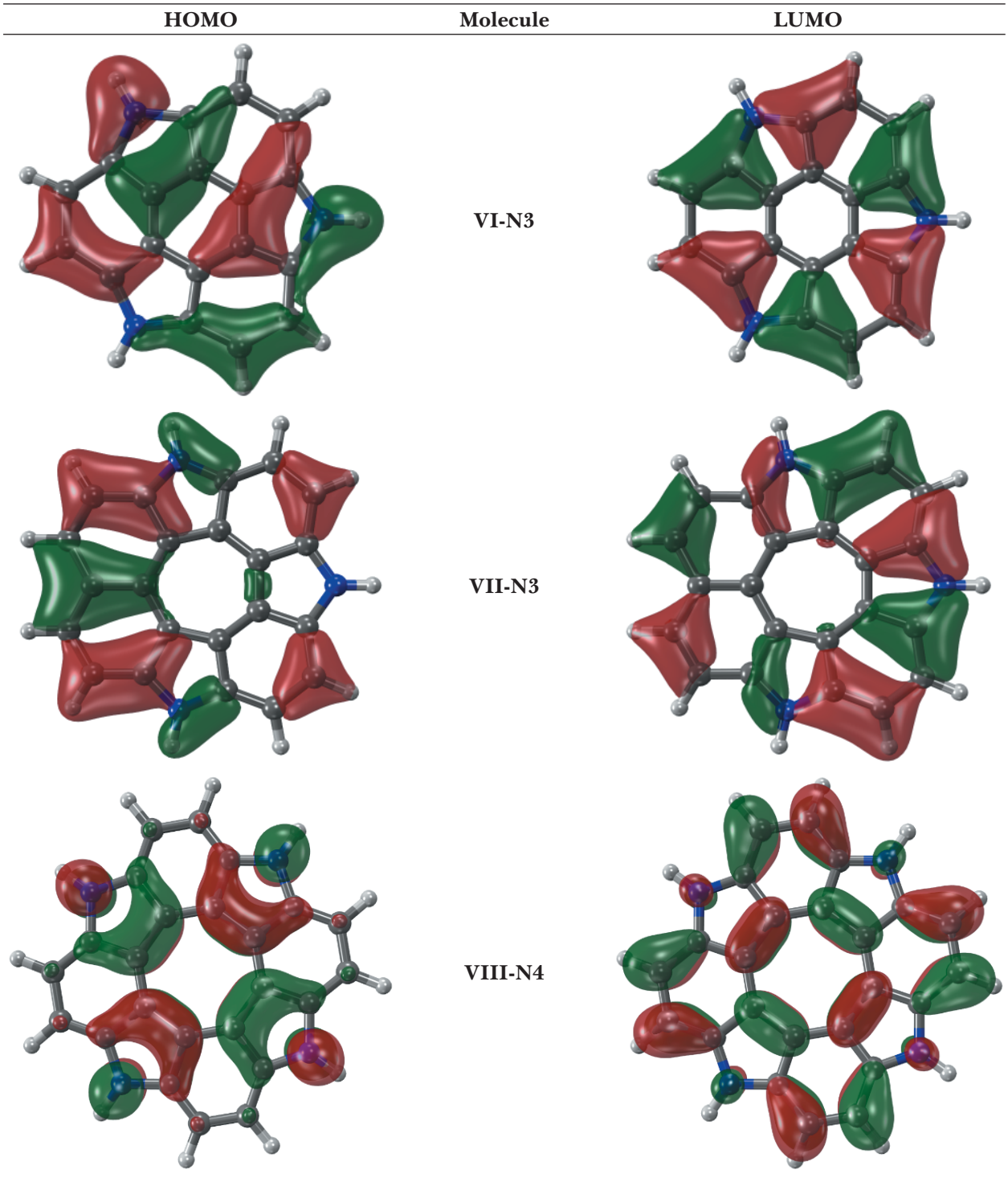

Fig. 4. Shapes of B3LYP frontier molecular orbitals for selected electroneutral planar molecules **VI-N3**, **VII-N3** and **VIII-N4**. Corresponding colors of atoms: black — carbon, white — hydrogen, blue — nitrogen. Depicted iso-surface value is 0.025 a.u.

α-sexithiophene and pentacene are of –5.3 eV and –5.0 eV (Sigma Aldrich, 2019), respectively. In case of the smallest planar **VI-N3** molecule, the B3LYP HOMO energy is of –5.26 eV and it is the lowest HOMO energy compared with the remaining studied molecules. The corresponding LUMO energy is of –0.90 eV. The maximal value of HOMO is of –4.10 eV for the saddle-shaped **IX-N9** molecule. Based on our results, HOMO energies of **VII-N3**, **VIII-N4** and **VI-N3** fall within the interval of HOMO energies typical for p-semiconductors (see Fig. 3).

The HOMO–LUMO energy gap (ΔE_g) value represents a theoretical parameter which corresponds to the electrochemical gap. The B3LYP/SVP ΔE_g energy is the highest for the smallest planar molecule **VI-N3** (4.36 eV) and the lowest for the bowl-shaped **VI-N6** molecule (2.62 eV).

With respect to the above-mentioned criteria, molecules **VII-N3**, **VIII-N4** and **VI-N3** could be used as potential p-type semiconductors because of their low reorganization energies and their HOMO energies falling within the interval typical for p-semiconductor LUMO energies. Moreover, planarity of these molecules supports their potential application in optoelectronics.

Shapes of frontier molecular orbitals of selected planar **VII-N3**, **VIII-N4** and **VI-N3** molecules reveal the typical π-type molecular orbital character. As it is demonstrated in Fig. 4 for the above-mentioned promising molecules, the lobes of HOMO for larger **VII-N3** and **VIII-N4** molecules

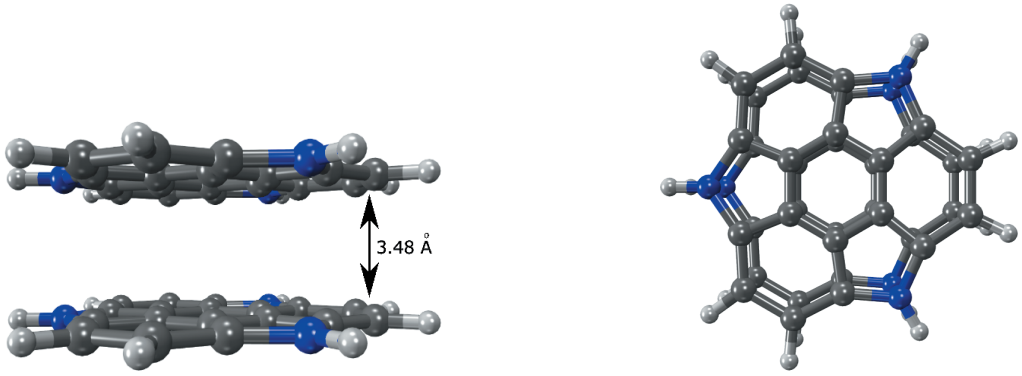

Side view Top view

VI-N3 (ΔE_{int}= –16.7 kJ · mol^{-1})

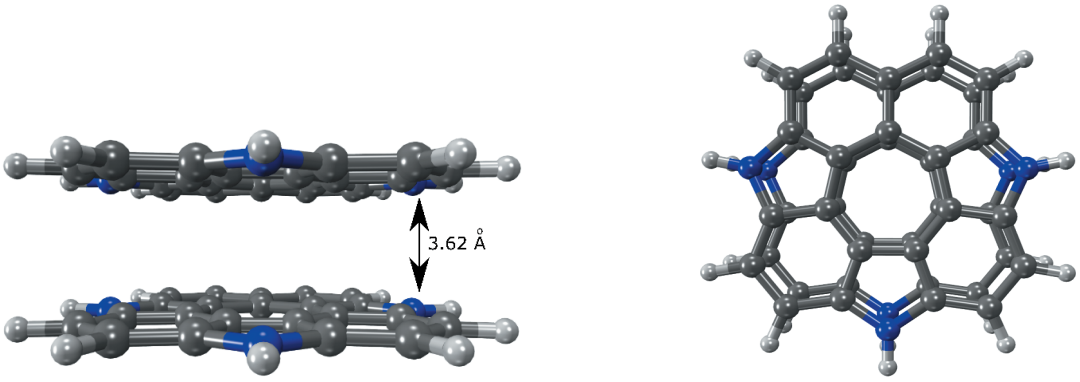

Side view Top view

VII-N3 (ΔE_{int}= –60.7 kJ · mol^{-1})

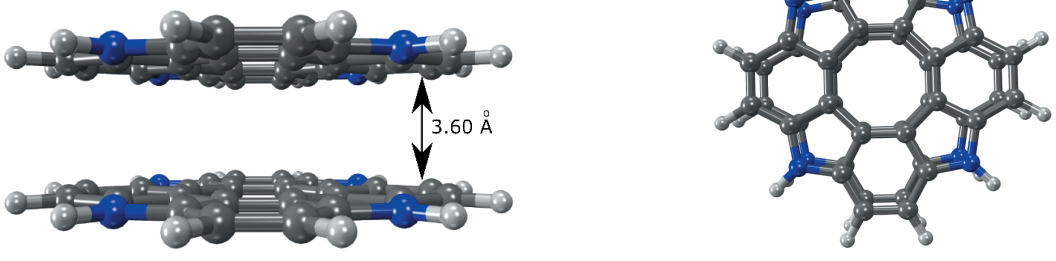

Side view Top view

VIII-N4 (ΔE_{int}= –44.0 kJ · mol^{-1})

Fig. 5. Side and top views of optimal geometries of model sandwich dimer configurations of **VI-N3**, **VII-N3** and **VIII-N4**. Counterpoise corrected B3LYP-D interaction energies ΔE_{int} are written in parentheses. Corresponding colors of atoms: black — carbon, white — hydrogen, blue — nitrogen.

are spoke-wheel oriented towards the central ring. Probably, the different shape of electron delocalization in the smallest **VI-N3** molecule is related to lower aromaticity of its central ring (see Tab. 1). A similar situation occurs in the delocalization of LUMO clouds where electrons are depleted from nitrogen atoms of pyrrole units. Interestingly, an increase of central ring HOMED causes a decrease of energy gaps of molecules.

Electrochemical properties of the investigated organic molecules as well as their air stability are also proportionally related to their ionization potentials (*IPs*) and electron affinities (*EAs*). These quantities are commonly used for the interpretation of electric solid-state experiments. According to previous studies, the adiabatic *IP* (*AIP*) of the selected air-stable p-type materials ranges from 5.9 eV to 6.8 eV, while the adiabatic *EA* (*AEA*) for the air-stable n-type ones should be lower than 4.0 eV but higher than 2.8 eV (Liu et al., 2010; Chang et al., 2010). The comparison of vertical ionization potentials (*VIP*), vertical electron affinities (*VEA*), adiabatic ionization potentials (*AIP*) and adiabatic electron affinities (*AEA*) listed in Tab. 2 supports the findings obtained from the analysis of energies of frontier molecular orbitals. The studied molecules are unsuitable organic n-semiconductors. However, the planar **VII-N3**, **VIII-N4** and **VI-N3** molecules could be perspective as p-type semiconductors.

Electric mobilities

Macroscopic properties of solid materials strongly depend on the internal molecular structure. However, it is impossible to calculate the exact value of microscopic electric quantities because they represent the statistical average value of local molecular assemblies. To estimate and compare the p-type semiconducting properties of selected perspective molecules (**VII-N3**, **VIII-N4** and **VI-N3**), model dimers in perfectly parallel-stacked configuration were investigated. As it is indicated in Fig. 5, the optimal intermolecular distances between molecular planes are of 3.48 Å, 3.60 Å and 3.62 Å for **VI-N3**, **VIII-N4** and **VII-N3** sandwich dimers, respectively. The corresponding interaction energies are of –16.7 kJ · mol^{-1} for **VI-N3**, –60.7 kJ · mol^{-1} for **VII-N3** and –44.0 kJ · mol^{-1} for **VIII-N4**.

Hole-transfer integrals reach values of 0.302 eV for **VI-N3**, 0.253 eV for **VII-N3** and 0.216 eV for **VIII-N4**. Consequently, according to equation (4), the hole-transfer rates are of 6.15 × 10^{14} s^{-1} for **VI-N3**, 0.74 × 10^{14} s^{-1} for **VII-N3** and 4.78 × 10^{14} s^{-1} for **VIII-N4**.

The drift hole mobilities evaluated by equation (5) for optimal geometries at T = 298 K are 7.33 cm^2 · V^{-1} · s^{-1} for **VI-N3**, 0.94 cm^2 · V^{-1} · s^{-1} for **VII-N3** and 6.02 cm^2 · V^{-1} · s^{-1} for **VIII-N4**. Additionally, the hole drift mobilities dependence on the distance between planes in the vicinity of the minimal interaction energy of an ideal dimer, i.e. d between 3 to 4 Å, was studied because the displacement between the molecular units can vary in real solid materials. As it is illustrated in Fig. 6, exponential decrease of the hole drift mobilities occurred given by:

$$\mu_{hole} = A\exp(-Bd) \tag{6}$$

Correlation coefficients of the fitted function are above 0.999. The lowest value of the preexpo-

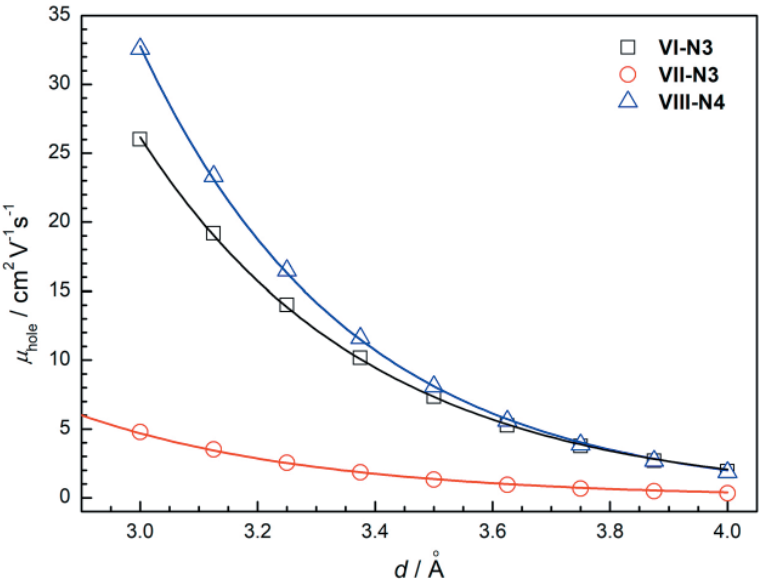

Fig. 6. Dependence of hole electric mobilities on the distance for promising model dimers of **VI-N3**, **VII-N3** and **VIII-N4**.

nential factor *A* was found for the **VII-N3** dimer and its value is of (7.7 ± 0.6) × 10^3 $cm^2 \cdot V^{-1} \cdot s^{-1}$. These values for **VI-N3** and **VIII-N4** dimers are of (54 ± 4) × 10^3 $cm^2 \cdot V^{-1} \cdot s^{-1}$ and (14 ± 1) × 10^4 $cm^2 \cdot V^{-1} \cdot s^{-1}$, respectively. Exponent arguments *B* (in $Å^{-1}$) are of 2.47 ± 0.03 for the **VII-N3** dimer, 2.54 ± 0.02 for the **VI-N3** dimer and 2.79 ± 0.03 for the **VIII-N4** sandwich dimer. It seems that the magnitude order of obtained values is comparable with the theoretical and experimental values reported in literature for hole mobility of typical organic p-type semiconductors. For example, the hole drift mobility simulated for perfect coronene and pentacene stacks were found to be 14.93 $cm^2 \cdot V^{-1} \cdot s^{-1}$ (Bag and Maiti, 2017) and 12.54 $cm^2 \cdot V^{-1} \cdot s^{-1}$ (Lukeš et al., 2018), respectively. However, experimental results for pentacene film layers are between 0.3 and 3.0 $cm^2 \cdot V^{-1} \cdot s^{-1}$ depending on the temperature and construction of field-effect transistors (Lin et al., 1997; Yakuphanoglu et al., 2012).

Conclusions

Ten model aza-[n]circulenes (n = 6, 7, 8 and 9) and their derivatives were studied at the density functional theory level. The obtained theoretical data show that local aromaticity of the central ring is strongly dependent on the number of benzene and pyrrole units and on their mutual position. The minimal steric repulsion among the aryl rings were found for the **VI-N3**, **VII-N3**, **VIII-N4**, **VIII-N8** and **IX-N5** molecules. Depending on the molecular structure, energies of the highest occupied and lowest unoccupied molecular orbitals change from –5.23 eV to –4.08 eV and from –1.97 eV to –0.41 eV, respectively. A comparison of frontier molecular orbital energies, ionization potentials and electron affinities with data for typical organic semiconductors showed that none of the studied molecules are suitable to be n-type semiconductors. On the other hand, based on the calculated electric properties, planar **VII-N3**, **VIII-N4** and **VI-N3** molecules are potential p-type semiconductors. For perfect-stacked sandwich dimers at optimal centroid-to-centroid distance, the hole drift mobility evaluated is maximal for **VI-N3** with the value of 7.33 $cm^2 \cdot V^{-1} \cdot s^{-1}$. Molecule **VII-N3** provides significantly lower hole drift mobility of 0.94 $cm^2 \cdot V^{-1} \cdot s^{-1}$.

Acknowledgment

The work has been supported by the Slovak Research and Development Agency (APVV-15-0053). The authors would like to thank for financial contribution from the STU Grant scheme for the Support of Young Researchers (1619). We are grateful to the HPC center at the Slovak University of Technology in Bratislava, which is a part of the Slovak Infrastructure of High Performance Computing (SIVVP project, ITMS code 26230120002, funded by the European region development funds, ERDF) for the computational time and resources made available.

References

Bag S, Maiti PK (2017) Phys. Rev. B 96(24): 245401. Doi: https://doi.org/10.1103/PhysRevB.96.245401.

Barth WE, Lawton RG (1966) J. Am. Chem. Soc. 88:380. Doi: https://doi.org/10.1021/ja00954a049.

Becke AD (1988) Phys Rev A 38: 3098—3100. Doi: https://doi.org/10.1103/PhysRevA.38.3098.

Bharat, Bhola, R, Bally T, Valente A, Cyrański MK, Dobrzycki Ł, Spain SM, Rempała P, Chin MR, King BT (2010) Angew. Chem. Int. Ed. 49: 399. Doi: https://doi.org/10.1002/anie.200905633.

Boys SF, Bernardi F (1970) Mol Phys 19: 553—566. Doi: https://doi.org/10.1080/00268977000101561.

Brédas JL, Beljonne D, Coropceanu V, Cornil J (2004) Chem Rev 104: 4971—5003. Doi: https://doi.org/10.1021/cr040084k.

Chai W, Jin R (2016) J. Mol. Struct. 1103: 177—182. Doi: https://doi.org/10.1016/j.molstruc.2015.09.023.

Chang YC, Kuo MY, Chen CP, Lu HF, Chao I (2010) J. Phys. Chem. C. 114: 11595—11601. Doi: https://doi.org/10.1021/jp1025625.

Chernichenko KY, Sumerin VV, Shpanchenko RV, Balenkova ES and Nenajdenko G (2006) Angew. Chem. 45(44): 7367—7370. Doi: https://doi.org/10.1002/anie.200602190.

Christoph H, Grunenberg J, Hopf H, Dix I, Jones PG, Scholtissek M, Maier G (2008) Chem. Eur. J. 14: 5604. Doi: https://doi.org/10.1002/chem.200701837.

Cornil J, Lemaur V, Calbert JP, Brédas JL (2002) Adv Mater 14: 726. Doi: https://doi.org/10.1002/1521-4095(200107)13:14<1053::AID-ADMA1053>3.0.CO;2-7.

Da Silva Filho DA, Kim EG, Brédas JL (2005) Adv. Mater. 17: 1072—1076. Doi: https://doi.org/10.1002/adma.200401866.

Dadvand A, Cicoira F, Chernichenko YK, Balenkova ES, Osuna RM, Rosei F, Nenajdenko VG, Perepichka DF (2008) Chem. Commun. 42: 5354—5356. Doi: https://doi.org/10.1039/B809259A.

Datta A, Pati SK (2007) J. Phys. Chem. C 19: 4487—4490. Doi: https://doi.org/10.1021/jp070609n.

Eichkorn K, Treutler O, Ohm H, Haser M, Ahlrichs R (1995) Chem. Phys. Lett., 240: 283—289. Doi: https://doi.org/10.1016/0009-2614(95)00621-A.

Eichkorn K, Weigend F, Treutler O, Ahlrichs R (1997) Theor. Chem. Acc. 97: 119—124. Doi: https://doi.org/10.1007/s002140050244.

Feng CN, Kuo MY, Wu YT (2013) Angew. Chem. Int. Ed. 52: 7791. Doi: https://doi.org/10.1002/anie.201303875.

Flukiger P, Luthi HP, Sortmann S, Weber J (2002) Molekel 4.3, Swiss National Supercomputing Centre, Manno, Switzerland.

Friederich P, Meded V, Poschlad A, Neumann T, Rodin V, Stehr V, Symalla F, Danilov D, Lüdemann G, Fink RF, Kondov I, von Wrochem F, Wenzel W (2016)

Adv. Funct. Mater. 26: 5757—5763. Doi: https://doi.org/10.1002/adfm.201601807.
Frisch MJ, Trucks GW, Schlegel HB, Scuseria GE, Robb MA, Cheeseman JR, Scalmani G, Barone V, Mennucci B, Petersson GA, Nakatsuji H, Caricato M, Li X, Hratchian HP, Izmaylov AF, Bloino J, Zheng G, Sonnenberg JL, Hada M, Ehara M, Toyota K, Fukuda R, Hasegawa J, Ishida M, Nakajima T, Honda Y, Kitao O, Nakai H, Vreven T, Montgomery JA Jr., Peralta JE, Ogliaro F, Bearpark M, Heyd JJ, Brothers E, Kudin KN, Staroverov VN, Keith T, Kobayashi R, Normand J, Raghavachari K, Rendell A, Burant JC, Iyengar SS, Tomasi J, Cossi M, Rega N, Millam JM, Klene M, Knox JE, Cross JB, Bakken V, Adamo C, Jaramillo J, Gomperts R, Stratmann RE, Yazyev O, Austin AJ, Cammi R, Pomelli C, Ochterski JW, Martin RL, Morokuma K, Zakrzewski VG, Voth GA, Salvador P, Dannenberg JJ, Dapprich S, Daniels AD, Farkas O, Foresman JB, Ortiz JV, Cioslowski J, Fox DJ (2009) Gaussian 09, Revision D.01, Gaussian Inc. Wallingford CT, Gaussian 09 Revis. C.01. (2010) Gaussian Inc., Wallingford CT. Doi: https://doi.org/10.1017/CBO9781107415324.004.
Frizzo CP, Martins MAP (2012) Struct Chem 23: 375—380. Doi: https://doi.org/10.1007/s11224-011-9883-z.
Gahungu G, Zhang J, Barancira T (2009) J. Phys. Chem. A 113: 255—262. Doi: https://doi.org/10.1021/jp804986b.
Grimme S, Antony J, Ehrlich S, Krieg H (2010) J Chem Phys 132(15): 154104. Doi: https://doi.org/10.1063/1.3382344.
Hensel T, Andersen NN, Plesner M, Pittelkow M (2016) Synlett. 27(04): 498—525. Doi: https://doi.org/10.1055/s-0035-1560524.
Hohenberg P, Kohn W (1964) Phys. Rev. 136: B864—B871. Doi: https://doi.org/10.1103/PhysRev.136.B864.
Huong VTT, Tai TB, Nguyen MT (2012) Phys. Chem. Chem. Phys. 14: 14832—14841. Doi: https://doi.org/10.1039/C2CP42474F.
Huong VTT, Tai TB, Nguyen MT (2015) RSC Adv. 5: 24167—24174. Doi: https://doi.org/10.1039/C4RA16485G.
Larsson S, Klimkans A, Rodriguez-Monge L, Duskesas G (1998) Theochem-Journal Mol. Struct. 425: 155—159. Doi: https://doi.org/10.1016/S0166-1280(97)00216-9.
Lee C, Yang W, Parr RG (1988) Phys Rev B 37: 785—789. Doi: https://doi.org/10.1103/PhysRevB.37.785.
Lin YY, Gundlach DJ, Nelson SF, Jackson TN (1997) IEEE Electron Device Lett. 18: 606—608. Doi: https://doi.org/10.1109/55.644085.
Liu CC, Mao SW, Kuo MY (2010) J. Phys. Chem. C. 114: 22316—22321. Doi: https://doi.org/10.1021/jp1099464.
Lukeš V, Cagardová D, Michalík M, Poliak P (2018) Synt. Met. 240: 67—76. Doi: https://doi.org/10.1016/j.synthmet.2018.03.014.
Maier SA, Ankerhold J (2010) Phys. Rev. E 81: 021107. doi: https://doi.org/10.1103/PhysRevE.81.021107.
Malagoli M, Brédas JL (2000) Chem Phys Lett 327: 13—17. Doi: https://doi.org/10.1016/S0009-2614(00)00757-0.
Malagoli M, Coropceanu V, Da Silva Filho DA, Brédas JL (2004) J. Chem. Phys. 120: 7490—7496. Doi: https://doi.org/10.1063/1.1687675.
Marcus RA (1993) Rev Mod Phys 65: 599—610. Doi: https://doi.org/10.1103/RevModPhys.65.599.
Mohakud S, Pati SK (2009) J. Mater. Chem.19: 4356—4361. Doi: https://doi.org/10.1039/B901014A.
Murphy AR, Fréchet JMJ (2007) Chem. Rev. 107: 1066—1096. Doi: https://doi.org/10.1021/cr0501386.
Nagata Y, Kato S, Miyake Y, Shinokubo H (2017) Org. Lett. 19: 2718—2721. Doi: https://doi.org/10.1021/acs.orglett.7b01074.
Nan G, Shi Q, Shuai Z, Li Z (2011) Phys. Chem. Chem. Phys. 13: 9736—9746. Doi: https://doi.org/10.1039/C1CP00001B.
Ośmiałowski B, Raczyńska ED, Krygowski TM (2006) J Org Chem 71(10): 3727—3736. Doi: https://doi.org/10.1021/jo052615q.
Runge E, Gross EKU (1984) Phys. Rev. Lett. 52: 997—1000. doi: https://doi.org/10.1103/PhysRevLett.52.997.
Sakamoto Y, Suzuki T (2013) J. Am. Chem. Soc. 135(38): 14074—14077. Doi: https://doi.org/10.1021/ja407842z.
Sakanoue K, Motoda M, Sugimoto M, Sakaki S (1999) J Phys Chem A 103: 5551—5556. Doi: https://doi.org/10.1021/jp990206q.
Scholl R; Meyer K (1932) Ber. Dtsch. Chem. Ges. 65: 902. Doi: https://doi.org/10.1002/cber.19370701104.
Sigma Aldrich (2019) website: https://www.sigmaaldrich.com/.
Simon S, Duran M, Dannenberg JJ (1996) J. Chem. Phys. 105: 11024—11031. Doi: https://doi.org/10.1063/1.472902.
Wang L, Li P, Xu B, Zhang H, Tian W (2014) Org. Electron. 15: 2476—2485. Doi: https://doi.org/10.1016/j.orgel.2014.07.003.
Xantheas SS (1996) J. Chem. Phys. 104: 8821—8824. Doi: https://doi.org/10.1063/1.471605.
Xiong X, Deng CL, Li Z, Peng XS, Wong HNC (2017) Org. Chem. Front. 4(5): 682—687. Doi: https://doi.org/10.1039/C6QO00662K.
Yakuphanoglu F, Mansouri S, Bourguiga R (2012) Synt. Met. 162: 918—923. Doi: https://doi.org/10.1016/j.synthmet.2012.04.003.
Yamamoto K, Harada T, Nakazaki M, Naka T, Kai Y, Harada S, Kasai N (1983) J. Am. Chem. Soc. 105: 7171. Doi: https://doi.org/10.1021/ja00362a025.
Zheng J, Xu X, Truhlar DG (2011) Theor Chem Acc 128: 295. Doi: https://doi.org/10.1007/s00214-010-0846-z.

sciendo

Application of photochromic pigment in mass dyed polypropylene fibres intended for intelligent textiles

Veronika Hrabovská, Marcela Hricová, Anna Ujhelyiová

Slovak University of Technology in Bratislava, Faculty of Chemical and Food Technology, Institute of Natural and Synthetic Polymers, Radlinskeho 9, 812 37 Bratislava, Slovakia
veronika.hrabovska@stuba.sk

Abstract: At the present time, characterised by worsening environmental conditions, the protection of human organism against irreversible damage is necessary. Protective clothing on base of smart textiles represents the future in human clothing. In this article, the effect of photochromic pigments on spinnability, drawability and properties of pigmented polypropylene (PP) fibres is presented.
Mechanical properties (tenacity and elongation at break, Young's modulus), thermo-mechanical properties and the factor of average orientation of fibres were evaluated and discussed. The obtained results indicate a possibility of fibres preparation with photochromic pigments.

Keywords: polypropylene, smart polymers, mechanical properties, thermal properties, photochromic materials

Introduction

We live in an overly-technological world. Everything is advanced, modern, electronic, comfortable, but also dangerous. These dangers have been created by ourselves. On one hand, we improve our living conditions and on the other, we are worsening the living conditions on Earth. One of the impacts is the formation of the ozone hole. The ozone layer absorbs dangerous UV rays coming to Earth (Frercks at al., 2009). Solar radiation is an important natural component because it is an important factor in the Earth's climate and it has a significant impact on the environment. Ultraviolet part of the solar spectrum (UV) plays an important role in many processes in the biosphere. UV radiation has several beneficial effects but it can also be very damaging if the UV level exceeds 'safe' limits (Vikova and Vik, 2009). UV radiation has shorter wavelength and higher energy than visible light. It is an invisible part of the spectrum of electromagnetic radiation with frequencies ranging from 1012 to 1014 Hz and wavelengths from 4 to 400 nm. Skin and eyes are organs with the highest exposure to sunlight UV radiation. Although hair and nails are also exposed to harmful UV radiation, they are less important from the medical point of view. UV radiation has little penetration, so protection against it is easy. Excessive exposure of human skin to the influence of UVA and UVB radiation leads to skin damage and aging, and long exposition to radiation leads to skin tumours. Only suitable clothing, gloves, glasses or sunscreen with a sufficiently high UV filter for uncovered parts of the body (Vanicek at al., 2000) can protect the body from UV radiation. Intelligent textiles with built-in UV sensitive sensors can be used in skin protection. People working in the exterior, who are exposed to sunlight, would wear garments indicating solar radiation intensity and the need for increased protection just by changing their colour intensity.

Smart textiles are specifically designed textile structures which in addition to fulfilling the functions of normal fabrics respond and react to external conditions and incentives of mechanical, electrical, chemical and radiant or heat exposure (Bamfield, 2001). According to the reaction, they can be divided into three classes: passive smart, active smart and very smart materials. Passive smart materials can only sense the environmental conditions or stimuli; active smart materials sense and react to the conditions or stimuli; very smart materials can sense, react and adapt themselves accordingly (Xiaoming, 2001).

One of the latest developments is the use of photochromic materials reacting to UV radiation by changing their colour. Flexibility of textile sensors and the possibility of their integration into the garment structure allow movement of the textile into which the sensor is inserted. One way of photochromic dyes application in textiles is using inkjet printing or exhaust dyeing. However, a reduction of the photochromic effect during UV-radiation exposure occurs due to photo-oxidation of photochromic dyes or washing (Dietz and El'tsov, 1990). The second way is the incorporation of photochromic pigment in polymer matrix in melt during spinning of fibres. The positive – pigment is dispersed in the mass of the fibre and is more stable during washing. These sensors, built-in textile materials

(T-shirt, swim suit, etc.), would warn if the UV radiation reached a high value and it is time to avoid excessive exposure to the sun.

Photochromism is the reversible transformation of a chemical species from one form to another by absorption of electromagnetic radiation, where the two forms have different absorption spectra. It is simply defined as the light induced reversible change of colour (Dürr and Bouas-Laurent, 2003). The original state referred to as A and the transformed state referred to as B are both excited simultaneously but the prevalent state depends on the electromagnetic radiation (Crano and Guglielmetti, 1999; Bouas-Laurent and Dürr, 2001). Simple photochromic processes can be described as described in Fig. 1.

$$\mathbf{A} \underset{h\nu_2 \Delta T}{\overset{h\nu_1}{\rightleftharpoons}} \mathbf{B}$$

Fig. 1. Scheme of a simple photochromic process (Vikova, 2009).

Photochromic compounds can be divided into five main classes: spiropyrans (spiroindolinobenzopyrans), spironaphtoxazines, naphtopyrans (chromenes), fulgides and diarylethenes. In terms of applicability to textile fibres, spiropyrans, spironaphtoxazines and chromenes have been found as the most suitable ones considering fatigue, life time and fastness properties (Durasevic at al., 2011). Based on the photochromic pigment, a simple textile sensor sensitive to UV radiation for visual identification of UV radiation has been developed. At present, there is a large number of photochemical dyes. To indicate the photochromic potential, these dyes have to be embedded in the matrix. Technically and economically most important matrices are polymers, especially thermoplastics. Photochromic functionalized polymers have specific characteristics and thus they are very sensitive to their environment – structure of polymer matrix or degradation of products and additives. Therefore, parameters of photochromic reactions such as speed, intensity, spectral distribution of colour change and fatigue phenomenon after prolonged UV irradiation could be used as matrix state sensors (Nechwatal and Nicolai, 2011).

Experimental part

Materials used

For the preparation of fibres, polypropylene Metocene HM562R (PP) from LyondellBasell Industries, c.o., Italy, was used. The characteristics of PP:

- melt flow rate MFR = 25 g/10 min (230 °C/2.016 kg)
- melting temperature Tm (DSC) = 145 °C

In the experimental part of the work, commonly available photochromic pigments Photopia® Aqualite Ink Purple AQ-R (PURPLE) from Matsui Shikiso Chemical Co.,Ltd., Japan, were used. These pigments are able to change their colour with sunlight or ultraviolet light. The photochromic pigments are in form of paste containing 30–50 wt. % of photochromic microcapsules.

Preparation of fibres

PP granules were mixed with photochromic pigments in form of paste in two ways. In the first one, the photochromic pigment was directly added to the PP granules and mechanically mixed. In the second one, the photochromic pigment was at first dissolved in a small amount of ethanol (EtOH), and then added to the PP granules. The amount of pigment added corresponded to the final concentration in the fibres. Concentrations of photochromic paste in the fibres were 0.5; 1; 1.5; 2 and 3 wt. %. The next step of prepared mixtures processing consisted in drying for one hour with occasional mixing at the drying temperature of 50 °C. Pigmented PP fibres were prepared by spinning of the blend using a laboratory spinning plant at the spinning temperature of 220 °C for all prepared samples. Then, the fibres were drawn using a laboratory drawing machine at mutual draw ratios $\lambda = 3$ and maximal draw ratios, λ_{max}, at the drawn temperature of 120 °C.

Methods used

Rheological properties of polymer melt: Rheological properties of the polymer blends were measured using a capillary extrusiometer Göttfert N 6967 with extruder ϕ of 20 mm at 220 °C. Measurement conditions were close to those in the spinning equipment, namely dynamic conditions in the extruder before blended melt extrusion. The Newton and Oswald de Waele laws for basic rheological parameters determination: apparent viscosity, η, and power law index, n, which characterize the non-Newtonian behaviour of the polymer melt, were used:

$$\eta = \tau/\dot{\gamma} \tag{1}$$

$$(\tau = k\dot{\gamma}^n) \tag{2}$$

where τ – shear stress, $\dot{\gamma}$ – shear rate, η – apparent viscosity, n – power law index, k – coefficient.

Mechanical properties: Mechanical properties (tenacity and elongation at break, Young's modulus) of PP and pigmented PP fibres were evaluated. The Instron (Type 3343) was used to measure the mechanical properties according to ISO 2062:1993 from 15 measurements. Initial length was 125 mm and the deformation time was about 20 s. Mechanical properties (tenacity and elongation at break, Young's

modulus) and their coefficients of variations were evaluated by the Instron Software Series IX.

Thermo-mechanical properties: Thermo-mechanical characteristics of PP and pigmented PP fibres were measured by a Schimadzu TMA 50. Deformation (extension or shrinkage) of fibres at constant load in the temperature range of 30—100 °C (heating speed of 5 °C/min.) were evaluated. The length of fibres was 9.8 mm.

Thermal properties: Thermal properties were measured by DSC 1/750 with a ceramic sensor FRS5 by the SW STARe software from Metler Toledo. Conditions used for the measurement were: 1. heating: 50—220 °C, cooling: 220—50 °C, 2. heating: 50—220 °C. The speed of heating or cooling was 10 °C/min and the measurements were made in inert nitrogen atmosphere. Glass temperature (T_g), melting temperature (T_m) and melting enthalpy (ΔH_m) were determined.

Orientation of fibres: The speed of sound in PP and pigmented PP fibres was measured by the Dynamic Modulus Tester PPM-SR and it was used according to standard PND 129-126-06. Factor of average orientation (f_α) of fibres was calculated by measuring the speed of sound in oriented fibres:

$$f_\alpha = 1 - \frac{c_n^2}{c^2} \qquad (3)$$

where: f_α — factor of average orientation of fibres, c_n — speed of sound in non-oriented fibres [km · s^{-1}], c — speed of sound in fibres [km · s^{-1}].

Results and discussion

Rheological properties of PP and PP/PURPLE blends

Rheological properties of polymer melts provide information about their behaviour, conditions of shear and elongation flow and the processing conditions. Rheological properties of polymer blends were measured to monitor the impact of the photochromic pigment content on the PP/PURPLE melts processability. The melt flow properties of PP and PP compositions were evaluated at different concentrations of photochromic pigments (0.5, 1, 1.5, 2, and 3 wt. %) prepared with EtOH or mechanically at 220 °C.

The results showed no influence of photochromic pigments on the rheological properties of PP melt nor on the PP/PURPLE blends preparation. Dependencies of shear stress, τ_s, on shear rate, $\dot{\gamma}$, for all PP/PURPLE samples prepared with EtOH or mechanically are almost identical with those of pure PP (Figures 2, 3). Values of the power law index, n, and viscosity, η, of PP and PP/PURPLE blends are very similar and these samples are characterized by good processability (Tables 1, 2).

Mechanical properties of PP and PP/PURPLE fibres

The aim of this work was to prepare PP fibres containing photochromic pigment with suitable mechanical properties. The effect of fibres preparation and photochromic pigments concentration were evaluated.

Tab. 1. Power law index, n, and viscosity, η, of *PP* and *PP/PURPLE* blends prepared mechanically at 220 °C.

composition	n	η [Pa·s]		
		$\dot{\gamma}$ = 300 s^{-1}	$\dot{\gamma}$ = 500 s^{-1}	$\dot{\gamma}$ = 1000 s^{-1}
PP 562 R	0.41	217	161	107
PP+0.5 % PURPLE mech.	0.42	214	159	106
PP+1 % PURPLE mech.	0.41	216	159	105
PP+1.5 % PURPLE mech.	0.41	216	160	106
PP+2 % PURPLE mech.	0.41	217	160	106
PP+3 % PURPLE mech.	0.41	217	160	106

Tab. 2. Power law index, n, and viscosity, η, of *PP* and *PP/PURPLE* blends prepared with EtOH at 220 °C.

composition	n	η [Pa·s]		
		$\dot{\gamma}$ = 300 s^{-1}	$\dot{\gamma}$ = 500 s^{-1}	$\dot{\gamma}$ = 1000 s^{-1}
PP 562 R	0.41	217	161	107
PP + 0.5 % PURPLE EtOH	0.40	219	161	106
PP + 1 % PURPLE EtOH	0.41	215	159	106
PP + 1.5 % PURPLE EtOH	0.41	217	160	106
PP + 2 % PURPLE EtOH	0.41	218	161	106
PP + 3 % PURPLE EtOH	0.40	216	159	110

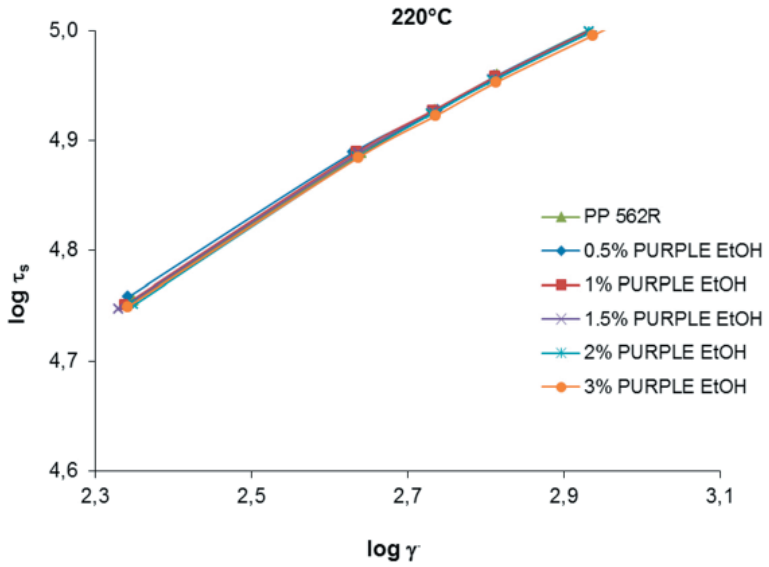

Fig. 2. Flow curves of *PP* and samples *PP/PURPLE EtOH* with all concentrations of photochromic paste.

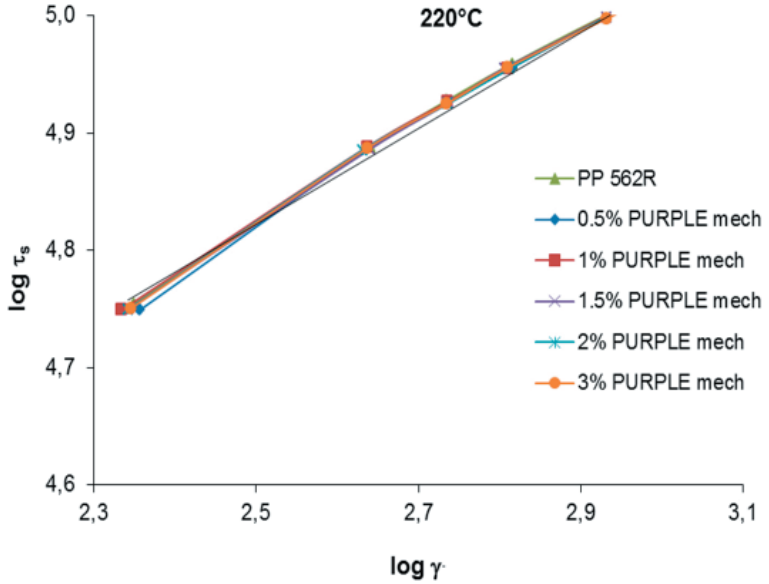

Fig. 3. Flow curves of *PP* and *PP/PURPLEmech.* samples mixed with all studied photochromic paste concentrations.

All prepared fibres were drawn at maximal draw ratio, λ_{max}, and one mutual drawn ratio, λ_3. Samples of PP fibres containing 3 wt. % of photochromic paste were prepared with minor problems. However, PP + 3 % of PURPLE EtOH were not able to spin at all.

Fibres from the PP/PURPLE mech. series drawn at λ_3 showed improved tenacity at break at the concentration of 0.5 wt. % compared to pure PP. Higher concentration of photochromic pigment in fibres, 1—3 wt. %, improved the tenacity of break, but no effect of the increasing photochromic pigment concentration in fibres was observed. Tenacity at break was 19.0—19.3 cN/tex with the exception of PP + 2 % PURPLE where it was 18.2 cN/tex, which is lower than for other pigmented fibres but still higher than for pure PP.

Fibres from the PP/PURPLE mech. series drawn at λ_{max} showed no significant effect of the increasing photochromic pigment concentration on the tenacity values. All fibres showed lower tenacity at break compared to PP with the exception of fibres concentration of 1.5 wt. %. Homogeneity of the polymer mass with photochromic pigment and pigment distribution in fibres were low because they were not prepared from polymer concentrate but by mechanical mixing of polymer granules and photochromic pigment before spinning. This assump-

tion is supported also by high values of structural non-uniformity of mechanical properties according to their variation coefficients. Very similar dependences were also shown for the Young's modulus PP/PURPLE mech. fibres (Tables 3 and 4).

Fibres from the PP/PURPLE mech. series drawn at λ_3 showed higher values of elongation at break compared to pure PP. No significant dependence on the increasing photochromic pigment concentration and the elongation at break was observed. Fibres with the photochromic pigment content of 0.5; 1.5 and 3 wt. % have very similar values of elongation at break (70—72 %). PP + 1 % PURPLE fibres show low elongation at break (54 %) and also low tenacity at break compared with other pigmented fibres. Photochromic pigment concentration of 2 wt. % caused significant increase of elongation at break (81 %).

For PP/PURPLE EtOH fibres drawn at λ_3, the tenacity at break decreased to 18.2 cN/tex (PP + 1 % PURPLE EtOH); for the highest photochromic pigment concentration (PP + 2 % PURPLE EtOH) is the tenacity at break the highest (Table 5 and 6).

For all PP/PURPLE EtOH fibres drawn at λ_{max}, with the increasing concentration of photochromic pigment, the values of tenacity at break and Young's modulus decrease as confirmed by the decreasing value of the maximal drawn ratio compared with pure PP. Conversely, values of elongation at break are higher than for pure PP. Higher values of elongation at break were measured for fibres with 1 and 1.5 wt. % of photochromic pigment. For no PP/PURPLE EtOH (λ_3 and λ_{max}) sample, dependence between the increasing photochromic pigment concentration and values of elongation at break for the prepared fibres was observed.

Non-uniformity of the fibres mechanical properties, such as tenacity and elongation at break and Young's modulus, results from the non-uniformity of the fibre macrostructure, the number of weaknesses, macro and micro defects of individual filaments, non-uniformity of the fibres cross section, and the non-uniformity of molecular, supramolecular and morphological structures. It is a realistic assumption that the cumulative effect of these variables is reflected in fibre deformation. The variation coefficients show the non-uniformity of PP fibres containing PURPLE photochemical pigment (Tables 3—6).

Thermo-mechanical properties of PP and PP/PURPLE fibres

Figures 4 and 5 provide graphical presentation of dimensional stability (deformation) for PP and PP/PURPLE fibres and the effect of photochromic pigment content and the preparation procedure on the deformation of these fibres in dependence on temperature in the defined temperature mode. Dimensional stability (deformation) of all fibres by their shrinkage is shown.

Tab. 3. Tenacity, σ, and elongation at break, ε, Young's modulus, E, and their coefficients of variation for *PP* and *PP/PURPLE mech* fibres drawn at λ_{max}.

Fibre	λ_{max}	σ [cN/tex]	CVσ [%]	ε [%]	CVε [%]	E [N/tex]	CV_E [%]
PP 562R	4.8	25.8	5.6	46	15.1	2.90	8.7
PP + 0.5 % PURPLE mech.	3.8	22.9	10.9	70	10.8	2.31	10.2
PP + 1 % PURPLE mech.	3.5	18.2	9.1	54	10.3	1.88	11.7
PP + 1.5 % PURPLE mech.	4.0	26.9	12.2	71	13.8	2.70	17.0
PP + 2 % PURPLE mech.	3.5	22.8	13.6	81	10.0	2.31	6.0
PP + 3 % PURPLE mech.	3.5	24.2	9.3	72	10.7	2.21	4.8

Tab. 4. Tenacity, σ, and elongation at break, ε, Young's modulus, E, and their coefficients of variation for *PP* and *PP/PURPLE mech* fibres drawn at λ_3.

Fibre	λ	σ [cN/tex]	CVσ [%]	ε [%]	CVε [%]	E [N/tex]	CV_E [%]
PP 562R	3.0	17.2	10.7	126	10.3	1.40	15.0
PP + 0.5 % PURPLE mech.	3.0	20.0	12.5	101	14.8	1.83	12.3
PP + 1 % PURPLE mech.	3.0	19.0	14.6	100	10.7	1.62	9.8
PP + 1.5 % PURPLE mech.	3.0	19.3	7.8	98	10.5	1.69	11.7
PP + 2 % PURPLE mech.	3.0	18.2	8.9	80	10.2	1.63	10.7
PP + 3 % PURPLE mech.	3.0	19.2	9.9	87	8.6	1.55	4.6

Tab. 5. Tenacity, σ, and elongation at break, ε, Young's modulus, E, and their coefficients of variation for *PP* and *PP/PURPLE EtOH* fibres drawn at λ_{max}.

Fibre	λ_{max}	σ [cN/tex]	CVσ [%]	ε [%]	CVε [%]	E [N/tex]	CV_E [%]
PP 562R	4.8	29.6	4.1	38	12.3	3.19	6.8
PP + 0.5 % PURPLE EtOH	4.2	27.1	10.4	58	7.4	2.66	10.4
PP + 1 % PURPLE EtOH	3.7	21.5	12.0	69	13.4	2.22	14.7
PP + 1.5 % PURPLE EtOH	3.4	19.1	10.6	67	9.8	1.79	16.3
PP + 2 % PURPLE EtOH	3.2	13.9	23.9	60	11.7	1.51	11.2
PP + 3 % PURPLE EtOH	1.0	–	–	–	–	–	–

Tab. 6. Tenacity, σ, and elongation at break, ε, Young's modulus, E, and their coefficients of variation for *PP* and *PP/PURPLE EtOH* fibres drawn at λ_3.

Fibre	λ	σ [cN/tex]	CVσ [%]	ε [%]	CVε [%]	E [N/tex]	CV_E [%]
PP 562R	3.0	19.9	10.7	115	12.3	1.55	9.3
PP+0.5 % PURPLE EtOH	3.0	17.7	7.7	100	9.8	1.51	9.6
PP+1 % PURPLE EtOH	3.0	16.4	22.0	78	8.9	1.67	17.7
PP+1.5 % PURPLE EtOH	3.0	15.9	11.2	81	15.3	1.51	16.1
PP+2 % PURPLE EtOH	3.0	21.5	8.1	91	11.5	1.91	13.7
PP+3 % PURPLE EtOH	1.0	–	–	–	–	–	–

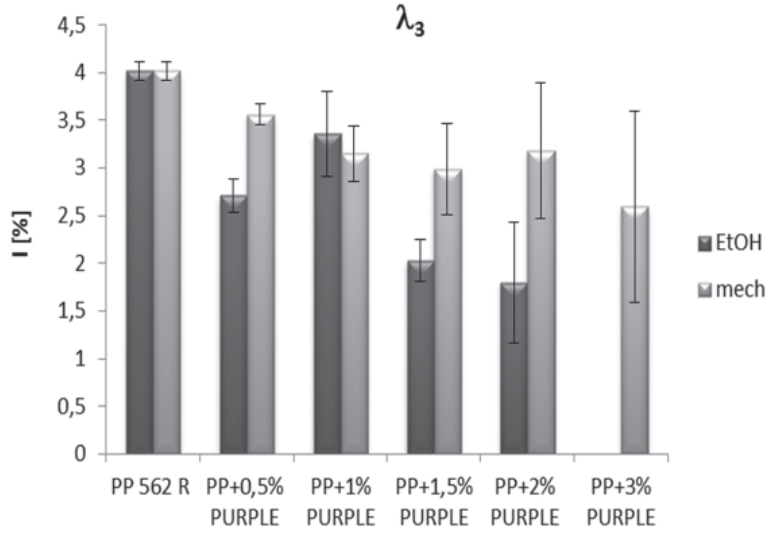

Fig. 4. Dependence of deformation — shrinkage l [%] of *PP* and *PP/PURPLE* fibres drawn at λ_3 on photochromic pigment concentration.

PP/PURPLE fibres drawn at λ_3 showed lower deformation and thereby better dimensional stability as pure PP fibres (Figure 4). Deformation of PP/PURPLE mech. fibres is almost the same and that of PP/PURPLE EtOH fibres, which decreases with the pigment content, is significantly lower. An exception are fibres with pigment concentration of 1 wt. %, which showed higher deformation probably due to higher pigment concentration in fibres causing an increase of the PP temperature resistance. PP/PURPLE fibres drawn at λ_{max} showed higher deformation as pure PP fibres (Figure 5) which can be a result of the action of internal stresses created during the orientation by spinning and drawing. PP/PURPLE EtOH fibres drawn at λ_{max} showed a very similar deformation. The exception are fibres with pigment concentration of 1 wt. %, which showed the highest deformation. For PP/PURPLE mech. drawn at λ_{max}, the deformation is different as it is not dependt on the pigment content. For

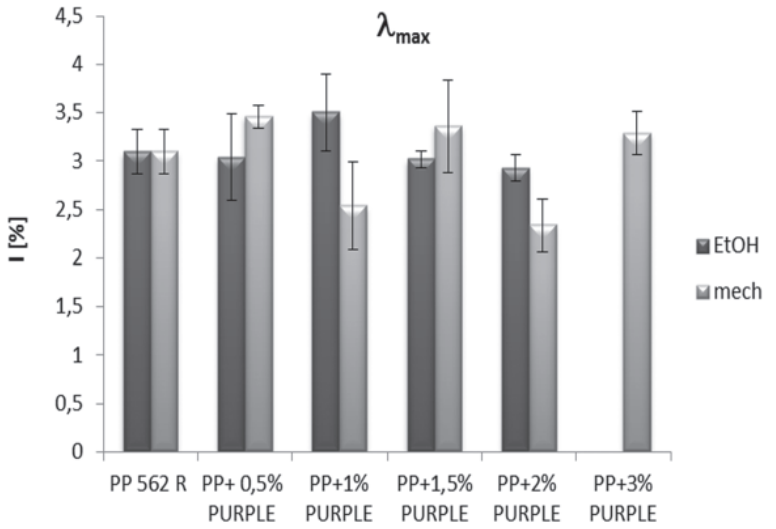

Fig. 5. Dependence of deformation — shrinkage l [%] of *PP* and *PP/PURPLE* fibres drawn at λ_{max} on photochromic pigment concentration.

fibres with pigment concentration of 0.5 wt. %, the highest deformation was found while lower deformation was determined for fibres with pigment concentration of 1 wt. % and 2 wt. % compared to pure PP fibres.

From the results in Tables 7 and 8 it can be seen that the concentration of photochromic pigment does not significantly affect the deformation temperature of PP and PP/PURPLE fibres drawn at λ_{max}. The highest temperature of deformation was determined for PP/PURPLE EtOH fibres with 0.5 wt. % of photochromic paste drawn at λ_3 while PP/PURPLE mech. fibres with the same concentration showed the lowest temperature of deformation.

Tab. 7. Temperature of deformation of *PP* and *PP/PURPLE* fibres drawn at λ_3.

Fibre	T [°C]	
	EtOH	mech.
PP 562R	65.9	65.9
PP + 0.5 % PURPLE	72.3	56.8
PP + 1 % PURPLE	60.1	67.9
PP + 1.5 % PURPLE	65.7	64.6
PP + 2 % PURPLE	53.8	58.7
PP + 3 % PURPLE	–	57.6

Tab. 8. Temperature of deformation of *PP* and *PP/PURPLE* fibres drawn at λ_{max}.

Fibre	T [°C]	
	EtOH	mech.
PP 562R	55.2	55.2
PP + 0.5 % PURPLE	57.1	55.5
PP + 1 % PURPLE	57.1	68.0
PP + 1.5 % PURPLE	53.7	62.3
PP + 2 % PURPLE	56.4	61.9
PP + 3 % PURPLE	–	59.3

Thermal properties

Thermal properties from the first heating show the effect of fibres processing and polymer mixing with pigment (Tables 9 and 10). Thermal properties were measured only for fibres drawn at the maximal drawn ratio, λ_{max}.

Fibres prepared by mechanical mixing of the pigment with polymer have lower T_{m1} than pure PP, except for PP + 1.5 % PURPLE fibres with the highest T_{m1} (Table 9). Fibres prepared by mixing of polymer with pigment in form of photochromic paste dissolved in a small amount of ethanol have higher T_{m1} values for pigment concentration of 1 wt. % and 1.5 wt. % than pure PP (Table 10). Melting temperature, T_{m2}, of all PP/PURPLE fibres is almost the same. No significant effect of the increasing photochromic pigment concentration. The pigment in the polymer has no nucleation effect, which results from constant T_{m2} value for the whole concentration range of pigment in polymer, regardless of the fibre preparation method.

Melting enthalpy of the first heating is slightly higher for PP/PURPLE mech. fibres compared to the PP/PURPLE EtOH fibres. Higher ΔH_m means higher crystalline portion in the fibres compared to non-oriented polymer. At the second heating, higher enthalpy was found for pigment concentration of 1—1.5 wt. % for both preparation methods (Tables 9 and 10).

Tab. 9. Melting temperature, T_m, and melting enthalpy, ΔH_m, of *PP* and *PP/PURPLE mech.* fibres drawn at λ_{max}.

Fibre	first heating		second heating	
	T_{m1} [°C]	ΔH_{m1} [J·g^{-1}]	T_{m2} [°C]	ΔH_{m2} [J·g^{-1}]
PP 562R	147.4	81.6	144.4	78.0
PP + 0.5 % PURPLE mech.	146.2	86.4	144.0	76.0
PP + 1 % PURPLE mech.	146.3	77.2	144.2	76.5
PP + 1.5 % PURPLE mech.	147.6	80.3	144.2	80.1
PP + 2 % PURPLE mech.	146.3	79.1	144.4	77.6
PP + 3 % PURPLE mech.	147.0	75.9	144.8	77.5

Tab. 10. Melting temperature, T_m, and melting enthalpy, ΔH_m, of *PP* and *PP/PURPLE EtOH* fibres drawn at λ_{max}

Fibre	first heating		second heating	
	T_{m1} [°C]	ΔH_{m1} [J·g^{-1}]	T_{m2} [°C]	ΔH_{m2} [J·g^{-1}]
PP 562R	147.4	81.6	144.4	78.0
PP + 0.5 % PURPLE EtOH	147.3	76.1	144.2	75.1
PP + 1 % PURPLE EtOH	148.1	77.6	144.7	82.5
PP + 1.5 % PURPLE EtOH	148.4	77.6	144.5	83.4
PP + 2 % PURPLE EtOH	146.0	69.6	144.3	76.1
PP + 3 % PURPLE EtOH	–	–	–	–

Orientation of fibres

Average orientation of fibres is determined by the speed of sound method and consequently by calculating the factor of average orientation, f_α.

Tab. 11. Factor of average orientation, f_α, of *PP* and *PP/PURPLE* fibres drawn at λ_{max}.

Fibre	f_α	
	EtOH	mech.
PP 562R	0.715	0.715
PP + 0.5 % PURPLE	0.698	0.670
PP + 1 % PURPLE	0.673	0.652
PP + 1.5 % PURPLE	0.626	0.708
PP + 2 % PURPLE	0.622	0.692
PP + 3 % PURPLE	–	0.653

Tab. 12. Factor of average orientation, f_α, of *PP* and *PP/PURPLE* fibres drawn at λ_3.

Fibre	f_α	
	EtOH	mech.
PP 562R	0.574	0.574
PP + 0.5 % PURPLE	0.566	0.671
PP + 1 % PURPLE	0.595	0.599
PP + 1.5 % PURPLE	0.663	0.628
PP + 2 % PURPLE	0.564	0.622
PP + 3 % PURPLE	–	0.613

Values of the factor of average orientation measured for PP/PURPLE fibres drawn at λ_{max} are almost the same for both series of prepared fibres and they are in the range of 0.6–0.72 (Tables 11). The best orientation was found for pure PP fibres, which corresponds to the highest drawn ratio, λ_{max}. A similar value of the factor of average orientation was determined for a sample with the photochromic paste concentration of 1.5 %, which agrees with the mechanical properties of these fibres and provides the most optimal pigment concentration in PP. For a mutual drawn ratio, λ_3, factors of average orientation are lower, probably because of the insufficiently drawn fibres at this ratio and thus their insufficient orientation (Table 12).

Conclusions

Experimental part of the present work has confirmed that it is possible to prepare PP fibres containing photochromic pigment in their mass and that these fibres show satisfying mechanical properties.

Two series of fibres containing photochromic pigments, which differ in the PP granulate and photochromic pigment mixing procedure, were prepared. Rheological properties of PP melt containing photochromic pigment showed that the photochromic pigment does not significantly affect the PP flow properties. Another goal of the

experiment was to evaluate the properties of prepared fibres. From the results obtained it cannot be clearly determined which method of pigmented PP fibres preparation is more advantageous. Dimensional stability of all fibres was manifested by their shrinkage. Fibres drawn at λ_3 showed lower deformation and thus better dimensional stability than fibres drawn at λ_{max}. Concentration of photochromic pigment in the mass of PP fibres does not significantly affect their deformation temperature. No significant effect of photochromic pigment concentration increase or the preparation method used on the factor of average orientation was observed. Properties of these fibres can be improved in future by optimizing the PP fibre preparation, conditions in the pigment blending process and spinning process.

Acknowledgement
This work was supported by the Slovak Research and Development Agency under the contract No: APVV-14-0175.

References

Bamfield P (2001) Chromic phenomena: The technological applications of colour chemistry. Cambridge, UK: The Royal Society of Chemistry.

Bouas-Laurent H, Dürr H (2001) Organic photochromism. Pure and Applied Chemistry, 73(4): 639–665.

Crano JC, Guglielmetti RJ (Ed) (1999) Organic photochromic and thermochromic compounds: Volume 1: Main Photochromic Families, New York, USA: Kluwer Academic Publishers.

Dietz F, El'tsov AV (1990) Theoretical studies of the photochromism of organic compounds. In: Organic Photochromes. Boston, MA: Springer.

Durasevic V, Osterman PD, Sutlovic A (2011) From Murex Purpura to sensory – photochromic textiles. In Prof. Peter Hauser (Ed.), Textile Dyeing (pp. 57–76). InTech.

Dürr H, Bouas-Laurent H (2003) Photochromism: Moleculs and Systems, Elsevier Science.

Frercks J, Weber H, Wiesenfeldt G (2009) Reception and discovery: the nature of Johann Wilhelm Ritter's invisible rays. Studies in History and Philosophy of Science, Part A, 40(2): 143–156.

Nechwatal A, Nicolai M (2011) Interactions between polypropylene and photochromic dyestuffs. Polymer Degradation and Stability, 96: 1648–1652.

Vanicek K, Frei T, Litynska Z, Schmalweiser A (2000) UV-Index for the public, EUR – COST 713 Action: UV-B forecasting. Luxembourg: Office for Official Publications of the European Communities.

Vikova M (2009) Methodology of measurement of chromic materials. In P. R. Somani (Ed), Chromic Materials, Phenomena and their Technological Applications (pp. 509–533). Maharashtra, India: Applied Science Innovations Private Limited.

Vikova M, Vik M (2009) Alternative UV sensors based on color-changeable pigments. Advances in Chemical Engineering and Science, 1(4): 224–230.

Xiaoming T (Ed.) (2001) Smart fibres, fabrics and clothing. Cambridge, UK: Woodhead Publishing.

sciendo

Substrate inhibition and pH effect on denitritation with granular biomass

Stanislava Kecskésová, Zuzana Imreová, Bibiána Kožárová, Ján Derco, Miloslav Drtil

Department of Environmental Engineering, Faculty of Chemical and Food Technology, Slovak University of Technology, Radlinskeho 9, 812 37 Bratislava, Slovak Republic
stanislava.vlckova@stuba.sk

Abstract: Undissociated HNO_2 (up to 2 mg dm^{-3}) was confirmed as substrate inhibitor for granular biomass from a denitritation upflow sludge bed reactor used for biological removal of nitrite. On the contrary, total nitrite nitrogen ($N\text{-}NO_2$ up to 500 mg dm^{-3}) and methanol (COD up to 2000 mg dm^{-3}) were not proven to be inhibitors. pH also affected the denitritation efficiency (optimal pH was 5.9). Reduction of HNO_2 concentration in the reactor by effluent recycling is recommended.

Keywords: denitritation, granulated biomass, methanol, pH, substrate inhibition, undissociated HNO_2

Introduction

Denitritation is a reaction in which nitrite nitrogen ($N\text{-}NO_2$) is biologically removed to gaseous N_2. This process can be used for the treatment of various wastewater types, e.g. industrial wastewater containing $N\text{-}NO_2$ or wastewater after partial nitrification (nitritation), where ammonium nitrogen ($N\text{-}NH_4$) is oxidized only to $N\text{-}NO_2$ with inhibited nitrite oxidizing bacteria (NOB) (Hellinga et al., 1998; Jenicek et al., 2004; Svehla et al., 2014). Denitritation can be realized in various reactor types, including activated sludge reactors with suspended biomass, biofilters with fixed bed biomass, and specific reactors, such as the upflow sludge bed (USB) reactors (Fig. 1) with granular biomass (Galbová et al., 2010; Pagáčová et al., 2009; Pagáčová et al., 2010). In USB reactors, biomass is exposed to a substrate

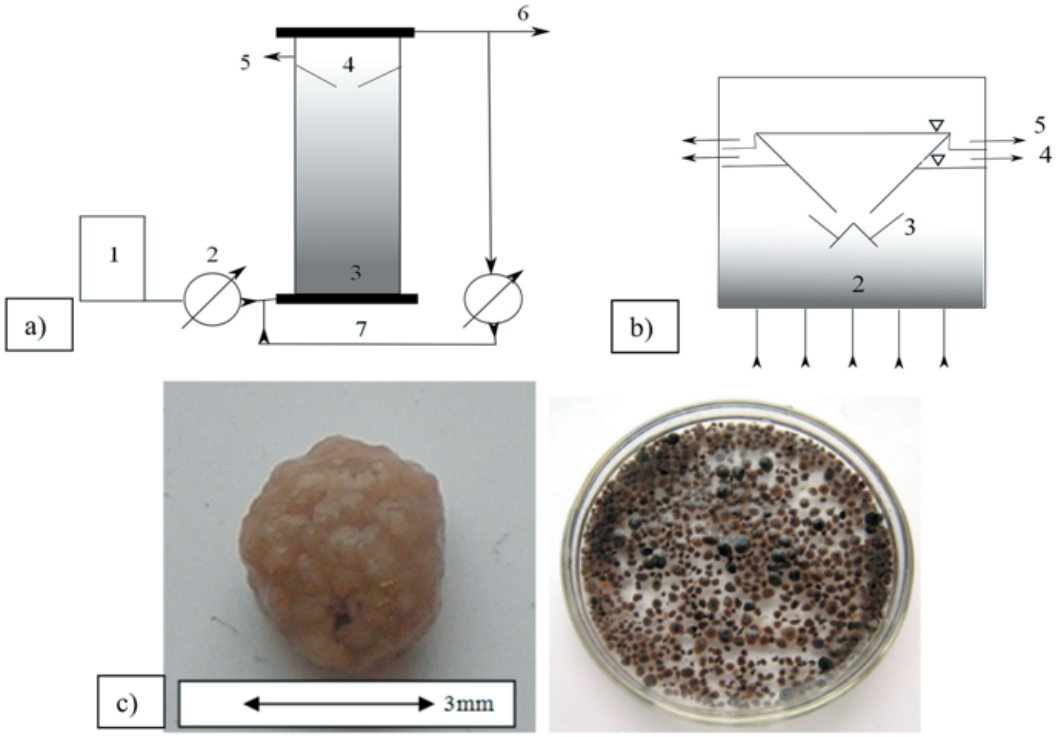

Fig. 1. a) Denitritation USB reactor: 1) substrate (wastewater with $N\text{-}NO_2$ and organic compound e.g. methanol); 2) influent pump; 3) sludge bed with granular biomass; 4) g/l/s separator; 5) denitritation gas (mainly N_2); 6) treated wastewater effluent; 7) recycle of treated wastewater. b) Details of g-l-s separator: 1) influent; 2) sludge bed; 3) separator; 4) denitritation gas; 5) effluent. c) granular denitritation biomass.

concentration gradient, with higher concentrations of substrate (N-NO_2 plus organic compound, e.g. methanol) in the bottom part of the reactor.

N-NO_2 is commonly described as a possible inhibitor of biological processes. However, most attention has been focused on the impact on nitrification (either in the dissociated form of NO_2^- (Buday et al., 1999) or the undissociated form of HNO_2 (Anthonisen et al., 1976; Park et al., 2010)). Here, also methanol was considered as a potential alternative inhibitor of biological processes.

Little information on the N-NO_2 or methanol inhibitory effect (substrate inhibition) on denitritation granular biomass is available. Only the effect of N-NO_2 on denitrification has been reported. According to Bilanovic et al. (1999) and Chen et al. (1991), concentrations of 100—200 mg dm^{-3} and 2000 mg dm^{-3} of total N-NO_2, respectively, did not inhibit denitrification (measured in experiments conducted with adapted biomass). Beccari et al. (1983) and Versefeld et al. (1977) observed denitrification inhibition at 10—150 mg dm^{-3} of total N-NO_2 with non-adapted biomass. According to Abeling et al. (1992), denitrification was inhibited by undissociated HNO_2, with an inhibitory limit of 0.13 mg dm^{-3} of HNO_2. Chen et al. (1991) determined that adapted denitrification bacteria can tolerate 0.02—0.16 mg dm^{-3} of HNO_2.

Potential risk of denitritation substrate inhibition was described in Babjaková et al. (2013). In USB reactors with granular biomass, the efficiency of denitritation with methanol as an external organic substrate was significantly reduced after the interruption of treated water recycle (Fig. 1a, stream 7). One possible explanation is that the inflow was not diluted with the recycle. This dilution reduced the negative influence of the substrate concentration on the denitritation biomass.

For this reason, a series of inhibition tests with granular denitritation biomass were performed. The effects of total N-NO_2 (dissociated plus undissociated form), undissociated HNO_2, methanol concentration, and pH were monitored with the aim to determine substrate inhibition on granular biomass. Methanol is a typical organic substrate used for denitritation or denitrification because it is easily biodegradable, relatively cheap and contains carbon with low oxidation number (–II). Compact granules with diameters from 1 to 3 mm (Fig. 1c) are generally considered to be more resistant to external influence because, compared to ambient water, relatively large volumes with different conditions are likely to occur inside the granules. For example, OH^- and HCO_3^- ions produced by denitritation can increase pH inside the granules (Drtil et al., 1995) or the substrate concentrations might be lower due to lower substrate diffusion into the granules.

In cases where that substrate is not an inhibitor, kinetics of substrate removal can be described by the Monod equation (Eq. 1, Fig. 2a). From this equation it follows that the removal rate increases with the increasing substrate concentration until the maximum removal rate is reached:

$$r_X = r_{X,\max} \cdot S/(K_S + S) \quad (1)$$

where r_x is the specific substrate removal rate (mg g^{-1} h^{-1}); mg of substrate per gram of biomass), $r_{x,\max}$ is the specific maximum substrate removal rate (mg g^{-1} h^{-1}), S is the substrate concentration (mg dm^{-3}) and K_S is the saturation constant (concentration of substrate S with removal rate equal to $r_{x,\max}/2$).

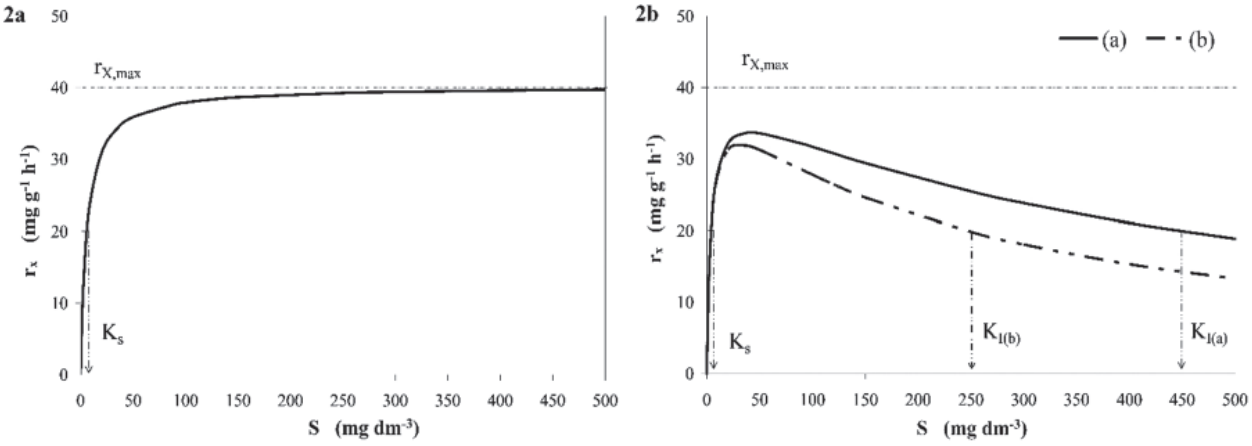

Fig. 2. Typical dependence of substrate kinetics according to the Monod equation (Fig. 2a, Eq. 1. No substrate inhibition: $r_{X,\max}$ = 40 mg g^{-1} h^{-1}, K_S = 10 mg dm^{-3}) and the Haldane equation (Figure 2b, Eq. 2. Substrate exhibits inhibition. Full line: $r_{X,\max}$ = 40 mg g^{-1} h^{-1}, K_S = 10 mg dm^{-3}, $K_{I(a)}$ = 450 mg dm^{-3}, intermittent line: $r_{X,\max}$ = 40 mg g^{-1} h^{-1}, K_S = 10 mg dm^{-3}, $K_{I(b)}$ = 250 mg dm^{-3}).

If the substrate is an inhibitor, r_x values are lower due to inhibition and r_x begins to decrease from a certain *S*. The Haldane equation is most commonly used to describe the substrate inhibition kinetics (Eq. 2, Fig. 2b) (Carrera et al., 2004):

$$r_X = r_{X,\,max} \cdot S/(K_S + S + S^2/K_I) \quad (2)$$

where r_x is the specific rate of substrate removal (mg g^{-1} h^{-1}), $r_{x,\,max}$ is the specific maximum substrate removal rate (mg g^{-1} h^{-1}), *S* is the substrate concentration (mg dm^{-3}), K_S is the saturation constant (concentration of substrate *S* with removal rate equal to $r_{x,\,max}/2$) and K_I is the inhibitory constant. The substrate inhibition is inversely correlated with the inhibitory constant K_I. Figure 2b shows that inhibition is more intensive if $K_{I(b)}$ (intermittent line) is lower than $K_{I(a)}$ (full line).

Materials and methods

Denitritation inhibition tests were realized with granular biomass samples taken from a laboratory USB reactor (Fig. 1) already adapted to denitritation with methanol (wastewater containing 500 mg dm^{-3} of $N\text{-}NO_2$ and 1500 mg dm^{-3} of $COD_{methanol}$ was treated with denitritation efficiency higher than 95 % at the loading of 2 kg $N\text{-}NO_2$ m^{-3} d^{-1} and the recycle ratio of 1). The biomass sample was mixed half a day before the test to reach endogenous conditions without exogenous substrate and was then repeatedly washed with drinking water without O_2 (water after nitrogen sparging). Initial biomass concentration in the test was 8 g dm^{-3} and its change during the experiment was negligible.

The denitritation tests were performed similarly to the batch kinetic tests. PO_4-P (KH_2PO_4) was added at the start of each test so that the weight ratio $COD_{methanol}$: P was 100 : 1, while pH was adjusted to the desired value with 1 M and 0.1 M HCl or NaOH. Subsequently, the mixture was sparged with nitrogen for 30 minutes to completely remove dissolved oxygen, and specific amounts of $N\text{-}NO_2$ and methanol were added to this mixture. Concentrations of $N\text{-}NO_2$ in the tests were in the range from 5 to 500 mg dm^{-3}, and those of $COD_{methanol}$ were in the range from 20 to 2000 mg dm^{-3}. The pH range in the tests was from 4.6 to 8.5. The relevant concentrations of undissociated HNO_2 were calculated according to Anthonisen et al. (1976) from the concentration of $N\text{-}NO_2$ and pH (Eqs. 3 and 4). Concentration range of HNO_2 was from 0.0002 to 2 mg dm^{-3}.

$$HNO_2 = (47/14) \cdot N\text{-}NO_2/(K_a \cdot 10^{pH}) \quad (3)$$

where HNO_2 and $N\text{-}NO_2$ are the concentrations in mg dm^{-3}, and K_a is the ionization constant of HNO_2.

$$K_a = e^{(-2300/T)} \quad (4)$$

where T is the temperature in Kelvin.

A total of 21 denitritation tests were performed. The biomass was mechanically stirred in 300 mL closed flasks during the tests. The stirrer speed was up to 100 min^{-1} (sufficient for mixing of granular biomass without its mechanical destruction). With regard to the production of OH^- in the denitritation, pH was continuously adjusted to the initial value by additions of 0.1 and 0.01 M HCl.

Activity of denitritation biomass was evaluated from the specific denitritation rates, r_X (mg of $N\text{-}NO_2$ per gram of biomass per hour) measured at various concentrations of methanol, $N\text{-}NO_2$, and at different pH values. The rates were calculated from the linear part of the $N\text{-}NO_2$ concentration decrease curve. Samples with the volume of 5 mL were taken in 10- to 30-min intervals, they were filtered immediately, and the $N\text{-}NO_2$ concentration was determined by a spectrophotometric method (APHA, 2005). Temperature in the tests was between 18—21 °C.

Results and discussion

Specific denitritation rates, r_X, are summarized in Figures 3—5. Dependencies in these figures were compared with the Haldane kinetics model (their correspondence with Eq. 2 and Fig. 2b). The correlation coefficients show the compliance with this equation (the closer the correlation coefficient is to 1, the higher the conformity with Eq. 2). Similarly, the substrate inhibition of nitrification was evaluated in Buday et al. (1999) and Carrera et al. (2004).

Comparing Figures 3 and 4 with Figure 2b, it is evident that $N\text{-}NO_2$ and methanol do not show any dependence, which confirms substrate inhibition. This conclusion was also confirmed by the very low calculated correlation coefficient values. Correlation coefficient for $N\text{-}NO_2$ was only 0.13 (other parameters from Eq. 2 were: $r_{x,\,max}$ = 2.1 mg g^{-1} h^{-1}, K_S = 5 mg dm^{-3}, K_I = 1950 mg dm^{-3}) and that for COD was 0.11 ($r_{x,\,max}$ = 2.5 mg g^{-1} h^{-1}; K_S = 76 mg dm^{-3}; K_I = 2670 mg dm^{-3}).

Substrate inhibition, which correlates with the Haldane kinetics and Eq. 2, was observed only with undissociated HNO_2 (Fig. 5). In this case, denitritation activity increased with the increasing HNO_2 concentration; reaching a maximum at the concentration of 0.01—0.1 mg dm^{-3}; then it begun to decrease with the increasing HNO_2 concentration. The calculated correlation coefficient was 0.79, which confirms the dependence according to Eq 2. Therefore, in Figure 5, experimentally measured values were compared with the dependence calculated according to Eq. 2 (intermittent

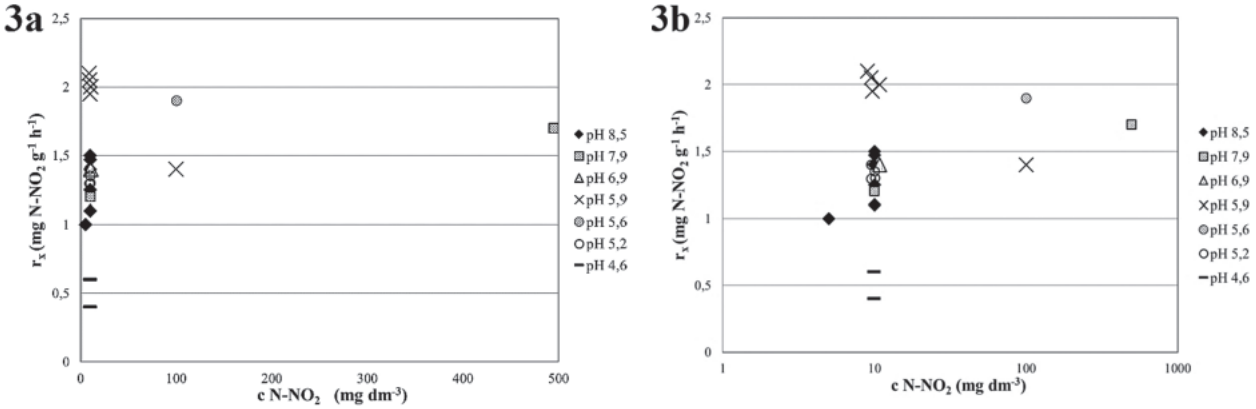

Fig. 3. Effect of N-NO_2 concentration on denitritation rate, r_X (3a). Graph with logarithmic scale (3b) is introduced to better distinguish r_x values at low N-NO_2 concentrations.

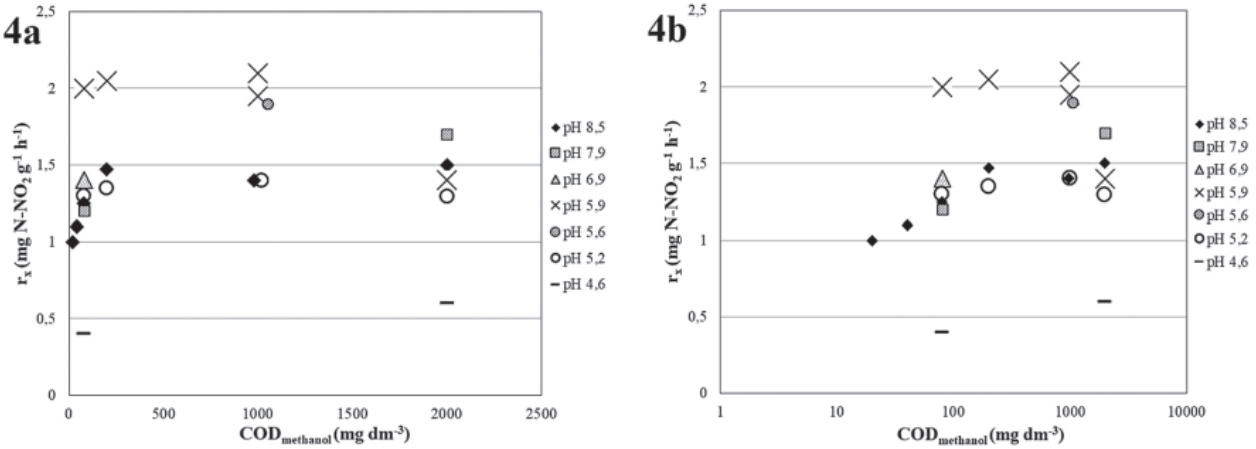

Fig. 4. Effect of methanol concentration on denitritation rate, r_X (4a). Graph with logarithmic scale (4b) is introduced to better distinguish r_x values.

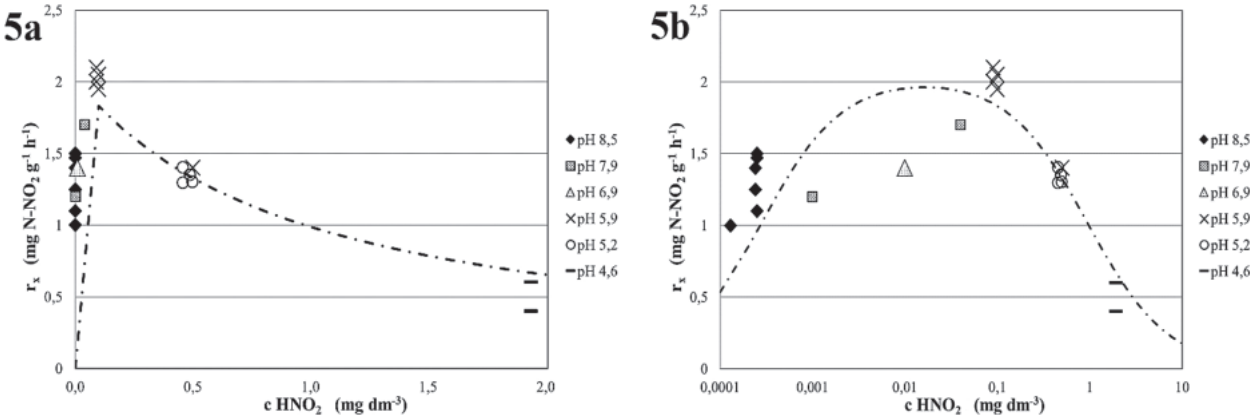

Fig. 5. Effect of HNO_2 concentration on denitritation rate, r_X (5a). Graph with logarithmic scale (5b) is introduced to better distinguish r_x values at low HNO_2 concentrations.

curve with calculated $r_{x,\ max}$ = 2.03 mg g^{-1} h^{-1}, K_S = 0.00028 mg dm^{-3}, K_I = 0.95 mg dm^{-3}, correlation coefficient = 0.79). Similar inhibition limit for denitrification (0.13 mg dm^{-3} HNO_2) was measured also by Abeling et al. (1992). The range of HNO_2 concentrations still tolerated by denitritation granular biomass (up to 1.9 mg dm^{-3} according to Fig. 5) is wider than the range reported by Chen et al. (1991) (up to 0.16 mg dm^{-3} HNO_2). However, the decrease of denitritation activity with the increasing HNO_2 concentration is significant (35 % inhibition compared to the maximum r_X at 0.5 mg dm^{-3} of HNO_2 and 75 % at 1.9 mg dm^{-3} of HNO_2; Fig. 5).

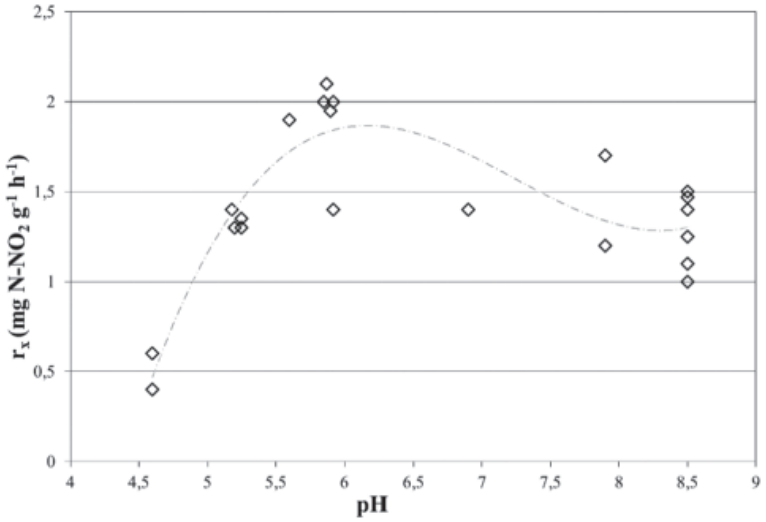

Fig. 6. Effect of pH on denitritation rates, r_X.

Inhibition found for undissociated HNO_2 explains the reduced denitritation efficiency in USB reactors without effluent recycle (Fig. 1a, without stream 7) Babjaková et al. (2013). Recycle dilutes the influent and reduces the HNO_2 concentration in the reactor, especially in the bottom part with the sludge bed. Therefore, effluent recycle is recommended for any upflow reactor with substrate concentration gradient.

The dependence of r_X and pH (Fig. 6) summarized from all tests shows that pH 5.9 is optimal for denitritation. The dependence of r_x and pH in Figure 6 is also highlighted by a trend line (intermittent curve with a calculated correlation coefficient of 0.93).

It is interesting that denitritation was observed also at very low pH = 4.6. This can be explained by higher internal pH in big and compact granules with diameters of up to 3 mm (Fig. 1c) compared to ambient water (due to denitritation producing OH^- and subsequently HCO_3^- ions, Drtil et al., 1995). Such internal conditions with pH different from ambient wastewater was detected also in the experiments with biomass fixed in polyurethane cubes used as biomass carrier (cubes with the size from 0,75 cm up to 1,5 cm, with fixed biomass concentration of up to 13.3 g dm^{-3}, Drtil et al., 1994). Simultaneous denitrification in deeper parts of the biomass carriers improved nitrification at acid pH of 4.2—6.2.

Figures 3—6 also illustrate the relatively low denitritation rates of granular biomass from a USB reactor in the range of 0.4 to 2.2 mg $N\text{-}NO_2\ g^{-1}\ h^{-1}$. Similar rates (0.4 mg $N\text{-}NO_2\ g^{-1}\ h^{-1}$) were obtained by Abeling et al. (1992). However, much higher values, up to 7.7 mg $N\text{-}NO_2\ g^{-1}\ h^{-1}$, were reported by Chen et al. (1991). Re-calculating the rates in Figures 3—6 to oxygen equivalents (1 mg of $N\text{-}NO_2$ is equivalent to 1.7 mg of O_2; 1 mole of nitrogen accepts 3 electrons, and 1 mole of oxygen accepts 2 electrons) provides rates equivalent to respiratory rates of 0.7—3.4 mg $O_2\ g^{-1}\ h^{-1}$. Such values are relatively low considering they represent the total rate including endogenous and exogenous denitritation with methanol (e.g., compare with Cech et al. (1984)). However, this fact does not handicap granular biomass in the USB reactor; due to excellent sedimentation properties of the granules, it is possible to maintain extremely high biomass concentrations in the USB reactor (up to 40—50 g dm^{-3}, Pagacova et al., 2010).

Conclusions

A series of inhibition tests have shown the effect of substrate inhibition on adapted granular denitritation biomass only for undissociated HNO_2. Total $N\text{-}NO_2$ and methanol were not confirmed as relevant substrate inhibitors in the tested concentration range. Optimal denitritation pH was 5.9. Denitritation rates higher than 0.4 mg $N\text{-}NO_2\ g^{-1}\ h^{-1}$ (with maximum of 2.2 mg $N\text{-}NO_2\ g^{-1}\ h^{-1}$) were measured with granular biomass at concentrations up to 500 mg dm^{-3} of $N\text{-}NO_2$, 2000 mg dm^{-3} of $COD_{methanol}$ and 2 mg dm^{-3} of undissociated HNO_2.

Acknowledgement

This research is a part of the project VEGA 1/0772/16 and was supported by the Scientific Grant Agency of the Slovak Republic. The Authors are grateful to American Manuscript Editors for English revision.

References

Abeling U, Seyfried CF (1992) Water Science Technology 26/5—6: 1007—1015.

Anthonisen AC, Loehr RC, Prakasam TB, Srinath EG (1976) Journal Water Pollution Control Federation 48/5: 835—850.
APHA (2005) Standard methods for the examination of water and wastewater, 21st edn. American Public Health Association, Washington, DC.
Babjaková L, Drtil M, Imreová Z, Jonatová I (2013) Vodní hospodářství 63/2: 36—41.
Beccari M, Passino RR, Tandoi V (1983) Journal of Water Pollution Control Federation 55/1: 58—64.
Bilanovic D, Battistoni P, Cecchi F, Pavan P, Mata-Alvarez J (1999) Water Research 33/15: 3311—3320.
Buday J, Drtil M, Hutňan M, Derco J (1999) Chemical Papers 53/6: 379—383.
Carrera J, Jubany I, Carvallo L, Chamy R, Lafuente J (2004) Process Biochemistry 39/9: 1159—1165.
Cech JS, Chudoba J, Grau P (1985) Water Science Technology 17/2—3: 259—272.
Chen SK, Juaw CK, Cheng SS (1991) Water Science Technology 23/7—9: 1417—1425.
Drtil M, Németh P, Kucman K, Bodík I, Kašperek V (1995) Water Research 29/5: 1353—1360.
Drtil M, Bodík I, Derco J, Hutňan M (1994) Nutrient Removal from Wastewaters: 103—108.
Galbová K, Pagáčová P, Drtil M, Jonatová I (2010) Chemical Papers 64/2: 132—138.
Hellinga C, Schellen AAJC, Mulder JW, van Loosdrecht MCM, Heijnen JJ (1998) Water Science Technology 37/9: 135—142.
Jenicek P, Svehla P, Zabranska J, Dohanyos M (2004) Water Science Technology 49/5—6: 73—79.
Pagáčová P, Galbová K, Drtil M, Jonatová I (2009a) Bioresource Technology 101/1: 150—156.
Pagáčová P, Drtil M, Galbová K (2009b) Chemical Papers 63/2: 125—130.
Park S, Bae W, Rittmann BE (2010) Environmental Science Technology 44/1: 335—342.
Svehla P, Bartacek J, Pacek L, Hrnciarova H, Radechovsky J, Hanc A, Jenicek P (2014) Chemical Papers 68/7: 871—878.
Versefeld Van HW, Meijer EM, Stouthamer AH (1977) Archives of Microbiology 112: 17—23.

sciendo

Bis(3-methylsalicylato)bis(picolinamide)copper(II) complex — preparation, spectral properties and supposed structure

Simona Matejová[a], Miroslava Puchoňová[a], Dominika Hrindová[a], Vladimír Jorík[a], Milan Mazúr[b], Dušan Valigura[c]

[a]*Department of Inorganic Chemistry, Faculty of Chemical and Food Technology, Slovak University of Technology, Radlinského 9, 812 37, Bratislava, Slovakia*
[b]*Department of Physical Chemistry, Faculty of Chemical and Food Technology, Slovak University of Technology, Radlinského 9, 812 37, Bratislava, Slovakia*
[c]*Department of Chemistry, University of SS Cyril and Methodius in Trnava, J. Herdu 2, 917 01 Trnava, Slovakia*
miroslava.puchonova@stuba.sk

Abstract: Blue methylsalicylatocopper(II) complex with picolinamide $Cu(3\text{-Mesal})_2(pnia)_2$ has been prepared and characterized by elemental analysis and spectral methods. Based on the infrared spectra, monodentate coordination of 3-methylsalicylate anion has been assumed and the coordination variability of the anion has been shown. By determination and refinement of the unit cell from powder diffraction data, the existence of a monomeric Cu(II) complex can be anticipated. EPR spectrum of the complex is in good agreement with these results. The *g*-factors fulfil the relation $g_{||} > g_{\perp} > 2.0023$, which is consistent with the $d_{x^2-y^2}$ ground electronic state and indicates coordination sphere of distorted tetragonal symmetry $\{CuN_2O_2O_2'\}$ for the central copper(II) ions.

Keywords: picolinamide, powder diffraction analysis, copper(II) complex, spectral properties, EPR spectroscopy

Introduction

Superoxide dismutase (SOD) is a copper containing enzyme present in most living systems which catalyzes dismutation of the superoxide anion. When the catalytical function of the enzyme is disturbed, various disorders can occur in the biosystem. Therefore, the preparation of low molecular weight analogues mimicking the SOD enzyme function has great potential in medicine. In previous studies, copper(II) complexes with nicotinamide (*nia*) derivatives have been examinated for many reasons e.g. their biological aspects (antiinflammatory, antibacterial, SOD mimetic activities) and of course for their magnetic or structural properties (Zvimba, 2007; Puchoňová, 2018; Shiekl, 2018). Information concerning the complex structure is important for understanding the interaction between molecules in a solution as well as in pure substance solid state and moreover in cocrystal formation. Different intermolecular interactions can lead to the formation of various supramolecular architectures which leads to variable structure modifications. It is well known that hydrogen bonds formation plays a significant role, therefore, these coordination compounds are interesting for solid state chemistry and bioinorganic chemistry (Moncol, 2008; Repická, 2010). Currently, *nia* derivatives like picolinamide (*pnia*) or isonicotinamide (*inia*) provide several structure motifs especially in this field of various carboxylatocopper(II) complexes. So, the final product formation and coordination mode of bonded ligands are influenced by the positional isomers of nicotinamide (Fig. 1.).

The most frequent coordination mode of *nia* and *inia* is monodentate by nitrogen atom of the pyridine ring (Özbek, 2017; Bozkurt, 2013, Köse, 2011, Hökelek, 2010). Only a few complexes containing these ligands are coordinated in the bridging mode where oxygen atom of the carboxamide group is bonded to the neighbouring central atom (Perec, 2011; Kozlevčar, 1999; Moncol, 2007). On the other hand, the picolinamide molecule (*pnia*) is dominantly coordinated only in the chelating bonding mode by the pyridine ring nitrogen atom and by the carboxamide group oxygen atom (Sieron, 2004). Only several examples of carboxylatocopper(II) complexes with *pnia* can be found in literature (Dačič, 2013).

Our attention has focused on the preparation of novel biologically (SOD) active copper(II) compounds with picolinamide and on their characterization. A new coordination compoud of the composition $Cu(3\text{-Mesal})_2(pnia)_2$, its chemical and physical properties, are presented. Possible structural motif

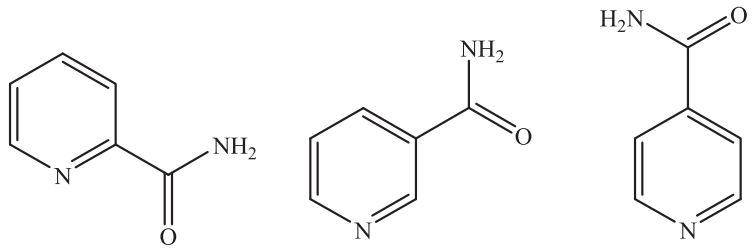

a) pnia b) nia c) inia

Fig. 1. Positional isomers of nicotinamide.

of the prepared complex and its purity were studied by elemental analysis (EA), powder diffraction analysis (XRPD), electronic absorption spectra (UV/Vis), infrared spectra (IR) and Electron Paramagnetic Resonance spectroscopy (EPR).

Coordination variability of the studied compoud $Cu(3\text{-}Mesal)_2(pnia)_2$ was compared with that of previously published $[Cu(3\text{-}Mesal)_2(inia)_2]_2$, $[Cu(3\text{-}Mesal)_2(nia)_2]$ complexes (Puchoňová, 2018; Puchoňová, 2015).

Experimental

Synthesis

Analytical grade (Sigma, USA or Acros Organics, USA) chemicals and solvents were used without further purification. Picolinamide (*pnia*) was washed down with a necessary amount of solvent (water or acetonitrile) into the aqueous solution of copper(II) acetate. Then, 3-methylsalicylic acid was added to the reaction mixture. The precipitate was filtered off and the mother liquid was left for crystallization. The product was characterized by available methods as elemental analysis, infrared spectra and powder X-ray diffraction.

Anal Calc for $Cu(3\text{-}Mesal)_2(pnia)_2$: C, 55.1; H, 4.3; N, 9.2. Found: C, 54.6; H, 4.4; N, 9.1.

Apparatus and physical measurement

Analyses of carbon, hydrogen and nitrogen were carried out on a CHNSO FlashEATM 1112 Automatic Elemental Analyzer. Infrared spectrum (4000—400 cm^{-1}) of the complex was measured on a NICOLET 5700 FT-IR spectrophotometer at room temperature using the ATR technique. Electronic spectrum (190—1100 nm) of the compound was measured in a Nujol suspension using a SPECORD 250 Plus spectrophotometer at room temperature.

The first derivative Cu(II) EPR spectrum of polycrystalline copper(II) complex was recorded on an X-band (≈ 9.4 GHz) EMX EPR spectrometer (Bruker, Germany) at room temperature. The spin Hamiltonian parameter values were obtained from the experimental EPR spectra using WinEPR (Thiele, 1992) and then they were further refined by computer simulation using SimFonia (Weber, 1995).

X-ray powder diffraction analysis was carried out on a parafocusing Bragg Brentano diffractometer Philips PW1820 using CoKα radiation (40 kV, 35 mA) equipped with an automatic divergence slit and a curved graphite monochromator placed in the diffracted beam. The polycrystalline sample was measured in Si zero-background sample holder in the 2θ range of 3—60 °, step size of 0.02 ° and the counting time of 1 s per step at room temperature. The structures were drawn using Mercury 2.0. (Macrae, 2008)

Result and discussion

A change of the reaction conditions (stoichiometric ratio = Cu : pnia : 3MesalH or solvent) led to the formation of a new complex of the composition $Cu(3\text{-}Mesal)_2(pnia)_2$ which was found based on EA. The blue product was formed in the stoichiometry of 1 : 2 : 2 in water. The prepared complex absorbed at 632 nm; this broad asymmetric ligand field band attributes to the *d←d* transition maxima which corresponds to its blue colour. There are also intraligand bands (250—300 nm) and charge transfer bands in the range of 300—350 nm.

Infrared spectrum of $Cu(3\text{-}Mesal)_2(pnia)_2$ comprises bands confirming the presence of all characteristic functional groups. The spectrum contains characteristic of a broad envelope of probably two or three overlapping medium intensity bands with their maxima in the region from 3250 to 3500 cm^{-1} assignable to OH stretches and two medium intensity band assignable to NH vibration at about 3180 cm^{-1} and 3305 cm^{-1}. The bands corresponding to $\nu_{as}(COO^-)$ and $\nu_s(COO^-)$ are at 1602 cm^{-1} and 1394 cm^{-1}. Differences between antisymmetric and symmetric stretch ($\Delta\nu = \nu_{as} - \nu_s$) are greater than $\Delta\nu$ for the ionic form. The $\Delta\nu$ value for the complex is consistent with the monodentate mode of the carboxylate group (Nakamoto, 2009).

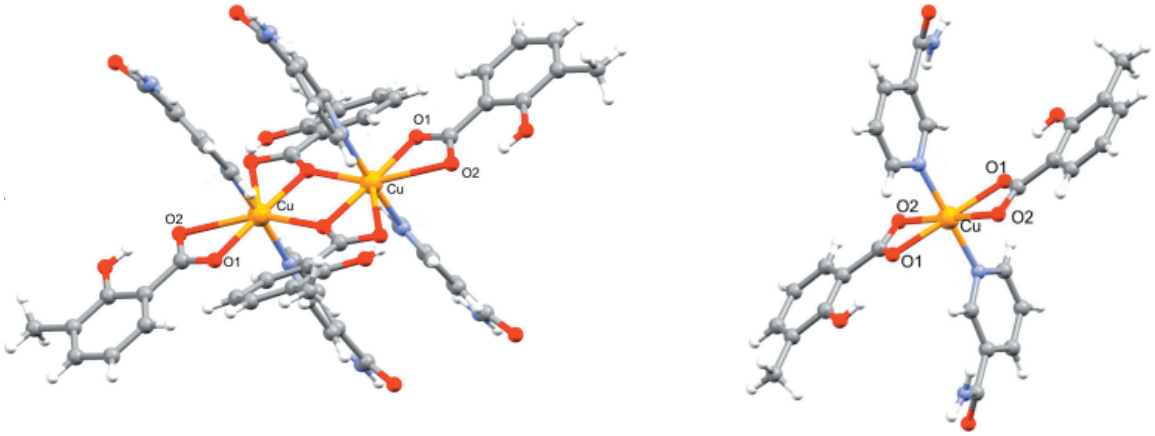

a) $[Cu(3\text{-}Mesal)_2(inia)_2]_2$ b) $[Cu(3\text{-}Mesal)_2(nia)_2]$

Fig. 2. Molecular structure of complexes (Puchoňová, 2018; Puchoňová, 2015).

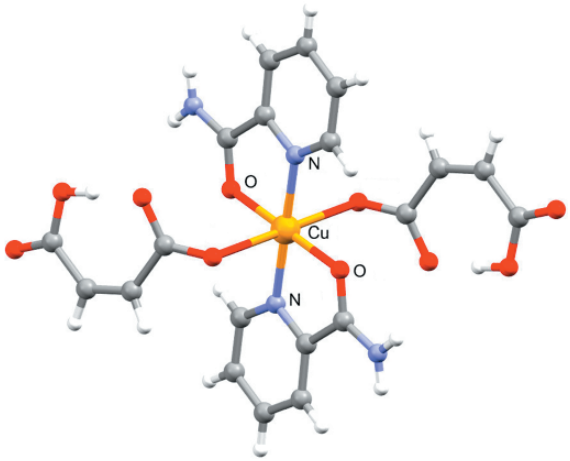

Fig. 3. Molecular structure of complex $[Cu(mal)_2(pnia)_2]$ (Sieron, 2007).

Literature data provide some evidence of 3-methylsalicylate variability of coordination modes which are shown in Fig. 2 (Puchoňová, 2018; Puchoňová, 2015) as well as a difference of the anion coordination mode in relation to the nicotinamide derivatives. Bidentate chelating mode is preferred in monomeric $[Cu(3\text{-}Mesal)_2(nia)_2]$ and bidentate chelating together with bridging mode were found in the dimeric $[Cu(3\text{-}Mesal)_2(inia)_2]_2$ complex. According to data from the Cambridge Structural Database, the length of Cu—O bond in methylsalicylate copper(II) complexes is in the range of 1.94–2.03 Å for chelating or monodentate mode, and 1.92–2.06 Å (Cu—O1 shorter bond) 2.35–2.78 Å (Cu—O2 longer bond) for bidentate chelating mode (CSD version 5.40 updates November 2018; Groom, 2016). For the presented compound, $Cu(3\text{-}Mesal)_2(pnia)_2$, monodentate bonding mode has been suggested from the anion spectral data.

Moreover, the absence of C=O vibration in the IR spectrum of $Cu(3\text{-}Mesal)_2(pnia)_2$ at about 1690 cm^{-1} allows us to suppose that oxygen atom of the *pnia* carboxamide group is bonded to the central atom (Bakiler, 2007). Literature and crystallographic database provide additional examples where the picolinamide molecule is bonded in the bidentate chelating mode by nitrogen atom of the pyridine ring and oxygen atom of the carboxamide group to central atom. One of them is carboxylatocopper(II) complex $[Cu(mal)_2(pnia)_2]$ where *mal* is monoanion of maleic acid (Fig. 3) (Sieron, 2007). In this type of copper(II) complexes, the length of Cu—O bond is in the range of 1.94–2.38 Å, and that of Cu—N is 1.96–2.00 Å. If derivatives of nicotinamide are joined to copper atom only by nitrogen atom, the distance of Cu—N is in the range of 1.94–2.38 Å (CSD version 5.40 updates November 2018; Groom, 2016).

EPR spectrum of the polycrystalline complex $Cu(3\text{-}Mesal)_2(pnia)_2$ measured at room temperature is shown in Figure 4. The corresponding computed EPR spectrum is indicated by the red line. An axially symmetric Cu(II) EPR spectrum with unresolved hyperfine splitting was obtained. Additionally, the EPR

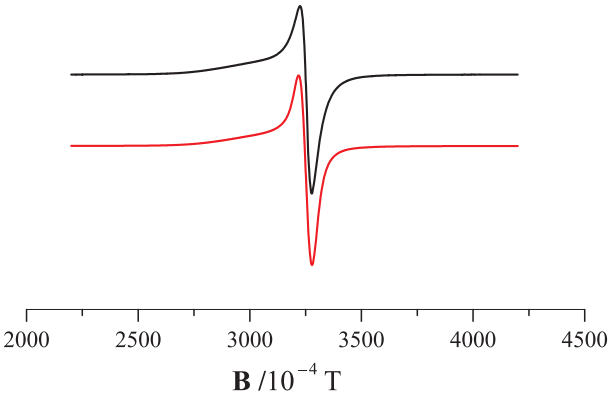

Fig. 4. Experimental (black line) and simulated (red line) EPR spectra of copper(II) complex recorded at room temperature.

spectrum of this copper(II) complex was measured in a wide sweep width of 800 mT. However, no typical EPR resonance due to the presence of copper(II) dimeric complex was observed.

The spin Hamiltonian parameters evaluated from the experimental Cu(II) EPR spectrum and further refined by computer simulation are $g_{||} = 2.267 \pm 0.002$, $g_{\perp} = 2.078 \pm 0.002$. The g-factor values of the axially symmetric Cu(II) EPR spectra fulfilled the usual relation of $g_{||} > g_{\perp} > 2.0023$, which is consisted with the $d_{x^2-y^2}$ ground electronic state and indicates distorted tetragonal symmetry of coordination spheres for copper(II) central atoms.

Finally, the geometric parameter $G = (g_{||} - 2)/(g_{\perp} - 2)$ was calculated. The *G*-value is 3.423 and the relation of $G < 4$ indicates the presence of exchange interaction between the copper(II) ions (Hathaway, 1970a; Hathaway,1970b). The above presented *g*-factor values are in good accordance with those for similar monomeric copper(II) complexes reported in literature (Hathaway,1970a; Hathaway,1970b; Goodman, 1970; Halaška, 2016; Öztürk, 2012).

When single crystals with suitable size and good stability are not available, powder diffraction analysis (XRPD) is an appropriate method for structure determination. In such situations, a high quality powder pattern should be recorded. However, in this case, XRPD was used only to verify the phase purity of the sample and to determine the lattice parameters. Profile fitting and *ab initio* indexing of powder diffraction patterns collected for the presented complex with *pnia* were done using the multipurpose program CMPR (Toby, 2005) with incorporated autoindexing program DICVOL06 (Boultif, 2004). The best solution is the triclinic crystallographic system with the figure of merit being M(20) = 22.5 and the following unit cell parameters: $a = 7.1734(34)$ Å, $b = 7.1855(53)$ Å, $c = 14.9808(66)$ Å, $\alpha = 83.249(43)°$, $\beta = 78.227(38)°$, $\gamma = 61.305(53)°$. Subsequently, the obtained unit cell parameters were refined with the Le Bail method using program Jana2006 (Petříček, 2014), where correction of the powder profile (Legendre polynomials with 25 terms for calculation, Pseudo-Voigt peak-shape function, asymmetry by Berar-Baldinozzi correction) was performed. The refined unit cell parameters are: $a = 7.1753(15)$ Å,

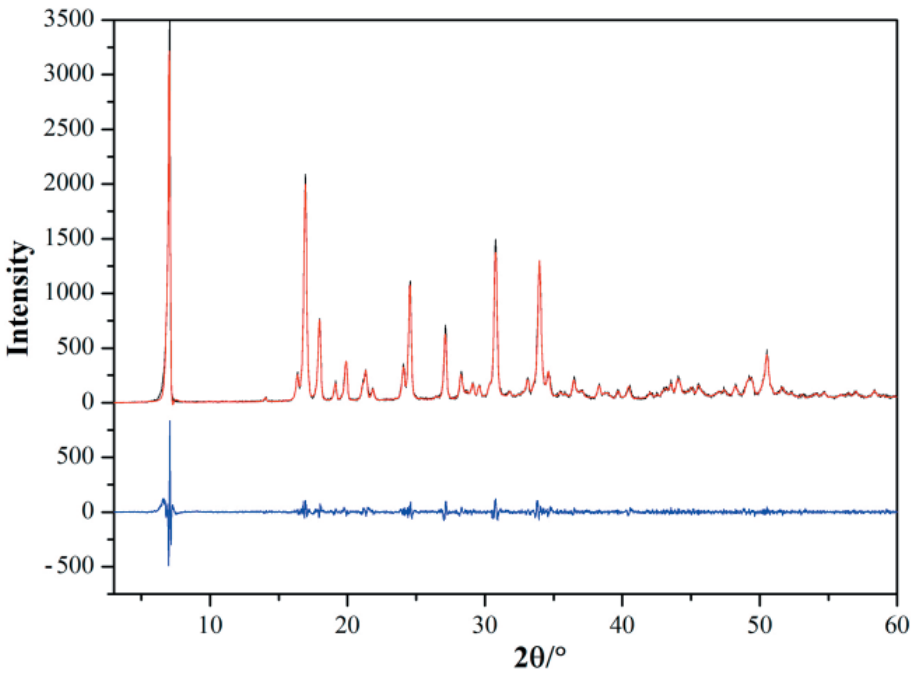

Fig. 5. Final Le Bail fit: measured data (black line), calculated data (red line) and difference curve (blue line) as a function of absolute diffracted intensity at the diffraction angle of 2θ.

Tab. 1. Comparison of unit cell volumes and crystal densities of Cu(II) complexes.

Chemical formula	Molecular formula	*Z*	*V* (Å^3)	Crystal density (g cm^{-3})
$[Cu(3\text{-}Mesal)_2(inia)_2]_2$	$2(C_{28}H_{26}CuN_4O_8)$	1	1345.56(14)	1.5058(2)
$[Cu(3\text{-}Mesal)_2(nia)_2]$	$C_{28}H_{26}CuN_4O_8$	4	2836.86(17)	1.4284(2)
$Cu(3\text{-}Mesal)_2(pnia)_2$	$C_{28}H_{26}CuN_4O_8$	1	664.4(2)	1.5247(3)

*all samples were measured at the room temperature

b = 7.1863(9) Å, c = 15.0034(22) Å, α = 83.219(13)°, β = 78.286(16)°, γ = 61.328(17)° and V = 664.4(2) Å^3. As shown in Fig. 5, the polycrystalline sample of $Cu(3\text{-}Mesal)_2(pnia)_2$ does not contain any impurities.

Based on the volume of the unit cell from JANA2006 (V = 664.4(2) Å^3) in comparison to densities and volumes considering number of formula units Z of previously solved crystal structures of complexes $[Cu(3\text{-}Mesal)_2(inia)_2]_2$ and $[Cu(3\text{-}Mesal)_2(nia)_2]$ (Table 1). We can claim that possible molecular structure of the complex is monomeric with the given chemical formula, which is in good agreement with the conclusion from EPR and infrared spectroscopy. Experimental errors for crystal densities of $[Cu(3\text{-}Mesal)_2(inia)_2]_2$ and $[Cu(3\text{-}Mesal)_2(nia)_2]$ were evaluated using the standard analysis errors (Taylor, 1997).

Conclusion

In conclusion, a new $Cu(3\text{-}Mesal)_2(pnia)_2$ complex was prepared and characterized by available methods (EA, UV/Vis, IR, EPR and XPRD). The polycrystalline complex EPR spectrum recorded at room temperature gave the g-factor values of $g_{||} > g_{\perp} > 2.0023$, which is consistent with the $d_{x^2-y^2}$ ground electronic state and indicates the coordination sphere of distorted tetragonal symmetry for central copper(II) ions. Based on infrared spectroscopy, we can suggest a monodentate bonding mode of the carboxylate group of 3-methylsalicylate and bidentate chelating mode of picolinamide can be proposed. The possibility of monomeric unit presence in this complex structure has been found from X-ray powder diffraction analysis, which was used only to verify the phase purity of the sample and to determine the lattice parameters of $Cu(3\text{-}Mesal)_2(pnia)_2$. However, collection of high quality powder diffraction data or growing of suitaible single crystal is necessary for structure determination. Up to today, any salicylatocopper(II) complex with *pnia* has not been found in the Cambridge Structural Database nor in literature. Therefore, the subsequent reaserch will be related to the synthesis of other methylsalicylatocopper(II) complexes with *pnia* and the study of their SOD mimetic activity which could be potencially used in medicine

Acknowledgement

This work was supported by courtesy of the Slovak Grant Agency (VEGA 1/0686/17, VEGA 1/0639/18) and by the Slovak Research and Development Agency under the contact No. APVV-15-0053. MM thanks the Ministry of Education, Science, Research and Sport of the Slovak Republic for funding within the scheme "Excellent research teams".

References

Bakiler M, Blukbasi O, Yilmaz A (2007) J. Mol. Struct. 826: 6.

Boultif A, Louer D (2004) J. Appl. Crystallogr. 37(5): 724.

Bozkurt N, Dilek N, Caylak Delibas N, Necefoglu H, Hökelek T, Saka G, Tercan B, Cimen E, Necefoglu H (2013) Acta Crystallogr. Sect. E: Struct. Rep. Online 69: m356.

Goodman BA, Raynor JB (1970) Adv. Inorg. Chem. Radiochem. 13: 135.

Groom CR, Bruno IJ, Lightfoot MP, Ward SC (2016) Acta Cryst. B72: 171.

Hathaway BJ, Tomlinson AAG (1970a) Coord. Chem. Rev. 5: 1.

Hathaway BJ, Billing DE (1970b) Coord. Chem. Rev. 5: 43.

Halaška J, Čechová D, Lawson MK, Růzičková Z, Jorík V, Koman M, Valko M, Kozlevčar B, Moncol J (2016) Chem. Papers 70: 101.

Hökelek T, Saka G, Tercan B, Cimen E, Necefoglu H (2010) Acta Crystallogr. Sect. E: Struct. Rep. Online 66: m955.

Kozlevčar B, Leban I, Turel I, Segedin P, Petric M, Pohleven F, White AJP, Williams DJ, Sieler J (1999) Polyhedron 18: 755.

Köse DA, Necefoglu H, Sahin O, Buyukgungor O (2011) J. Chem. Cryst. 41: 297.

Macrae CF, Bruno IJ, Chisholm JA, Edgington PR, McCabe P, Pidcock E, Rodriguez-Monge L, Taylor R, van de Streek J, Wood PA (2008)J. Appl. Cryst. 41: 466.

Moncol J, Maroszova J, Koman M, Melnik M, Valko M, Mazur M, Lis T (2008) J. Coord. Chem. 61: 3740.

Moncol J, Mudra M, Lonnecke P, Hewitt M, Valko M, Morris H, Svorec J, Melnik M, Mazúr M, Koman M (2007) Inorg. Chim. Acta 360: 3213.

Nakamoto K (2009) Infrared and Raman spectra of inorganic and coordination compounds, Part B, John Wiley&Sons, Inc, 118.

Özbek FE, Sertcelik M, Yuksek M, Necefoglu H, Celik RC, Nayir GY, Hökelek T (2017) J. Mol. Struct. 1150: 112.
Öztürk F, Bulut A, Paşaoglu H, Bulut I, Büyükgüngör O (2012) Spect. Chim. Acta: Part A: 97: 24.
Petříček V, Dušek, M, Palatinus L (2014) Z. Kristallogr. Cryst. 229(5): 345.
Puchoňová M, Matejová S, Jorík V, Šalitroš I, Švorc Ľ, Mazúr M, Moncol J, Valigura D (2018) Polyhedron 151: 152.
Puchoňová M, Repická Z, Moncol J, Růžičková Z, Mazúr M, Valigura D (2015) J. Mol. Struct. 1092: 1.
Repická Z, Moncol J, Puchoňová M, Jorík V, Mikloš D, Lis T, Padělková Z, Mazúr M, Valigura D (2010) Struct. Chem. 21(5): 1093.
Shiekh RA, Said MA, Malik MA, Hashmi AA (2018) Trop. J. Pharm. Research. 17 (5): 865.
Sieron L (2004) Acta Crystallogr. Sect. E: Struct. Rep. Online 60: m297.
Sieron L (2007) Acta Crystallogr. Sect. E: Struct. Rep. Online 63: m862.
Taylor JR (1997) An introduction to error analysis. Sausalito, Calif: University Science Books.
Thiele H, Etstling J, Such P, Hoefe P (1992) WINEPR, Bruker Analytic Gmb, Germany.
Toby BH (2005) J. Appl. Crystallogr. 38(6): 1040.
Valigura D, Moncol J, Korabik M, Pučeková Z, Lis T, Mrozinski J, Melník M (2006) Eur. J. Inorg. Chem. 3813.
Zvimba JN, Jackson GE (2007) J. Inorg. Biochem. 101: 148.
Weber RT (1995) WINEPR SimFonia, EPR Division, Bruker Instr. Inc., Billerica, USA.

sciendo

Recombinant human erythropoietin separation using a cation-exchange multimodal adsorbent

Marta Ostrihoňová, Jana Adamíková, Tomáš Molnár, Monika Antošová, Milan Polakovič

Department of Chemical and Biochemical Engineering, Institute of Chemical and Environmental Engineering, Faculty of Chemical and Food Technology, Slovak University of Technology, Radlinského 9, 812 37 Bratislava, Bratislava, Slovakia
milan.polakovic@stuba.sk

Abstract: This work deals with the capture of human recombinant erythropoietin (rhEPO) from a mixture of proteins in a concentrated postcultivation supernatant. Cation-exchange multimodal adsorbent Capto MMC ImpRes was selected as potential chromatographic separation material. Its equilibrium properties were investigated in batch adsorption experiments. The effect of pH in the range of 5.5—7.5 and NaCl concentration in the range of 0—300 mM on the adsorption of rhEPO and contaminant proteins was examined. Optimal conditions found in these equilibrium experiments were applied to rhEPO adsorption in a chromatographic column. Several experiments were carried out at different elution conditions to optimize the rhEPO yield and selectivity.

Keywords: erythropoietin, multimodal adsorbent, selectivity, elution chromatography

Introduction

Erythropoietin is a human hormone involved in the formation of red blood cells. Recombinant human erythropoietin (rhEPO) is a commercially available drug used to treat anaemia and other diseases. rhEPO produced by mammalian cells is secreted into the growth medium and subsequently isolated and purified to the required purity.

During purification, all foreign proteins, viruses and toxins have to be removed because they can cause an undesirable immune response. Different chromatographic methods are used for rhEPO purification (Adamíková et al., 2019). Size-exclusion, ion-exchange, hydrophobic, affinity and multimodal interactions between protein molecules and adsorbent are the most commonly applied in rhEPO purification.

Multimodal chromatography is the novel process separation mode which was originally developed for monoclonal antibodies purification. Multimodal adsorbents contain several different functional groups, which allows simultaneous binding of proteins through different interactions. Multimodal adsorbents offer different selectivity compared to classical ion exchangers and have larger operating range in terms of adsorption buffer conductivity (Holstein et al.). Nowadays, there are several applications of multimodal adsorbents for recombinant proteins purification, but applications for rhEPO purification are rare (Koticha and Chaudhari, 2011; Bandi et al., 2017). Our main goal was to determine optimal conditions of rhEPO binding to adsorbent Capto MMC ImpRes from a real mixture and to find appropriate elution of bound proteins.

Materials and methods

Adsorbent

Multimodal adsorbent Capto MMC ImpRes (GE Healthcare, Uppsala) has a matrix consisting of agarose chains. Its ligand is shown in Fig. 1. This ligand can provide ionic interactions (1), hydrogen bonds (2), hydrophobic interactions (3) and thiophilic bridges (4) with molecules.

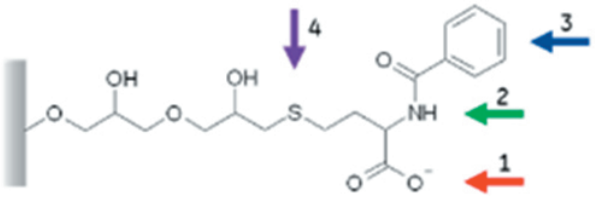

Fig. 1. Structural formula of ligand Capto MMC ImpRes.

rhEPO post-culture supernatants

Two different batches of a post-culture supernatant containing rhEPO produced by human embryonic kidney cells 293 were used (Molnár et al., 2019). The first one was concentrated and desalted using different membrane filtration processes (Molnár et al., 2019). The final rhEPO concentration and total protein concentration were 0.05 g/l and 0.8 g/l, respectively. This protein solution was used in batch equilibrium experiments and separation runs S1—S5 (Table 1). The second batch contained 0.08 g/l

of rhEPO and 2.1 g/l of total proteins and was used in the separation run S6 (Table 1). This post-culture supernatant was not treated via membrane processes. Only pH was set by concentrated HCl and 300 mM NaCl was added into the supernatant before adsorption.

Batch adsorption

Adsorbent in the amount of 25 mg was placed into a syringe filter, washed three times with 1 ml of distilled water and five times with 1 ml of 50 mM citrate phosphate buffer. The equilibrated adsorbent was suspended in 1 ml of adjusted rhEPO-containing solution and the suspension was stirred for 20 hours at the frequency of 80 rpm using a rotary shaker. The content of rhEPO and total proteins in the solution before and after the adsorption were determined and the adsorbed rhEPO/total protein amount was calculated from the material balance.

Column separation

System ÄKTA FPLC™ (GE Healthcare) was used for rhEPO separation from the rhEPO concentrate. Chromatographic column Tricorn (GE Healthcare) was filled with the adsorbent Capto MMC ImpRes. The column adsorbent volume was 1.198 ml when the bed height and diameter were 6.1 cm and 0.5 cm, respectively.

Tab. 1. Eluent composition in separation runs.

Run	Eluent*
S1	Shock-wave gradients: B1 → B2 → B6
S2	Shock-wave gradients: B3 → B4 → B6
S3	Shock-wave gradients: B5 → B6
S4	Linear gradient B1/B5 → shock-wave gradient B6
S5	Shock-wave gradients: B7 → B8 → B6
S6	Shock-wave gradients: B3 → B4 → B6

*Symbols B1—B8 refer to different buffers specified in Table 2.

Tab. 2. Elution buffers.

Buffer code	Buffer type*
B1	Tris, pH 7
B2	Tris/1 M NaCl, pH 7
B3	Tris, pH 8
B4	Tris/1 M NaCl, pH 8
B5	Tris, pH 9
B6	Tris/1 M NaCl, pH 9
B7	CF/2 M NaCl, pH 5.5
B8	CF/2 M NaCl/2 M urea, pH 5.5

*Tris — 50 mM Tris–HCl buffer, CF — 50 mM citrate-phosphate buffer.

The adsorbent was first equilibrated with 30 ml of the 50 mM citrate-phosphate buffer containing 300 mM NaCl at pH 5.5. The feed pH and composition were adjusted to pH 5.5 and NaCl concentration of 300 mM. The feed volume was either 9 ml (runs S1—S5) or 13ml (run S6) and the feed flow rate was 0.5 ml/min. After the feed loading was finished, the bed was washed with 3.6 ml of the adsorption buffer. Several ways of gradient elution to recover rhEPO from the column were tested (Table 1). The eluent composition was adjusted using different buffers labelled B1—B8 (Table 2). The elution flow rate was 0.5 ml/min and the UV and conductivity signals were monitored during the whole experiment. Elution fractions were collected and the rhEPO/total protein concentration was determined.

Protein assays

BCA method

Protein concentration in batch equilibrium experiments was determined using the BCA method. Working solution was prepared by mixing bicinchoninic acid (BCA) from Sigma-Aldrich (St. Louis, USA) with a 4 % $CuSO_4$ solution in the ratio of 50 : 1. First, a 25 µl sample was pipetted into a microplate well. Using a multichannel pipette, 200 µl of the working solution was added to the sample. The microplate was incubated for 30 minutes at the temperature of 37 °C. The sample absorbance was measured at the wavelength of 562 nm. Bovine serum albumin (BSA) in the concentration range of 0.05—1 g/l was used for calibration.

Bradford method

Protein concentration in elution chromatography samples was determined using the Bradford method due to the interference of Tris–HCl buffer with the BCA reagent. The Bradford agent is a mixture of 0.01 % Coomassie Brilliant Blue G-250, 4.7 % ethanol, and 8.5 % phosphoric acid in deionized water. It was filtered before use. Then, 20 µl of the analysed sample and 1500 µl of the Bradford agent were pipetted into test tubes. After 10—15 minutes, absorbance was measured at two wavelengths, 590 and 450 nm. BSA solution in the concentration range of 0.05—2 g/l was used for calibration.

ELISA method

rhEPO concentration was determined using a commercial kit of sandwich ELISA method (Sigma-Aldrich). The sample volume of 100 µl was transferred into a microplate well which was incubated for 2.5 hours at the temperature of 25 °C. It was then washed four times with 300 µl of wash solution. After adding 100 µl of biotinylated detection antibody into

each well, the well plate was incubated for one hour at room temperature. The wells were again washed four times as before. A streptavidin-HRP solution (100 µl) was added into each well and the well plate was incubated for 45 minutes at gentle shaking. The washing was repeated again. Finally, 100 µl of ELISA colorimetric reagent TMB were added into each well and the well plate was incubated for 30 minutes in dark at gentle shaking. To stop the reaction, 50 µl of 0.2 M sulphuric acid were added and the absorbance at 450 nm was measured.

In run S6, a recently developed indirect ELISA method was used (Molnár et al., 2019).

Results and discussion

Equilibrium experiments for the determination of optimal rhEPO adsorption conditions were done in the pH range of 5.5–7.5 and NaCl concentration range from 0 to 300 mM. Equilibrium adsorbed amounts of rhEPO, q_{EPO}, and total proteins, q_{Prot}, are shown in Figs. 2a and 2b. It is evident that higher pH has negative influence on the adsorption of both rhEPO and total proteins. On the other hand, higher salt concentration promotes rhEPO binding in spite of lower binding of total proteins. This effect is advantageous for selective separation already in the adsorption phase. Fig. 2a shows that the highest amount of rhEPO was adsorbed at pH 5.5 and 300 mM NaCl. Therefore, these conditions were chosen for chromatography feed.

Efficiency of rhEPO separation was examined in six elution chromatography runs (Fig. 3). For efficient elution, desorption by 1 M NaCl was first examined in runs S1–S3. Different pH was also applied in runs S1–S3. Each of these runs started with feeding a salt-free eluent. The NaCl concentration was later increased to 1 M in a shock-wave gradient. In the final elution phase, a shock-wave gradient increase of pH from 7 (run S1) or 8 (run S2) to the value of 9 was applied. Figs. 3a–3c show abrupt increase of outlet protein concentration demonstrated by the increase of UV signal after the application of each gradient change. Numbered peaks denote each elution phase.

These results demonstrate a synergistic effect of pH and NaCl concentration on protein recovery. The existence of several elution peaks implies strong protein binding albeit not so strong as in case of multimodal anion exchanger applied to the separation of this product (Kurák et al., 2019). A significant fraction of adsorbed proteins was eluted using salt-free eluents (peak 1 in Figs. 3a–3c). The protein yield increased from 23 % at pH 7 to 50 % at pH 8 and finally to 74 % at pH 9. The application of 1 M NaCl in the second elution phase led then to almost complete protein recovery. Only in run S1, 6 % of proteins were recovered in the third phase. Unfortunately, sensitivity of the ELISA method allowed only semi-quantitative estimation of the eluted rhEPO. This was much higher in the second fraction than in the first one in runs S1 and S2. In run S3, approximately equal amounts of rhEPO were detected in both fractions.

Following these results, a linear pH gradient from 7 to 9 and salt-free eluent were applied in the first phase of run S4. Fig. 3d shows that no positive effect was achieved and the separation performance was very similar as in run S1. Considering the distribution of rhEPO and impurity proteins in individual fractions in runs S1–S4, the best selectivity of rhEPO separation was achieved in run S2 carried out at pH 8.

Fig. 3e presents the results of run S5 which was designed at the same pH in both the loading and the elution phases. An eluent with stronger desorption effect had to be applied from the beginning of the elution. It is clear that neither 2 M NaCl nor 2 M NaCl/2M urea were efficient enough. Complete protein desorption was achieved only when pH was increased to 9 in the final elution phase.

Fig. 3f presents the results of run S6 in which the same process conditions were used as in run S2 ex-

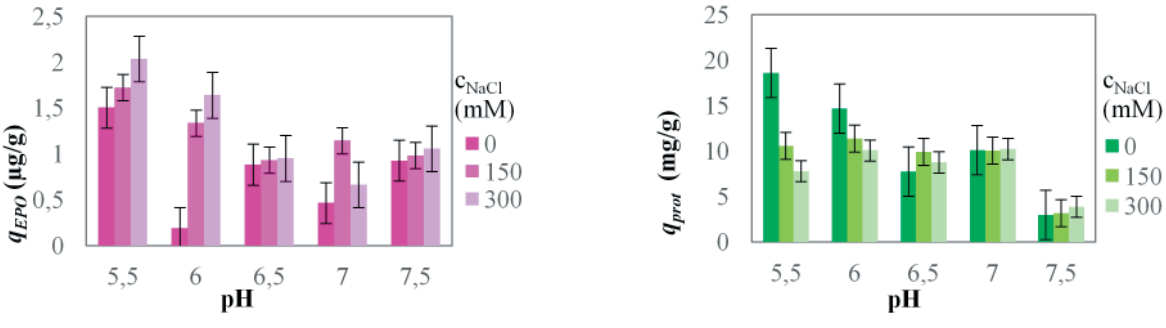

a) b)

Fig. 2. pH and NaCl concentration influence on adsorbed amount of a) rhEPO and b) total proteins.

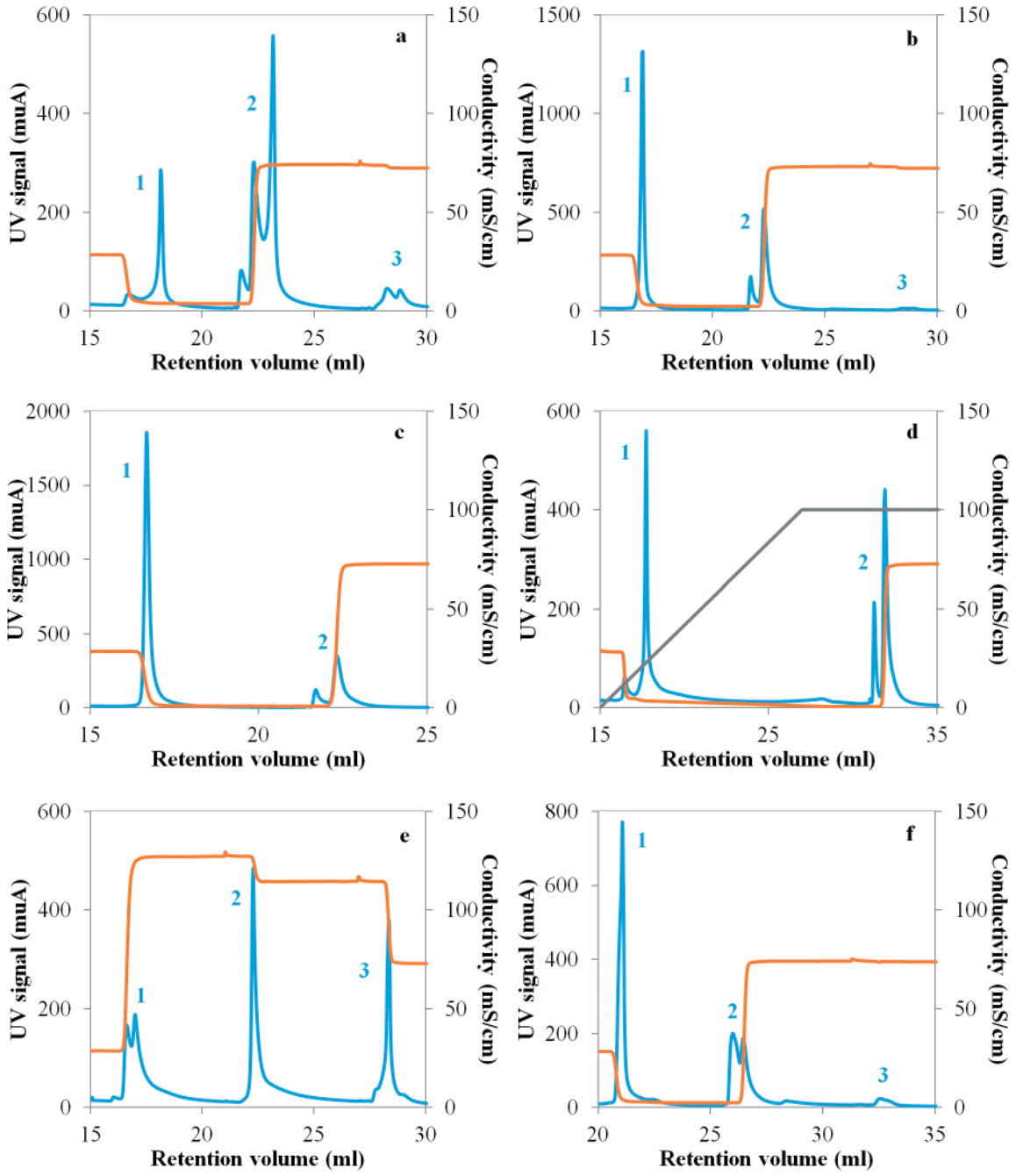

Fig. 3. Chromatograms of individual separation runs: a) S1, b) S2, c) S3, d) S4, e) S5, and f) S6. Blue and orange lines represent UV and conductivity signals, respectively. Peak numbers denote individual elution phases.

cept for a higher feed volume. Since a product from a different cultivation batch was used in this run, the rhEPO and protein loads were more than twice higher. Figs. 3b and 3f show that the chromatograms of runs S2 and S6 are very similar. The protein recovery yields in both phases were almost identical again. Due to a higher rhEPO feed concentration in run S6 and better reproducibility of a recently developed analytical method (Molnár et al., 2019), the rhEPO concentration in the elution fractions, the measurement reliability was higher. It was found that the rhEPO purity was around 90 % in the first elution fraction (peak 1) and 60 % in the second elution fraction (peak 2). The total rhEPO yield was however only slightly below 50 %, similarly as for a multimodal anion exchanger in our previous work (Kurák et al., 2019).

Conclusions

Adsorbent Capto MMC ImpRes has been proven to be a good candidate for rhEPO capture step in rhEPO separation. The most selective binding of rhEPO from a post-cultivation supernatant was

observed at pH 5.5 and NaCl concentration of 300 mM in batch equilibrium experiments. Chromatographic runs were used to optimize elution conditions. Two shock-wave gradients, in which pH was increased to 8 and the NaCl concentration to 1 M, provided the best separation performance. The rhEPO purity of about 80 % was reached when the yield of this target protein was 50 %.

Acknowledgments

This work was supported by grants from the Agency of the Ministry of Education, Science, Research and Sport of the Slovak Republic for the Structural Funds of EU (Grant number: ITMS 26240220071) and the Slovak Research and Development Agency (Grant number: APVV-14-0474). Dr. Mária Bartošová from the Institute of Virology, Slovak Academy of Sciences, is kindly acknowledged for the preparation of post-culture supernatant of HEK 293.

References

Adamíková J, Antošová M, Polakovič M (2019) Biotechnol. Lett. 41: 483–493.

Bandi VK, Reddy BRB, Mugthihalli SM, Iyer PK, Pasupuleti P (2017) EP3153522.

Holstein MA, Parimal S, McCallum SA, Cramer SM (2012) Biotechnol. Bioeng. 109: 176–186.

Koticha D, Chaudhari AB (2011) WO2011063195.

Kurák T, Molnár T, Polakovič M (2019) Chem. Pap. 73: 1805–1811.

Molnár T, Bartošová M, Antošová M, Škultéty Ľ, Polakovič M (2019) Chem. Pap. 73: 713–718.

sciendo

Thermodynamics of primary antioxidant action of flavonols in polar solvents

Martin Michalík[a], Ján Rimarčík[b], Vladimír Lukeš[a], Erik Klein[a]

[a]*Institute of Physical Chemistry and Chemical Physics, Slovak University of Technology in Bratislava, Radlinského 9, SK-812 37 Bratislava, Slovakia.*
[b]*Department of Chemistry, University of SS. Cyril and Methodius, J. Herdu 2, SK-917 01 Trnava, Slovak Republic.*
martin.michalik@stuba.sk

Abstract: Very recently, a report on the antioxidant activity of flavonoids has appeared, where authors concluded that Hydrogen Atom Transfer mechanism represents the thermodynamically preferred mechanism in polar media (https://doi.org/10.1016/j.foodres.2018.11.018). Unfortunately, serious errors in the theoretical part of the paper led to incorrect conclusions. For six flavonols (galangin, kaempferol, quercetin, morin, myricetin, and fisetin), reaction enthalpies related to three mechanisms of the primary antioxidant action were computed. Based on the obtained results, the role of intramolecular hydrogen bonds (IHB) in the thermodynamics of the antioxidant effect is presented. Calculations and the role of solvation enthalpies of proton and electron in the determination of thermodynamically preferred mechanism is also briefly explained and discussed. The obtained results are in accordance with published works considering the Sequential Proton-Loss Electron-Transfer thermodynamically preferred reaction pathway.

Keywords: phenolic antioxidant; intramolecular hydrogen bond; DFT calculation; sequential proton-loss electron-transfer; solvent effect

Introduction

Phenolic compounds are naturally present in almost all plant materials and represent an integral part of human diet. Tocopherols, flavonoids and (poly)phenolic acids are considered the most important groups of naturally occurring phenolic antioxidants.

Flavonoids were identified in almost all parts of plants, such as leaves, stems, roots, fruits or seeds. Besides the antioxidant action, they exhibit other biological effects: antiviral, antibacterial, anti-inflammatory, anticancer, vasodilatory and anti-ischemic (Procházková et al., 2011). From the structural point of view, they consist of benzene ring, A, condensed with heterocyclic ring, C, and phenyl ring, B, attached on C2 carbon atom (Fig. 1). Experimental reports on flavonoids radical scavenging activity (primary antioxidant effect) have shown that the following structural features are required (Bors, et al., 1990; Burda and Oleszek, 2001; Croft, 1998; Procházková et al., 2011; Rice-Evans et al., 1996):

(*i*) catechol (*ortho*-dihydroxy) structure of the B ring enabling electron delocalization in the formed phenoxy radical,
(*ii*) C2═C3 double bond conjugated with C4═O keto group in the C ring providing electron delocalization from the B ring,
(*iii*) hydroxy OH groups at positions 3 and 5 providing hydrogen bonds to C4═O group.

In general it is expected that radical scavenging activity of flavonoids is mainly related to the B ring. The number and positions of OH groups in this ring play an important role. However, the total number of OH groups in flavonoids also affects their antioxidant activity, because OH groups present in the C ring (3-OH neighboring with C2═C3 double bond) and A ring also contribute to the overall observed effect (Musialik et al., 2009; Rice-Evans et al., 1996; Trouillas et al., 2006).

Flavonoids as primary (chain-breaking) antioxidants scavenge free radicals via three mechanisms (Foti et al., 2004; Galano et al., 2016; Ingold and Litwinienko, 2005; Litwinienko and Ingold, 2003, 2004; Musialik et al., 2009):

1. Hydrogen atom transfer (HAT) — one step mechanism where homolytic cleavage of phenolic O—H bond takes place; O—H bond dissociation enthalpy, BDE, represents the reaction enthalpy of this process.
2. Single Electron Transfer–Proton Transfer (SET-PT), also known as Sequential Electron Proton Transfer (SEPT) — two-step mechanism, where electron abstraction from antioxidant is followed by proton transfer.
3. Sequential Proton-Loss Electron-Transfer (SPLET) — two-step mechanism, where OH group deprotonation is followed by electron transfer.

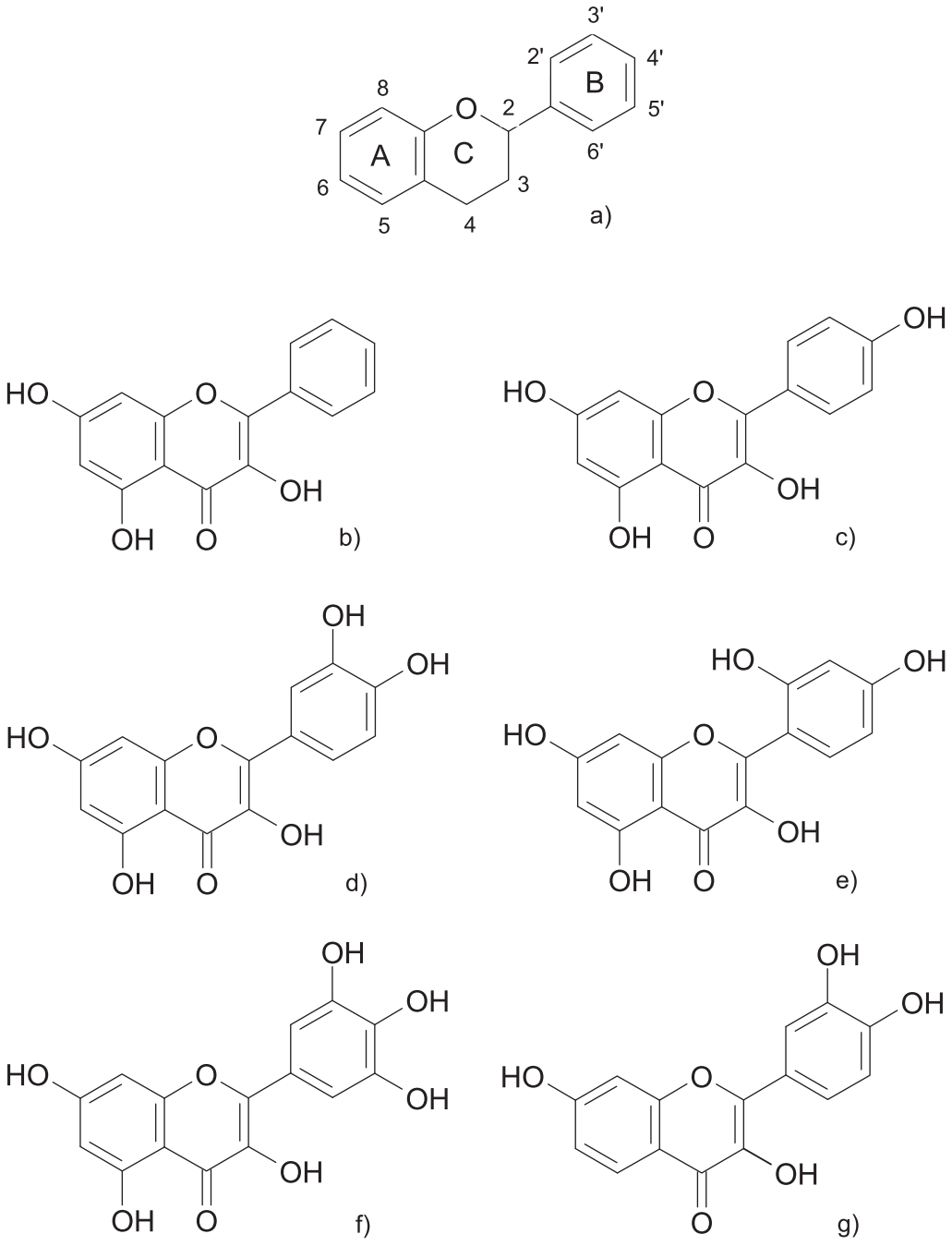

Fig. 1. Atom numbering and ring denotation in flavonoids (a) and studied flavonols: galangin (b), kaempferol (c), quercetin (d), morin (e), myricetin (f), and fisetin (g).

Thermodynamics of the Single Electron Transfer–Proton Transfer (SET-PT) mechanism is described by Ionization Potential (IP) and Proton Dissociation Enthalpy (PDE). Proton Affinity (PA) of the phenoxide anion and Electron Transfer Enthalpy (ETE) represent reaction enthalpies related to the Sequential Proton-Loss Electron-Transfer (SPLET) mechanism.

Very recently, Chen et al. (2018) published a paper focused on the theoretical and experimental study of antioxidant activity of flavonoids. Unfortunately, theoretical calculations show serious inaccuracies. Erroneous thermodynamic data for HAT, SET-PT and SPLET mechanisms enabled the authors to draw incorrect conclusions which disagree with available literature. Therefore, the aims of this work are: (*i*) to explain all details and general rules of a reliable theoretical study of primary antioxidant action thermodynamics, (*ii*) to present re-calculated reaction enthalpies for six flavonols (galangin, kaempferol, quercetin, morin, myricetin, and fisetin) in ethanol and acetone, and (*iii*) to confirm that found values allow drawing conclusions in agreement with available experimental and theoretical reports.

Computational details

All calculations were performed using the Gaussian 09 program package (Frisch et al., 2013). The geometry of each flavonoid molecule (Fl—OH), phenoxy radical (Fl—O$^{\bullet}$), radical cation (Fl—OH$^{\bullet+}$) or phenoxide anion (Fl—O^{-}) were optimized using the Density Functional Theory (DFT) method with M06-2X (Zhao and Truhlar, 2008) functional without any constraints (energy cut-off of 10^{-5} kJ mol^{-1}, final RMS energy gradient under 0.01 kJ mol^{-1} Å^{-1}). Calculations were performed using the 6-311+G(d,p) basis set (Binkley et al., 1980; Rassolov et al., 2001). Solvent (ethanol and acetone) contribution to the total enthalpies was computed employing SMD polarized continuum model (Solvation Model based on the quantum mechanical charge density of a solute molecule interacting with a continuum) developed by Marenich et al. (2009). Optimized structures were confirmed to be real minima by frequency analysis. O—H bond dissociation enthalpies, BDE, ionization potentials, IP, proton dissociation enthalpy PDE, phenoxide anion proton affinity, PA, and electron transfer enthalpies, ETE, values were calculated

$$\mathrm{BDE} = H(\mathrm{Fl{-}O^{\bullet}}) + H(\mathrm{H^{\bullet}}) - H(\mathrm{Fl{-}OH}) \quad (1)$$

$$\mathrm{IP} = H(\mathrm{Fl{-}OH^{\bullet+}}) + H(\mathrm{e^{-}}) - H(\mathrm{Fl{-}OH}) \quad (2)$$

$$\mathrm{PDE} = H(\mathrm{Fl{-}O^{\bullet}}) + H(\mathrm{H^{+}}) - H(\mathrm{Fl{-}OH^{\bullet+}}) \quad (3)$$

$$\mathrm{PA} = H(\mathrm{Fl{-}O^{-}}) + H(\mathrm{H^{+}}) - H(\mathrm{Fl{-}OH}) \quad (4)$$

$$\mathrm{ETE} = H(\mathrm{Fl{-}O^{\bullet}}) + H(\mathrm{e^{-}}) - H(\mathrm{Fl{-}O^{-}}) \quad (5)$$

where H(Fl—OH) represents total enthalpy of the flavonoid, H(Fl—OH$^{\bullet+}$) is total enthalpy of the flavonoid radical cation, H(Fl—O$^{\bullet}$) and H(Fl—O^{-}) are total enthalpies of the phenoxy radical and phenoxide anion, respectively.

Proton and electron solvation enthalpies were also computed using the (SMD) M06-2X/6-311+G(d,p) approach to obtain values compatible with total enthalpies of the studied species. For hydrogen atom solvation enthalpy, $\Delta_{sol}H(\mathrm{H^{\bullet}})$, published values of 3.7 kJ mol^{-1} and 4.5 kJ mol^{-1} (Parker, 1992) for acetone and ethanol were employed, respectively.

Results and Discussion

For the studied flavonols, calculated solution-phase reaction enthalpies are compiled in Tables 1 (ethanol) and 2 (acetone) which also show results published by Chen et al. (2018). Table 1 summarizes also data for quercetin found using identical computational approach, i.e. (SMD) M06-2X/6-311+G(d,p) (Zheng et al., 2017a). In the tables, the lowest values of individual reaction enthalpies for each flavonol are set in italic.

Structure of flavonoids and the role of intramolecular hydrogen bonds

Optimum geometries of the studied flavonoids must preserve all possible intramolecular hydrogen bonds (IHB). Geometries used for the calculations significantly affect the electronic structure of the studied species and consequently the energetics of homolytic or heterolytic O—H bonds cleavage. If the hydrogen atom of OH group participates in IHB, HAT or proton loss requires also the disruption of the hydrogen bond. As a result, an increase in O—H BDE, PDE or PA values can be observed. Therefore, 5-OH BDE, PDE and PA are usually the highest ones in flavonols, as it is evident from our results in Tables 1 and 2. Analogously, in case of the *ortho*-dihydroxy structure of the B ring, values for the 3´-OH group are higher than those obtained for the 4´-OH group (see results for quercetin and fisetin in Tables 1 and 2).

In galangin, kaempferol, quercetin, morin, myricetin, chrysin, apigenin, and luteolin, Chen et al. (2018) neglected the C4═O···H—O5 intramolecular hydrogen bond (IHB). Besides, the proposed optimum structure of fisetin assumes no IHB between 3´-OH and 4´-OH groups, while in other molecules, the mutual orientation of the two OH groups on the B ring is correct. In Fig. 2, correct geometries of quercetin and fisetin obtained in this work are depicted.

For quercetin, Galano et al. (2016) showed that IHB between 3´-OH and 4´-OH groups leads to a more stable conformation, by 18.0 kJ mol^{-1}, compared to the conformation lacking IHB. This IHB also stabilizes the 4´-O$^{\bullet}$ phenoxy radical and results in a 12.5 kJ mol^{-1} decrease in 4´-OH BDE. In case of C4═O···H—O5, even stronger IHB is expected (Nazarparvar et al., 2012; Zheng et al., 2017b, 2018). In the solution-phase, the effect of IHB on phenolic O—H groups cleavage is lower compared to that in the gas-phase, but 5-OH BDE, PDE and PA values still belong to the highest ones obtained in flavonoids (Lengyel et al., 2013; Lucarini et al., 2002; Marković et al., 2012, 2013; Vagánek et al., 2012, 2014; Zheng et al., 2019, 2018, 2017a, 2017b). Using model compounds catechol, pyrogalol, and resorcinol, Thavasi et al. (2006) confirmed the importance of IHBs for the antioxidant effect of polyphenols.

In literature, various reports on flavonoids with correct geometries, which are in agreement with

Tab. 1. (SMD) M06-2X/6-311+G(d,p) reaction enthalpies in kJ mol^{-1} for selected flavonoids in ethanol: Chen et al. (2018) / this work, or Zheng et al. (2017a[a]). The lowest values for a molecule are in italic.

Flavonoid	BDE	IP	PDE	PA	ETE
Galangin		675/549			
3-OH	*313/349*		*488/9*	630/149	*533/409*
5-OH	335/395		510/55	*603*/154	582/450
7-OH	355/396		530/55	604/ *134*	601/471
Kaempferol		656/531			
4´-OH	325/367		519/45	618/147	557/429
3-OH	*306/343*		*500/21*	630/153	*526/399*
5-OH	335/395		528/73	604/155	581/449
7-OH	352/393		546/71	*603/135*	598/468
Quercetin		652/530			
3´-OH	314/349		512/29	616/143	547/416
4´-OH	314/ *343*		512/ *22*	622/ *133*	541/418
3-OH	*307/343*		*504*/23	631/152	*526/400*
5-OH	336/395		534/74	603/155	583/449
7-OH	352/393		549/73	*601*/135	599/468
Morin		655/529			
2´-OH	333/375		527/55	619/146	564/438
4´-OH	335/374		529/54	620/146	564/437
3-OH	*308/343*		*502/23*	631/151	*526/401*
5-OH	336/397		530/76	602/152	583/453
7-OH	355/395		549/75	*601/132*	603/472
Myricetin		654/528			
3´-OH	*298*/354		*494*/36	611/142	534/422
4´-OH	320/ *326*		516/ *7*	615/ *124*	555/410
5´-OH	326/354		522/35	633/142	542/420
3-OH	307/344		503/25	630/149	*527/404*
5-OH	336/395		532/76	*604*/154	582/449
7-OH	352/394		548/75	*604*/134	598/469
Fisetin		656/528			
3´-OH	310/349		504/30	*617*/143	543/414
4´-OH	318/ *341*		512/ *22*	618/ *134*	550/415
3-OH	*308*/345		*502*/27	626/158	*532/396*
7-OH	353/390		546/72	607/136	595/463
Quercetin[a]		652/536			
3´-OH	314/361		512/7	616/133	547/424
4´-OH	314/344		512/-10	622/ *108*	541/430
3-OH	*307/343*		*504/–11*	631/123	*526/404*
5-OH	336/397		534/43	603/131	583/449
7-OH	352/395		549/50	*601*/111	599/468

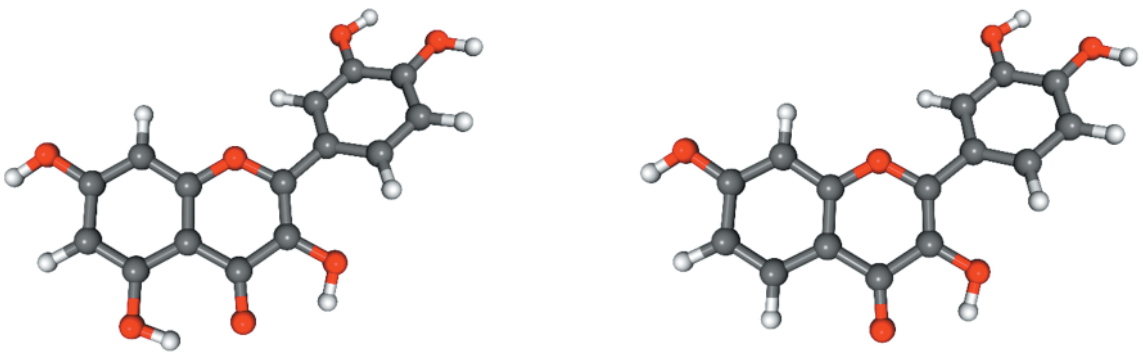

a) b)

Fig. 2. Optimum geometries of quercetin (a) and fisetin (b).

Tab. 2. (SMD) M06-2X/6-311+G(d,p) reaction enthalpies in kJ mol^{-1} for selected flavonoids in acetone: Chen et al. (2018)/this work. The lowest values for a molecule are in italic.

Flavonoid	BDE	IP	PDE	PA	ETE
Galangin		700/483			
3-OH	*312/349*		*466/8*	681/181	*486/310*
5-OH	331/402		485/62	637/193	549/351
7-OH	349/391		503/51	*636/159*	568/375
Kaempferol		682/462			
4´-OH	320/363		492/43	651/173	524/332
3-OH	*305/344*		*477/24*	683/187	*477/299*
5-OH	331/402		503/82	638/195	548/350
7-OH	346/389		518/69	*635/160*	566/372
Quercetin		675/463			
3´-OH	*306*/343		486/23	637/168	524/318
4´-OH	313/*336*		493/*15*	664/*154*	504/324
3-OH	*306*/345		*485*/24	665/186	*495/301*
5-OH	332/402		512/81	*627*/195	560/349
7-OH	348/390		528/70	635/160	567/372
Morin		686/463			
2´-OH	330/374		498/53	655/178	529/338
4´-OH	329/371		498/50	652/173	532/341
3-OH	*308/345*		*476/24*	685/186	*477/302*
5-OH	332/404		501/83	633/190	554/356
7-OH	348/392		517/71	*631/155*	572/379
Myricetin		659/463			
3´-OH	*292*/349		*487*/29	636/167	511/325
4´-OH	310/*318*		505/*-3*	636/*142*	529/318
5´-OH	324/349		519/29	681/168	498/324
3-OH	306/344		501/24	678/181	*482/305*
5-OH	331/402		527/81	625/193	561/351
7-OH	347/379		542/58	*622*/159	579/362
Fisetin		673/463			
3´-OH	*304*/342		*486*/27	652/169	508/315
4´-OH	314/*334*		516/*18*	*635/157*	533/319
3-OH	306/346		487/31	656/197	*504/291*
7-OH	335/385		516/70	*635*/163	554/364

Fig. 2, can be found, see for example Ajitha et al. (2012), Álvarez-Diduk et al. (2013), Galano et al. (2016), Leopoldini et al. (2006), Marković et al. (2012, 2013), Mendoza-Wilson et al. (2011), Osorio et al. (2013), Sadasivam and Kumaresan (2011), Zheng et al. (2018, 2017). Leopoldini et al. (2011) and Trouillas et al. (2006) also presented optimum geometries of phenoxy radicals and phenoxide anions of various flavonoids.

Thermodynamically preferred mechanism vs solvation enthalpies of proton and electron

Solution phase calculations of reaction enthalpies related to SET-PT and SPLET require the application of total enthalpies of electron, $H(e^-)$, and proton, $H(H^+)$, in the studied solvent (eqs. 2—5). Using implicit solvation models, such as variants of the Polarized Continuum Model (PCM), solvation enthalpies of proton, $\Delta_{sol}H(H^+)$, and electron, $\Delta_{sol}H(e^-)$, can be simply calculated from the definition of the solvation enthalpy as follows (Marković et al., 2016; Rimarčík et al., 2010)

$$\Delta_{sol}H(H^+) = H[(S—H)^+, sol] - H(S, sol) - H(H^+, g) \quad (6)$$

$$\Delta_{sol}H(e^-) = H[(S—e)^{\bullet -}, sol] - H(S, sol) - H(e^-, g) \quad (7)$$

using the computed total enthalpies of solvent molecule S, solvated by the solvent itself $H(S, sol)$ and total enthalpies of $(S—H)^+$ and $(S—e)^{\bullet -}$ species that represent proton and electron added to the single solvent molecule, respectively.

Marković et al. (2016) performed calculations of H^+ and e^- solvation enthalpies using the SMD solvation model and the 6-311++G(d,p) basis set. The calculations were performed using *ab initio* (MP2) method and the Density Functional Theory (DFT) approach. Results for ten functionals, including the most frequently employed ones, i.e. B3LYP, M05-2X, and M06-2X, were reported. For ethanol, the obtained DFT proton solvation

enthalpies lie in the range from –1063 kJ mol^{-1} to –1076 kJ mol^{-1} and electron solvation enthalpies are in the range from –44 to –76 kJ mol^{-1}. In acetone, the DFT proton solvation enthalpies are similar, from –1049 to –1067 kJ mol^{-1}. Electron solvation enthalpy values obtained in acetone are more negative in comparison to those obtained in ethanol: from –112 kJ mol^{-1} to –133 kJ mol^{-1}. Hydration enthalpies of proton and electron were found in the range from –1052 kJ mol^{-1} to –1064 kJ mol^{-1} and from –66 kJ mol^{-1} to –101 kJ mol^{-1}, respectively. Rimarčík et al. (2010) performed analogous (IEF-PCM) B3LYP/6-311++G(d,p) calculations. Although different solvation models, SMD (Marenich et al., 2009) and IEF-PCM (Cances and Mennucci, 1998; Cances et al., 1997), were used in the two works, B3LYP results in the two papers can be considered similar (Marković et al., 2016). Table 3 summarizes B3LYP, M05-2X, and M06-2X solvation enthalpies for common solvents (ordered by their increasing polarity) published in the two papers, as well as (SMD) M06-2X/6-311+G(d,p) solvation enthalpies corresponding to the computational method employed in this work.

Chen et al. (2018) did not specify the employed total or solvation enthalpies of proton and electron. However, the IPs, PDEs, PAs, and ETEs determined indicate the use of incorrect values. Due to BDEs being lower than IP and PA values, the authors anticipate that HAT represents the thermodynamically preferred reaction mechanism of antioxidant activity of flavonoids in ethanol and acetone. Comparing our results with data obtained by Chen et al. (2018), discrepancies in PAs and PDEs reached roughly 500 kJ mol^{-1} in ethanol (Table 1) and more than 400 kJ mol^{-1} in acetone (Table 2). Differences in IP and ETE values exceed 120 kJ mol^{-1} and 200 kJ mol^{-1} in ethanol and acetone, respectively.

Correct conformations with all intramolecular hydrogen bonds induce considerable changes in the results obtained for the 5-OH group. In some cases, different conformations cause a change in the thermodynamically preferred OH group of the flavonoid (see for example PA values for quercetin in Tables 1 and 2). For quercetin, available calculated reaction enthalpies in aqueous solution are provided in Table 4. Although shifts in IP, PDE, PA, and ETE values are apparent, all methods provide practically identical general trends. The observed shifts stem from the application of different computational approaches (functionals, basis sets, and solvation models) employed in the published works. Also, the used solvation enthalpies of electron and proton may contribute to the uniform shifts considerably and therefore total or solvation enthalpies of proton and electron used in all calculations of reaction enthalpies have to be specified.

From the thermodynamics point of view, the tendency to enter a reaction mechanism is driven by BDE, IP and PA because in the two-step SET-PT and SPLET mechanisms, the energetics of the first step is determining. Despite the differences induced by various computational methods, data in Tables 1, 2, and 4 unambiguously show that SPLET is the thermodynamically preferred mechanism in polar solvents such as ethanol, acetone and water.

It is also worth to point out that confrontation of solution-phase reaction enthalpies summarized in Tables 1, 2, and 4, as well as other available computational results for the polar organic solvents

Tab. 3. Solvation enthalpies of H^+ and e^- in common solvents for widely used functionals.[a]

Solvent	$\Delta_{solv}H(H^+)$/kJ mol^{-1}			$\Delta_{solv}H(e^-)$/kJ mol^{-1}		
	B3LYP	M05-2X	M06-2X	B3LYP	M05-2X	M06-2X
benzene	–903.9 (–894)	–879.3	–877.4	–16.5 (–7)	–8.7	–10.5
toluene	–937.9 (–925)	–913.7	–911.7	–21.7 (–13)	–13.9	–15.2
aniline	–1108.5 (–1092)	–1101.7	–1100.5	–78.9 (–51)	–77.2	–77.4
acetone	–1060.2 (–1070)	–1056.1	–1053.6 –1054[b]	–132.9 (–119)	–119.8	–116.6 –116[b]
ethanol	–1068.4 (–1045)	–1064.5	–1064.0 –1065[b]	–73.6 (–76)	–43.6	–56.3 –39[b]
methanol	–1067.9 (–1038)	–1065.2	–1065.4	–80.0 (–86)	–48.7	–61.4
acetonitrile	–1043.8 (–1031)	–1031.7	–1032.4	–132.2 (–95)	–116.7	–113.0
DMSO	–1119.6 (–1115)	–1120.3	–1119.7	–53.0 (–84)	–25.6	–42.9
water	–1055.4 (–1022)	–1052.0	–1055.7	–101.1 (–105)	–66.8	–77.5

[a]Calculations in 6-311++G(d,p) basis set and SMD solvation method (Marković et al., 2016). B3LYP data in parentheses were calculated using IEF-PCM method (Rimarčík et al., 2010).

[b](SMD) M06-2X/6-311+G(d,p) – this work.

Tab. 4. Published DFT and semi-empirical PM6 reaction enthalpies in kJ mol^{-1} for quercetin in aqueous solution. The lowest values for a molecule are in italic.

Method	BDE	IP	PDE	PA	ETE
(SMD) M05-2X/6-311G+(d,p) (Marković et al., 2013)					
		334			
3´-OH	349		14	116	232
4´-OH	*333*		*-1*	*93*	240
3-OH	334		0	108	*226*
5-OH	383		48	112	270
7-OH	383		49	94	289
(SMD) M06-2X/6-311+G(d,p) (Zheng et al., 2017a)					
		535			
3´-OH	351		15	126	424
4´-OH	336		1	*106*	430
3-OH	*333*		*-2*	116	*416*
5-OH	385		49	124	460
7-OH	386		50	107	478
(IEF-PCM) B3LYP/6-311++G(d,p) (Vagánek et al., 2014)					
		447			
3´-OH	316		68	174	341
4´-OH	*305*		*56*	*159*	344
3-OH	317		68	192	*324*
5-OH	369		120	205	363
7-OH	351		103	170	380
(COSMO) PM6 (Amić et al., 2013)					
		361			
3´-OH	311		–51	51	*260*
4´-OH	*298*		*–63*	31	267
3-OH	305		–57	35	269
5-OH	373		11	22	350
7-OH	383		21	*14*	368

and water (Amić et al., 2013; Marković et al., 2013; Vagánek et al., 2014; Zheng et al., 2019, 2018, 2017a, 2017b) indicate that the three polar solvents exert similar effect on the reaction enthalpies for processes involving charged species, where solvation plays an important role. On the contrary, solvent induces only minute changes in BDEs because they are calculated from the total enthalpies of neutral species only.

Our values compiled in Tables 1 and 2 are in accordance with previously published experimental (Foti et al., 2004; Ingold and Litwinienko, 2005; Litwinienko and Ingold, 2003, 2004; Musialik et al., 2009; Staško et al., 2007) and theoretical reports (Amić et al., 2013; Lengyel et al., 2013; Marković et al., 2013; Toscano and Russo, 2016; Vagánek et al., 2012, 2014; Vakarelska-Popovska and Velkov, 2016; Zheng et al., 2019, 2018, 2017a, 2017b) concluding that SPLET is the favored reaction pathway in polar solvents.

Preferred reaction sites in studied flavonols

For the HAT mechanism, data in Tables 1 and 2 indicate that the lowest BDE values were found for 4´-OH group on the B ring or for the 3-OH group on the C ring. Comparing the results for kaempferol, quercetin and myricetin possessing one, two and three OH groups on the B ring, BDE values reveal that 4´-OH BDE in myricetin with pyrogallol (trihydroxy) structure of the B ring is the lowest one, while in kaempferol with only one OH group on the B ring, 4´-OH BDE is the highest one in this series. In kaempferol, the lowest BDE was found for 3-OH group analogously to galangin that has no OH group on the B ring. For morin with two OH groups on the B ring, the corresponding BDEs are significantly higher because the two groups are mutually in *meta* position, where OH group shows electron-withdrawing effect resulting in the increased BDE (Klein and Lukeš, 2006). In morin, the 3-OH group shows the lowest BDE. For quercetin in ethanol, 3-OH and 4´-OH BDE reached identical values. 5-OH and 7-OH groups of the A ring have the lowest tendency to homolytic O—H bond cleavage. From the thermodynamic cycle it follows that identical trends hold also for proton dissociation enthalpies in the SET-PT mechanism as the second step of the SET-PT mechanism also results in phenoxy radical formation.

Another key factor of radical species stability, spin density, is shown for quercetin in ethanol in Fig. 3. The 7-OH radical has the highest spin density on the O-atom and BDE compared to the 3-OH and 4´-OH radicals having the lowest spin density on the O-atom and BDEs. This means that the formation of the latter radicals is more favorable as the spin density is more delocalized over the whole molecule and the species are more stabilized. In case of 5-OH BDE, the higher value is caused by hydrogen bond cleavage during hydrogen atom transfer and not by the spin density distribution. These results are comparable with those obtained by Zheng et al. (2017a).

For SPLET, data in Tables 1 and 2 indicate that in galangin, kaempferol, and morin, the 7-OH group is most prone to deprotonation. In quercetin, myricetin and fisetin, the 4´-OH group is the preferred one. However, for quercetin and fisetin, 4´-OH and 7-OH PA values in ethanol can be considered practically identical, the difference is only 2 kJ mol^{-1}. In acetone, 4´-OH and 7-OH PA values of the two flavonols are again close and the differences do not exceed 6 kJ mol^{-1}. These data, as well as the published reaction enthalpies for quercetin in aqueous solution in Table 4, unambiguously indicate the significant role of the 7-OH group (ring A) in the overall antioxidant activity. For quercetin, Musialik et al. (2009) experimentally confirmed that the anion formed at position 7 in ionization-supporting solvents is responsible for very fast kinetics of the quercetin/dpph• reaction because of the participation of both mechanisms: HAT (from catechol moiety in ring B) and SPLET (from ionized 7-hydroxyl in ring A). For isoflavones, Lengyel et al. (2013) found that deprotonation of the 7-OH group is thermodynamically favored in aqueous solution as well as in non-polar environment (benzene).

Thermodynamics of primary antioxidant action vs antioxidant activity

Activity of individual flavonoids does not depend solely on their structure and the polarity of the environment. The type of scavenged radical and the kinetics related to the individual reaction pathways also play important roles (Galano et al., 2016;

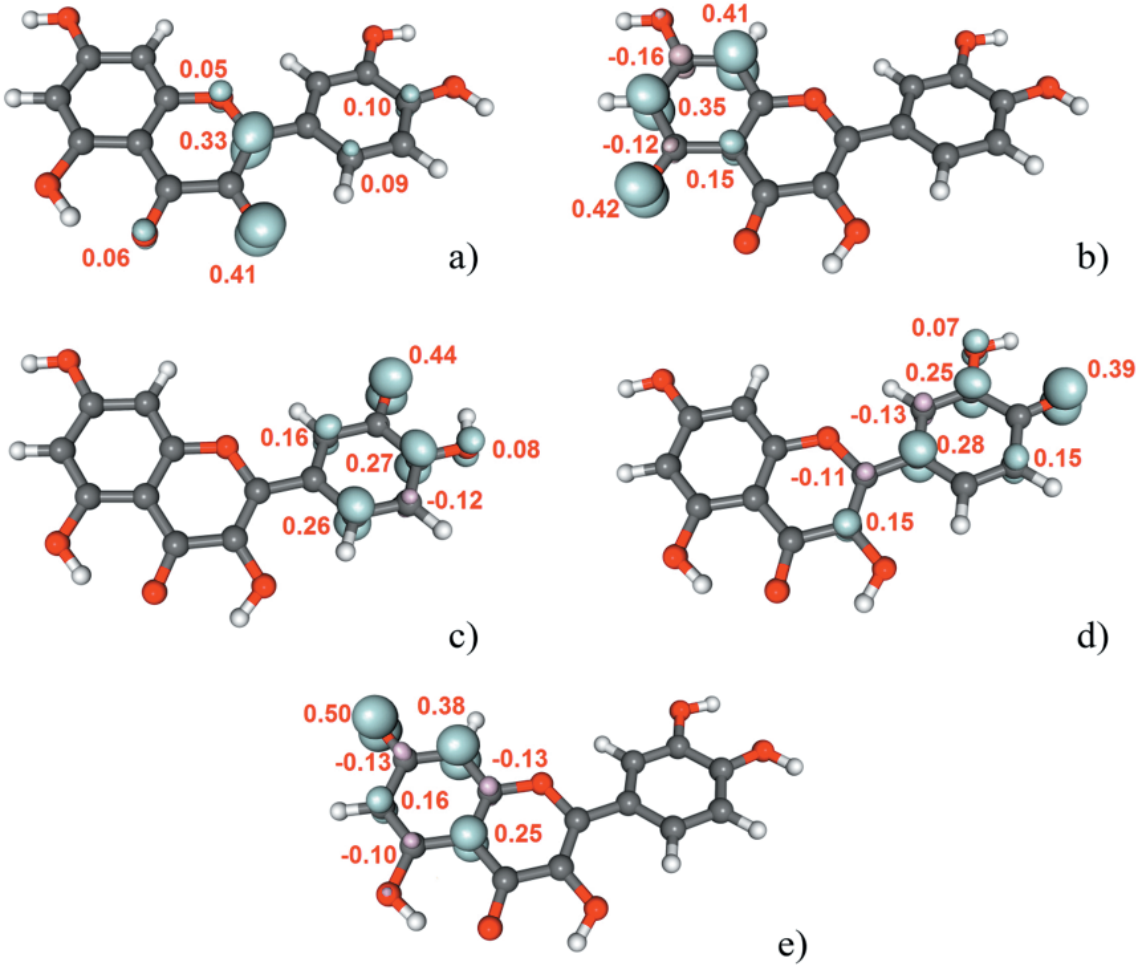

Fig. 3. Spin densities (values are in a.u.) of quercetin radicals in ethanol: a) 3-OH, b) 5-OH, c) 3´-OH, d) 4´-OH, e) 7-OH (M06-2X/6-311G, isosurface value 0.01).

Galano and Raúl Alvarez-Idaboy, 2019; Marković et al., 2013; Procházková et al., 2011; Rice-Evans et al., 1996).

In general, other processes can also affect the experimentally observed radical scavenging activity of flavonoids in polar environment. Recently, it has been shown that HAT from deprotonated flavonoids is more thermodynamically feasible in comparison to parent (non-dissociated) flavonoids; see for example Galano et al. (2016), Galano and Raúl Alvarez-Idaboy (2019), Klein et al. (2016). This mechanism has been denoted as SPLHAT (Galano et al., 2016; Galano and Raúl Alvarez-Idaboy, 2019) because it represents the combination of the first step of SPLET (deprotonation of phenolic OH group) followed by HAT from a different OH group of the formed anion. Relevance of both, SPLET and SPLHAT mechanisms for phenolic antioxidants in the polar ionization supporting solvents was indicated by many experiments and rationalized also by theoretical studies (Álvarez-Diduk et al., 2013; Dueñas et al., 2010; Foti et al., 2004; Galano et al., 2011; Ingold and Litwinienko, 2005; Klein et al., 2016; Lemańska et al., 2001, 2004; León-Carmona et al., 2012; Litwinienko and Ingold, 2003, 2004; Musialik et al., 2009; Staško et al., 2007). Experimentally observed increase of free radical scavenging activity of polyphenols with the increase in pH can be related to lower O—H BDEs in deprotonated species. It can be assumed that the SPLHAT mechanism considerably contributes to the observed antioxidant action of flavonoids in aqueous solutions.

Conclusion

In this report, a theoretical study of the thermodynamics of three mechanisms of primary antioxidant action of six flavonols in two polar solvents is presented. Another important aim of this work was to provide an explanation of all issues to be aware of in order to perform reliable theoretical calculations providing correct values of the investigated reaction enthalpies.

In general, computational chemistry offers reasonable predictions of antioxidant action thermodynamics for solution-phase reactions where no experimental data are available. Published theoretical papers allow deeper insight and explanation of the experimentally observed antioxidant effect. However, to obtain reliable theoretical results, certain general rules have to be obeyed:

(*i*) It is necessary to use a suitable computational method. In antioxidant research, DFT methods are dominant. Previous studies have confirmed the applicability of B3LYP (probably still the most popular one) (Becke, 1993; Lee et al., 1988) and newer M05-2X (Zhao et al., 2006) and M06-2X (Zhao and Truhlar, 2008) functionals. For solvent effect description, implicit solvent models (polarized continuum models — PCM) are usually employed. Sufficiently large basis sets including both, diffuse and polarization, functions are recommended for balanced description of molecules, radicals and charged species. Pople's basis sets, such as 6-311++G(d,p) or 6-311+G(d,p), are widely used in this field.

(*ii*) Conformational analysis of the studied molecules is necessary to identify conformation with the lowest energy, i.e. to identify the most stable conformation. In this step, it is inevitable to consider possible intramolecular hydrogen bonds. Their presence often affects the obtained results significantly.

(*iii*) In solution-phase thermochemistry of proton and electron transfer, proton and electron solvation enthalpies represent important quantities. On the other hand, solvation does not significantly alter the thermodynamics of homolytic bond dissociation in neutral molecules. Hydrogen atom $H^{\bullet}$ solvation enthalpy values in various solvents are within several units of kJ mol^{-1} (Parker, 1992; Wilhelm and Battino, 1973). The authors should always specify the employed total or solvation enthalpies of $H^{\bullet}$, H^{+}, and e^{-} used in the calculations. Application of different available values of solvation enthalpies can shift the obtained results by tens of kJ mol^{-1}. If the employed solvation enthalpies are not specified, mutual comparison of various published values is questionable.

It should also be noted that the Gibbs free energy represents the general criterion of the thermodynamically favored mechanism. However, in case of the studied reactions, the absolute values of the entropic term, $-T\Delta_r S$, are only a few units or tens of kJ mol^{-1} and the reaction Gibbs free energies, $\Delta_r G = \Delta_r H - T\Delta_r S$, are just slightly shifted compared to the reaction enthalpies (Dewar, 1990; Klein and Lukeš, 2006; Rimarčík et al. 2010). Thus, BDE, IP and PA values indicate the thermodynamically preferred mechanism. In polar solvents, the differences between them are in hundreds of kJ mol^{-1}.

Acknowledgement

The work has been supported by the Slovak Grant Agency (1/0416/17) and the Slovak Research and Development Agency (APVV-15-0053). V. L. and E. K. thank the Ministry of Education, Science, Research and Sport of the Slovak Republic for funding within the scheme "Excellent Research Teams".

References

Ajitha MJ, Mohanlal S, Suresh CH, Jayalekshmy A (2012) Journal of Agricultural and Food Chemistry 60: 3693–3699.

Álvarez-Diduk R, Ramírez-Silva MT, Galano A, Merkoçi, A (2013) The Journal of Physical Chemistry B 117: 12347–12359.

Amić D, Stepanić V, Lučić B, Marković Z, Dimitrić Marković JM (2013) Journal of Molecular Modeling 19: 2593–2603.

Becke A (1993) The Journal of Chemical Physics 98: 5648–5652.

Binkley JS, Pople JA, Hehre WJ (1980) Journal of the American Chemical Society 102: 939–947.

Bors W, Heller W, Michel C, Saran M (1990) Methods in Enzymology 186: 343–355.

Burda S, Oleszek W (2001) Journal of Agricultural and Food Chemistry 49: 2774–2779.

Cances E, Mennucci B (1998) Journal of Mathematical Chemistry 23: 309–326.

Cances E, Mennucci B, Tomasi J (1997) The Journal of Chemical Physics 107: 3032–3041.

Chen X, Deng Z, Zhang C, Zheng S, Pan Y, Wang H, Li H (2018) Food Research International, in press. https://doi.org/10.1016/j.foodres.2018.11.018.

Croft KD (1998) Annals of the New York Academy of Sciences 854: 435–442.

Dewar MJS (1990) The Molecular Orbital Theory of Organic Chemistry. McGraw-Hill, New York.

Dueñas M, González-Manzano S, González-Paramás A, Santos-Buelga C (2010) Journal of Pharmaceutical and Biomedical Analysis 51: 443–449.

Foti MC, Daquino C, Geraci C (2004) The Journal of Organic Chemistry 69: 2309–2314.

Frisch MJ, Trucks GW, Schlegel HB, Scuseria GE, Robb MA, Cheeseman JR, et al. Gaussian 09, Revision D.01 Gaussian Inc, Wallingford, CT (2013).

Galano A, Mazzone G, Álvarez-Diduk R, Marino T, Raúl Alvarez-Idaboy J, Russo N (2016) Annual Review of Food Science and Technology 7: 335–352.

Galano A, Raúl Alvarez-Idaboy J (2019) International Journal of Quantum Chemistry 119: e25665.

Galano A, Raúl Alvarez-Idaboy J, Francisco-Mańquez M (2011) The Journal of Physical Chemistry B 115: 13101–13109.

Ingold KU, Litwinienko G (2005) The Journal of Organic Chemistry 70: 8982–8990.

Klein E, Lukeš V (2006) Chemical Physics 330: 515–525.

Klein E, Rimarčík J, Senajová E, Vagánek A, Lengyel J (2016) Computational and Theoretical Chemistry 1085: 7–17.

Lee C, Yang W, Parr RG (1988) Physical Review B 37: 785–789.

Lemańska K, Szymusiak H, Tyrakowska B, Zieliński R, Soffers AEMF, Rietjens IMCM (2001) Free Radical Biology and Medicine 31: 869–881.

Lemańska K, van der Woude H, Szymusiak H, Boersma MG, Gliszczyńska-Świgło A, Rietjens IMCM, Tyrakowska B (2004) Free Radical Research 38: 869–881.

Lengyel J, Rimarčík J, Vagánek A, Klein, E (2013) Physical Chemistry Chemical Physics 15: 10895–10903.

Leopoldini M, Russo N, Chiodo S, Toscano M (2006) Journal of Agricultural and Food Chemistry 54: 6343–6351.

Leopoldini M, Russo N, Toscano M (2011) Food Chemistry 125: 288–306.

León-Carmona JR, Raúl Alvarez-Idaboy J, Galano A (2012) Physical Chemistry Chemical Physics 14: 12534–12543.

Litwinienko G, Ingold KU (2003) The Journal of Organic Chemistry 68: 3433–3438.

Litwinienko G, Ingold KU (2004) The Journal of Organic Chemistry 69: 5888–5896.

Lucarini M, Mugnaini V, Pedulli GF (2002) The Journal of Organic Chemistry 67: 928–931.

Marenich AV, Cramer CJ, Truhlar DG (2009) The Journal of Physical Chemistry B 113: 6378–6396.

Marković Z, Amić D, Milenković D, Dimitrić-Marković JM, Marković S (2013) Physical Chemistry Chemical Physics 15: 7370–7378.

Marković Z, Milenković D, Đorović J, Dimitrić Marković JM, Stepanić V, Lučić B, Amić D (2012) Food Chemistry 134: 1754–1760.

Marković Z, Tošović J, Milenković D, Marković S (2016) Computational and Theoretical Chemistry 1077: 11–17.

Mendoza-Wilson AM, Santacruz-Ortega H, Balandrán-Quintana RR (2011) Journal of Molecular Structure 995: 134–141.

Musialik M, Kuzmicz R, Pawlowski TS, Litwinienko, G (2009) The Journal of Organic Chemistry 74: 2699–2709.

Nazarparvar E, Zahedi M, Klein E (2012) The Journal of Organic Chemistry 77: 10093–10104.

Osorio E, Pérez EG, Areche C, Ruiz LM, Cassels BK, Flórez E, Tiznado W (2013) Journal of Molecular Modeling 19: 2165–2172.

Parker VD (1992) Journal of the American Chemical Society 114: 7458–7462.

Procházková D, Boušová I, Wilhelmová N (2011) Fitoterapia 82: 513–523.

Rassolov V, Pople JA, Ratner M, Redfern PC, Curtiss LA (2001) Journal of Computational Chemistry 22: 976–984.

Rice-Evans CA, Miller NJ, Paganga G (1996) Free Radical Biology and Medicine 20: 933–956.

Rimarčík J, Lukeš V, Klein E, Ilčin M (2010) Journal of Molecular Structure: THEOCHEM 952: 25–30.

Sadasivam K, Kumaresan R (2011) Spectrochimica Acta Part A: Molecular and Biomolecular Spectroscopy 79: 282–293.

Staško A, Brezová V, Biskupič S, Mišík V (2007) Free Radical Research 41: 379–390.

Thavasi V, Leong LP, Bettens RPA (2006) Journal of Physical Chemistry A 110: 4918–4923.

Toscano M, Russo N (2016) Computational and Theoretical Chemistry 1077: 119–124.

Trouillas P, Marsal P, Siri D, Lazzaroni R, Duroux J-L (2006) Food Chemistry 97: 679–688.

Vagánek A, Rimarčík J, Dropková K, Lengyel J, Klein E (2014) Computational and Theoretical Chemistry 1050: 31–38.

Vagánek A, Rimarčík J, Lukeš V, Klein E (2012) Computational and Theoretical Chemistry 991: 192–200.

Vakarelska-Popovska MH, Velkov Z (2016) Computational and Theoretical Chemistry 1077: 87—91.
Wilhelm E, Battino R (1973) Chemical Reviews 73: 1—9.
Zhao Y, Schultz NE, Truhlar DG (2006) Journal of Chemical Theory and Computation 2: 364—382.
Zhao Y, Truhlar DG (2008) Theoretical Chemistry Accounts 120: 215—241.
Zheng Y-Z, Chen D-F, Deng G, Guo R, Fu Z-M (2018) Journal of Molecular Modeling 24: 149.
Zheng Y-Z, Chen D-F, Deng G, Guo R, Lai R-C (2019) Phytochemistry 157: 1—7.
Zheng Y-Z, Deng G, Chen D-F, Guo R, Lai R-C (2017a) Scientific Reports 7: 7543.
Zheng Y-Z, Zhou Y, Liang Q, Chen D-F, Guo R, Xiong, C-L, Xu X-J, Zhang Z-N, Huang Z-J (2017b) Dyes and Pigments 141: 179—187.

sciendo

Influence of hydrotalcite preparation conditions on its physico-chemical properties

Miroslava Mališová[a], Michal Horňáček[a], Pavol Hudec[a], Jozef Mikulec[b], Vladimír Jorík[c], Elena Hájeková[a]

[a]Department of Organic Technology, Catalysis and Petroleum Chemistry, Faculty of Chemical and Food Technology, Slovak University of Technology, Radlinského 9, 812 37 Bratislava, Slovakia
[b]Research Institute of Petroleum and Hydrocarbon Gases, Vlčie Hrdlo, 820 03 Bratislava, Slovakia
[c]Department of Inorganic Chemistry, Faculty of Chemical and Food Technology, Slovak University of Technology, Radlinského 9, 812 37 Bratislava, Slovakia
mamiroslava@gmail.com

Abstract: The aim of the research was to prepare and characterize hydrotalcite synthesized under different preparation conditions. The most common hydrotalcite preparation is the co-precipiaton method. The preparation process strongly influences the catalytic properties of hydrotalcite; therefore, optimal conditions have to be determined. During the study, seven samples of the catalyst were prepared in the pH range from 8 to 12 and the synthesis temperature range from 25 to 55 °C. Based on several catalyst properties, optimal synthesis pH 10 was found. Ideal temperature of the preparation was determined to be 35 °C, but the temperature does not have a significant effect on the catalyst properties.

Key words: hydrotalcite, preparation conditions, co-precipitation, catalyst

Introduction

Several types of layered double hydroxides (LDH) were studied for various applications depending on their crystallinity and catalyst properties. LDH synthesis dates from 1930, when precipitation was used to prepare samples (Sato et al., 1988). A wide range of applications of this special layered structure have been studied. For example, oil adsorbents, sorption agents for industrial, sensors in electrochemistry and flame retardants in polymer nanocomposites (Cavani et al., 1991, Salomão et al., 2013).

Hydrotalcite (HT) belongs to the group of LDH, also known as anionic clays. In comparison to cationic clays, anionic clays are not very common in nature but their preparation in laboratory is much easier. The most widely used HT is magnesium-aluminum type with the chemical formula $[M_n^{2+}M_m^{3+}(OH)_{2(n+m)}]_m^{+}[A_x^{-}]_{m/x} \cdot {}_yH_2O$, where M^{2+} and M^{3+} are divalent and trivalent metal cations and A_x is the interlayer anion. An identical formula was found for the natural mineral hydrotalcite (Nishimura et al., 2013). Layered structure is based on rotation of positively charged octahedral layers and interlayer space. Charge balancing anions and water molecules occupy the interlayer space (Baskaran et al., 2015). The range of metal cations from the positive charge layer is relatively wide and is determined by their size, which should be similar to that of Mg^{2+} for divalent cations and that of Al^{3+} for trivalent cations (Basąg et al., 2016).

Scheme 1 shows a simplistic representation of the hydrotalcite structure (Baskaran et al., 2015).

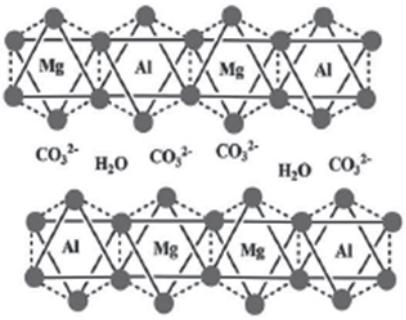

Scheme 1. Simplistic representation of hydrotalcite structure (Baskaran et al., 2015).

Synthesis

Co-precipitation is the most common method to prepare LDH like hydrotalcite. There are two different way of preparation: co-precipitation at variousable pH and at constant pH values. At constant pH, preparation is based on addition of NaOH solution to maintain the pH value constant during the whole time of preparation. In the variable pH method, a solution containing salts of the cations (divalent and trivalent) is added to an alkaline solution containing the anion to be interlayered. With the increasing concentration of alkaline metals, pH decreases. Co-precipitation is usually carried out at relatively low temperatures, usually up to 55 °C,

to prevent secondary formation reaction of simple hydroxides (Salomão R, et al., 2013).

Hydrotalcite application

Thanks to its special layered structure, hydrotalcite can be used for a variety of applications such as base, redox and photo-catalyst, as well as adsorbents. As a base catalyst, hydrotalcite can catalyze a wide range of reactions such as aldol condensation, hydroxylation, isomerization and others. Nowadays, many studies deal with hydrotalcite use as an adsorbent to reduce emissions of NO_x and SO_x because of its large sorption capacity. Hydrotalcite has drawn attention also as a catalyst to produce biofuels as it is very effective for transesterification of vegetable oils to produce biofuels. Easy preparation by co-precipitation, which is quick and not complicated, as well as its great catalyst properties are its advantage.

Experimental

One of the most common methods to prepare hydrotalcite was used to prepare seven samples. First solution (A) was Na_2CO_3 ($c = 0.5$ mol/dm^3) dissolved in 1 L of deionized water. Solution of metal nitrates (solution B) prepared from $Mg(NO_3)_2$ and $Al(NO_3)_3$ with the concentration of 1.0 mol/dm^3 was slowly added (10,44 ml/min) to solution A for 1 hour. Preparation of hydrotalcite samples was realized in the pH range from 8 to 12 and temperature range from 25 to 55 °C. The pH value was kept constant by addition of NaOH solution with the concentration $c = 3.0$ mol/dm^3. Addition of NaOH was controlled by a pH electrode measuring the pH value throughout the reaction. Temperature was monitored by a temperature sensor connected to a heating plate. Each sample aged for 24 hours. After the solution sedimentation, the sediment was washed with at least 2 L of distilled water and filtered. Drying was carried out for 1—2 hours at 80 °C. After the preparation, all samples were stored in an airtight container and subsequently calcined at 150 °C and 450 °C. Prepared samples were used for further measurements.

Crystalline phase identification and phase purity determination of the prepared samples were carried out by XRD analysis using a STOE THETA-THETA diffractometer, with CoKα radiation, scan range of 2.90 ° — 90.00 ° 2Θ and at the step size of 0.02 °.

Surface characteristics were measured by physical adsorption of nitrogen at –196 °C using ASAP-2400 (Micromeritics). Overnight evacuation of the samples at 150 °C and 450 °C preceded the adsorption analysis. Specific surface area, S_{BET}, was obtained using the conventional BET isotherm ($p/p_0 = 0.05 — 0.30$). The surface of mesopores, S_t, and the volume of micropores, V_{micro}, were calculated from the t-plot using the Harkins–Jura master isotherm. The value of the total pore volume, V_a, was determined from adsorption data at relative pressure $p/p_0 = 0.99$. From desorption branches of the isotherms, pore size distribution was calculated using the BJH method.

Temperature programmed desorption of carbon dioxide as a probe molecule (TPD-CO_2) was carried out in equipment with a TCD detector. The catalyst amount of 200 mg (grain of 0.4—0.71 mm) was placed in a quartz reactor. Before the TPD experiment, the catalysts were activated at 450 °C for 80 minutes in helium flow (75 mL/min). Subsequently, the catalysts were cooled down to 25 °C and treated with CO_2 flow (99 % purity, 50 mL/min) for 30 minutes. The weakly adsorbed CO_2 was removed by flushing the sample with helium (110 mL/min) at 25 °C for 80 minutes. Desorption of CO_2 was measured by heating the catalyst from 25 °C to 500 °C at the heating rate of 5 °C/min in helium flow. The amount of basic sites was calculated from the area of CO_2 desorption peaks with help of calibration using a known amount of CO_2 desorbed from $MgCO_3$ decomposition.

SEM images were taken using field emission JEOL JSM-7600F SEM at the accelerating voltage of 5 kV and working distance of 4.5 mm.

Result and Discussion

Seven samples of aluminum-magnesium hydrotalcite were prepared for the study under various synthesis conditions. Temperature of the synthesis as well as pH were varied for each sample. Table 1 presents symbols of individual samples together with their preparation conditions. All samples were prepared with the same amount of metal nitrates and Na_2CO_3 solution.

Tab. 1. Samples preparation conditions.

Sample	pH of synthesis	Temperature of synthesis [°C]
HTT/10/25	10	25
HTT/08/25	8	25
HTT/09/25	9	25
HTT/12/25	12	25
HTT/10/45	10	45
HTT/10/55	10	55
HTT/10/35	10	35

Temperature was controlled by means of a temperature sensor connected to a heating plate while pH was maintained at a constant value during the reaction by NaOH solution. Designation of the samples was as follows: HTT/pH/temperature.

Specific surface area – BET

One of the most important properties of a catalyst is its specific surface area. It tells us about the catalyst adsorption capability. With the increasing specific surface area, hydrotalcite gains better properties for the catalysis of various reactions.

The determined specific surface areas of samples calcined at 150 °C and 450 °C with different preparation pH can be seen in Table 2. HTT/10/25 prepared at pH 10 shows the highest specific surface area and pore volume at both calcination temperatures.

A graphical comparison of the samples prepared at 25 °C and calcined at 150 °C and 450 °C with different pH can be seen in Figure 1. A significant increase in the specific surface area for the sample prepared at pH 10 can be observed.

Tab. 2. Determined surface area of samples with different preparation pH.

Sample	150 °C		450 °C	
	S_{BET} [m²/g]	V_a [cm³/g]	S_{BET} [m²/g]	V_a [cm³/g]
HTT/08/25	27	0.127	175	0.279
HTT/09/25	38	0.177	177	0.411
HTT/10/25	131	0.468	236	0.759
HTT/12/25	24	0.078	86	0.256

Based on Table 2 it is clear that from the point of view of surface area, optimal pH for hydrotalcite preparation is 10. In Table 3, calculated specific surface areas of samples prepared at pH 10 can be seen. The range of preparation temperature was from 25 to 55 °C and after the preparation, samples were calcined at 150 °C and 450 °C. It can be seen that the sample of HTT/10/35 synthesized at 35 °C shows the highest specific surface area compared to other samples.

However, in Figure 2 it can be seen that the synthesis temperature does not significantly affect

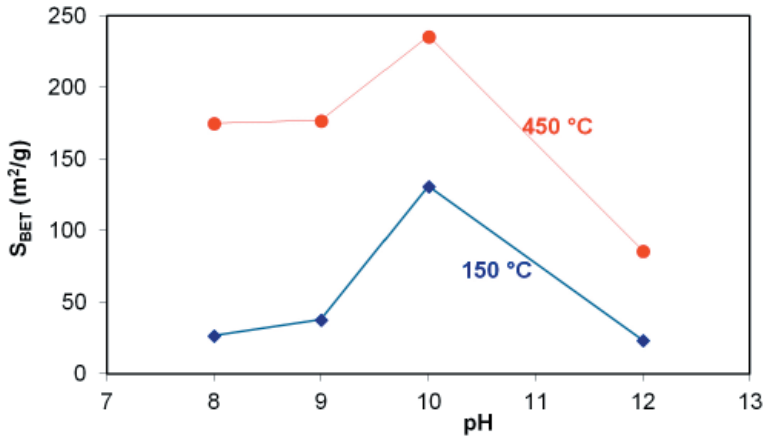

Fig. 1. Comparison of samples prepared with different pH calcined at 150 °C and 450 °C.

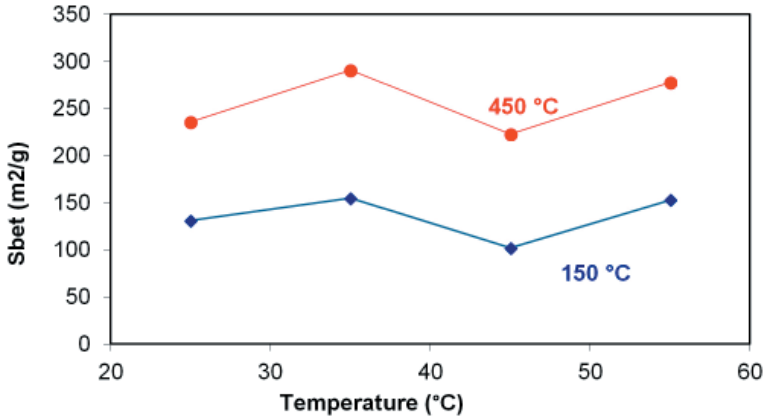

Fig. 2. Comparison of surface area of samples prepared at different synthesis temperatures and calcined at 150 °C and 450 °C.

Tab. 3. Determined surface area of samples with different preparation temperatures.

Sample	150 °C		450 °C	
	S_{BET} [m²/g]	V_a [cm³/g]	S_{BET} [m²/g]	V_a [cm³/g]
HTT/10/25	131	0.468	235	0.759
HTT/10/35	155	0.630	291	0.856
HTT/10/45	102	0.457	223	0.721
HTT/10/55	153	0.620	278	0.907

the specific surface area of hydrotalcite; however, four samples are not enough to make a conclusion whether the preparation temperature affects the specific surface area at all.

XRD

Influence of preparation temperature and synthesis pH on hydrotalcite properties has been investigated also by X-ray diffraction. XRD patterns of samples prepared at constant calcination temperature of 450 °C and different preparation temperatures are shown in Figure 3. This calcination temperature was chosen because hydrotalcite layered structure changes to mixed metal oxides structure. Higher calcination temperatures caused destruction of the layered structure and led to the formation of spinel structure.

The XRD pattern shows typical peaks of mixed metal oxide structure consisting of a symmetrical and sharp peak with high intensity at low 2θ angle (8—10) and asymmetric broad peaks at high 2θ angle. These

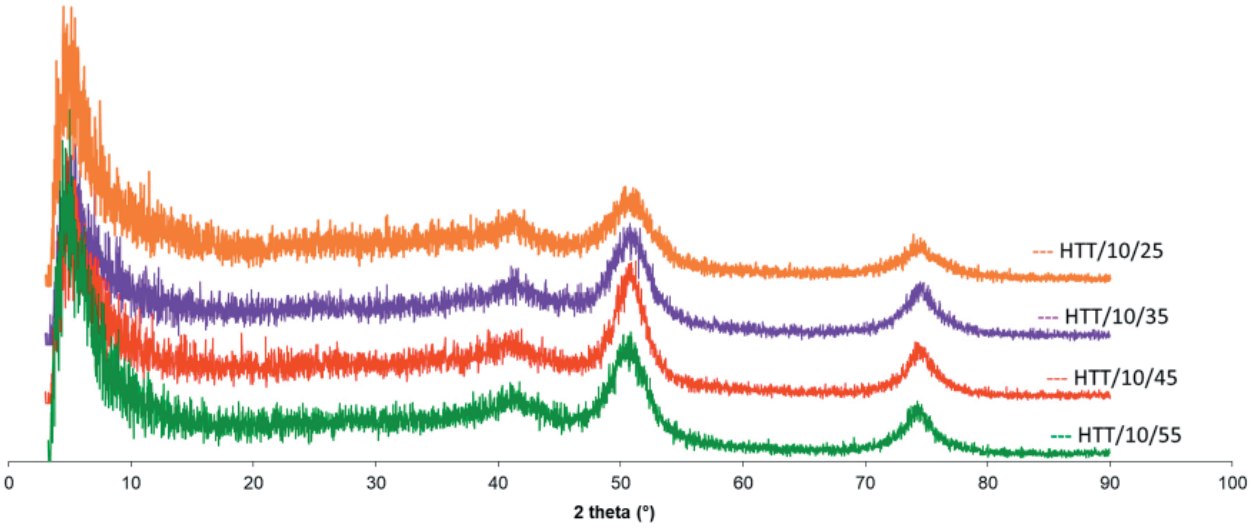

Fig. 3. XRD patterns of samples prepared at constant pH calcined at 450 °C.

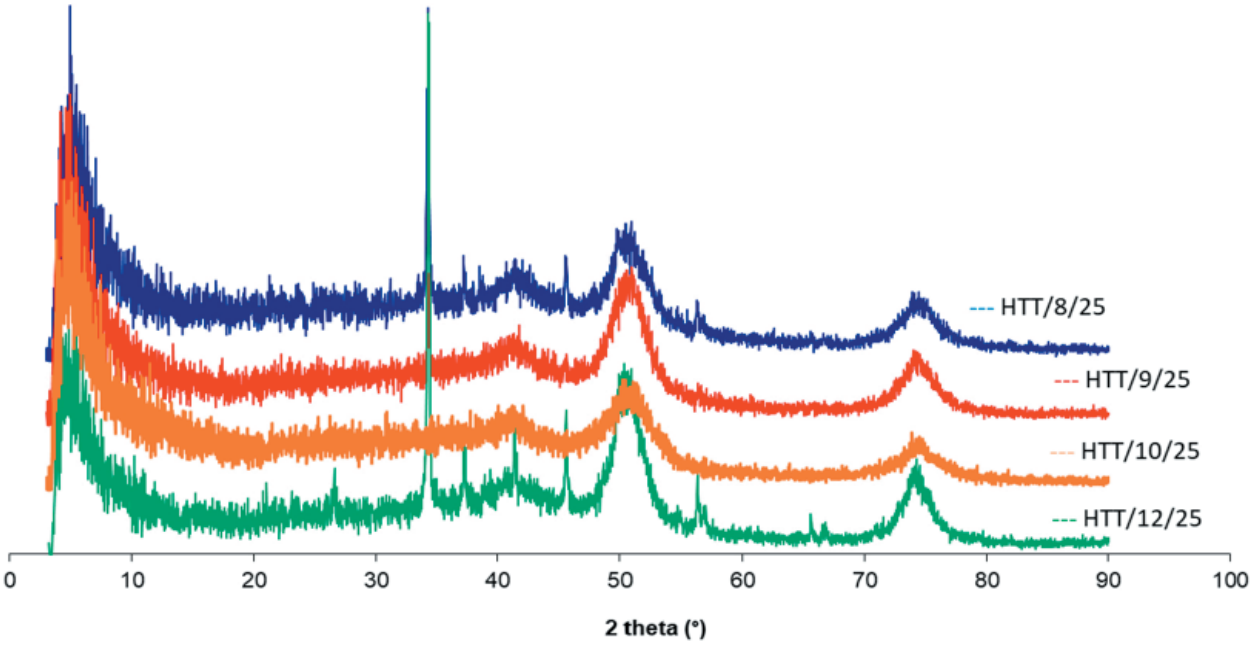

Fig. 4. XRD patterns of samples prepared at constant temperature and calcined at 450 °C.

diffraction patterns indicate good crystallinity of the prepared hydrotalcite (Wiyantoko et al., 2015). The influence of synthesis temperature on crystallinity is small which can be seen as just a little difference between the intensity of each peak.

In Figure 4, XRD pattern of samples prepared at constant temperature (25 °C) but different synthesis pH can be seen. Samples were calcined at the temperature of 450 °C. The XRD pattern also shows typical peaks of mixed metal oxide structure. In the sample prepared at pH 12, intense reflection at 2θ values of 35 ° and several smaller reflections in the 2θ range of 25 ° — 70 ° can be seen. These peaks can be attributed to $NaNO_3$ crystals and their presence may be caused by insufficient sample washing during filtration. Filtration of HTT/12/25 (pH 12) is difficult probably due to the crystal size of the prepared sample. The influence of synthesis pH on the crystallinity of hydrotalcite is considerably higher than that of the preparation temperature. In the 2θ range from 30 ° to 45 °, there are not very intense peaks in samples HTT/08/25 and HTT/12/25 prepared at pH 8 and 12, which are not characteristic peaks for mixed oxides structure.

SEM

Based on XRD, differences between the sample crystals obtained under different preparation conditions are minimal. Crystallinity of the prepared samples was in line with the characteristic reflections from the XRD pattern. (Wiyantoko et al., 2015) Figure 5 shows a SEM image of HTT/10/25 prepared at 25 °C and pH 10, which proved to be the best preparation conditions. The image shows very thin crystals. The morphology of prepared hydrotalcite was formed by accumulation of nanoparticle aggregates (Wang et al., 2012).

Adsorption-desorption isotherm

The following graphs show the adsorption-desorption isotherms of samples calcinated at 150 °C and 450 °C. Based on their shape, mesoporous texture of the samples can be seen. As a result of capillary condensation, a hysteresis loop is formed caused by a different mechanism of pores filling and emptying. These hysteresis loops are formed due to the presence of mesopores. Distribution of mesopores is in average 5—50 nm, some are up to 70 nm when it comes to macropores. The volume of micropores was evaluated using the t-plot and it was found to be negligible; specific surface area of mesopores, S_t, was practically the same as S_{BET}. When comparing the effect of preparation temperature on the adsorption isotherm, the total pore volume is slightly increased in the sample prepared at 35 °C. The effect of calcination temperature can also be seen at greater pore volumes at higher calcination temperatures, which is positive for the catalyst properties.

Temperature-programmed desorption of CO_2 (TPD-CO_2)

Hydrotalcite belongs to basic catalysts. With increasing basicity, catalytic properties of hydrotalcite are better. TPD-CO_2 was used to determine basicity of all hydrotalcite samples calcinated at 450 °C. As it can be seen in the previous section, after calcination at temperatures below 450 °C, hydrotalcite structure changes from layered to mixed metal oxides. Table 4 shows calculated values based on CO_2 desorption measurements. Sample prepared at pH 10 and at 35 °C achieved the highest basicity. The strong basicity in mixed oxides is connected to the presence of alkaline metals. (Fraile et al., 2015).

In Figures 7 and 8, dependence of the measured signal from the calcination temperature can be

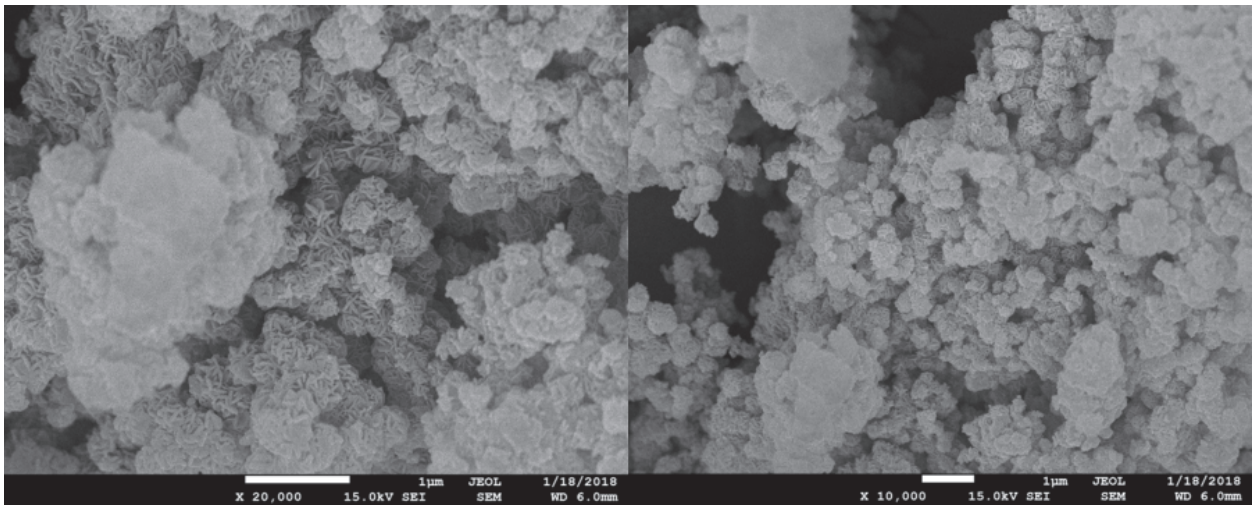

Fig. 5. SEM image of sample HTT/10/25 prepared at pH 10 and preparation temperature of 25 °C.

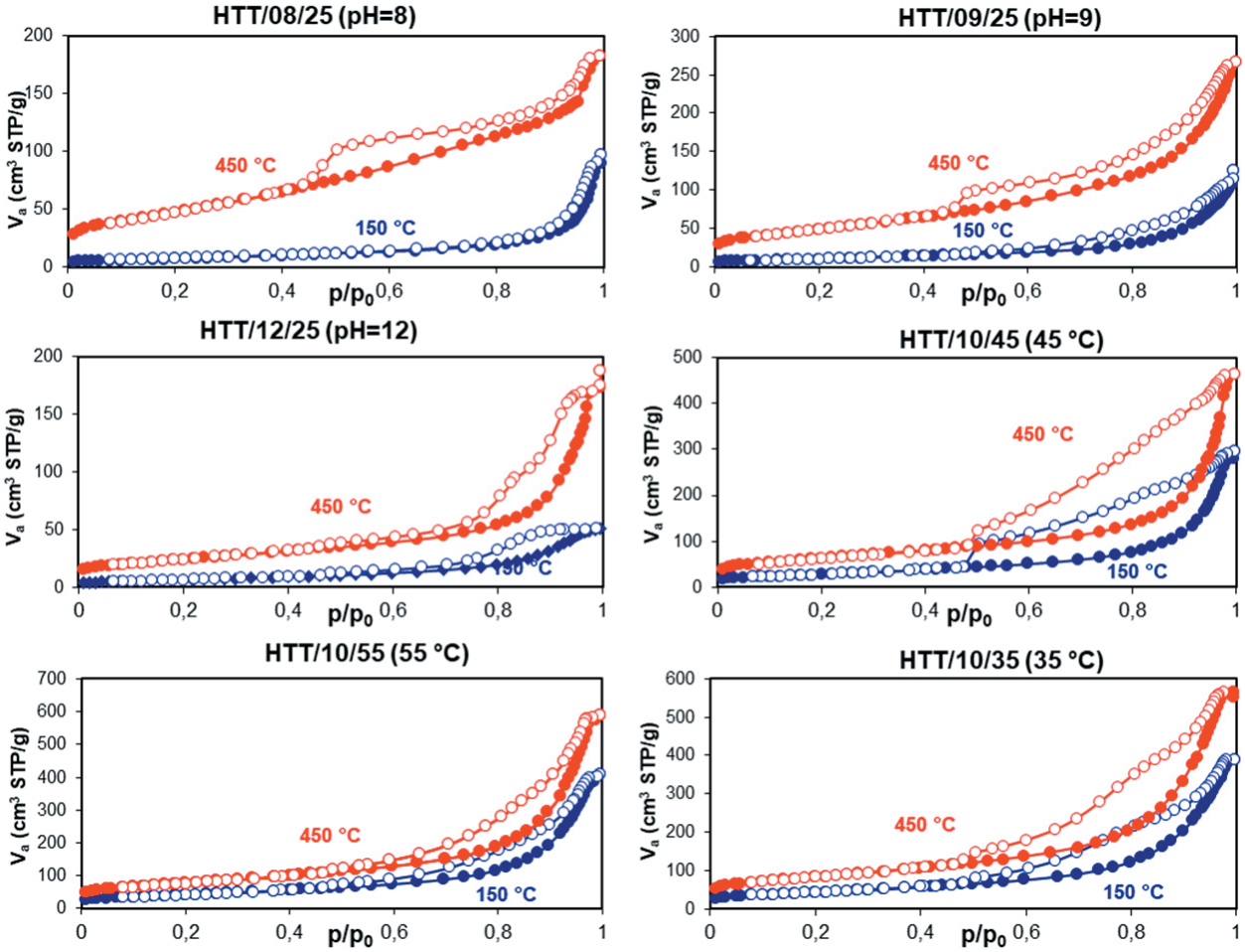

Fig. 6. Adsorption-desorption isotherms of prepared samples.

Tab. 4. Calculated values of basicity based on CO_2 desorption measurements.

Sample	HTT/10/25	HTT/08/25	HTT/09/25	HTT12/25	HTT/10/45	HTT/10/55	HTT/10/35
mmol CO_2/g	1.04	1.35	1.10	0.92	0.78	1.38	1.44

seen. Through the calcination of hydrotalcite, basic centers are formed. At temperatures below 100 °C, weak basic centers are visible. At higher calcination temperatures, from 100 °C to 200 °C, medium-basic sites, and at temperatures above 200 °C, strong basic sites occur (Navajasa et al., 2018). The sample prepared at pH 8 shows an intense maximum in the area of weak basic centers, which can be seen in Figure 7. In contrast, the HTT/10/25 sample does not reach such high intensity as the HTT/08/25 sample, but its signal indicates the presence of medium-basic or strong basic sites. In case of preparation temperature effect on sample basicity, high maximum in sample HTT/10/35 can be seen in the area of weak basic center, but high signal at other temperatures indicates the presence of medium-weak and strong basic sites. In Table 4, a comparison of basicity of all samples is shown, sample HTT/10/35 has the highest basicity among all samples.

Conclusion

Because of its wide range of application and easy preparation, hydrotalcite is an interesting substance. Preparation of hydrotalcite at different preparation temperatures and pH values provides information on the influence to hydrotalcite properties. Preparation by co-precipitation is the most common method to prepare this catalyst with the required structure to catalyze basic reactions. Basicity of hydrotalcite is one of the key properties. Preparation pH can influence basicity as it can be seen for sample HTT/10/35 prepared at pH 10, where basicity reached the highest value of all samples. In case of specific surface area, sample HTT/10/25 prepared at pH 10 showed the highest surface area. Preparation temperature does not have any significant effect on the specific surface area. Hydrotalcite is a mesoporous material as indicated by the hysteresis loop. In case of samples

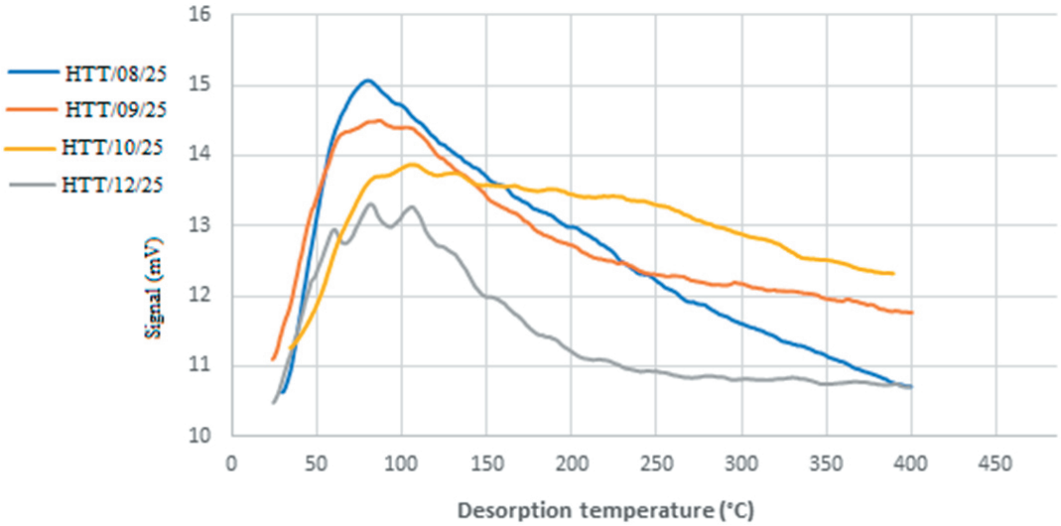

Fig. 7. Desorption curve of samples prepared at different pH.

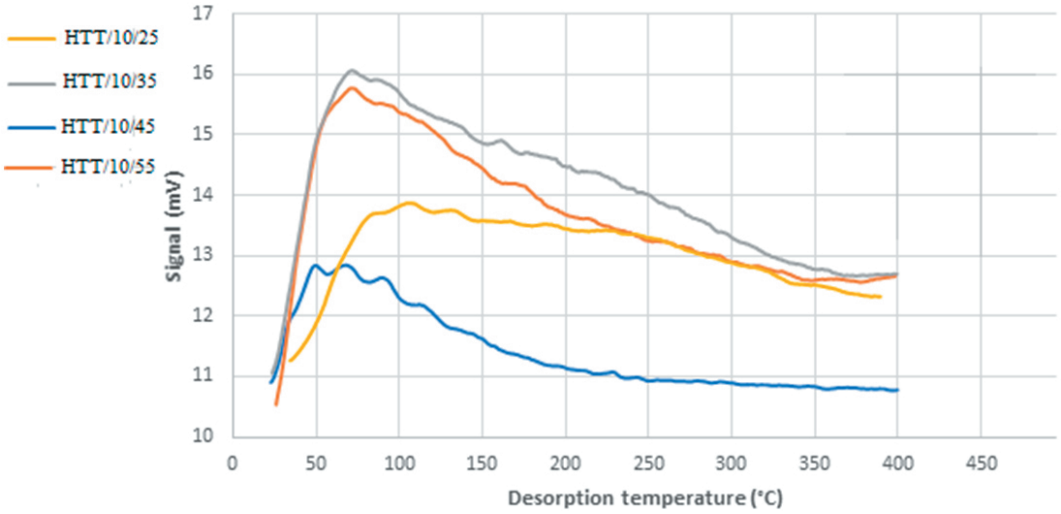

Fig. 8. Desorption curve of samples prepared at different temperatures.

prepared at 35 °C, higher pore volume can be seen. With higher pore volume, the sorption capacity of hydrotalcite increases, which is important when it is used as an adsorbent to reduce NO_x and SO_x emissions from industry. XRD patterns showed good crystallinity of prepared samples with peaks typical for mixed metal oxide structure. In sample HTT/12/25 prepared at pH 12, high intensity peaks can be seen which was attributed to $NaNO_3$ crystals present due to insufficient washing of sample during filtration.

Acknowledgement

This research has been financially supported by the Slovak Research and Development Agency under No. APVV-16-0097.

References

Fraile JM et al. (2015) The basicity of mixed oxides and the influence of alkaline metals: the case of transesterification reactions. Departamento de Química Orgánica. ICMA. C.S.I.C. 2015, Zv. Universidad de Zaragoza. Pedro Cerbuna 12, E-50009 Zaragoza (Spain).

Wiyantoko B et al. (2015) Synthesis and Characterization of Hydrotalcite at Different Mg/Al Molar Ratios. Procedia Chemistry 17: 21–26.

Cavani F. et al. (1991) Hydrotalcite-type anionic clays: Preparation, properties and applications. Catalysis Today. 11: 173.

Bezerra DM et al. (2017) Structural, vibrational and morphological properties of layered double hydroxides containing Ni^{2+}, Zn^{2+}, Al^{3+} and Zr^{4+} cations. Materials Characterization. 2017, 29–36.

Cavani F, Trifirb F, Vaccari A (1991) Hydrotalcite-type anlonlc clays: preparation, properties and applications. Catalysis Today. 173—301.

Muriithi GN et al. (2016) Synthesis and characterization of hydrotalcite from South African Coal fly ash. Powder Technology. 2. November 2016, 299—309.

Yang C, Liao L et al. (2016) Synthesis and characterization of Mn intercalated Mg-Al hydrotalcite. Journal of Colloid and Interface Science. 1. April 2016, 115—120.

Kloprogge1 JT, Frost RL (1999) Fourier Transform Infrared and Raman Spectroscopic Study of the Local Structure of Mg-, Ni-, and Co-Hydrotalcites. Journal of Solid State Chemistry. 506—515.

Pérez-Ramírez J et al. (2001) In situ Fourier transform infrared and laser Paman spectroscopic study of the thermal decomposition of Co-Al and Ni-Al hydrotalcites. Vibrational Spectroscopy. 75—88.

He J et al. (2005) Preparation of Layered Double Hydroxides. Struct Bond. 89—119.

Wiley J and sons, Kirk-Othmer Encyclopedia of Chemical Technology.

Jitianu M et al. (2000) IR structural evidence of hydrotalcites derived oxidic forms. Vibrational Spectroscopy. 75—86.

Kikhtyanin O, Tišler Z, Velvarská R, Kubička D (2016) Reconstructed Mg-Al hydrotalcites prepared by using different rehydration and drying time: Physico-chemical properties and catalytic performance in aldol condensation. Applied Catalysis A: General. 19. December 2016, 85—96.

Salomão R et al. (2013) Hydrotalcite ($Mg_6Al_2(OH)_{16}(CO_3)\cdot 4H_2O$): A Potentially Useful Raw Material for Refractories. Interceram — refractories manual. 187.

Sato T et al. (1988) Synthesis of hydrotalcite-like compounds and their physico chemical properties. Reactivity of Solids. 219—228.

Nishimura S et al. (2013) Characterization, synthesis and catalysis of hydrotalcite-related materials for highly efficient materials transformations. Green Chemistry.

Basąg S et al. (2016) Cu-Mg-Al hydrotalcite-like materials as precursors of effective catalysts for selective oxidation of ammonia to dinitrogen — The influence of Mg/Al ratio and calcination temperature. Applied Clay Science. 4. March 2016, 122—130.

Baskaran T et al. (2015) Progress on layered hydrotalcite (HT) materials as potential support and catalytic materials. Royal society of chemistry. 26. September 2015.

Wang Q et al. (2012) Morphology and composition controllable synthesis of Mg-Al-CO_3 hydrotalcites by tuning the synthesis pH and the CO_2 capture capacity. Applied Clay Science. 18—26.

sciendo

Analysis of C3 fraction splitting system performance by mathematical modeling in MATLAB environment

Miroslav Variny[a], Patrik Furda[a], Norbert Kováč[b], Otto Mierka[a]

[a]Slovak University of Technology, Faculty of Chemical and Food Technology, Department of Chemical and Biochemical Engineering, Radlinského 9, 812 37 Bratislava, Slovak Republic
[b]SLOVNAFT, a.s. Vlčie hrdlo 1, 824 12 Bratislava, Slovak Republic
miroslav.variny@stuba.sk

Abstract: Propane-propylene mixture splitting by industrial conventional rectification incorporating a heat pump for energy intensity decrease was modeled in the Matlab environment. The constructed model was verified by comparing its results with operational data of a real C3 fraction splitting unit. As documented, increased product quality can be obtained at zero additional costs due to specific features of the system design. Process capacity and product purity limitations have to be considered in future C3 fraction production increase plans. Further compressor and its driving unit design features have to be incorporated in the calculation model to reliably assess the C3 fraction processing costs and provide a reliable tool for process operation optimization.

Key words: C3 fraction, industrial heat pump, mathematical modeling, product purity

Introduction and study objectives

Refining and petrochemicals production belong to energy intensive industry sectors, accounting for more than 7 % of the total industrial energy consumption in the OECD countries in 2012 (EIA 2016) and predicted to keep this share at least until 2040. Similarly, the share of chemical industry sector including refining and petrochemicals production on the total industrial energy demand was more than 15 % in Slovak Republic in 2011 (Vall, 2011). Facing the expected decrease in fossil fuel demand for individual transportation, many refining companies, including MOL GROUP, focus their attention on new technologies implementation and material and energy efficiency improvement in those expected to continue playing a key role in their future business (MOL, 2016).

The issue of refining industry energy intensity decrease has been tackled in numerous studies in recent years. Many published studies, including Alhajji and Demirel (2015); Al-Rowaili and Ba-Shammakh (2017), and Li et al. (2016), apply computational modeling based both on the laws of thermodynamics and on the mass and energy balances together with heat and mass transfer equations and economic considerations. Environmental aspects are considered in the energy intensity and profit optimization calculations of entire production clusters as documented by Alhajji and Demirel (2015), Al-Rowaili and Ba-Shammakh (2017) and Morrow III et al. (2015).

Individual production units are frequent subjects of optimization calculations as well as simulations, e.g. crude distillation unit (Gadalla et al., 2015), isomerization process (Chuzlov and Molotov, 2016), isopropylbenzene production plant (Chudinova et al., 2016) or other plants (Vilarinho et al., 2016; You et al., 2016). The role of robust software for extensive calculations seems to be very important in achieving units profitability increase by operational or design changes. Best industrial practice and energy auditing procedures as established by DeCarolis et al. (2017), Hasanbeigi and Price (2010) and Worell et al. (2015) employ computational approach also in identification and reduction of process and design inefficiencies.

Traditional solutions and best practice applied in refining energy intensity decrease are summed up in recent studies by Danilov et al. (2018) and Worell et al. (2015), identifying, among others, heat driven refrigeration units, heat pipes and heat pumps as suitable technologies to achieve this goal. Several authors assessed the potential of industrial heat pumps application in the refining sector in recent research outcomes (Gadalla et al., 2015; Kazemi et al., 2016; You et al., 2016), corroborating the earlier findings of Demirel (2004) and Fonyo and Benkö (1998) together with the industrial experience of properly designed and operated industrial heat pump reducing the process energy consumption by 30 to 50 % compared to traditional design. Best results have been achieved in applications where substances with similar boiling point have to be separated by rectification (Demirel, 2004; Fonyo and Benkö, 1998), such as light alkane-alkene mixtures or light isomer mixtures. Especially ethane-ethylene and propane-propylene splitters

are frequently equipped with mechanical vapor recompression heat pumps (Morrow III et al., 2015; Variny et al., 2013; Variny et al., 2015; Worrel et al., 2015).

Earlier work of the authors compared traditional and heat pump driven propane-propylene separation units in SLOVNAFT a.s. (Variny et al., 2013). The prospective of C3 fraction production boost with the C3 splitter expected to be one possible bottleneck, the future C3 splitter operation with increased feed and/or changed feed composition has to be modeled, which represents the main objective of the presented study. To achieve this goal, a reliable and robust mathematical model of this part of the Fluid Catalytic Cracking Unit (FCC) was developed in the Matlab environment, verified on real operational data and used to predict the impact of feed quantity and quality changes on products purity and system energy intensity.

Materials and Methods

Modeled system

C3 fraction splitting can be characterized by high energy demand as the propylene-propane mixture is a close boiling mixture (Demirel, 2004). Propylene polymerization to which the produced propylene is submitted requires high purity propylene (> 99.6 %). To achieve this via conventional approach, numerous equilibrium stages and high reflux ratio are necessary (Demirel, 2004).

In the SLOVNAFT refinery, components of the C3 fraction are separated in two production units: Ethylene Unit and Fluid Catalytic Cracking (FCC) Unit. The Ethylene Unit operation provides sufficient amount of disposable heat for the column reboiler. Thus, the process in the Ethylene Unit is realized conventionally. On the contrary, the Propylene Recovery Unit of the FCC operates as an industrial heat pump utilizing latent heat of compressed product vapors in the column reboiler. A simplified flow scheme of the FCC C3 splitting process is provided in Fig. 1.

During normal operation, preheated feedstock (1) is delivered to the feed stage of the tray rectification column. Distillate vapors leaving the head of column (2) are led to heat pump compressor (K) driven by condensation turbine (T). A part of the compressed vapors (5) continues to column reboiler (E1) where it condenses and the heat of condensation serves as the heat supply for the column. The excess heat is disposed of in heat exchanger (E2) cooled by cooling water. Condensate (6, 8) is subsequently expanded to the head pressure level in flash vessel (F). Evaporated gas phase (12) is led back to the compressor and liquid phase (9) is pumped

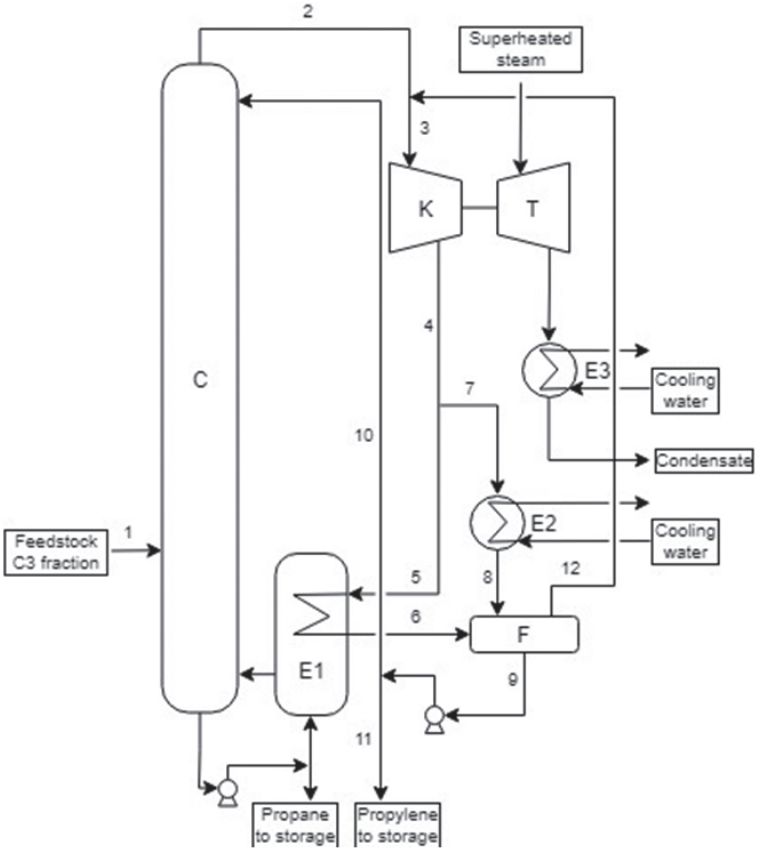

Fig. 1. Process flow diagram.

partly as reflux to the head of the column (10) and partly as product flow (11) to storage.

Mathematical model

The model setup reflects the physical plant structure as shown in Fig. 1 and includes the following assumptions:

- Feedstock is supplied as a boiling liquid.
- Both feedstock constituents are considered to have identical molar isobaric heat capacities in liquid and in gas phase as well as identical molar heats of evaporation at constant temperature. Available data in Perry (1997) justify this simplification: molar isobaric heat capacities in the liquid phase differ by less than 7 % for propane and propylene in the relevant temperature interval from 300 to 320 K. The same conclusion was achieved for their molar isobaric heat capacities in the gaseous phase and also for molar heats of evaporation. Thus, the liquid molar flow changes only on the feed stage and that of vapor is constant along the whole column.
- Ideal gas and ideal liquid behavior is assumed.
- Pressure profile along the column is linear with no radial pressure gradient.
- There is no radial temperature gradient.
- Column reboiler operates as a total condenser and reflux enters the column as boiling liquid.
- Gaseous phase leaving each stage of the column is in thermodynamic equilibrium with the liquid phase.
- Vapor and liquid phases leaving each stage of the column are of the same temperature and composition as vapor and liquid phases at the stage, respectively.
- Heat losses in the system as well as the pressure losses in the pipelines are negligible.

The mathematical model consists of two connected parts; the first calculates the column conditions in terms of concentration and temperature profiles and energy requirements considering the assumptions formulated above and the latter calculates the heat pump performance.

Model equations (1) to (35) are provided below and the calculation diagram shown in Fig. 2a, 2b implemented in the Matlab environment provides a comprehensive overview of the calculation procedure and its complexity. Physico-chemical input data used for molar enthalpies calculation and for equations (5), (18) and (27) were obtained from Perry, 1997.

To calculate the concentration and temperature profile along the column, overall mass balance (Eq. (1) to (4)) along with balances of each stage (Eq. (8) to (13)) were calculated considering phase equilibrium at each stage (Eq. (5) to (7)). The energy balance (14) reflects the column energy requirements. As a result, the model provides information regarding distillate mass flow and thus enables heat pump performance calculation. Alternatively, distillate composition if the heat pump performance is given.

$$\dot{n}_{L,n} = R\dot{n}_D \tag{1}$$

$$\dot{n}_{L,m} = \dot{n}_F + \dot{n}_{L,n} \tag{2}$$

$$\dot{n}_V = \dot{n}_D + \dot{n}_{L,n} \tag{3}$$

$$\dot{n}_W = \dot{n}_F - \dot{n}_D \tag{4}$$

$$P^0_{i,j} = e^{\left[C1_i + \frac{C2_i}{T_j} + C3_i \ln\left(T_j\right) + C4_i T_j^{C5_i}\right]} \tag{5}$$

$$x_{A,j} = y_{A,j}\frac{P_j}{P^0_{A,j}} \tag{6}$$

$$y_{B,j} = \frac{P^0_{B,j}}{P_j}\left(1 - x_{A,j}\right) \tag{7}$$

$$fval_{j,1} = \dot{n}_V y_{A,j} - \dot{n}_D x_{A,j} - \dot{n}_{L,n} x_{A,j} \tag{8}$$

$$fval_{j,1} = \dot{n}_{L,n} x_{A,j-1} + \dot{n}_V y_{A,j+1} - \dot{n}_{L,n} x_{A,j} - \dot{n}_V y_{A,j} \tag{9}$$

$$\begin{aligned} fval_{j,1} = {} & \dot{n}_{L,n} x_{A,j-1} + \dot{n}_V y_{A,j+1} + \\ & + \dot{n}_F x_F - \dot{n}_{L,m} x_{A,j} - \dot{n}_V y_{A,j} \end{aligned} \tag{10}$$

$$fval_{j,1} = \dot{n}_{L,m} x_{A,j-1} + \dot{n}_V y_{A,j+1} - \dot{n}_{L,m} x_{A,j} - \dot{n}_V y_{A,j} \tag{11}$$

$$fval_{j,1} = \dot{n}_{L,m} x_{A,j-1} - \dot{n}_W x_{A,j} - \dot{n}_V y_{A,j} \tag{12}$$

$$fval_{j,2} = y_{A,j} + y_{B,j} - 1 \tag{13}$$

$$\begin{aligned} \dot{Q}_{RB} = {} & \dot{n}_W \left[h^{T_{RB}}_{A,l} x_{A,N} + h^{T_{RB}}_{B,l}\left(1 - x_{A,n}\right)\right] + \\ & + \dot{n}_D \left(R+1\right)\left[h^{T_1}_{A,g} y_{A,1} + h^{T_1}_{B,g}\left(1 - y_{A,1}\right)\right] - \\ & - \dot{n}_F \left[h^{T_F}_{A,l} x_F + h^{T_F}_{B,l}(1 - x_{F)}\right] - \\ & - \dot{n}_D R\left[h^{T_1}_{A,l} y_{A,1} + h^{T_1}_{B,l}\left(1 - y_{A,1}\right)\right] \end{aligned} \tag{14}$$

Given the column energy requirements it is possible to calculate the actual condensate flow through the reboiler and ultimately the mass flow through the heat pump compressor. The calculation prerequisite is the knowledge of the actual condensate temperature. In order to obtain this information, design condensate flow evaluation is necessary. The calculation is relatively straightforward, including a simple iteration.

$$\dot{Q}_{RB,design} = \dot{Q}_{RB}\frac{\dot{n}_{V,design}}{\dot{n}_V} \tag{15}$$

$$fval = P_{out,design} - P_{out,iter} \tag{16}$$

$$h_{cond,design} = h_{A,l}^{T_{cond,design}} y_{A,1} + h_{B,l}^{T_{cond,design}} \left(1 - y_{A,1}\right) \quad (17)$$

$$h_{comp,design} = \frac{\overline{z} R_m T_{in,design} \frac{\overline{n}}{\overline{n}-1} \left[\left(\frac{P_{out,design}}{P_{in,design}} \right)^{\frac{\overline{n}-1}{\overline{n}}} - 1 \right]}{\eta_p} \quad (18)$$

$$h_{in,design} = h_{A,g}^{T_{in,design}} y_{A,1} + h_{B,g}^{T_{in,design}} \left(1 - y_{A,1}\right) \quad (19)$$

$$h_{out,design} = h_{in,design} + h_{comp,design} \quad (20)$$

$$\dot{n}_{cond,design} = \frac{\dot{Q}_{RB,design}}{h_{out,design} - h_{cond,design}} \quad (21)$$

The overall heat transfer coefficient in Eq. (22) is proportional to the mass flow through the heat exchanger. Thus, the design-to-actual heat flux ratio can be expressed as shown in Eq. (23).

$$\dot{Q} = kA\Delta T \quad (22)$$

$$\frac{\dot{Q}_{RB,design}}{\dot{Q}_{RB}} = \left(\frac{\dot{m}_{design}}{\dot{m}} \right)^a \frac{\Delta T_{design}}{\Delta T} \quad (23)$$

$$\Delta T = \frac{\dot{Q}_{RB}}{\dot{Q}_{RB,design}} \left(\frac{\dot{m}}{\dot{m}_{design}} \right)^{-a} \Delta T_{design} \quad (24)$$

$$\Delta T = T_{cond} - T_{RB} \quad (25)$$

Assuming a constant fraction exponent, the final equation for condensate temperature calculation is as follows:

$$T_{cond,iter} = \frac{\dot{Q}_{RB}}{\dot{Q}_{RB,design}} \left(\frac{\dot{n}_{cond,iter}}{\dot{n}_{cond,design}} \right)^{-0,6} \times \times \left(T_{cond,design} - T_{RB} \right) + T_{RB} \quad (26)$$

Empirical correlations for heat transfer coefficient (α) incorporate its dependence on the Reynolds number as $\alpha \sim Re^m$ where m varies between 0.4 and 0.8 depending on particular heat transfer conditions and heat exchanger design. The Reynolds number is directly proportional to mass (molar) flow; heat exchanger duty estimated from the heat transfer equation can therefore be related to the mass flow to the power of m. Average value of m = 0.6 was considered in this study – Eqs. (23), (24), (26). Using an analogous approach as in Eqs. (17) to (21), the actual condensate flow was calculated.

$$h_{comp,iter} = \frac{\overline{z} R_m T_1 \frac{\overline{n}}{\overline{n}-1} \left[\left(\frac{P_{out}}{P_1} \right)^{\frac{\overline{n}-1}{\overline{n}}} - 1 \right]}{\eta_p} \quad (27)$$

$$h_{in,iter} = h_{A,g}^{T_1} y_{A,1} + h_{B,g}^{T_1} \left(1 - y_{A,1}\right) \quad (28)$$

$$h_{out,iter} = h_{in,iter} + h_{comp,iter} \quad (29)$$

$$h_{cond,iter} = h_{A,l}^{T_{cond,iter}} y_{A,1} + h_{B,l}^{T_{cond,iter}} \left(1 - y_{A,1}\right) \quad (30)$$

$$\dot{Q}_{RB,iter} = \dot{n}_{cond,iter} \left(h_{out,iter} - h_{cond,iter} \right) \quad (31)$$

$$fval = \dot{Q}_{RB,iter} - \dot{Q}_{RB} \quad (32)$$

Combining mass and heat balance of the flash vessel, actual flow through the heat pump compressor (Eq. 35) and vapor generation rate in the flash vessel (Eq. 34) are calculated.

$$h_{reflux} = h_{A,l}^{T_1} y_{A,1} + h_{B,l}^{T_1} \left(1 - y_{A,1}\right) \quad (33)$$

$$\dot{n}_{flash} = \frac{h_{cond} - h_{reflux}}{h_{in} - h_{reflux}} \dot{n}_{cond} \quad (34)$$

$$\dot{n}_{comp} = \frac{\dot{n}_V}{1 - \frac{h_{cond} - h_{reflux}}{h_{in} - h_{reflux}}} \quad (35)$$

Input data for the model simulation in form of average daily operational values were provided by SLOVNAFT a.s. and evaluated for a 500-day period. Typical operational values are depicted in Table 1. Data regarding column and compressor design parameters were obtained from equipment documentation and from the refinery staff and are summarized in Tables 2 and 3.

Tab. 1. Feedstock properties.

Parameters	Numerical Value
Typical Mass Flow [t/h]	8.2
Typical Composition [mol % propylene]	81.2

Tab. 2. Column parameters.

Parameters	Numerical Value
Column Stages	165
Feed Stage	46
Head Pressure [MPa]	1.17
Bottom Pressure [MPa]	1.32

Tab. 3. Design compressor parameters.

Parameters	Numerical Value
Mass Flow [t/h]	147.7
Inlet Pressure [MPa]	1.17
Inlet Temperature [°C]	26
Discharge Pressure [MPa]	1.78
Discharge Temperature [°C]	50
Polytropic Efficiency [%]	84.4

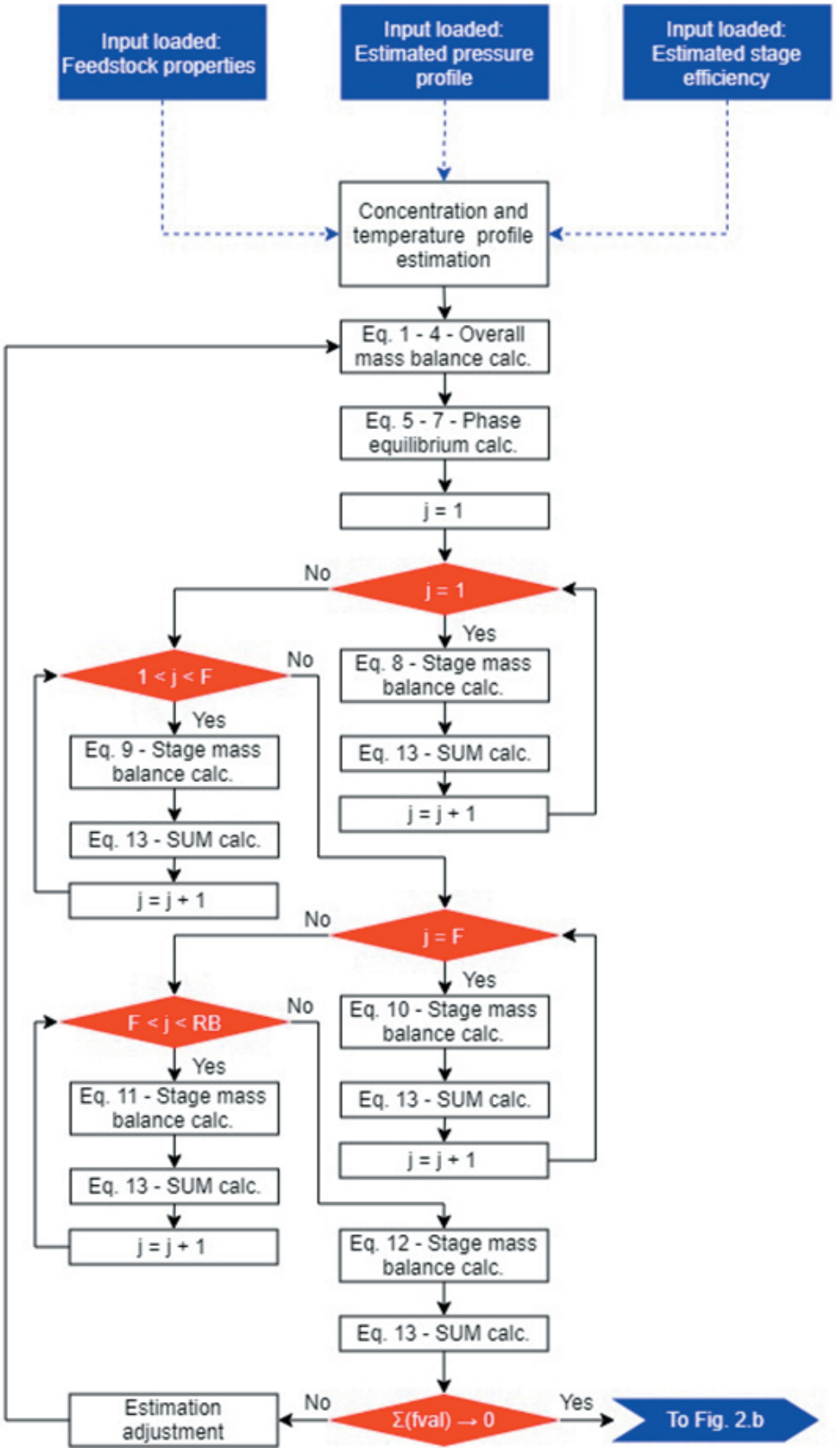

Fig. 2a. Calculation diagram: Column performance.

The following Figs. 2a, 2b serve as calculation process visualization in the Matlab environment, allowing for easy functional module addition, which is important for future work aimed at the compressor and its driving unit performance curves adoption in the model. For each converged iteration loop, the function value *fval* has to reach the value of 10^{-6}. Therefore, 15 to 25 iterations on average have to be done regarding the loop complexity.

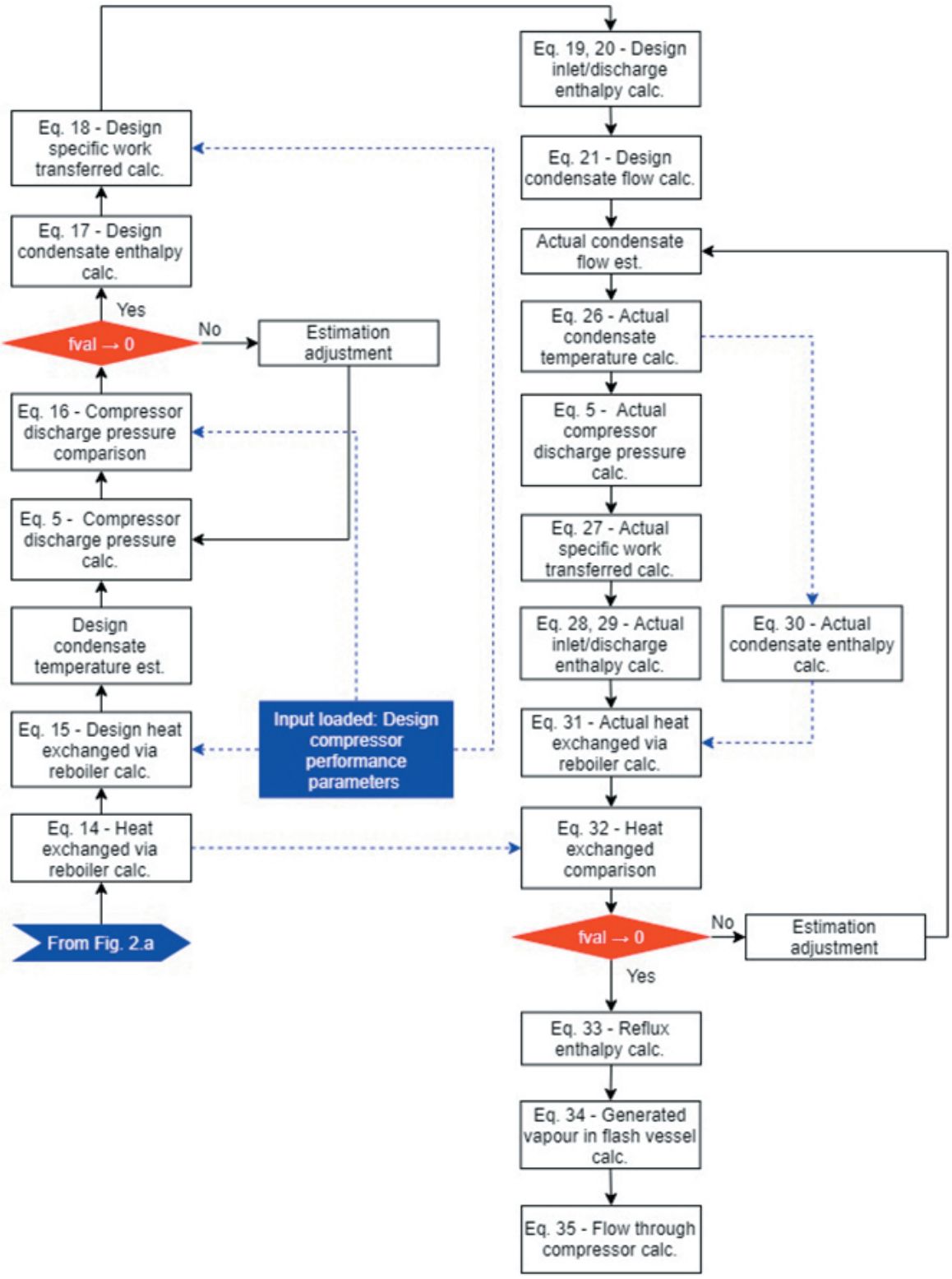

Fig. 2b. Calculation diagram: Heat pump performance.

Results and discussion

Results of software calculations were reprocessed into charts shown in Figs. 3, 4. Fig. 3 serves for model verification, comparing the calculated and measured mass flow of vapors compressed in the heat pump compressor. Very good agreement can be seen during periods with the measured mass flow above 100 t/h. With decreasing vapors mass flow, the calculated and model based values diverge; the calculated ones being by 20 to 30 t/h lower than the measured ones. Explanation for such discrepancy was obtained by studying the compressor performance curves that have not been a part of the calculation model – the

compressor design limits proper compressor operation above 100 t/h of compressed vapors to avoid the surge occurrence danger. At lower column feeds, mass flow of vapors below 100 t/his sufficient to achieve the desired product purity (99.5 to 99.6 % wt. propylene). This, however, requires regulated opening of the compressor antisurge by-pass to increase the compressed vapors mass flow. In the end, a part of the compression work is wasted to recompress the by-pass stream, which lowers the heat pump energy efficiency.

An alternative approach, as documented in Fig. 4 and preferred by staff, allows for the production of even higher purity propylene product (around 99.7 % wt.); due to very close propane and propylene molar masses, the propylene molar and weight fraction in the propylene product is almost identical (Fig. 4) at no additional cost: the column reflux ratio can be increased above the usual value during periods with lower column feed. Therefore, sufficient compressed vapors mass flow through the heat pump compressor is retained and the antisurge by-pass valve can remain closed.

The applied compressor load controlled by the frequency converter couples the compressor discharge pressure and throughput. The possibility of compressor discharge pressure optimization is unused by staff at the moment keeping the discharge pressure at almost constant value. However, optimization would yield specific compression work decrease as well as a modest decrease of the minimum compressor throughput needed to avoid surge occurrence. This possibility will be considered in further work.

An alternate means of compressor load control – by a variable inlet guide vane – seems to be more suitable in this application as it allows operating the compressor in a broader throughput range than the frequency converter while decoupling the discharge pressure and throughput control. An analysis of additional implementation possibilities of such compressor load control is out of the scope of this paper.

It can be concluded that increased product purity at zero incremental cost can be achieved in the studied system during periods with lower C3 fraction feed

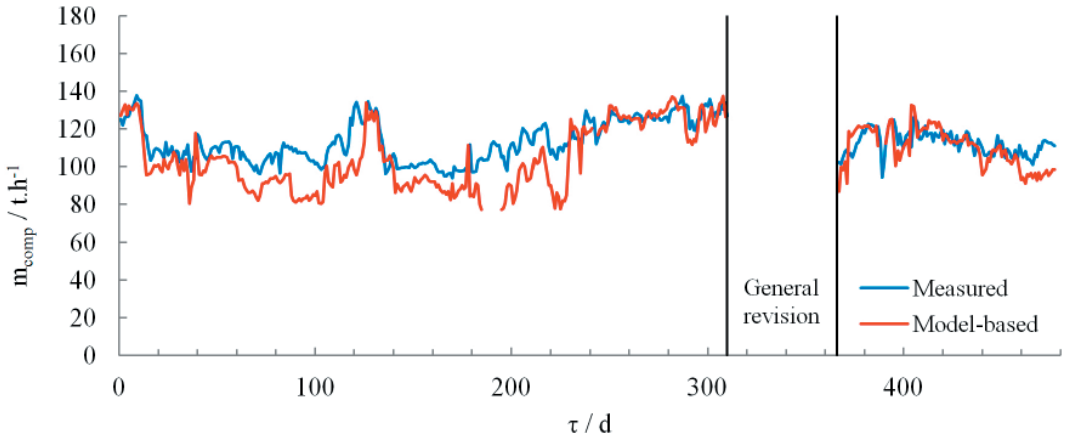

Fig. 3. Calculation model verification – comparison of calculated and measured values of compressed vapor mass flow in the heat pump compressor.

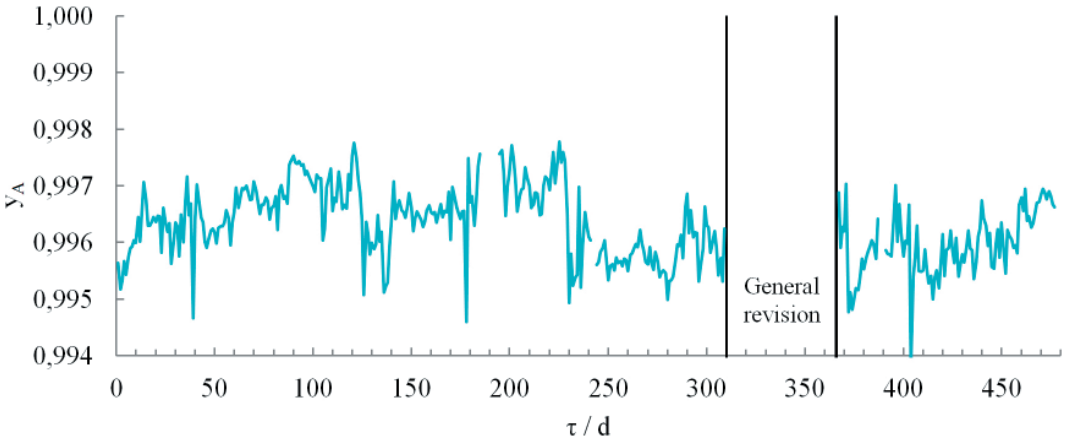

Fig. 4. Achievable propylene product purity.

to the splitter, allowing for production costs reduction in the polypropylene production plant, as lower amount of inert (propane) has to be removed from the reaction gas purification section in such a case. Alternative point of view yields that increasing the C3 splitter load above a certain value may limit the achievable product purity which is an important fact to be taken into account when evaluating the C3 fraction production increase possibility in the FCC unit.

Conclusions

The presented paper provides a comprehensive overview of industrial C3 fraction splitter modeling incorporating a heat pump. The model has been developed based on the system layout and taking into account the system mass and heat balance as well as the vapor-liquid equilibrium and compression work calculation. Comparison of model calculated and measured vapor mass flow compressed in the heat pump compressor showed very good agreement. Periods with differences in these values stemmed from the compressor antisurge protection system activated at lower vapor throughputs. This remains a challenge to be addressed in future work together with the heat pump driver performance assessment. It is expected that implementation of these equipment limitations and features in the C3 splitter mathematical model will enable calculating the incremental C3 fraction splitting costs reliably, thus providing a tool for system operation optimization.

List of symbols and abbreviations

a exponent in equations (23) and (24); a = 0.6 [–]
C_1 to C_5 constants used in pure substance saturated vapor pressure calculation – equation (5)
$fval$ function value [–]
h molar enthalpy [kJ kmol^{-1}]
k overall heat transfer coefficient [kW m^{-2} K^{-1}]
$\dot{m}$ mass flow [kg s^{-1}]
$\dot{n}$ molar flow [kmol s^{-1}]
$\bar{n}$ average value of polytropic coefficient [–]
P pressure [kPa]
P^0 saturated vapour pressure of pure substance [kPa]
$\dot{Q}$ heat flux [kW]
R reflux ratio [–]
R_m universal gas constant [kJ kmol^{-1} K^{-1}]
T thermodynamic temperature [K]
x molar fraction in liquid phase [–]
y molar fraction in gas phase [–]
$\bar{z}$ average value of compressibility coefficient [–]
ΔT mean temperature difference [K]
η_p polytropic compression efficiency [–]

Subscripts

$_{A,B}$ components (propane and propylene)
$_{comp}$ related to compressor
$_{cond}$ related to condenser
$_D$ distillate (stream)
$_{design}$ design (operational or construction) parameter
$_F$ feed (stream)
$_{flash}$ related to flash vessel
$_g$ gas phase
$_i$ component
$_{in}$ inlet conditions
$_{iter}$ value in iterative calculation
$_j$ stage numbering
$_l$ liquid phase
$_n$ stages above the feed stage
$_m$ stages below the feed stage
$_{out}$ outlet (discharge) conditions
$_{RB}$ related to reboiler
$_{reflux}$ reflux (stream)
$_V$ vapor (phase)
$_W$ waste (stream)

Superscripts

^{T} calculated at temperature T

Acknowledgements
The authors would like to express many thanks to all SLOVNAFT a.s. employees who contributed to the final scope and form of this paper. This work was financially supported by the Slovak Scientific Agency, Grant No. VEGA 1/0659/18 and by the Slovak Research and Development Agency, Grant No. APVV-15-0148. The authors also gratefully acknowledge the support from the project Science and Technology Park STU Grant no. ITMS26240220084, co-financed by the European Regional Development Fund.

References

Alhajji M, Demirel Y (2015) Energy and environmental sustainability assessment of a crude oil refinery by thermodynamic analysis. International Journal of Energy Research 39: 1925—1941.

Al-Rowaili FN, Ba-Shammakh MS (2017) Maximisation of an oil refinery profit with products quality and NO_2 constraints. Journal of Cleaner Production, 165: 1582—1597.

Danilov Y, Sinkevich I, Lavrova I, Mardupenko A, Tulskaya A (2018) Energy saving technologies in the petroleum refining processes, Petroleum and Coal 60(1): 128—133.

DeCarolis J, Daly H, Dodds P, Keppo I, Li F, McDowall W, Pye S, Strachan N, Trutnevyte E, Usher W, Winnig H, Yeh S, Zeyringer M (2017) Formalizing best practice

for energy system optimization modeling. Applied Energy, 194: 184—198.
Demirel Y (2004) Thermodynamic Analysis of Separation Systems. Papers in Thermal Mechanics, 39: 3897—3942.
EIA (2016) International Energy Outlook 2016. Washington, USA: Energy Information Administration, U.S. Department of Energy. https://www.eia.gov/outlooks/ieo/pdf/0484(2016).pdf. Accessed on 15. 1. 2019.
Fonyo F, Benkö N (1998) Comparison of various heat pump assisted distillation configurations. Chemical Engineering Research and Design, 76(3): 348—360.
Gadalla MA, Abdelaziz OY, Kamel DA, Ashour FH (2015) A rigorous simulation-based procedure for retrofitting an existing Egyptian refinery distillation unit. Energy, 83: 756—765.
Hasanbeigi A, Price L (2010) Industrial Energy Audit Guidebook: Guidelines for Conducting an Energy Audit in Industrial Facilities. https://eetd.lbl.gov/sites/all/files/publications/lbl-3991e-industrial-audit-guidebookoct-2010.pdf. Accessed on 3. 9. 2018.
Chudinova AA, Buchatskaya NI, Podgornyi VV, Gavrikov AA, Ivashkina EN, Dolganova IO (2016) Increase of efficiency isopropylbenzene manufacturing with use of integrated mathematical models. Petroleum and Coal, 58(2): 155—160.
Chuzlov VA, Molotov KV (2016) Development of computer modeling system as a tool for light naphtha isomeration improvement. Petroleum and Coal, 58(1): 47—55.
Kazemi A, Hosseimi M, Mehrabani-Zeinabad A, Faizi V (2016) Evaluation of different vapor recompression distillation configurations based on energy requirements and associated costs, Applied Thermal Engineering, 94: 305—313.
Li J, Xiao X, Boukouvala F, Floudas ChA, Zhao B, Du G, Su X, Liu H (2016) Data-Driven Mathematical Modeling and Global Optimization Framework for Entire Petrochemical Planning Operations. AIChE Journal, 62: 3020—3040.
MOL (2016) MOL GROUP strategy 2030, business presentation. https://molgroup.info/strategy2030/. Accessed on 21. 1. 2019.
Morrow III WR, Marano J, Hasanbeigi A, Masanet E, Sathaye J (2015) Efficiency improvement and CO_2 emission reduction potentials in the United States petroleum refining industry. Energy, 93: 95—105.
Perry RH et al (1997) Physical and Chemical Data.In: Perry's Chemical Engineers' Handbook — 7th Edition, London, McGraw — Hill Professional.
Vall J (2011) Industry and its impact on the environment in Slovak republic in 2011 — sector report. (in Slovak) Slovak Environment Agency Banská Bystrica. https://www.enviroportal.sk/uploads/report/sprava-priem-2013-final.pdf. Accessed on 16. 1. 2019.
Variny M, Blahušiak M, Mierka O, Kováč N (2013) Analysis of energy effectiveness of C3 fraction splitting techniques implemented in Slovnaft refinery. In: Proceedings of the 4th International Conference on Chemical Technology ICCT 2013, Mikulov, Česká republika: 78—82.
Variny M, Mierka O, Gašparovič L (2015) Experiences and future prospects of GRUCON — SLOVNAFT cooperation in energy auditing field. In Proceedings of the 42nd International Conference of SSCHE. Bratislava: Slovak Society of Chemical Engineering, 2015: 351—358.
Vilarinho AN, Campos JBLM, Pinho C (2016) Energy and exergy analysis of an aromatics plant. Case Studies in Thermal Engineering, 8: 115—127.
Worell E, Corsten M, Galitsky Ch (2015) Energy Efficiency Improvement and Cost Saving Opportunities for Petroleum Refineries. An ENERGY STAR® Guide for Energy and Plant Managers. A document prepared for The United States Environmental Protection Agency. www.energystar.gov/industry. Accessed on 17. 1. 2019.
You X, Rodriguez-Donis I, Gerbaud V (2016) Reducing process cost and CO_2 emissions for extractive distillation by double-effect heat integration and mechanical heat pump.Applied Energy, 166: 128—140.

sciendo

Agile manoeuvres using model predictive control

Kristína Fedorová, Peter Bakaráč, Michal Kvasnica

Faculty of Chemical and Food Technology, Slovak University of Technology, Radlinského 9, 812 37 Bratislava

Abstract: This paper shows how model predictive control (MPC) can be used to perform agile manoeuvres in a pendulum-on-a-cart system, which is an abstraction of many mechanical systems commonly used in the industry, such as cranes. Specifically, the problem of moving a cart on which a pendulum is mounted using a free joint is rapidly moved from one position to another one while mitigating the swings of the pendulum. To achieve this goal, an optimization-based MPC strategy is employed that selects the control moves while minimizing the chosen cost function and, simultaneously, enforcing constraint satisfaction. As the controlled system is nonlinear, two options are considered. The first one solves the nonlinear MPC problem in an approximate fashion using the so-called random shooting approach. The second method is based on the first one approximating the nonlinear system by a linear one, followed by applying convex MPC techniques. The performance of both strategies was compared by means of real-time experiments.

Keywords: nonlinear model predictive control, convex model predictive control, random shooting, linearization

Introduction

Chemical reactors, heat exchangers and many other processes in the chemical industry perform with nonlinear dynamics which makes their control a challenging task. Especially when the operation of such processes accentuate safety. Control strategy offering the most benefits is model predictive control (MPC) (Maciejowski, 2002) due to its ability to perform optimized control actions while state and input constraints are enforced. Therefore, MPC has become the most preferred and popular control approach in the process industry, as proven by the survey of Qin and Badgwell (2003). Many successful applications of the MPC strategy control chemical reactors (Oravec and Bakošová, 2012; Bakošová and Oravec, 2014; Oravec and Bakošová, 2015; Bakošová et al., 2013), heat exchangers (Oravec et al., 2016a, 2018), and distillation columns (Martin et al., 2013). Alternatively, MPC can also be used as a supervisory control layer that can be coupled with conventional PID controllers (Klaučo et al., 2017).

The principle of MPC is to solve an optimization problem based on a mathematical model of the controlled system. Additionally, future behavior of the system is predicted and control inputs are optimized over the whole prediction horizon. In case of a linear model of the system, the evaluation of control input can be fast and relatively easy. Limitations of the linear model stem in a narrow range of its validity and often insufficient description of all the distinctions of the real process. To tackle these limitations, a nonlinear model of the process can be used. Performing nonlinear MPC can lead to non-convex optimization problems that require increased computational power. In fact, obtaining such a solution is unattainable within one sampling period if the process is characterized by fast dynamics.

In recent years, reducing of computational complexity affiliated with non-convex optimization problems within nonlinear MPC (NMPC) has become a serious research field (Allgöwer and Zheng, 2012). Various methods intended for the solution of such optimization problems have been described (Wright and Nocedal, 1999; Čižniar et al., 2009; Kirkpatrick et al., 1983; Poli et al., 2007). Some of the methods are focused on searching for the minimum in a certain local area. Therefore, there is always a possibility of solution suboptimality. Searching for the global minimum can be performed in a stochastic or deterministic way. Simulated annealing is a stochastic method based on inspecting an enormous number of solutions and subsequent convergence to the lowest value of the cost function of the NMPC. On the other hand, the drawback of the deterministic methods lies in their applicability in small size problems.

One of the systems with fast and nonlinear dynamics is also a pendulum-on-a-cart. The problem of unwanted oscillations at the output occurs during the system control. The pendulum system represents a crane moving cargo. If this crane is in the vicinity of other objects, its oscillation is very undesirable as it can cause considerable damage. At the same time, the speed at which the crane transmits objects plays an important role. The faster the device runs, the more it can transfer and the more efficient it is. Higher speeds, however, cause larger oscillations to be mitigated. The com-

promise between the speed of operation and the oscillation amplitude is agile maneuvers which operate with the device the fastest way possible to avoid violation of the constraints given for the oscillation amplitude.

This paper focuses on the solution of this NMPC problem employing the random shooting approach (Dyer et al., 2014). Application of this method is spread in machine learning (Sahoo et al., 2018) or robotics (Piovesan and Tanner, 2009) fields. Elegance and simplicity of the method is based on the fast randomly generated control input sequences pursued by investigation of the constraints enforcing and evaluating the cost function value. The sequence with the lowest value of the performance index is considered as the solution. Due to the random selection, solution sub-optimality can occur, while increased number of random sequences reduces the extent of such sub-optimality. However, the solution is feasible and it guarantees safe operation of the manipulated system.

Control performance of NMPC and MPC based on the linear model were compared in this paper. Scenarios of the agile maneuvers control in the pendulum-on-a-cart system were the same for both control strategies.

Theoretical

We considered a control of a system in the discrete-time domain represented by the state-update equation

$$x(t+\Delta) = f(x(t),\, u(t)), \tag{1}$$

and the output equation

$$y(t) = g(x(t),\, u(t)), \tag{2}$$

where $x(t) \in \mathbb{R}^n$ represents the state vector at time t, $u(t) \in \mathbb{R}^m$ are the control commands, and $y(t) \in \mathbb{R}^p$ are the controlled outputs. Additionally, $x(t+\Delta)$ represents the successor state. Finally, $f{:}\mathbb{R}^n \times \mathbb{R}^m \to \mathbb{R}^n$ and $g{:}\mathbb{R}^n \times \mathbb{R}^m \to \mathbb{R}^p$ are, in general, nonlinear functions.

The objective of model predictive control is to use system equations (1) and (2) to predict future evolution of the system and to optimize the control inputs to achieve optimal behavior while meeting all system constraints. Mathematically, the MPC problem can be stated as

$$J^*(x_0) = \min_{u_0,\ldots,u_{N-1}} \sum_{k=0}^{N-1} \left(\|x_k - x_{\text{ref}}\| + \|u_k\| \right), \tag{3a}$$

$$\text{s.t. } x_{k+1} = f(x_k,\, u_k),\ k = 0,\ \ldots,\ N-1, \tag{3b}$$

$$y_k = g(x_k,\, u_k),\ k = 0,\ \ldots,\ N-1, \tag{3c}$$

$$x_k \in \mathcal{X},\ k = 0,\ \ldots,\ N-1, \tag{3d}$$

$$u_k \in \mathcal{U},\ k = 0,\ \ldots,\ N-1, \tag{3e}$$

$$y_k \in \mathcal{Y},\ k = 0,\ \ldots,\ N-1, \tag{3f}$$

$$x_0 = x(t), \tag{3g}$$

where x_k, u_k, y_k are the state, input, and output predictions at the k-th step of the prediction horizon, respectively, $||\cdot||$ is any vector norm, and $\mathcal{X}$, $\mathcal{U}$, $\mathcal{Y}$ are state, input, and output constraint sets, respectively. Optimization is performed over a finite prediction horizon N and yields the sequence $\{u^*_0, \ldots, u^*_{N-1}\}$ of control moves that are optimal for the given initial condition, $x(t)$ per (3g) and the given reference value, x_{ref}.

The trouble with optimal control inputs from (3) is that if functions $f(\cdot)$ and $g(\cdot)$ in (3b)—(3c) are nonlinear, or if the constraints sets are non-convex, (3) becomes a non-convex optimization problem that is difficult to solve to global optimality. In the subsequent sections, two principal ways allowing (3) to be solved quickly are reviewed.

The first method to solve a nonlinear MPC problem of (3) quickly is the so-called random shooting method, introduced in more details in Bakaráč and Kvasnica (2018). In principle, the method investigates a (possibly large) number of randomly generated control sequences $\{u_0, \ldots, u_{N-1}\}$. For each random sample, the response of the nonlinear system, i.e., the sequences $\{x_1, \ldots, x_N\}$ and $\{y_0, \ldots, y_{N-1}\}$ are calculated by (1) and (2), respectively, as a forward simulation of the nonlinear system starting from $x_0 = x(t)$. Subsequently, the validity of constraints in (3d)—(3f) is checked and any infeasible trajectories are discarded. Among the feasible trajectories, the random shooting method selects the sequence that yields the lowest value of the cost function (3a).

The advantage of random shooting is that it can cope with arbitrary nonlinear dynamics in (1) and (2) since only forward simulations are required. Moreover, arbitrary non-convex constraint sets can be employed. Therefore, the procedure can be used to investigate a very large number of randomly generated input trajectories in a short time. However, the obvious disadvantage is that the resulting control actions are merely sub-optimal. Moreover, due to their random generation, they can exhibit significant chattering and oscillations, which might not be desirable from a practical point of view. However, the sub-optimality can be mitigated by resorting to a very large number of random sequences (e.g. one million).

Another approach is to linearize the nonlinear dynamics in (1)—(2) around some chosen operating

point, e.g. x_S and u_S. Applying the truncated Taylor expansion yields the linear approximation:

$$x(t+\Delta) \approx \frac{\partial f(x,u)}{\partial x}|_{x_s,u_s}(x-x_s) + \\ + \frac{\partial f(x,u)}{\partial u}|_{x_s,u_s}(u-u_s), \tag{4}$$

and

$$y(t) \approx \frac{\partial g(x,u)}{\partial x}|_{x_s,u_s}(x-x_s) + \\ + \frac{\partial g(x,u)}{\partial u}|_{x_s,u_s}(u-u_s), \tag{5}$$

which can be written as

$$x(t+\Delta) = Ax(t) + Bu(t), \tag{6a}$$

$$y(t) = Cx(t) + Du(t), \tag{6b}$$

where matrices A, B, C, D result from the partial derivatives of $f(\cdot)$ and $g(\cdot)$.

The advantage of the linear prediction in (6) is that when it is used in (3b)—(3c), the MPC problem becomes a convex optimization problem, which can be easily solved using conventional optimization techniques, provided the constraint sets $\mathcal{X}$, $\mathcal{U}$, $\mathcal{Y}$ are convex sets. If they are not, their respective inner convex approximations can be derived e.g. by maximization of the inscribed ellipsoid volume, or by searching for the largest inscribed hyper-box. The latter approach is preferred as the constraints in (3d)—(3f) become linear and are easier to tackle compared to quadratic constraints arising from an ellipsoid inner approximation. If, moreover, the norms in (3a) are squared 2-norms, the MPC problem (3) becomes a convex quadratic program that can be solved e.g. by active-set or interior-point methods.

Experimental

In this work, model predictive control was applied to control a laboratory mechanical system consisting of a cart on which a pendulum is mounted using a free joint, shown in Fig. 1. Such a system represents a crane moving a cargo from one position to another one as quickly as possible while mitigating the swings of the cargo to prevent collision with obstacles. Dynamics of the pendulum is represented by four nonlinear state equations in the continuous-time domain:

$$\dot{x}_1 = x_2, \tag{7a}$$

$$\dot{x}_2 = \frac{3}{4L}u\cos(x_1) + \frac{3g}{4L}\sin(x_1) - bx_2, \tag{7b}$$

$$\dot{x}_3 = x_4, \tag{7c}$$

$$\dot{x}_4 = u, \tag{7d}$$

along with the output equation

$$y = L\sin(x_1) + x_3. \tag{8}$$

Here, x_1 represents the pendulum's angle, x_2 is the angular velocity of the pendulum, x_3 is the position of the cart, and x_4 is its velocity. The input of the system is u, the acceleration of the cart. The output from the system, y is the x-position of the pendulum's endpoint. Model parameters in (7) are L = 21 cm, g = 9,81 m s^{-2}, and b = 1. The control objective is to change the position of the end point of the pendulum in the shortest possible time. The trajectory of the movement has to be such that all states of the system enforce the state and input constraints:

$$-\infty < x_1 < \infty, \tag{9a}$$

$$-\infty < x_2 < \infty, \tag{9b}$$

$$-0.25 \le x_3 \le 0.25, \tag{9c}$$

$$-2.0 \le x_4 \le 2.0, \tag{9d}$$

$$-\infty < y \le 0.45, \tag{9e}$$

$$-4 \le u \le 4. \tag{9f}$$

Naturally, as the cart moves it induces oscillations of the pendulum, which are not desired as they may lead to the pendulum's endpoint colliding with obstacles. Therefore, the $y \le 0.45$ constraint must be met at all times to avoid such collisions.

To achieve a collision-free transition from one position to an another, model predictive control was applied. Specifically, the continuous-time system in (7) was first discretized using the sampling time Δ = 0.02 s and the forward Euler discretization. Specifically, given a continuous-time state equation $\dot{x} = f(x, u)$, its discrete-time version was achieved:

$$x(t+\Delta) = x(t) + \Delta f(x, y), \tag{10}$$

Alternatively, if the forward Euler discretization is imprecise, explicit Runge-Kutta discretization can also be applied. Specifically, the second-order explicit Runge-Kutta method yields the discrete-time system:

$$x(t+\Delta) = x(t) + \\ + \Delta f(x(t) + 0.5\Delta f(x(t), u(t)), u(t) + 0.5\Delta). \tag{11}$$

With the discrete-time version of the dynamics in (7) at hand, the MPC problem in (3) was formulated with a prediction horizon of N = 20 steps. The cost

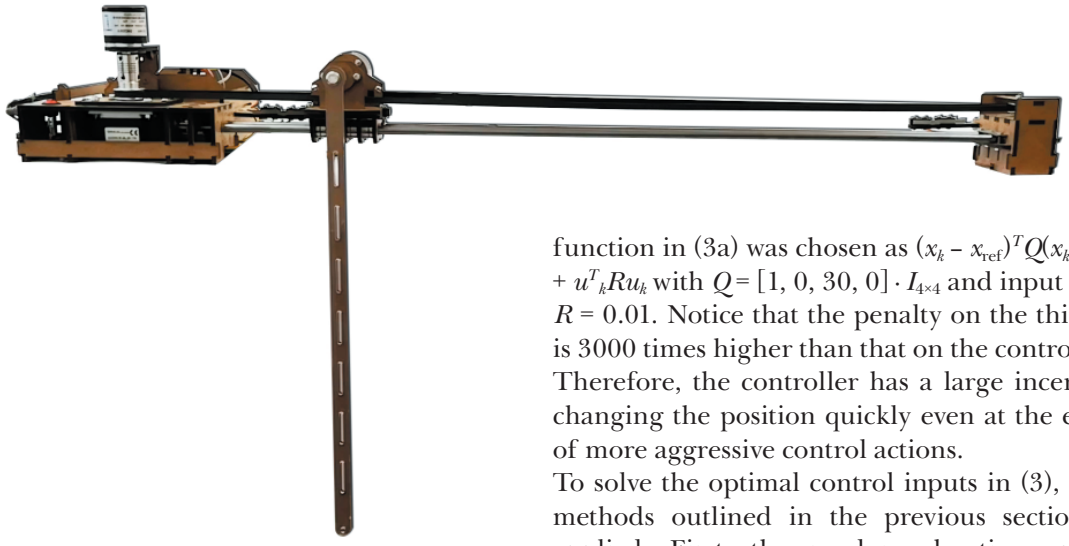

Fig. 1. Laboratory Pendulum.

function in (3a) was chosen as $(x_k - x_{\text{ref}})^T Q(x_k - x_{\text{ref}}) + u^T_k R u_k$ with $Q = [1, 0, 30, 0] \cdot I_{4\times4}$ and input penalty $R = 0.01$. Notice that the penalty on the third state is 3000 times higher than that on the control input. Therefore, the controller has a large incentive of changing the position quickly even at the expense of more aggressive control actions.

To solve the optimal control inputs in (3), the two methods outlined in the previous section were applied. First, the random shooting approach was applied in conjunction with the discretized

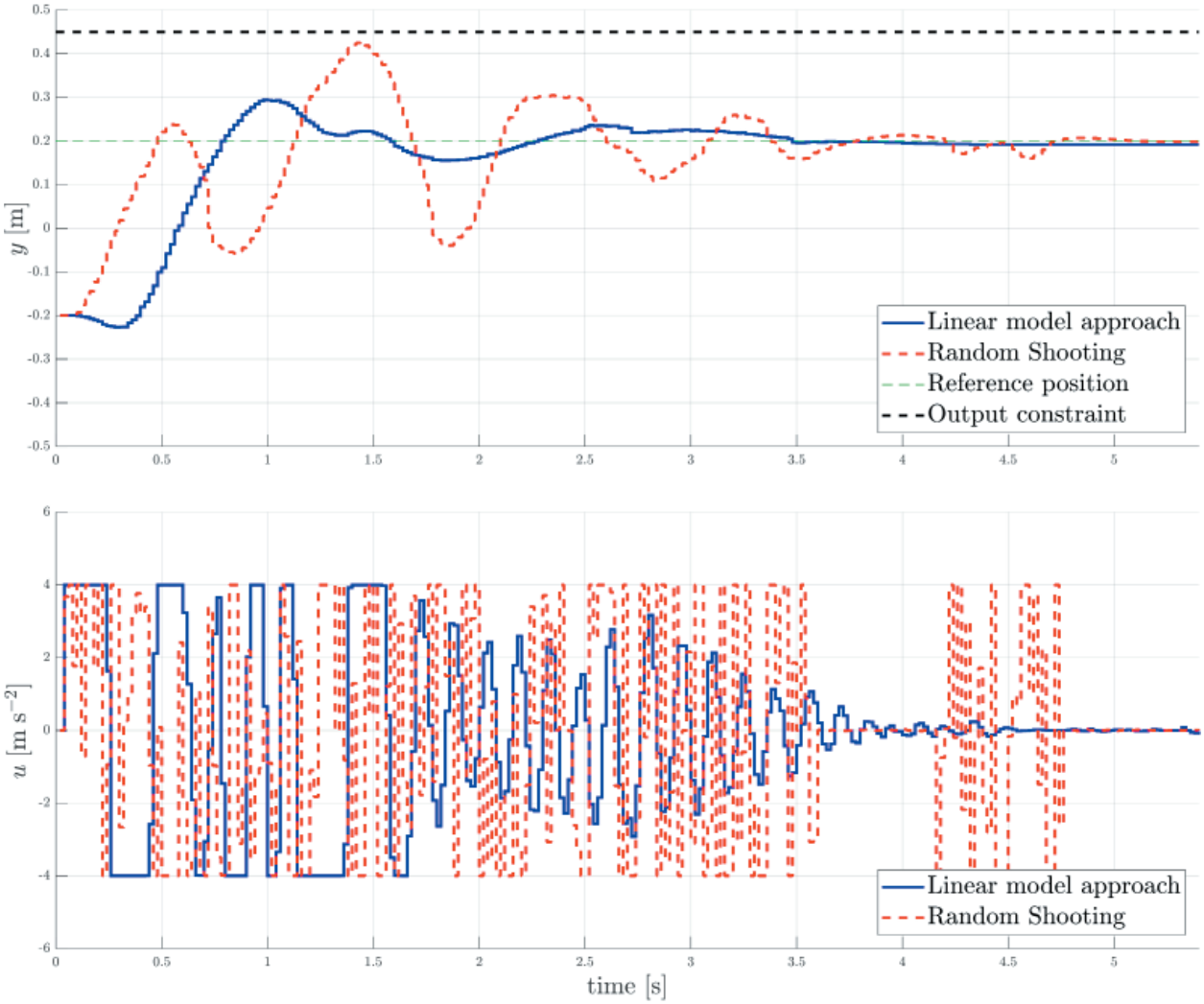

Fig. 2. First graph shows the position of the pendulum's endpoint over time. The blue solid line represents performance under linearization-based MPC, while the profiles for random shooting are shown using red dashed lines. The reference position of the pendulum's endpoint is represented by green dashed line and the constraint for this output by the black dashed line.
Secong graph shows the respective control actions over time using the same color scheme.

nonlinear dynamics from (7). The random shooting controller was constructed using the RandShootMPCController method of the MPT toolbox, which also allows compiling the controller into a mex function for faster execution. To apply convex MPC, the dynamics was first linearized around a zero position and speed, providing (after discretization) the linear prediction model (6). Note that all constraints in (9) are already linear (thus the sets $\mathcal{X}$, $\mathcal{U}$, $\mathcal{Y}$ in (3d)—(3f) are convex), therefore no further processing was necessary. The resulting quadratic program was then solved using the Gurobi solver.

Both approaches were tested in experiments using a laboratory pendulum lab process, described in more details in Oravec et al. (2016b). However, not all state variables could be directly measured. Specifically, only x_1 (pendulum's angle) and x_3 (cart's position) can be directly accessed. As MPC is a state-feedback control policy, the remaining states have to be estimated by devising a suitable state observer, such as the Luenberger observer. The state estimation as well as computation of control actions from (3) and all data processing were implemented in Matlab on a PC connected to the pendulum via a USB cable. The MPC controller ran on a sampling time of 20 ms using the fixed-rate periodic timer in Matlab.

Results and discussion

To compare the control performance of each strategy, the following scenario was considered. A cart carrying a pendulum is in the initial position $x_3(0) = -0.2$ m in relation to the center of the range of its possible movements. At the beginning, the pendulum is in a steady downright position with $x_1(0) = x_2(0) = 0$. The objective of the controller is to move the cart to the desired final position $x_3(T) = 0.2$ m while satisfying all constraints presented in (9). Specifically, the pendulum's endpoint position must not exceed 0.45 m while the cart changes its position from –0.2 m to 0.2 m.

Experimental results are shown in Fig. 2. The first graph shows the measured position of the pendulum's endpoint over time. As it can be seen, both approaches are able to move the cart to the desired position within four seconds while respecting the constraints on the pendulum's endpoint position. However, the linearization-based method performs significantly better, exhibiting a smaller overshoot. The random shooting method, on the other hand, shows more oscillations, which is due to the fact that it generates control actions at a random basis. This can be observed from the bottom graph in Fig. 2. However, both controllers meet the specified control goal with a similar settling time.

It should be noted that the oscillatory behavior of the control actions is partly due to the physical construction of the device which only provides a finite resolution of measurements. Therefore, only sensory data are sampled, which leads to deteriorated performance.

Conclusions

This paper shown how MPC can be applied to perform agile manoeuvres using the cart-and-pole laboratory setup. Two versions of the MPC problem were considered. The first one employed a full nonlinear description of the processes but provided only a sub-optimal solution to the optimization problem. The second version was based on linearization of the nonlinear dynamics, followed by formulation and solution of the MPC problem as a convex quadratic program. Both versions of the controller were implemented in real time with satisfactory results using a sampling time of 20 ms.

Acknowledgements

The authors gratefully acknowledge the contribution of the Slovak Research and Development Agency under project APVV 15-0007 and of the Scientific Grant Agency of the Slovak Republic under grant 1/0585/19, as well as the Research & Development Operational Programme for project University Scientific Park STU in Bratislava, ITMS 26240220084, supported by Research 7 Development Operational Programme funded by the ERDF.

References

Allgöwer F, Zheng A (2012) Nonlinear model predictive control, volume 26. Birkhäuser.

Bakaráč P, Kvasnica M (2018) Fast nonlinear model predictive control of a chemical reactor: a random shooting approach. Acta Chimica Slovaca, 11(2): 175—181.

Bakošová M, Oravec J (2014) Robust mpc of an unstable chemical reactor using the nominal system optimization. Acta Chimica Slovaca, 7(2): 87—93.

Bakošová M, Oravec J, Matejičková K (2013) Model predictive control-based robust stabilization of a chemical reactor. Chemical Papers, 67(9): 1146—1156.

Čižniar M, Podmajerský M, Hirmajer T, Fikar M, Latifi MA (2009) Global optimization for parameter estimation of differential-algebraic systems. Chemical Papers, 63(3): 274—283.

Dyer M, Kannan R, Stougie L (2014) A simple randomised algorithm for convex optimisation. Mathematical Programming, 147(1—2): 207—229.

Kirkpatrick S, Gelatt C, Vecchi M (1983) Optimization by simulated annealing. Science, 220(4598): 671—680.

Klaučo M, Kalúz M, Kvasnica M (2017) Real-time implementation of an explicit mpc-based reference governor for control of a magnetic levitation system. Control Engineering Practice, (60): 99—105.

Maciejowski J (2002) Predictive control: with constraints. Pearson education.

Martin P, Odloak D, Kassab F (2013) Robust model predictive control of a pilot plant distillation column. Control Engineering Practice, 21(3): 231—241.

Oravec J, Bakošová M (2012) Robust constrained mpc stabilization of a cstr. Acta Chimica Slovaca, 5(2): 153—158.

Oravec J, Bakošová M (2015) Robust model-based predictive control of exothermic chemical reactor. Chemical Papers, 69(7).

Oravec J, Bakošová M, Mészáros A, Míková N (2016a) Experimental investigation of alternative robust model predictive control of a heat exchanger. Applied Thermal Engineering, 105: 774—782.

Oravec J, Bakošová M, Trafczynski M, Vasičkaninová A, Mészáros A, Markowski M (2018) Robust model predictive control and pid control of shell-andtube heat exchangers. Energy, 159: 1—10.

Oravec J, Kalúz M, Bakaráč P, Bakošová M (2016b) Improvements of educational process of automation and optimization using 2d plotter. In Preprints of the 11th IFAC Symposium on Advances in Control Education, volume 11, pp. 16—21.

Piovesan J, Tanner H (2009) Randomized model predictive control for robot navigation. In IEEE International Conference on Robotics and Automation, pp. 94—99.

Poli R, Kennedy J, Blackwell T (2007) Particle swarm optimization. Swarm intelligence, 1(1): 33—57.

Qin S, Badgwell T (2003) A survey of industrial model predictive control technology. Control engineering practice, 11(7): 733—764.

Sahoo S, Lampert C, Martius G (2018) Learning equations for extrapolation and control. arXiv preprint arXiv:1806.07259.

Wright S, Nocedal J (1999) Numerical optimization. Springer Science, 35(67—68): 7.

sciendo

An active indirect solar system for food products drying

Abdul Wasim Noori[a, b], Mohammad Jafar Royen[a, b], Juma Haydary[a]

[a]*Institute of Chemical and Environmental Engineering, Slovak University of Technology in Bratislava, Radlinského 9, 81237 Bratislava, Slovakia, juma.haydary@stuba.sk*
[b]*Faculty of Chemical Technology, Kabul Polytechnic University, Kart-e Mamoorin, Kabul, Afghanistan, awnoori@kpu.edu.af*

Abstract: An energy independent active indirect solar drying system for the study of food products drying at specific climate conditions was developed and tested. As a model material, sliced tomato was selected because of its short shelf live, high humidity and potential to be a high value dried product. Indirect solar dryer enabled complete protection of the dried material against sunlight, birds, insects, rain and dust during the drying process. The solar dryer system design includes a rectangular section (1000 × 600 × 400) mm chamber and a flat solar collector (1500 × 600 × 100) mm with the surface area of 0.9 m^2. Air flow was induced by a fan installed at the inlet of the collector and powered by a photovoltaic solar panel and a battery system. Temperature and humidity of air were monitored at the collector inlet, collector outlet and the drying chamber outlet. The key element of the collector is a 10.5 m long rectangular section aluminum pipe (55 × 35) mm coated with an absorption layer. The maximum dryer capacity is around 3 kg of wet material (sliced tomato) per batch. Average air temperature increase in the collector was measured to be 30 °C during the winter season. Air relative humidity decreased from 21 % to 15 % after passing through the collector. The moisture of tomato slices decreased from the initial value of 92 % down to 22 % during the time of the experiment (30 h). Quality of tomatoes dried using the designed solar dryer differed significantly in color as well as in texture from those dried by the commonly used methods, like an open sun drying system. Equilibrium moisture content of the product was reached after 30 h in December when the maximum outside temperature was 17.6 °C. The tomato mass decreased from 333 g to 33.15 g; the mass loss being approximately 90 %. The heated air temperature and humidity at the dryer inlet and outlet were influenced by the change of the ambient temperature and humidity during the day. Variation of the drying rate with the change of the ambient temperature and humidity was observed. During summer, when the sun radiation increases, the drying time for sliced tomato with 9 mm thickness decreased from 25 h to 15 h. The sample thickness also has an impact on the drying process. When the sample thickness increased from 9 mm to 12 mm, the drying time increased from 15 h to 20 h of active device time.

Key words: Active indirect solar dryer, renewable energy, drying, upland condition, sliced tomatoes

Introduction

Most food products require some kind of preservation to enhance their shelf life since the production usually exceeds the market demand during the harvest season. For example: application of heat or cold, chemical substances, fermentation, mechanical methods and combinations of two or more of the mentioned methods (Mathavi et al., 2013), as well as modern methods like ultraviolet light processing and pulsed light processing (Rahman, 2007; Abida et al., 2014), microwave preservation (Barrett and Lloyd, 2012), high-pressure processing (Kadam et al., 2012), ionizing radiation, ultraviolet radiation (Abida et al., 2014), biopreservation (Acuña et al., 2011), etc., are used. Drying is the most used and most suitable method for agricultural products preservation (Srisittipokakun et al., 2012).

The most popular and current techniques for agricultural products dehydration include open sun drying (Akpinar, 2010), solar drying (direct and indirect) (Mohamed et al., 2008), convective drying (Royen et al., 2018), drum drying (Mujumdar, 2014), spray drying (Sormoli and Langrish, 2016), fluidized-bed drying (Senadeera et al., 2013), freeze drying (Kudra and Mujumdar, 2009), microwave drying (Pu et al., 2016), osmotic drying (Karam et al., 2016), vacuum drying (Sagar and Kumar, 2010), ultrasound drying (Mulet et al., 2003), etc. However, drying is generally an energy-intensive operation and it can significantly affect the cost of the product. High prices and shortages of fossil fuels increase the emphasis on the use of solar energy as an alternative energy source, especially in developing countries (Tiris et al., 1996). Indirect solar drying represents a cost effective method for food products drying in many countries including Afghanistan where this research was done.

Afghanistan is a landlocked country located in the center of Asia. Economy of the country is based on agribusiness (Finck-Pastrana, 2014; World bank, 2014) as agriculture creates approximately 1/3 of

Acta Chimica Slovaca, Vol. 12, No. 1, 2019, pp. 142—149, DOI: 10.2478/acs-2019-0020

the gross domestic product, GDP, and employs an estimated 80 % of the Afghan population directly or indirectly (Ward and Jalal, 2011). Afghanistan's climate is perfectly suitable for high-valued fruits, vegetables and herbal plants' cultivation (Shukla et al., 2017). Environmental conditions of the country are highly favorable for many tree crops, vegetable species and herbal plant production (Kemal-ur-Rahim, 2003; Bhardwaj, 2012). Dry products which are famous all over the world also include almonds, walnuts and pistachios, apricots, cherries, plums and raisins (Rasoly and Chandrashekar, 2018; Ministry of Industry and Commerce, Islamic Republic of Afghanistan, 2018). The world popular herbal plants which are grown and cultivated here are saffron, onions, peppermint, garlic, chamomile, chicory, flixweed, liquorice, fumitory, sage, marshmallow, dill, fennel, harmal or syrian rue (Amini and Hamdam, 2017). The major export agriculture product is dried fruits (27 %), medicinal plants (10 %) and fresh fruits (7 %) (Salman, 2017). However, one of the major limitations in dried product business in Afghanistan is to meet the standards and requirements for hygiene of the drying process. Open sun drying, which is the most often used method, does not meet these requirements. On the other hand, conventional hot air drying is very energy intensive. Solar drying under controlled conditions can be an alternative to the hot air and open sun drying methods, especially in locations with good sunshine during the harvest season (Sunil et al., 2012). A wide variety of solar dryers have been designed by many researchers (Mehta et al., 2018; Sengar et al., 2009; Rathore and Panwar, 2010; Sharma et al., 2009). Solar dryers are classified into two types, active and passive ones, each working in three modes: direct, indirect and mixed (Sharma et al., 2009; Srisittipokakun et al., 2012; Boughali et al., 2009; Wang et al., 2018; Zoukit et al., 2019; Shamekhi-Amiri et al., 2018; El Khadraoui et al., 2017). Solar drying systems, especially indirect active ones need shorter time for the drying process completion than the open sun light systems (Sunil et al., 2012), lower energy consumption than conventional hot air drying systems and they enable control of the hygienic conditions of the process.

Indirect active solar cabinet dryers are considered more advanced compared to typical cabinet dryers because they generally consist of two separate components: a collector that heats air with solar radiation and a drying chamber in which scales or planks of the product are accommodated. The operating principle is similar to that of a cabinet dryer; however, ambient air is driven to the collector by a ventilator (fan or blower). Active indirect solar dryer is more suitable for agricultural products with high moisture content, such as fruits, vegetables and herbal plants (El Khadraoui et al., 2017; Mujumdar, 2014).

Advantages of indirect forced solar dryer are that the samples are not exposed to solar radiation, the product quality does not decrease significantly and unstable vitamins and nutrients content is not reduced as much, drying rate is higher than in unforced systems and it is controllable (Phadke et al., 2015). Disadvantages of this system include higher initial costs and higher operation expenses due to intense circulation of heated air by fan or another kind of blower (Sontakke and Salve, 2015).

Afghanistan is one of the countries with a huge potential for using solar energy as it has more than 300 sunny days per year and high potential of solar energy production with the average capacity of 4—6.5 kWh/m^2/day (Jahangiri et al., 2019). Nowadays, solar energy is used for cooking, lighting, water heating and food drying in Afghanistan (Shukla et al., 2017). However, traditional open sun drying methods without quality control and standard hygiene conditions fulfilment are still applied (Abur et al., 2014).

The principal objective of this work was to design and test an energy independent solar drying system for food products drying in the indirect mode to achieve complete protection of fruit and vegetable against sunlight, birds, insects, rain and dust during the drying process producing standard dried products for worldwide market (Sontakke and Salve, 2015; Aiswarya and Divya, 2015). As a model material, sliced tomato was selected because of its short shelf live, high humidity and its potential to be a high added-value dried product. Tomato (*Lycopersicum esculentum*) is an herbaceous plant which is part of the family Solanaceous like potato (Manaa et al., 2013).

Materials and Methods

Solar Dryer

A scheme of the designed solar dryer system is shown in Fig. 1. The system includes a rectangular (1000 × 600 × 400) mm chamber and a flat solar collector (1500 × 600 × 100) mm with the surface area of 0.9 m^2. Air flow was induced by a fan installed at the inlet of the collector and powered by a photovoltaic solar panel and a battery system. Temperature and humidity of air were monitored at the collector inlet, collector outlet and the drying chamber outlet. The key element of the collector is a 10.5 m long rectangular section aluminum pipe (55 × 35) mm coated with an absorption layer. The dryer capacity is around 3 kg of wet material (sliced tomato) per batch.

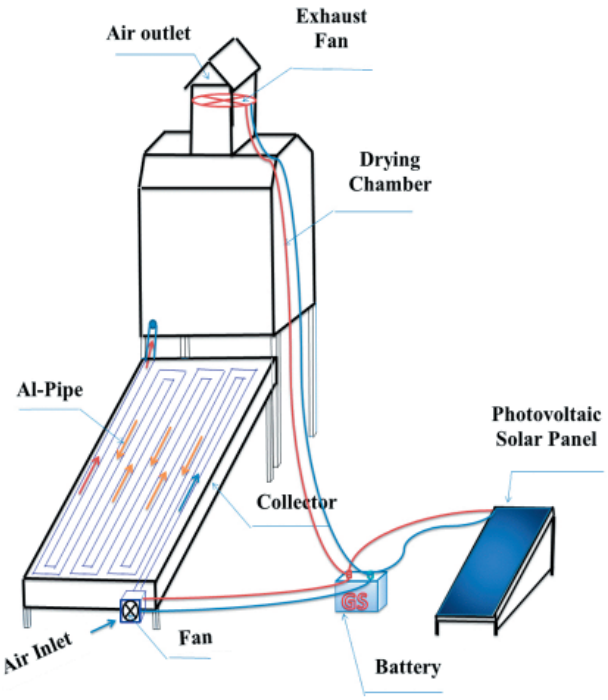

Fig. 1. Characteristics of solar dryer collector and chamber.

Samples

Fresh and ripe tomatoes with approximately equal size and color were selected and purchased from a Kabul local market. Then, they were washed with tap water before sliced to pieces with circular shape with 9 mm and 12 mm thickness using a stainless steel knife. The average diameter of tomatoes was around 5 cm. For each batch, around 323 g of sliced tomatoes were distributed in a single layer in the dryer chamber. The samples were weighted by a digital balance with the capacity ranging from 0.01 g up to 500 g with ± 0.01 g precision.

Experimental procedure

Chamber and trays were washed and cleaned before the samples were distributed. Initial moisture content of tomato slices measured by a laboratory moisture analyzer equipped with an analytical moisture balance (capacity 0.001–160 g, VWR, Italy) was 0.95 (wet base). Duration of the experiments and active drying time during the day depended on the season. In summer, experiments started at 8:00 AM and were finished at 5:00 PM, 9 h; while in winter, the experiments started at 9:30 AM and continued until 2:30 PM for 5 consecutive hours. After every 60 min, the sample mass loss was recorded. During the active drying periods, the temperature and relative humidity of air stream at the solar collector inlet, solar collector outlet and at the chamber outlet were monitored. During winter, the maximum ambient temperature was around 18 °C and in the summer it was 38 °C. The range of ambient air relative humidity was (13–21 %), and the air pressure was around 80–82 kPa. The data were recorded by an automatic data logger. The last step of the drying process was the device discharging. The average air velocity measured at the outlet of the solar collector (circular part of the pipe with a diameter of 50.8 mm) was 0.6 m/s.

Results and discussion

The collector efficiency was tested by measuring the air temperature before and after the collector during the winter season (December), under extreme conditions (minimum sunshine time and lowest ambient temperatures in Kabul). Temperature behavior during the measurement days are presented in Fig. 2. The collector inlet temperature during the active measurement period was between 10 °C and 18 °C. The maximum increase of air temperature after passing the collector was from 17 °C up to 47 °C. Also, the effect of temperature changes during the day can be seen in this figure. The maximum air outlet and inlet temperature difference (maximum collector efficiency) corresponds to conditions at noon, when the sun radiation angle is more perpendicular to the collector surface. These measurements showed that the system can be used during the whole year including the winter season when the temperature is low and sunshine time is short.

Fig. 3 shows the sample mass loss versus time in winter season. Active drying time (time with hot air flow inside the chamber) was 5 h per day. Total time needed for complete drying was five days. In experiments done in summer (June), the total drying time was reduced to two days (Fig. 4). Total mass loss of the sample was around 90 % in winter and 92 % in summer. Equilibrium moisture content of the product was reached after 25 h of active drying during winter season and after 15 h of active drying during summer season.

Of course, the dryer works more effectively during the summer season when ambient temperature is higher (30–40 °C in Kabul). Fig. 4 presents the mass loss variation with time for two samples with different slice thickness obtained in summer when ambient lowest and highest air temperatures were 18 °C and 36 °C, respectively. When the slice thickness increased from 9 mm to 12 mm, the time required to achieve equilibrium moisture content increased from 15 h (two device working days) to 20 h (three device working days). As it results from Fig. 4, in the initial drying period when free water from the sample surface is evaporated, the drying rate is not

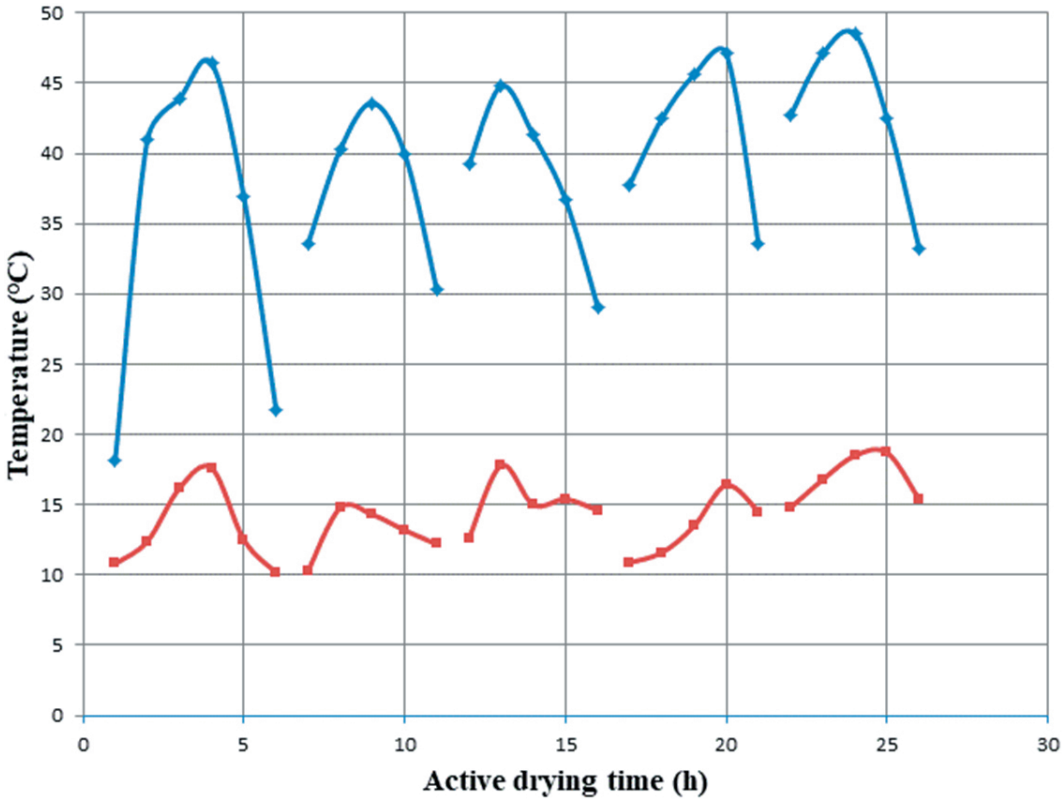

Fig. 2. Collector efficiency shown as air temperature increase after passing the collector. Gapes between the curves represent measurement discontinuance during the night.

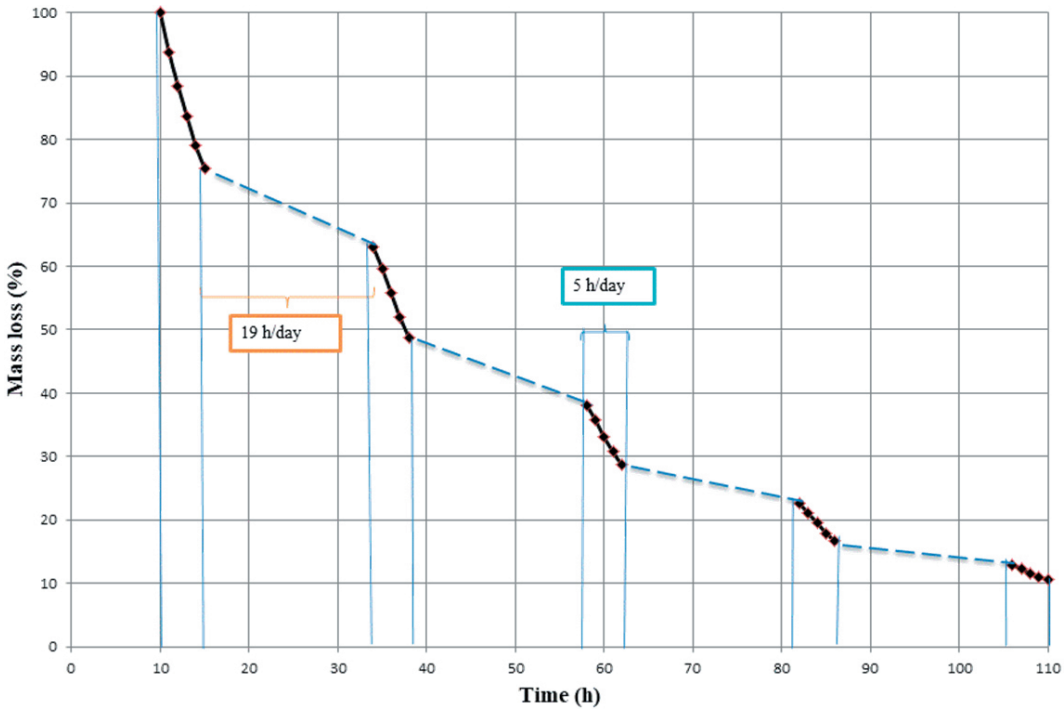

Fig. 3. Sample mass loss versus drying time.

influenced by the slice thickness. Later, when water diffusion to the surface takes place, drying rate is influenced by the sample slice thickness.

Comparing active solar drying periods (periods with forced air circulation) and periods with only natural circulation (Figs. 3 and 4), the effect of hot air circulation can be observed. Drying rate obtained during the forced air circulation periods is in average around 7.8 times higher than that observed during the natural air circulation periods.

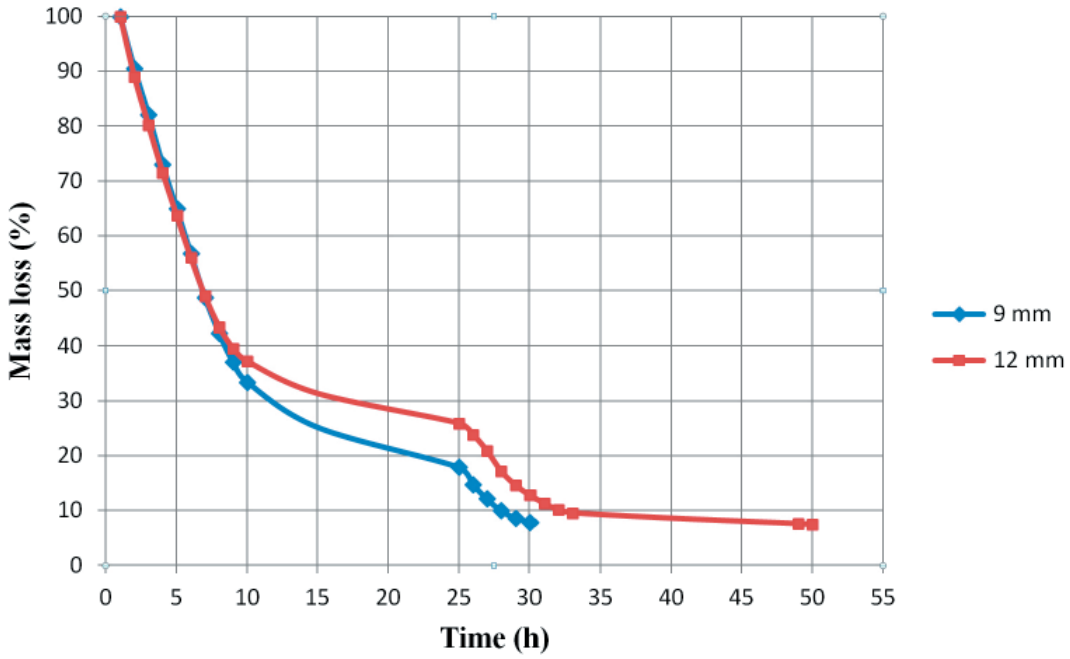

Fig. 4. Effect of tomato slice thickness on drying time.

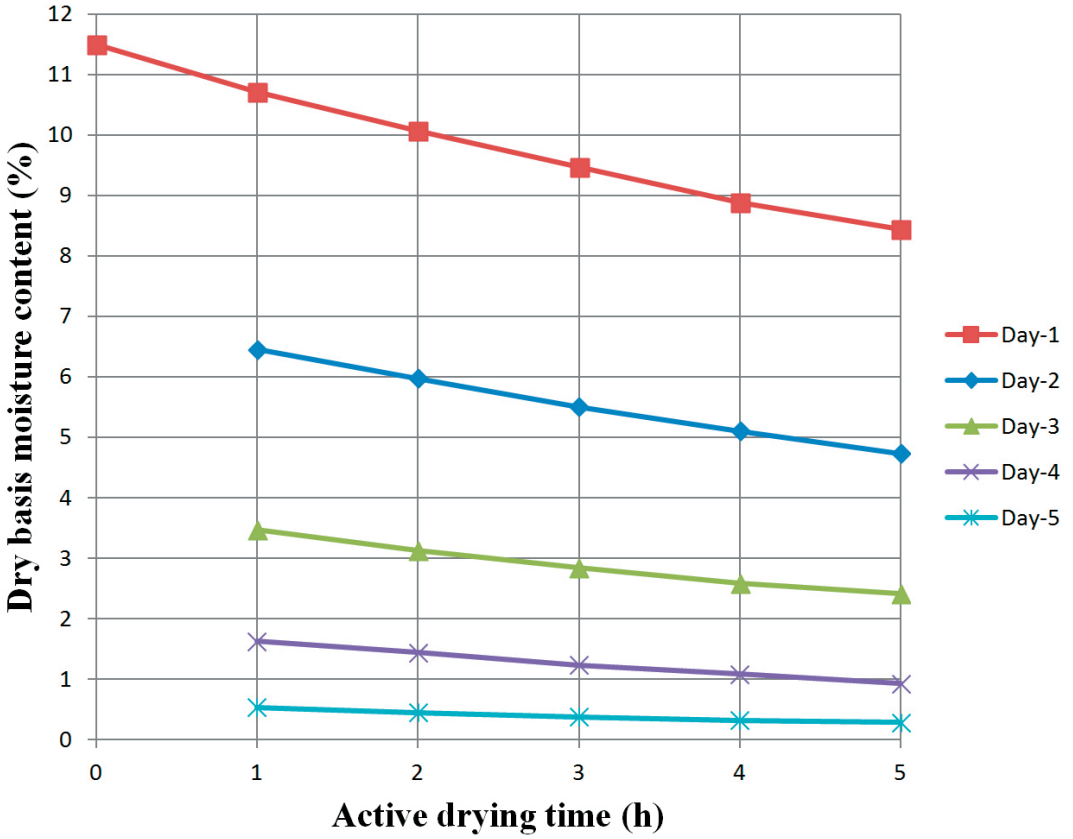

Fig. 5. Decrease of wet material moisture content with the drying time.

In winter, the device worked in active mode just for 5 h each day. In Fig. 3, the gaps between measurement points shown by dashed lines represent 19 h off-time per day. The decrease of the tomato moisture content (dry basis) for each day is shown in Fig. 5. The dry basis moisture content in tomato slices decreased from the initial value of 11.5 (92 % wet basis) down to 0.3 (22 % wet basis) during 25 h of active drying.

One of the most important parameters influencing the rate of drying is air relative humidity. Relative humidity of air was measured in three different points: in the stream entering the collector (relative humidity of ambient air), after the collector (at the drying chamber

inlet) and at the chamber outlet. Fig. 6 shows the air humidity in all three points during the active mode of the device. Air humidity changed during the process and also during the day. The range of ambient air relative humidity was (13—21 %), the air relative humidity decreased to (6—17 %) after passing the collector, and it increased to (40—75 %) at the chamber outlet. As it results from Fig. 6, the change of temperature during the day influenced also the ambient air relative humidity. It is most visible for the air leaving the drying chamber. These measurements provide very important information that at geographical locations such as Afghanistan, the device can work with acceptable driving force also under extreme winter conditions and at low air velocity. At higher air velocities, smaller change in air relative humidity in the device can be expected, which means higher driving force for the mass transfer.

Drying rate is affected mainly by air relative humidity and air temperature. Eq. (1) was used to

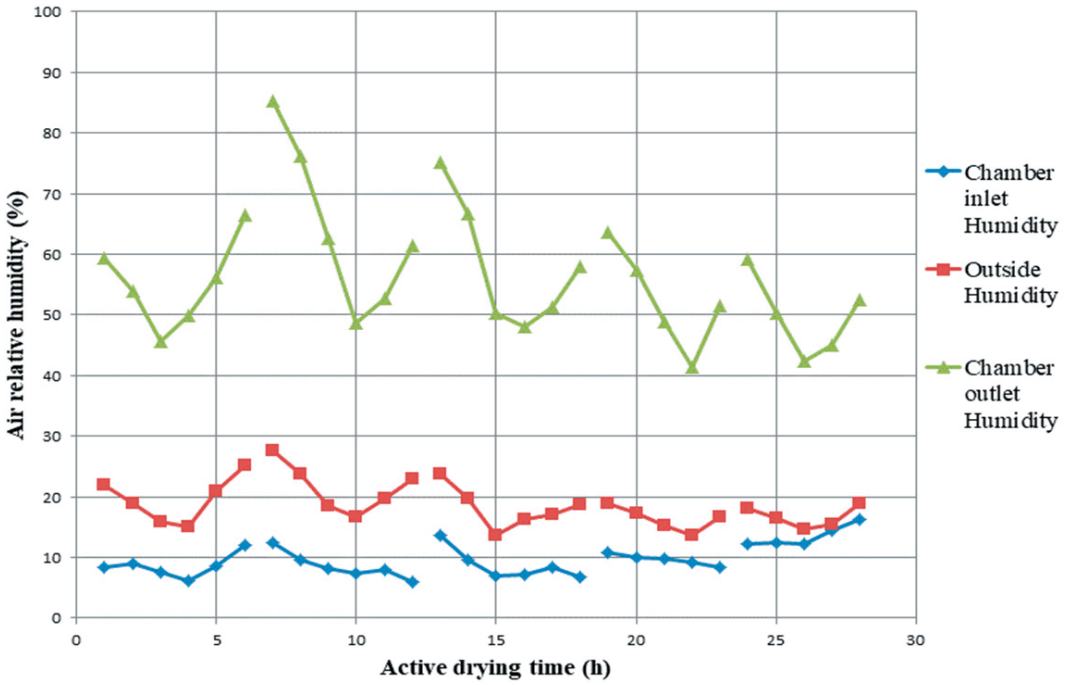

Fig. 6. Humidity change in three different locations in the device during the drying time.

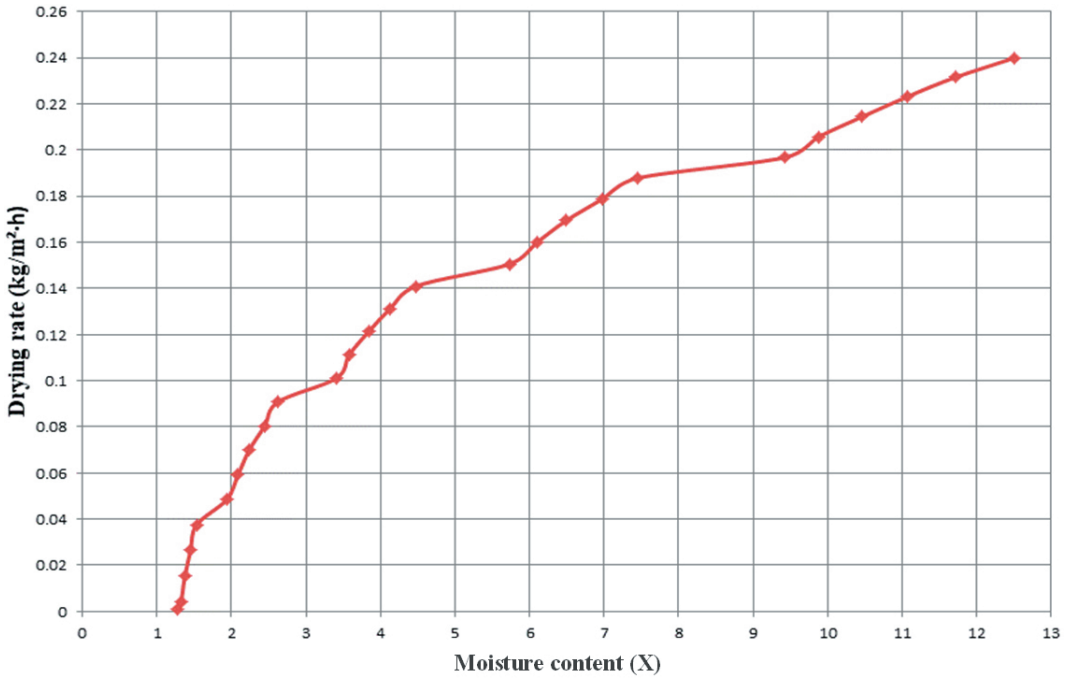

Fig. 7. Dependence of drying rate on moisture content.

calculate the drying rate.

$$DR = -\frac{m_s}{A_a}\frac{\mathrm{d}X}{\mathrm{d}t} \quad (1)$$

Where m_s is mass of the bone-dry material in dried product (kg), A_a is fresh tomato slices surface area (m^2) and (dX/dt) is a derivative of the moisture content (dry basis) relative to time. (dX/dt) was obtained by derivation of a third degree polynomial function of the moisture content versus active drying time. The polynomial function was obtained using a trend line of the measured experimental data. Fig. 7 shows the variation of drying rate with the solid phase moisture content. When the moisture content of tomato slices decreases, the drying rate also decreases. Despite the high moisture content of tomato slices, the drying curve does not show any constant drying rate period. However, the drying rate decrease at the beginning of the process is much slower. Non-smooth behavior of the drying curve shown in Fig. 7 is due to the intermittent active drying mode.

The sample surface area, A_a, was considered to be constant during the drying in this study. However, the sample shrinkage can influence the shape of the drying curve. The effect of the sample shrinkage can dim the drying rate decrease at lower solid phase moisture content.

Conclusions

An energy independent indirect solar dryer was developed and tested by drying tomato slices. Measurement of air temperature and air relative humidity change after passing the collector and drying chamber showed that at the given geographical location, the dryer can effectively work also during winter season.

Under the climatic conditions in Kabul (Afghanistan) at the period of the experiment (end of December, winter, ambient day temperature: 10–17 °C, air relative humidity: 13–23 %, air pressure: 80–82 kPa), five days (five hours per day) were sufficient for 9 mm thickness sliced tomato drying in an energy independent indirect solar dryer. The average air temperature increase after passing through the collector was 30 °C. The air relative humidity decreased by around 7 % after passing through the collector and increased by around 30 % after passing through the drying chamber. During summer, when the sun radiation is more intensive, the drying time for sliced tomato with a 9 mm thickness of slices decreased from 25 h to 15 h. Under these conditions, only two days of drying (7.5 h of sunshine each day) were necessary for sliced tomatoes drying compared to five days required in winter. The sample thickness showed the same effect as well. By increasing the sample thickness from 9 mm up to 12 mm, the active drying time in summer season increased from 15 h up to 20 h, which took three days of drying.

Approximately 90 % of the product mass was lost during the drying process. Lower relative humidity and lower ambient pressure of upland geographical locations enable effective indirect solar drying also during the winter season.

Acknowledgement

This work was supported by the Grant APVV-15-0148 from the Agency for Supporting Research and Development of Slovakia and the project SAMRS/2016/AFG/01/01 of the Slovak Agency for International Development Cooperation.

References

Abida J, Rayees B, Masoodi FA (2014) International Food Research Journal 21: 839–848.

Abur BT, Dan-Dakouta H, Egbo G (2014) International Journal of Advanced Engineering and Research Studies 3: 166–171.

Acuña L, Morero RD, Bellomio A (2011) Food and Bioprocess Technology 4: 1029–1049.

Aiswarya MS, Divya CR (2015) International Research Journal of Engineering and Technology 2: 1948–1953.

Akpinar EK (2010) Energy Conversion and Management. 51: 2407–2418.

Amini MH, Hamdam SM (2017) International Journal of Pharmacognosy & Chinese Medicine 1(3): 000118.

Barrett DM, Lloyd B (2012) Journal of the Science of Food and Agriculture 92: 7–22.

Bhardwaj ML (2012) In: Bhardwaj ML, Sharma HD, Kumar M, Kumar, R, Kansal S, Thakur K, Singh SP, Kumar D, Kumari S, Gupta M, Sharma V (Eds) Vegetable production under changing climate scenario (pp 13–18). Dr Y S Parmar University of Horticulture and Forestry, Nauni, Solan, Himachal Pradesh, India.

Boughali S, Benmoussa H, Bouchekima B, Mennouche D, Bouguettaia H, Bechki D (2009) Solar Energy 83: 2223–2232.

El Khadraoui A, Bouadila S, Kooli S, Farhat A, Guizani A (2017) Journal of Cleaner Production 148: 37–48.

Finck-Pastrana AG (2014) Energy Procedia 57: 2984–2993.

Jahangiri M, Haghani A, Mostafaeipour A, Khosravi A, Raeisi HA (2019) Renewable & Sustainable Energy Reviews 99: 169–190.

Kadam PS, Jadhav BA, Salve RV, Machewad GM (2012) Journal of Food Processing and Technology 3: 135.

Karam MC, Petit J, Zimmer D, Djantou EB, Scher J (2016) Journal of Food Engineering 188: 32–49.

Kemal-ur-Rahim K (2003) FAO Horticulture Project (pp 7–45). FAO, Kabul.

Kudra T, Mujumdar AS (2009) Advanced Drying Technologies. CRC Press, Boca Raton.

Manaa S, Younsi M, Moummi N (2013) Energy Procedia 36: 511–514.

Mathavi V, Sujatha G, Bhavani Ramya S, Karthika Devi B (2013) International Journal of Advances in Engineering & Technology 5: 176—187.
Mehta P, Samaddar S, Patel P, Markam B, Maiti S (2018) Solar Energy 170: 671—681.
Ministry of Industry and Commerce, Islamic Republic of Afghanistan (2018) Afghanistan's National Export Strategy 2018—2022: Dried Fruits and Nuts Sector. International Trade Centre, Geneva.
Mohamed LA, Kane CSE, Kouhila M, Jamali A, Mahrouz M, Kechaou N (2008) Energy Conversion and Management 49: 940—946.
Mujumdar AS (Ed) (2014) Handbook of Industrial Drying (4th ed). CRC Press, Boca Raton.
Mulet A, Cárcel JA, Sanjuán N, Bon J (2003) Food Science and Technology International 9: 215—221.
Phadke PC, Walke PV, Kriplan VM (2015) ARPN Journal of Engineering and Applied Sciences 10: 3360—3371.
Pu HJ, Li ZF, Hui J, Vijaya Raghavan GS (2016) Journal of Food Engineering 190: 167—175.
Rahman MS (Ed) (2007) Handbook of Food Preservation (2nd ed). CRC Press, Boca Raton.
Rasoly M, Chandrashekar HM (2018) International Journal of Research in Business Studies and Management 5(5): 16—22.
Rathore NS, Panwar NL (2010) Applied Energy 87: 2764—2767.
Royen MJ, Noori AW, Haydary J (2018) Acta Chimica Slovaca, 11: 134—140.
Sagar VR, Kumar PS (2010) Journal of Food Science and Technology 47: 15—26.
Salman DA (2017) Protecting food, environmental, and water security in the Middle East and South Asia: Opportunities for Iraq and Afghanistan. New Mexico State University, Las Cruces.
Senadeera W, Alves-Filho O, Eikevik T (2013) Food and Bioproducts Processing 91: 549—557.
Sengar SH, Khandetod YP, Mohod AG (2009) African Journal of Environmental Science and Technology 3: 265—271.
Shamekhi-Amiri S, Gorji TB, Gorji-Bandpy M, Jahanshahi M (2018) Case Studies in Thermal Engineering 12: 677—686.
Sharma A, Chen CR, Lan NV (2009) Renewable and Sustainable Energy Reviews 13: 1185—1210.
Shukla AK, Sudhakar K, Baredar P (2017) Resource-Efficient Technologies 3: 342—346.
Sontakke MS, Salve SP (2015) International Refereed Journal of Engineering and Science 4(4): 29—35.
Sormoli ME, Langrish TAG (2016) LWT — Food Science and Technology 72: 1—8.
Srisittipokakun N, Kirdsiri K, Kaewkhao J (2012) Procedia Engineering 32: 839—846.
Sunil V, Sharma A, Sharma N (2012) Procedia Engineering 38: 3260—3269.
Tiris C, Tiris M, Dincer I (1996) Applied Thermal Engineering. 16: 183—187.
Wang W, Li M, Hassanien RHE, Wang YF, Yang LW (2018) Applied Thermal Engineering 134: 310—321.
Ward M, Jalal A (2011) GAIN Report AF-2011-10: 2011 Afghan Agricultural Economy Update. US Department of Agriculture, Washington D.C.
World Bank (2014) Islamic Republic of Afghanistan Agricultural Sector Review: Revitalizing Agriculture for Economic Growth., Job Creation and Food Security. Report No: AUS9779. World Bank, Washington D.C.
Zoukit A, El Ferouali H, Salhi I, Doubabi S, Abdenouri N (2019) Renewable Energy 133: 849—860.

sciendo

Use of zeolites for macronutrients removal from wastewater

Barbora Urminská, Ján Derco, Ronald Zakhar, Adriana Korpicsová

Institute of Chemical and Environmental Engineering, Department of Environmental Engineering, Faculty of Chemical and Food Technology, Slovak University of Technology, Radlinského 9, Bratislava, 812 37, Slovakia
b.urminska@gmail.com

Abstract: Natural or synthetic zeolites have unique physical, chemical and structural properties that predetermine their use in many processes, including wastewater treatment. This study presents the results of our preliminary research in the field of nitrogen and phosphorus removal using adsorption and adsorptive ozonation with natural and modified zeolites. Iron-modified zeolite was the most efficient for the removal of ammonium nitrogen by adsorption. Phosphorus removal efficiency using adsorption was relatively low and natural zeolite was not suitable for the phosphorus removal at all. Ozone had no significant impact on the removal efficiency. Regeneration of loaded zeolites with ozone has also been studied. This method was partly efficient but it needs be further examined.

Keywords: adsorption, nitrogen and phosphorus removal, wastewater treatment, zeolites

Introduction

Wastewater contains various pollutants of diverse chemical nature. Wastewater treatment techniques have progressed over the past decades. One of the possibilities is to use adsorbent materials, either for adsorption alone or in combination with other technologies.

Activated carbon, biomaterials, zeolites, clays and some industrial solid wastes are widely used for adsorption of ions and organic matter in wastewater. Natural or synthetic zeolites have unique physical, chemical and structural properties that predetermine their use in many processes. Properties of zeolites can be further improved by chemical treatment. Modified zeolites can also be used as catalysts in catalytic ozonation (Fontanier et al., 2006; Valdés and Zaror, 2006; Qu et al., 2007, Wang et al., 2011) as well as in combined processes, e.g., adsorptive ozonation (Fujita et al., 2004).

By altering the reaction conditions, the surface of zeolites or their internal structure can be changed (Földesová and Hudec, 2006). Zeolites have a porous structure and they are able to adsorb various sorbates, for example, pesticides, polar and non-polar inorganic and organic molecules. Natural clinoptilolite has a high affinity to the NH_4^+ cation and toxic metal cations; therefore, it can be used for their removal from wastewater (Reháková et al., 2003).

Nitrogen and phosphorus are essential macronutrients for all living forms. On the other hand, they are also significant pollutants due to their high content, particularly in municipal wastewater. Release of these macronutrients into receiving water has to be minimized due to their negative impact on aquatic environment and their removal is an essential part of the prevention of eutrophication problems. Specific production of nitrogen varies according to household equipment; it is approximately 12 g per person per day. Other significant sources of nitrogen are also animal wastes from agriculture, fertilizers, and the food industry (Pitter, 2015). Anthropogenic sources of inorganic phosphorus are washing and cleaning powders, degreasing and washing agents, as well as fertilizers. Animal waste contains phosphorus of both organic and inorganic origin. Specific phosphorus production is approximately 2—3 g per person per day (Pitter, 2015). Nitrogen and phosphorus can be efficiently removed from wastewaters by biological treatment which is commonly used at many wastewater treatment plants. Adsorption is one of the alternative methods that can be used when it is not possible to use activated sludge process, or in case it is necessary to include a tertiary treatment. The main advantage is that the adsorbents can also retain persistent pollutants that would otherwise only pass through the activated sludge bioreactor.

Ozonation is a perspective oxidation technology used for water and wastewater treatment. Adsorptive ozonation combines the benefits of both processes — ozonation and adsorption. Ozone has the ability to cleave organic molecules into smaller ones which then bind to the adsorbent. Adsorption also leads to a local increase in the concentration of pollutants and ozone at the adsorbent-liquid interface, which can contribute to increased pro-

cess efficiency (Tsai et al., 2005; Melicher, 2013). Some adsorption materials (e.g., activated carbon, zeolites) may also serve as catalysts for the decomposition of ozone to hydroxyl radicals. Thus, the mechanism of direct ozone reactions, i.e., the mechanism of ozonolysis is changed to a radical reaction mechanism, which can lead to an increase in the efficiency of ozone reactions. Ruffino and Zanetti (2011; 2012) applied bromide as a catalyst for ammonia, bicarbonate and organic carbon depletion in ozonized systems.

Another combined process using ozone is the adsorption–regeneration process. Ishii et al. (1979) patented the ozonation method for regenerating an oxidation catalyst. Ozone can be used for the regeneration of loaded zeolites after the adsorption (Zhang et al., 2014). The authors successfully applied this process for adsorption of trichlorophenol on zeolite and adsorption regeneration with ozone. The adsorption capacity was kept stable for at least eight cycles of adsorption and regeneration. Fe-active zeolites were successfully applied in two cycles of the adsorption/oxidation approach of adsorption/wet peroxide oxidation of the non-ionic surfactant TX-100 (Shahbazi at al., 2014).

This study presents the results of our preliminary research in the field of wastewater treatment in adsorption and adsorptive ozonation processes for nitrogen and phosphorus removal. Natural zeolites, iron and manganese modified zeolites were used as adsorbents. Another aim of the research was to assess the possibilities of ozone regeneration of zeolites after adsorption applied for municipal wastewater treatment. These single and combined processes can be potentially applied in the treatment of sludge liquids and tertiary treatment of wastewater.

Theoretical

Adsorption can be defined as a process in which material (adsorbate) travels from a gas or liquid phase and forms a surface layer on a solid or liquid phase (Crawford and Quinn, 2017). The most common models describing the adsorption process kinetics are pseudo-first (Eq. 1) and pseudo-second (Eq. 2) order kinetics (Lin and Wang, 2009; Simonin, 2016, Naushad et al., 2016; Tan and Hameed, 2017). The pseudo-first order kinetic equation, originally described by Lagergren, assumes that the adsorption sites occupancy rate is proportional to the number of vacant sites. If film diffusion is the rate controlling process, the constant of the equation will vary inversely with the particle size and the film thickness (Ho and McKay, 1999).

Pseudo-first order kinetic model

$$q_t = q_e \left(1 - e^{-k_1 t}\right) \quad (1)$$

where q_t, q_e express the quantity of adsorbate retained by the unit amount of adsorbent (adsorption capacity) at time t and at equilibrium, respectively [mg g^{-1}], k_1 is the pseudo-first order rate constant [min^{-1}].

The pseudo-second order kinetic model is based on the assumption that the adsorption sites occupancy rate is proportional to the square of vacant sites. This model assumes that the overall sorption rate is controlled by the rate of adsorbate diffusion within the sorbent pores (Plazinski et al., 2013). Both these models were used in this study for the adsorption kinetics evaluation with model and municipal wastewater.

Pseudo-second order kinetic model

$$q_t = q_e \frac{k_2\, q_e\, t}{1 + k_2\, q_e\, t} \quad (2)$$

where q_t, q_e express the quantity of adsorbate retained by the unit amount of adsorbent (adsorption capacity) at time t and at equilibrium, respectively [mg g^{-1}], k_2 is the pseudo-second-order rate constant [g mg^{-1} min^{-1}].

Mass transfer during the adsorption process can also be controlled by external and internal diffusion (intra-particle diffusion). When the adsorbate diffusion in adsorbent pores is the adsorption rate-determining step, the intra-particle diffusion rate constant can be obtained from the Weber and Morris equation (Nagy et al., 2013; Li et al., 2016)

$$q_t = \mathrm{k_{ip}}\, t^{0.5} \quad (3)$$

where q_t is the quantity of adsorbate retained by the unit amount of adsorbent [mg g^{-1}] at time t [min], $\mathrm{k_{ip}}$ is the intra-particle diffusion rate constant [mg g^{-1} min$^{-0.5}$] and C represents the boundary-layer effect. When external diffusion is the rate determining step, the liquid film diffusion model can be used (Nagy et al., 2013):

$$\ln(1 - F) = \mathrm{k_{fd}}\, t \quad (4)$$

where $F = q_t/q_c$ is the fraction attainment at equilibrium, and k_{fd} is the liquid film diffusion rate constant [L min^{-1}].

The adsorption isotherm is a dependence of the quantity of the adsorbate adsorbed by the adsorbent (adsorption capacity) on pressure or adsorbate concentration under equilibrium conditions at constant temperature (Bleam, 2017). The most commonly used isotherms are Langmuir (Eq. 5) and Freundlich (Eq. 6) isotherms. The Langmuir isotherm is commonly used to describe

the adsorption process on a homogeneous surface with negligible interactions between the adsorbed molecules. The model assumes uniform adsorption energy on the surface, and the maximum quantity of adsorbate depends on the level of the monolayer saturation. The Freundlich isotherm is known as an empirical, two-parameter, equation describing the adsorption process equilibrium. Unlike the Langmuir isotherm, Freundlich's model has no apparent adsorption maximum (Bleam, 2017). It can be applied to non-ideal and reversible adsorption, useful for heterogeneous surfaces as well as for multi-layer sorption.

Langmuir isotherm

$$q = \frac{q_{max}\, b\, C}{1 + b\, C} \tag{5}$$

where q is the adsorption capacity [mg g^{-1}], q_{max} represents the maximum monolayer adsorption capacity [mg g^{-1}], C is the equilibrium concentration of adsorbate [mg L^{-1}], and b is the equilibrium constant of interaction [L mg^{-1}].

Freundlich isotherm

$$q = k\, C^{\frac{1}{n}} \tag{6}$$

where q is the adsorption capacity of adsorbate [mg g^{-1}], C is the equilibrium concentration of adsorbate [g L^{-1}], and k and n are empirical constants [$mg^{(1-1/n)} g^{-1} L^{1/n}$], [–] (Bowman, 1982).

Critical properties of the Langmuir isotherm can also be affirmed from the viewpoint of equilibrium parameter (R_L, also called the separation factor), a dimensionless constant defined by Eq. 7. The value of R_L indicates the shape of the isotherms to be either unfavorable ($R_L > 1$), linear ($R_L = 1$), favorable ($0 < R_L < 1$) or irreversible ($R_L \approx 0$) (Das et al., 2014; Foo and Hameed, 2010; Nethaji et al., 2013).

$$R_L = \frac{1}{1 + bC_0} \tag{7}$$

The Freundlich empirical constant $1/n$ as a function of the adsorption strength in the adsorption process was also considered. The value of $1/n$ in the range from zero to one also indicates a favorable sorption process (Das et al., 2014; Nethaji et al., 2013).

Materials and methods

Adsorption and adsorptive ozonation

Glass laboratory reactors with a volume of 1 L stirred by a magnetic stirrer were used in all adsorption experiments. Model wastewater was prepared from deionized water and NH_4OH, so the concentration of ammonium nitrogen corresponded to the content in municipal wastewater (approximately 70 mg L^{-1}). Municipal wastewater was sampled from the municipal wastewater treatment plant in Bratislava-Vrakuňa. Natural zeolite with the fraction size of over 1 mm, two zeolites modified by manganese (fraction size 0.3—2.5 mm and 1—2.5 mm) and one modified by iron (fraction size 1—2.5 mm) were used for the experiments. The zeolites were supplied by Zeocem, Slovakia. The adsorbent amount was 20 g per 1 L of water. The experiments were carried out at laboratory temperature of 20 ± 2 °C with the main aim to evaluate and asses the adsorption potential of natural and modified zeolites for nitrogen and phosphorus removal. Another goal was to determine the adsorption equilibrium time, describe the adsorption kinetics and determine the values of parameters of adsorption isotherms for the evaluation of adsorption potential of the investigated zeolite samples.

A Lifetech ozone generator with a maximum ozone production of 5 g L^{-1} was used for ozone production from pure oxygen. Ozone concentration in the gas phase at the inlet and outlet of the reactor was measured using a Lifetech ODU 200 UV laboratory detector. The system was operated in a batch configuration: wastewater samples and adsorbents were added to the reactor at the start of each experiment. The mixture of ozone and oxygen was fed into the reactor through a glass frit to form fine bubbles and thus to increase the efficiency of ozone transfer to the liquid phase. A magnetic stirrer was used to stir the reaction mixture. During the ozonation, the ozone generator power was set to 50 % and the oxygen flow was maintained at 1 L min^{-1}. Municipal wastewater was used in the experiments. The amount of adsorbent was 20 g per 1 liter of wastewater. Ozonation without any sorbent was also performed. Ozonation time was 60 min.

Repeated adsorption was carried out with municipal wastewater to investigate the adsorption-regeneration process with the ozone regeneration of zeolites. For each zeolite, five cycles of adsorption (2 h, 20 g of zeolite, 1 L of wastewater) were performed and followed by 15 min ozone regeneration using the reactor and conditions described above.

Analytical methods

Ammonium nitrogen concentrations were determined using the absorption spectrophotometric method with the Nessler reagent. In a test tube, 5 mL of the sample was mixed with 1—2 drops of a potassium-sodium tartrate solution (500 g L^{-1}) and 100 µL of the Nessler's reagent (10 g of HgI_2 and 7 g of KI in 100 mL of 10 % NaOH). A yellow-brown colloidal complex was formed. The color intensity

was measured after 10 min by a spectrophotometer at the wavelength of 425 nm (Horáková et al., 2003). Phosphate phosphorus concentrations were also measured spectrophotometrically. Five mL of the sample were mixed in a test tube with 0.5 mL of the agent solution prepared by mixing 125 mL of sulfuric acid (2.5 mol L^{-1}), 50 mL of ammonium molybdate solution (30 g L^{-1}), 25 mL of antimony-potassium tartrate solution (1.36 g L^{-1}) and 50 mL of ascorbic acid solution (21.6 g L^{-1}). After 15 minutes, the absorbance was measured by a spectrophotometer at 690 nm (Horáková et al., 2003).
Values of COD and TOC were determined by the National Water Reference Laboratory, Water Research Institute in Bratislava.

Experimental data processing
Nonlinear regression was used for data analysis and fitting the values in the models. Parameter values of Eqs. 1, 2, 5 and 6 were determined by the grid search optimization procedure. The values of correlation coefficient and residual sum of squares between the measured and calculated data were used to compare the adsorption potential of the investigated zeolites and to evaluate the quality of the mathematical description of the experimental data. We strongly support the conclusion of authors Lin and Wang (2009) that nonlinear form of kinetic equations should be primarily used to obtain kinetic parameters. The reason is that linearization can distort the basic assumption of the least square method, i.e., constant Gaussian distribution of values of the dependent variable for all values of the independent variable.

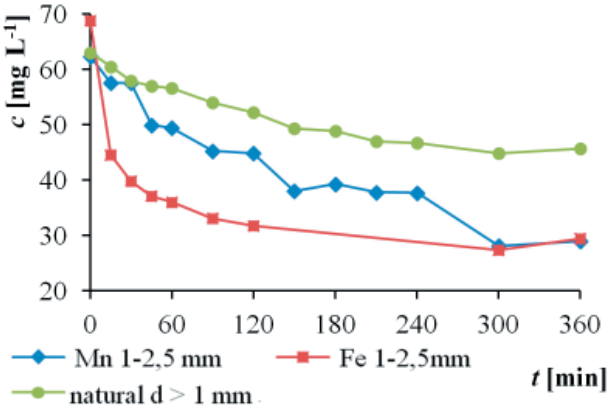

Fig. 1. Time dependence of ammonium nitrogen concentration in model wastewater.

Results and discussion

Adsorption with model wastewater
The first set of experiments was carried out with model wastewater containing ammonium nitrogen as the only pollutant. Fig. 1 shows that the equilibrium time in the adsorption with model wastewater was about 300 min. However, most of the ammonium nitrogen was adsorbed in the first two hours. This time was therefore used for the measurements of equilibrium data and determination of adsorption isotherm parameters. Unmodified zeolite (in Fig. 1 marked as "natural d >1 mm") performed the lowest decrease of N-NH_4. The best results were obtained using Fe-modified zeolite (in Fig. 1 marked as Fe 1–2,5 mm). The pseudo-first and pseudo-second order kinetic parameters are shown in Tables 1 and 2.

Tab. 1. Parameter values of pseudo-first order kinetics and statistical characteristics for N-NH_4 adsorption from model wastewater (S_R^2 – residual sum of squares of experimental and calculated values; S_Y^2 – dispersion of dependent variable values; R_{xy} – correlation coefficient).

Zeolite	q_e [mg g^{-1}]	k_1 [min^{-1}]	S_R^2 [$mg^2 g^{-2}$]	S_Y^2 [$mg^2 g^{-2}$]	R_{xy} [–]
Natural	0.980	0.00750	0.00154	0.0910	0.989
Fe-modified	1.80	0.0698	0.0142	0.389	0.964
Mn-modified	1.28	0.0170	0.00150	0.180	0.991

Tab. 2. Parameter values of pseudo-second order kinetics and statistical characteristics for N-NH_4 adsorption from model wastewater (S_R^2 – residual sum of squares of experimental and calculated values; S_Y^2 – dispersion of dependent variable values; R_{xy} – correlation coefficient).

Zeolite	q_e [mg g^{-1}]	k_2 [g mg^{-1} min^{-1}]	S_R^2 [$mg^2 g^{-2}$]	S_Y^2 [$mg^2 g^{-2}$]	R_{xy} [–]
Natural	0.860	0.0208	0.0100	0.0910	0.890
Fe-modified	1.92	0.0592	0.00720	0.389	0.982
Mn-modified	1.42	0.0172	0.00460	0.180	0.974

The pseudo-first order model corresponded with the experimental values obtained with the Mn-modified zeolite and the natural zeolite better than the pseudo-second order one. The pseudo-second order model had a slightly higher correlation coefficient in case of Fe-modified zeolite but the difference was negligible. The highest rate constants were obtained for Fe-modified zeolite according to both kinetic models.

Results of the experiments aiming to determine the parameters of adsorption isotherms and provide an insight on adsorption mechanisms with model wastewater are summarized in Table 3 and Fig. 2. Comparison of the values of correlation coefficients indicates that the Langmuir isotherm better corresponded with the experimental data than the Freundlich isotherm. The Fe-modified zeolite was again the most efficient, i.e., the highest adsorption quantities were reached; while natural zeolite was the least efficient adsorbent. The calculated values of equilibrium parameter R_L (Eq. 7) were in the range from 0.17 to 0.62 for natural zeolite, from 0.16 to 0.65 for Mn-modified zeolite and from 0.18 to 0.71 for Fe-modified zeolite, depending on the initial concentration values. It can be concluded that for all investigated zeolites, the values of equilibrium parameter were <1 and >0 for all initial ammonium nitrogen concentrations, which indicates favorable adsorption. Values of the Freundlich empirical constant $1/n$ also lie between 0 and 1 for all types of zeolites, which also indicates favorable sorption process.

According to Eq. 3 and data shown in Fig. 1, linear plot of the equation passes through the origin in case of natural (R_{xy} = 0.986) and Mn-modified zeolite (R_{xy} = 0.981). Based on the values of the correlation coefficient (R_{xy}), it can be concluded that for these two zeolites, internal diffusion is the rate determining step. This is not the case of Fe-modified zeolite (R_{xy} = 0.820). According to Eq. 4 and data shown in Fig. 1, linear plot of the equation passes through the origin in case of natural zeolite (R_{xy} = 0.978) and Mn-modified zeolite (R_{xy} = 0.956). It can be concluded that for these two zeolites, kinetics of the adsorption process was controlled by diffusion through the liquid film surrounding the adsorbent. In case of Fe-modified zeolite, the value of the correlation coefficient was lower, 0.904.

Adsorption with municipal wastewater

Fig. 3 shows the decrease in ammonium nitrogen concentration for unmodified zeolite (natural d > 1 mm) and modified zeolites with manganese and iron (Mn 1—2.5 mm and Fe 1—2.5 mm). Unmodified zeolite showed the lowest efficiency while the highest efficiency was again achieved by the Fe-modified zeolite. Equilibrium time for natural and Fe-modified zeolite was around

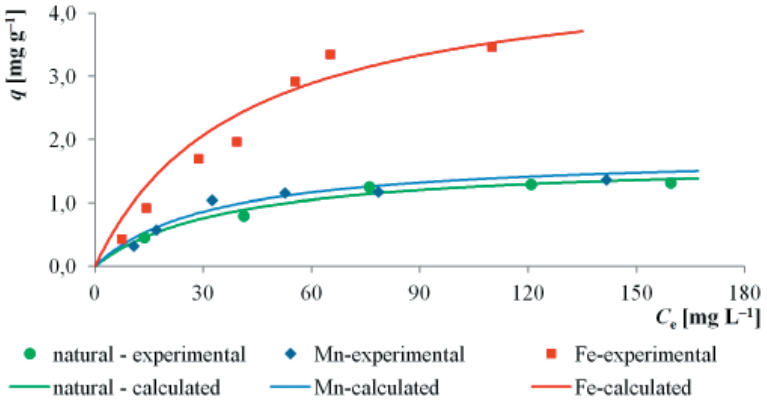

Fig. 2. Experimental values of adsorption capacities dependence on equilibrium concentration of ammonium nitrogen adsorption from model wastewater and calculated values using Langmuir isotherm.

Tab. 3. Adsorption isotherm parameters and correlation coefficients (R_{xy}) for N-NH_4 adsorption from model wastewater obtained by nonlinear regression.

Zeolite	Langmuir isotherm			Freundlich isotherm		
	q_{max} [mg g^{-1}]	b [L mg^{-1}]	R_{xy} [–]	k [mg$^{(1-1/n)}$ g^{-1} L$^{1/n}$]	$1/n$ [–]	R_{xy} [–]
Natural	1.69	0.0273	0.984	0.118	0.500	0.942
Fe-modified	4.80	0.0252	0.942	0.247	0.547	0.980
Mn-modified	1.79	0.0311	0.960	0.138	0.518	0.923

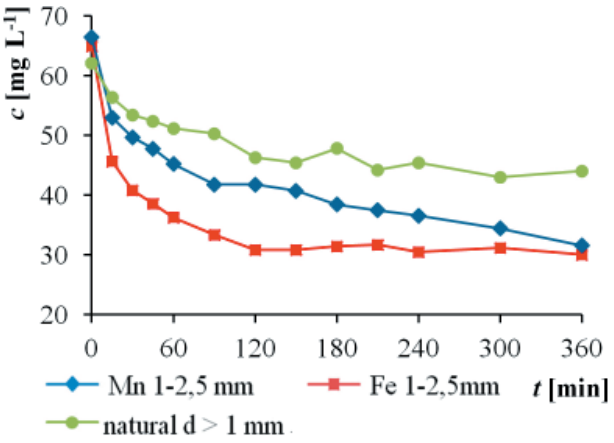

Fig. 3. Time dependence of ammonium nitrogen concentration in municipal wastewater.

120 min; in case of Mn-modified zeolite, the equilibrium was not reached even after 360 min, but the majority of ammonium nitrogen was adsorbed within 120 min.

The pseudo-first and pseudo-second order kinetic parameters for this process are shown in Tables 4 and 5. The equilibrium times and adsorption quantities were about the same as in the experiments with model water. The pseudo-first order model better corresponded with the experimental data for all three zeolites; the correlation coefficients were significantly higher compared to the pseudo-second order model. The highest rate constants were again obtained for the Fe-modified zeolite.

Results of the adsorption isotherm parameters determination and insight on the adsorption mechanisms with municipal wastewater are summarized in Tables 6 and Fig. 4. Comparison of the correlation coefficient values indicates that the Langmuir isotherm described the experiment more accurately than the Freundlich one. Again, Fe-modified zeolite exhibited the highest ammonium nitrogen removal capacity. The presence of other pollutants in wastewater did not seem to negatively influence the process of ammonium nitrogen adsorption; on the contrary, higher maximal quantities of adsorbate were reached for all three zeolites with municipal wastewater than with model wastewater.

The calculated values of equilibrium parameter (R_L) were more or less constant for all studied zeolites, i.e., 0.37 for natural zeolite, 0.47 for Mn-modified zeolite and 0.55 for Fe-modified zeolite for all initial concentration values. Values of the equilibrium parameter were <1 and >0 for all investigated zeolites and all initial ammonium nitrogen concentrations, which indicates favorable adsorption. Values of the Freundlich empirical constant ($1/n$) for all types of zeolite are also in the interval of 0 to 1, which again indicates favorable sorption process.

According to Eq. 3 and data given in Fig. 3, linear plot of the equation passes through the origin in case of natural zeolite (R_{xy} = 0.916). Based on the value of correlation coefficient R_{xy} it can be concluded that for this zeolite, internal diffusion is the rate determining step. This is not the case of Mn-modified zeolite (R_{xy} = 0.854) and Fe-modified zeolite (R_{xy} = 0.756) According to Eq. 4 and data shown in Fig. 3, linear plot of the equation passes through the origin in case of natural zeolite (R_{xy} = 0.930) and Mn-modified zeolite (R_{xy} = 0.909). It can be concluded that for these two zeolites, kinetics of the adsorption process is also controlled by diffusion through the liquid film surrounding the adsorbent.

Tab. 4. Parameters of pseudo-first order kinetics and statistical characteristics for N-NH_4 adsorption from municipal wastewater (S_R^2 — residual sum of squares of experimental and calculated data; S_Y^2 — dispersion of dependent variable values; R_{xy} — correlation coefficient).

Zeolite	q_e [mg g^{-1}]	k_1 [min $^{-1}$]	S_R^2 [mg^2 g^{-2}]	S_Y^2 [mg^2 g^{-2}]	R_{xy} [–]
Natural	0.874	0.0174	0.00428	0.0790	0.946
Fe-modified	1.68	0.0425	0.00563	0.238	0.976
Mn-modified	1.49	0.0228	0.0173	0.213	0.919

Tab. 5. Parameters of pseudo-second order kinetics and statistical characteristics for N-NH_4 adsorption from municipal wastewater (S_R^2 — residual sum of squares of experimental and calculated data; S_Y^2 — dispersion of dependent variable values; R_{xy} — correlation coefficient).

Zeolite	q_e [mg g^{-1}]	k_2 [g mg $^{-1}$min $^{-1}$]	S_R^2 [mg^2 g^{-2}]	S_Y^2 [mg^2 g^{-2}]	R_{xy} [–]
Natural	0.86	0.0450	0.00742	0.079	0.906
Fe-modified	1.70	0.0581	0.00617	0.238	0.974
Mn-modified	1.39	0.0485	0.0277	0.213	0.870

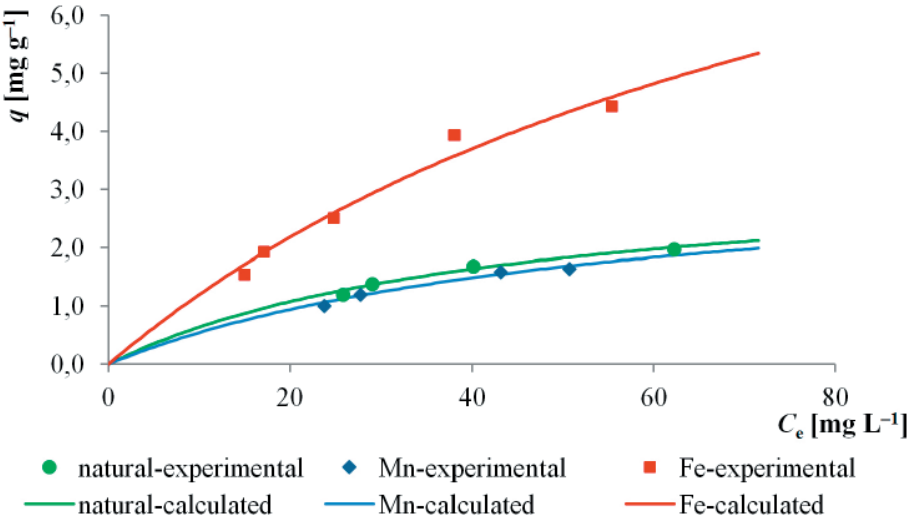

Fig. 4. Experimental values of adsorption capacities dependence on equilibrium concentration of ammonium nitrogen adsorption from municipal wastewater and calculated values using Langmuir isotherm.

Tab. 6. Adsorption isotherm parameter values and correlation coefficient values (R_{xy}) for N-NH_4 adsorption in municipal wastewater

Zeolite	Langmuir isotherm			Freundlich isotherm		
	q_{max} [mg g^{-1}]	b [L mg^{-1}]	R_{xy} [-]	k [$mg^{(1-1/n)}$ g^{-1} $L^{1/n}$]	$1/n$ [-]	R_{xy} [-]
Natural	3.40	0.0232	0.996	0.283	0.472	0.993
Fe-modified	12.2	0.0109	0.985	0.283	0.744	0.979
Mn-modified	3.49	0.0185	0.997	0.0760	0.803	0.981

In case of Fe-modified zeolite, the correlation coefficient was lower, 0.574.

The next series of experiments were performed with Mn-modified zeolite of the fraction size 0.3—2.5 mm. Mn-modified zeolite with the fraction size 1.0—2.5 mm and iron modified zeolite of the same fraction size (1.0—2.5 mm) were also used. The decrease in concentrations of ammonium nitrogen (N-NH_4), total nitrogen (N_{tot}), phosphate phosphorus (P-PO_4), chemical oxygen demand (COD) and total organic carbon (TOC) over time is shown in Figs. 5—9. All three zeolites showed similar rates of N-NH_4, N_{tot}, COD and TOC removal. However, for the removal of P-PO_4, Fe-modified zeolite showed significantly lower efficiency than Mn-modified zeolites. Most pollution was eliminated in the first

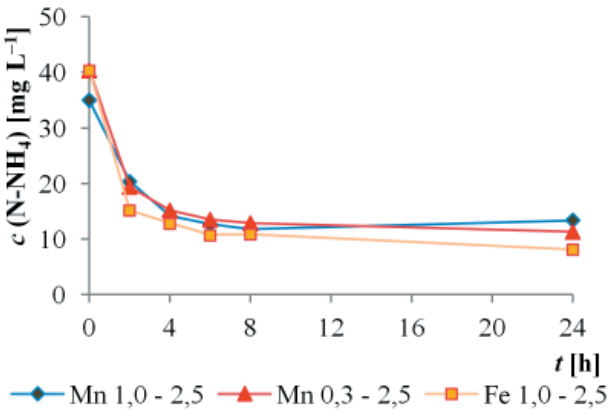

Fig. 5. Time dependence of ammonium nitrogen concentration in municipal wastewater during adsorption on three types of modified zeolites.

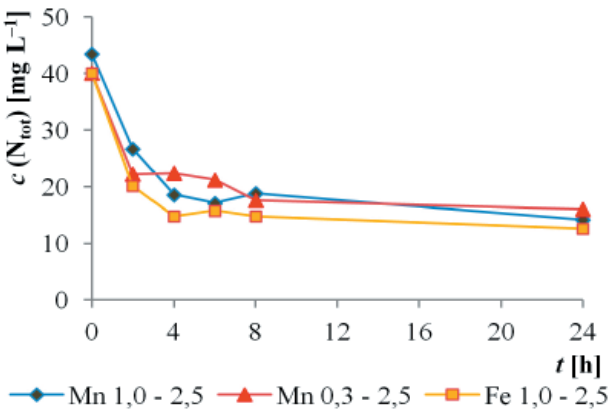

Fig. 6. Time dependence of total nitrogen concentration in municipal wastewater during adsorption on three types of modified zeolites.

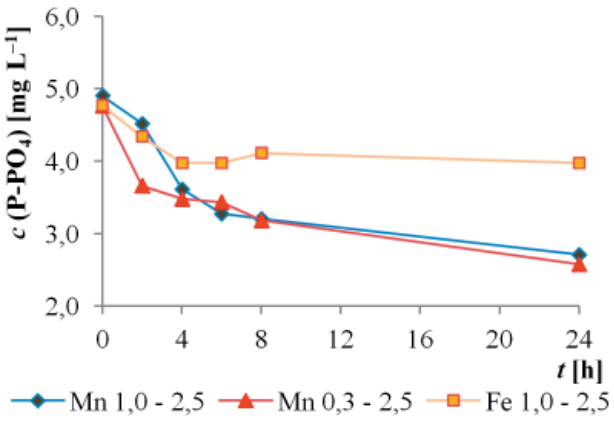

Fig. 7. Time dependence of phosphate phosphorus concentration in municipal wastewater during adsorption on three types of modified zeolites.

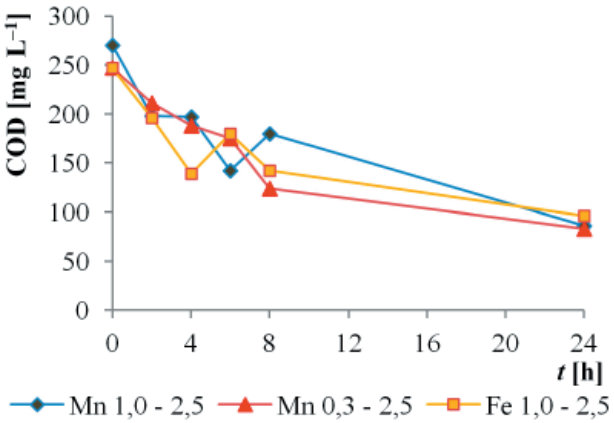

Fig. 8. Time dependence of chemical oxygen demand (COD) in municipal wastewater during adsorption on three types of modified zeolites.

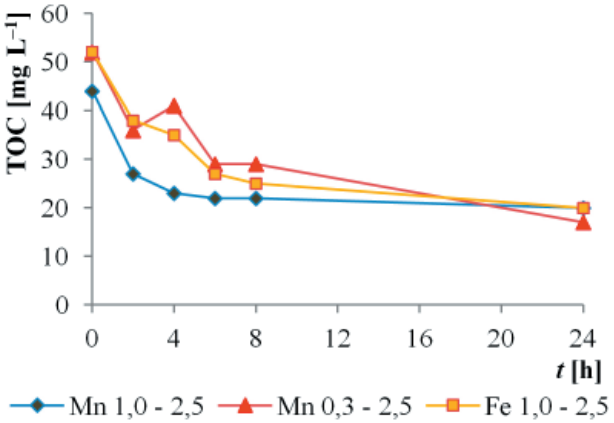

Fig. 9. Time dependence of total organic carbon concentration (TOC) in municipal wastewater during adsorption on three types of modified zeolites.

two hours of adsorption, but the equilibrium time was around six hours in most measurements. The fraction size of Mn-modified zeolite did not have a significant impact on the adsorption efficiency.

Adsorptive ozonation

Zeolites modified with Mn and Fe (fraction size 1.0–2.5 mm) and natural zeolite (fraction size of over 1 mm) were used in this part of the study. Fig. 10 shows the decreasing values of ammonium nitrogen concentrations during ozonation and adsorptive ozonation. Ozonation alone was the least efficient compared to adsorptive ozonation. The removal efficiency was only 5.7 % while modified zeolites were more efficient. The highest efficiency was achieved with Fe-modified zeolite. However, the efficiency was approximately the same as after adsorption alone (without ozonation), so adsorptive ozonation was not efficient in this case. The efficiency of each zeolite also corresponds to the results obtained in the adsorption experiments, where Fe-modified zeolite was the most and natural zeolite was the least efficient.

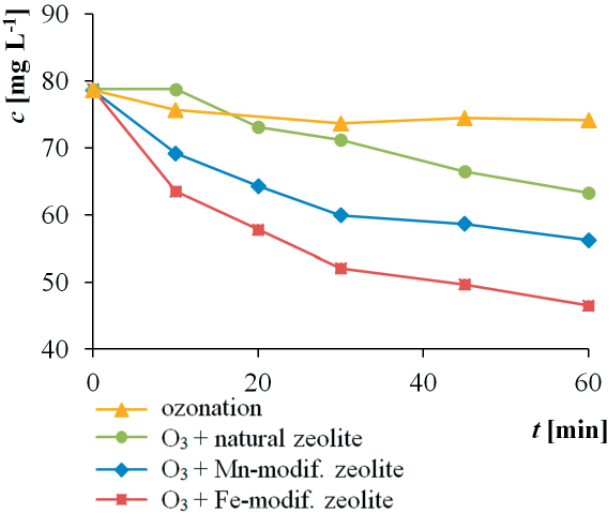

Fig. 10. Time dependence of $N\text{-}NH_4$ concentration during ozonation and adsorptive ozonation.

Fig. 11 shows COD concentrations during the ozonation and adsorptive ozonation processes. During ozonation, the highest COD decrease can be seen after ten minutes of the process. COD removal efficiency reached 15 % after 60 minutes. For adsorptive ozonation, the highest decrease in COD was achieved by the Fe-modified zeolite (39 % decrease); the least efficient was the natural zeolite which removed 26.7 % of COD from the effluent. The Mn-modified zeolite efficiency was about 33 %. In this case, the process of adsorptive ozonation seems to be more efficient than adsorption alone (Fig. 6) probably thanks to strong oxidizing properties of ozone which is capable of removing organic pollution expressed as COD. However, the difference is not very significant and using ozone is not feasible due to operation costs.

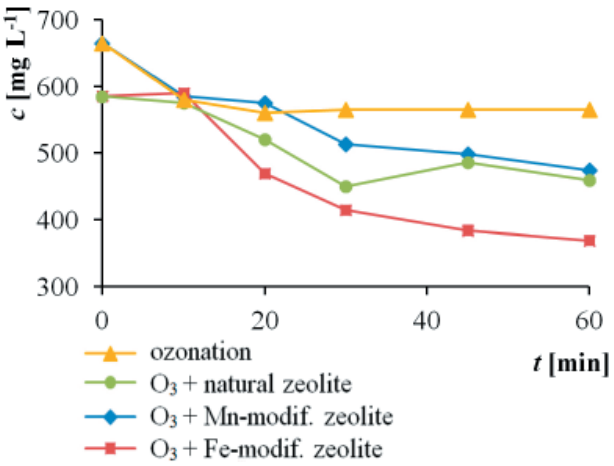

Fig. 11. Time dependence of COD concentration during ozonation and adsorptive ozonation.

Regeneration of zeolites using ozone

Fig. 12 shows the efficiency of ammonium nitrogen removal by repeated adsorption followed by regeneration. Decreasing tendency of the ammonium nitrogen removal efficiency for all types of zeolites is evident, which means that sorption capacity of the zeolites was not completely recovered. In Figs. 13—16, decrease in the concentrations of N-NH_4, P-PO_4, COD and TOC during the adsorption are expressed in the positive direction of the *y*-axis while the amounts desorbed from the zeolite during regeneration are in the negative direction of the *y*-axis. The amounts of nitrogen released from the zeolites in four regeneration cycles ranged from 4.4 mg L^{-1} to 13.1 mg L^{-1} and the amounts of phosphorus ranged from 0.1 mg L^{-1} to 0.3 mg L^{-1}. Residual concentrations of ammonium nitrogen and phosphate phosphorus in the liquid phase after the regeneration of individual zeolites with ozone are a little higher than those after the desorption without the presence of ozone (performed in a stirred reactor using deionized water), where only about 1 mg L^{-1} of ammonium nitrogen and less than 0.8 mg L^{-1} of phosphate phosphorus were desorbed in the same time.

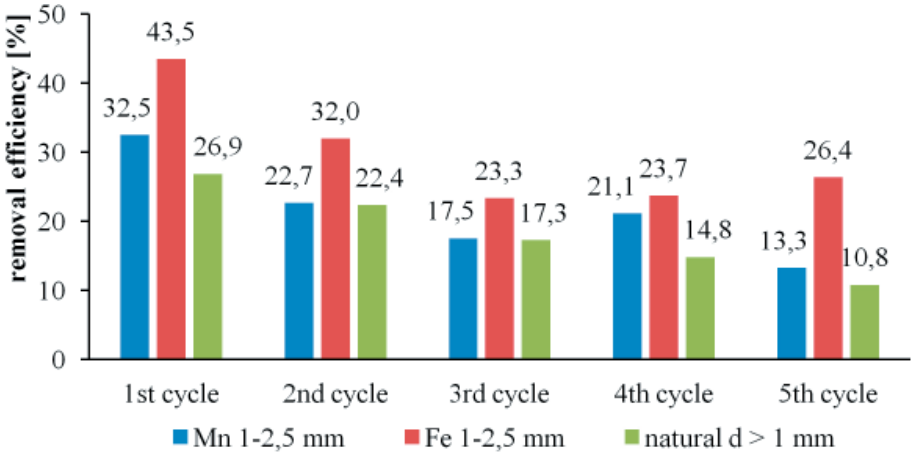

Fig. 12. Efficiency of N-NH_4 removal from real wastewater in five cycles of adsorption and regeneration with O_3.

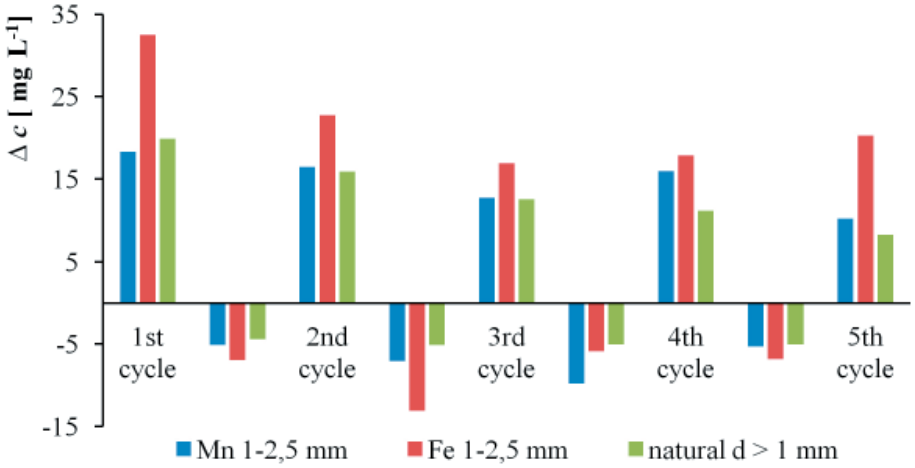

Fig. 13. Change of N-NH_4 concentration in five cycles of adsorption followed by regeneration with O_3.

This suggests that regeneration by ozone takes place on the zeolites surface. The mechanism of adsorptive ozonation can be caused by increased amount of pollutants and ozone concentration on the surface of zeolites and the subsequent oxidation reactions. Another possible mechanism of regeneration is catalytic ozonation, which is accompanied by the formation of free hydroxyl radicals. In case of the studied zeolites, a combination of both mechanisms can be assumed. Another possible explanation is the recovery of free adsorption sites for ammonium nitrogen adsorption by oxidation of the adsorbed

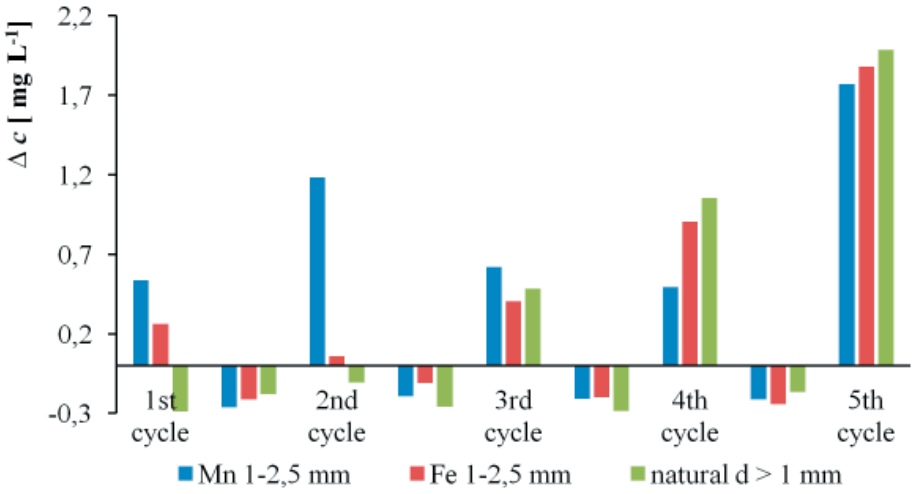

Fig. 14. Change of P-PO_4 concentration in five cycles of adsorption followed by regeneration with O_3.

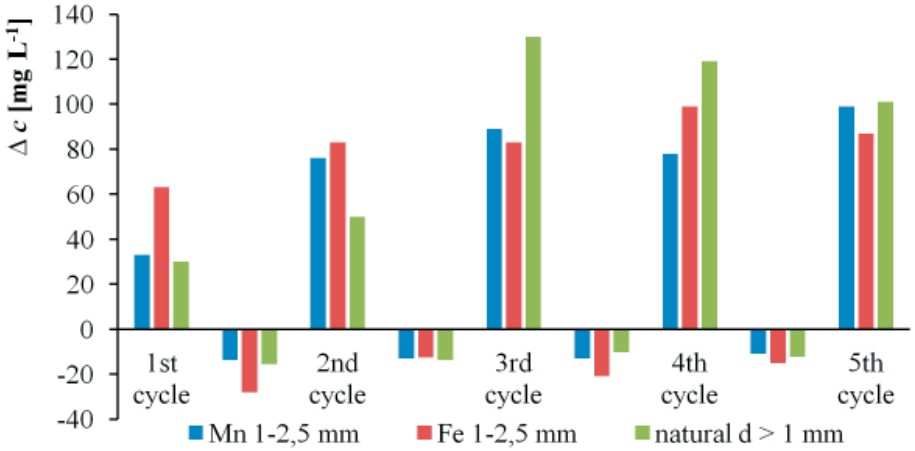

Fig. 15. Change of COD in five cycles of adsorption followed by regeneration with O_3.

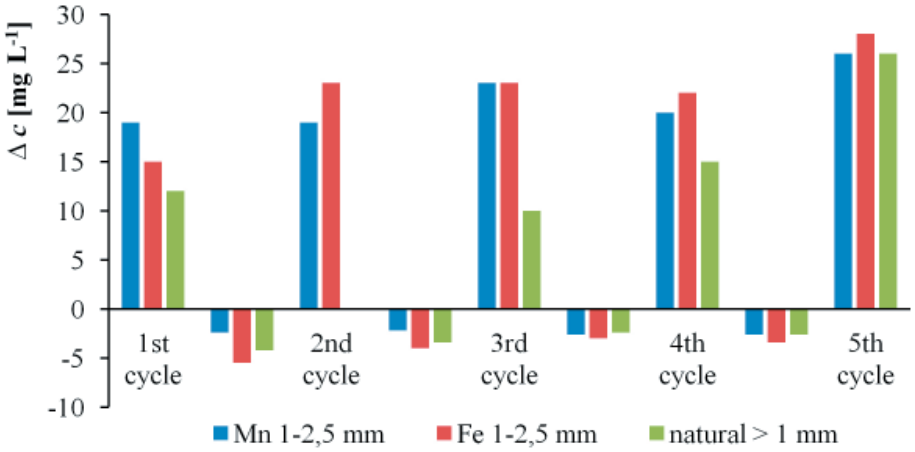

Fig. 16. Change of TOC concentration in five cycles of adsorption followed by regeneration with O_3.

organic pollution. However, further experimental research is needed to verify this hypothesis, including more detailed monitoring of the emerging oxidation intermediates and products.

Natural zeolite caused an increase in the phosphorus concentration in wastewater in the first two adsorption cycles (Fig. 14) probably due to washing-out/desorption from the zeolite. However, from the third cycle on, a significant increase in the adsorption efficiency was observed. Increase of the efficiency was also observed for COD (Fig. 15) and partially also for TOC (Fig. 16) adsorption, which can be attributed to continual cleaning of adsorption sites after longer ozonation time.

Conclusions

All used zeolites showed good adsorption capacities, and while modified zeolites were more efficient, their disadvantage is in their higher price. Fe-modified zeolite was the most efficient in the removal of ammoniacal nitrogen by adsorption, with the highest values of rate constants and the highest adsorption capacity. This zeolite was also more efficient in COD and TOC removal. Phosphate phosphorus removal efficiency using adsorption was relatively low but Mn-modified zeolite was slightly more efficient than the Fe-modified zeolite. Natural zeolite was not suitable for phosphorus removal. Adsorption kinetics was described using the pseudo-first and pseudo-second order models. The pseudo-first order model fitted the experimental data better than the pseudo-second order one.

Comparing adsorptive ozonation with adsorption alone, it can be concluded that adsorption is more efficient for ammonia nitrogen removal since ozone has no significant impact on the removal efficiency. For COD removal, adsorptive ozonation is slightly more efficient but from the economical point of view, adsorption is preferable.

Regeneration of zeolites by ozone has to be further examined. The results obtained show that the ammoniacal nitrogen removal efficiency decreased by approximately 18 % after five adsorption cycles, which means that ozone did not completely recover the adsorption capacity of zeolites. On the other hand, for phosphate phosphorus, COD and TOC removal, adsorption efficiency slightly increased in the five cycles, probably due to adsorption sites cleaning after a longer ozonation time. It seems that regeneration of zeolites by ozone is a possible method, but the mechanism has to be clarified and different ozonation times and number of adsorption cycles have to be tested.

Acknowledgements

This study was supported by the Agency for Research and Development under the contract APVV-0656-12. We also wish to thank the company ZEOCEM, a.s., Slovakia, which has provided zeolites for the experiments.

Abbreviations

COD chemical oxygen demand
$N\text{-}NH_4$ ammonium nitrogen
N_{tot} total nitrogen
$P\text{-}PO_4$ phosphate phosphorus
TOC total organic carbon

References

Bleam W (2017) Surface Chemistry and Adsorption. Soil and Environmental Chemistry. Elsevier: 385—443.

Bowman BT (1982) Conversion of Freundlich Adsorption K Values to the Mole Fraction Format and the Use of SY Values to Express Relative Adsorption of Pesticides. Soil Science Society of America Journal 46(4): 740—743.

Crawford CB, Quinn B (2017) The interactions of microplastics and chemical pollutants. Microplastic Pollutants. Elsevier: 131—157.

Das B, Mondal NK, Bhaumik R, Roy P (2014) Insight into adsorption equilibrium, kinetics and thermodynamics of lead onto alluvial soil. J. Environ. Sci. Technol 11(4): 1101—1114.

Földesová M, Hudec P, Dillinger P (2006) Study of natural sorbent surfaces by physical nitrogen adsorption [*In Slovak*]. Bratislava: FCHPT STU: 27—32.

Fontanier V, Farines V, Albert J, Baig S, Molinier J (2006) Study of catalyzed ozonation for advanced treatment of pulp and paper mill effluents. Wat. Res. 40, 303—310.

Foo KY, Hamed BH (2010) Insight into modeling of adsorption isotherm systems. Chemical Engineering Journal 156: 2—10.

Fujita H, Izumi Y, Sagehashi M, Fuji T, Sakoda A (2004) Adsorption and decomposition of water-dissolved ozone on high silica zeolites. Water Research 38: 159—165.

Ho YS, McKay G (1999) Pseudo-second order model for sorption processes. Process Biochemistry 34(5): 451—465.

Horáková M et al. (2003) Analytika vody. Vysoká škola chemicko-technologická v Praze.

Ishii H, Matsuzawa H, Kobayashi M, Kato M (1978) Method for regenerating an oxidation catalyst. Mitsubishi Rayon Co., Ltd. Japan.

Li D, Yan J, Liu Z (2016) Adsorption kinetic studies for removal of methylene blue using activated carbon prepared from sugar beet pulp. Int. J. Environ. Sci. Technol. 13: 1815—1822.

Lin J, Wang L (2009) Comparison between linear and non-linear forms of pseudo-first-order and pseudo-second-order adsorption kinetic models for the removal of methylene blue by activated carbon. Frontiers of Environmental Science & Engineering in China 3(3): 320—324.

Melicher M (2013) Removal of toxic and resistant substances using ozone [*In Slovak*]. Dissertation thesis, Bratislava: Faculty of chemical and food technology, STU.

Nagy B, Andrada Maicaneanu A, Indolean C, Silvia Burca S, Silaghi-Dumitrescu L, Majdik C (2013) Cadmium (II) Ions Removal from Aqueous Solutions Using Romanian Untreated fir Tree Sawdust — a Green Biosorbent. Acta Chim. Slov. 60 (2): 263—273.

Naushad M, Alothman ZA, Awual MR, Alfadul SM, Ahamad T (2016) Adsorption of rose Bengal dye from aqueous solution by amberlite Ira-938 resin: kinetics, isotherms, and Thermodynamic studies. Desalination and water treatment 57: 13527—13533.

Nethaji S, Sivasamy A, Mandal AB (2013) Adsorption isotherms, kinetics and mechanism for the adsorption of cationic and anionic dyes onto carbonaceous particles prepared from Juglans regia shell biomass. International Journal of Environmental Science and Technology 10 (2): 231—242.

Pitter P (2015) Hydrochemie. 5th edition. VŠCHT Praha.

Plazinski W, Dziuba J, Rudzinski W (2013) Modeling of sorption kinetics: the pseudo-second-order equation and the sorbate intraparticle diffusivity. Adsorption 19(5): 1055—1064.

Qu X, Zheng J, Zhang Y (2007) Catalytic ozonation of phenolic wastewater with activated carbon fiber in a fluid bed reactor. J. Colloid Interface Sci. 390: 429—434.

Reháková M et al. (2003) Utilization of natural zeolite — type clinoptilolite in agrochemistry and agriculture: research report [*In Slovak*]. Košice: Department of inorganic chemistry, University of PJ Šafárik: 260—264.

Ruffino B, Zanetti MC (2011) Bicarbonate and Ammonia Depletion in Ozonized Systems with Bromide Ion, Ozone: Science & Engineering 33 (6): 425—433.

Ruffino B, Zanetti MC (2012) Experimental study on the abatement of ammonia and organic carbon with ozone. Desalination and Water Treatment 37: 130—138.

Shahbazi A, Gonzalez-Olmos R, Kopinke FD, Pezhman Zarabadi-Poor P, Georgi A (2014) Natural and synthetic zeolites in adsorption/oxidation processes to remove surfactant molecules from water. Separation and Purification Technology 127: 1—9.

Simonin JP (2016) On the comparison of pseudo-first-order and pseudo-second-order rate laws in the modeling of adsorption kinetics. Chemical Engineering Journal 300: 254—263.

Tan KL, Hameed BH (2017) Insight into adsorption kinetics models for the removal of contaminants from aqueous solutions. Journal of the Taiwan Institute of Chemical Engineers 74: 25—48.

Tsai T, Sagehashi M, Fuji T, Sakoda A (2005) Adsorptive Ozonation of Organic Pollutants in Zeolite Monolith: a Kinetic Study. In: Proceedings of 2005 AIChE Annual Meeting: Environmental Division: Environmental Applications of Adsorption.

Valdés H, Zaror CA (2006) Ozonation of benzothiazole saturated-activated carbons: Influence of carbon chemical surface properties. J. Hazard. Mater. B137: 1042—1048.

Wang S, Peng Y (2010) Natural zeolites as effective adsorbents in water and wastewater treatment. Chemical Engineering Journal 156-1: 11—24.

Zhang, Y, Mancke, RG, Sabelfeld, M, Geißen, SU (2014) Adsorption of trichlorophenol on zeolite and adsorbent regeneration with ozone. Journal of Hazardous Materials 271: 178—184.